Atomistic Modelling for the Design of Optoelectronic Perovskite Materials

Doctorate of Philosophy Thesis



Allison Nicole Arber

St. Anne's College

Department of Materials Science

University of Oxford

Abstract

Perovskite halides are promising candidates for the development of next-generation optoelectronic devices. Their performance and stability are largely governed by defect physics, ion migration, and surface effects. This thesis employs a range of multiscale computational modelling techniques including DFT, molecular dynamics, and machine learning interatomic potentials to study these key features across a range of perovskite systems and device architectures. The first part of this work explores the role of ion migration in γ-$CsPbI_3$, a promising solar cell thin film material, and investigates how the introduction of cation dopants impacts the presence of ion migration. The second part of this thesis explores the impact of ancillary ligands and dopants on the synthesis of α-$CsPbI_3$ perovskite nanoplatelets for use in polarised light emission devices. The final two studies explore strategies for improving photovoltaic device performance and stability. This includes improving tandem solar cell efficiencies by developing a new Pb–Sn-based absorber material that targets the near-IR region of the solar spectrum and investigates 2D-3D heterostructures as a method of improving device stability via the use of 2D perovskites as capping layers on 3D perovskite thin films. Together, this body of modelling work demonstrates how new atomistic insights into ion migration, material stability, and surface chemistry can guide the design of improved perovskite materials for more stable and efficient optoelectronic devices.

Dedication

This thesis is dedicated to my husband, Alexander James White, without whom this work would not have been possible.

Acknowledgements

First and foremost, I would like to express my sincere gratitude to my supervisor, Prof. Saiful Islam, for his guidance and support throughout my DPhil, particularly in the preparation of this thesis. I am also grateful to the Department of Materials for providing the funding that made this degree possible.

My deepest thanks go to Dr. Vikram, who has gone above and beyond in his role as a postdoctoral supervisor. Much of the work presented in this thesis would not have been possible without his expertise, and I am especially appreciative of the considerable time he dedicated to helping me revise this manuscript.

Furthermore, I am thankful to Dr. Lei Zhu, Dr. Felix C. Mocanu, Dr. Kit McColl, and Chris Davies for sharing their knowledge and insight throughout my degree and for generously helping with the preparation of manuscripts and this thesis. I wish to give special acknowledgement to Mikey Staines for his friendship and for our Branca lunches. I also thank Joanna Lopusinska for her efforts in supporting the entire research group.

I am grateful to my experimental collaborators: Dr. Woo Hyeon Jeong, Dr. Junzhi Ye, and Ashish Gaurav in Prof. Robert Hoye's group in Oxford Chemistry and George Morgan and Dr. Krishanu Dey in Prof. Henry Snaith's group in Oxford Physics. Their contributions and collaboration were invaluable to this work.

In addition, I would like to express my gratitude for the tutors at St. Anne's College, in particular Prof. Sebastian Bonilla and Prof. Chris Grovenor, for their support as well as the Materials Science undergraduates I had the pleasure of teaching. My time teaching first year mathematics as a Graduate Development Scholar was truly a wonderful

experience.

I would also like to acknowledge two close friends. I am deeply grateful to Kipras Tellat Kelpša for always being there for me. I also remember Dr. Adrian Pugh who tragically passed away but will never be forgotten.

Finally, I would like to express my deepest gratitude to my parents, Michael and Jill Arber, for their unwavering belief in me and for their constant support. This thesis would not have been possible without them.

Glossary

ACE Atomic Cluster Expansion
AIMD *Ab initio* Molecular Dynamics
ASE Atomic Simulation Environment

BA Butyl Ammonium
BAc Benzoic Acid
BDA Butyl Diammonium
BFGS Broyden–Fletcher–Goldfarb–Shanno
BPAc Benzyl Phosphonic Acid
BSAc Benzene Sulphonic Acid

CBM Conduction Band Minimum
CI-NEB Climbing Image Nudged Elastic Band

DJ Dion–Jacobson
DOS Density of States
DPPAc Diphenyl Phosphoric Acid

$\mathbf{E}_a$ Activation Energy
ECI Effective Cluster Interactions
EQE Electronic Quantum Efficiency
ETL Electron Transport Layer

FA Formamidinium
FIRE Fast Inertial Relaxation Engine
FTIR Fourier Transformed Infrared
FTO Fluorine-Doped Tin Oxide

GGA Generalized-Gradient Approximation
GNN Graph Neural Network

HOMO Highest Occupied Molecular Orbital
HTL Hole Transport Layer

ICET Integrated Cluster Expansion Toolkit
IR Infrared

LAMMPS Large-scale Atomic/Molecular Massively Parallel Simulator
LBFGS Limited-memory Broyden–Fletcher–Goldfarb–Shanno
LCD Liquid Crystal Display

LDA Local Density Approximation
LED Light-Emitting Diode
LUMO Lowest Unoccupied Molecular Orbital

MA Methylammonium
MACE Multi-Atomic Cluster Expansion
MAE Mean Absolute Error
MHP Metal Halide Perovskite
MPNN Message Passing Neural Network
MSD Mean Square Distribution

NEB Nudged Elastic Band
NMR Nuclear Magnetic Resonance
NPL Nanoplatelet

PAW Projector Augmented Wave
PCE Power Conversion Efficiency
PDOS Partial Density of States
PES Photoemission Spectroscopy
PL Photoluminescence
PLQY Photoluminescence Quantum Yield
PV Photovoltaic
Pymatgen Python Materials Genomics

QD Quantum Dot
QLED Quantum Dot Light Emitting Diode

RDF Radial Distribution Function
RMSE Root Mean Square Error
RP Ruddlesden–Popper

SCF Self-Consistent Field
SOAP Smooth Overlap of Atomic Positions
SOC Spin-Orbit Coupling

VASP Vienna *Ab initio* Simulation Package
VBM Valence Band Maximum
VTST Variable Transition State Theory

XPS X-ray Photoelectron Spectroscopy

Contents

Abstract i

Dedication iii

Acknowledgements v

Glossary vi

1 Introduction 1
- 1.1 A Brief History of Perovskite Optoelectronics . . . 1
- 1.2 The Perovskite Structure . . . 3
  - 1.2.1 Electronic Structure and Band Gap Tunability . . . 6
  - 1.2.2 Point Defect Properties . . . 8
- 1.3 Optoelectronic Applications . . . 9
  - 1.3.1 Perovskite Solar Cell Devices and Architectures . . . 10
  - 1.3.2 Multi-Junction Devices . . . 14
  - 1.3.3 LEDs for Polarised Emission . . . 16
- 1.4 Thesis Aims and Overview . . . 20

2 Methodology 23
- 2.1 Density Functional Theory . . . 24
  - 2.1.1 Time Independent Schrödinger Equation . . . 24
  - 2.1.2 Many-Body Schrödinger Equation . . . 25
  - 2.1.3 Born–Oppenheimer Approximation . . . 28
  - 2.1.4 Slater Determinants . . . 29
  - 2.1.5 Mean-Field Approximation . . . 30
  - 2.1.6 Hartree–Fock Method . . . 30
  - 2.1.7 Hohenberg–Kohn Theorems . . . 32
  - 2.1.8 Kohn–Sham Equations . . . 34
  - 2.1.9 Functionals . . . 35
  - 2.1.10 Plane-Wave DFT . . . 38
  - 2.1.11 Self-Consistent Field Calculations . . . 42
  - 2.1.12 Electronic Structure . . . 43
- 2.2 Numerical Energy Minimisation Algorithms . . . 46
- 2.3 Nudged Elastic Band Calculations . . . 48
- 2.4 Surface Calculations . . . 49
- 2.5 Cluster Expansions . . . 50

2.6 Molecular Dynamics . . . 52
2.6.1 *Ab Initio* Molecular Dynamics . . . 54
2.7 Machine Learning Interatomic Potentials . . . 54
2.7.1 Descriptor Frameworks . . . 56

3 Ion Migration and Dopant Effects in the γ-$CsPbI_3$ Thin Film Solar Cell Material 63
3.1 Introduction . . . 63
3.2 Methodology . . . 66
3.2.1 *Ab initio* Simulations . . . 66
3.2.2 Machine Learning Methods . . . 68
3.3 Results and Discussion . . . 71
3.3.1 Ion Migration in Pristine γ-$CsPbI_3$ . . . 71
3.3.2 Inorganic Dopant Effects on Ion Migration Activation Energies . . . 78
3.3.3 Machine Learning MD Model of Ion Diffusion in γ-$CsPbI_3$ . . . 83
3.4 Chapter Summary . . . 90

4 Ancillary Ligand and Dopant Effects in α-$CsPbI_3$ Nanoplatelets for Polarised Light Emission 93
4.1 Introduction . . . 93
4.2 Methodology . . . 96
4.3 Nanoplatelet Surface Passivation . . . 99
4.3.1 Ligand–Surface Binding Energies . . . 99
4.3.2 Ligand–Surface Electronic Effects . . . 106
4.3.3 Experimental Results and Calculated Charge Analysis . . . 109
4.4 Effects of Zn Addition . . . 111
4.4.1 Zn-Doping Investigation . . . 113
4.4.2 Zn Surface Passviation Investigation . . . 116
4.5 Proposed Mechanism and Supporting Experimental Results . . . 119
4.6 Chapter Summary . . . 122

5 Pb–Sn–S-Based Low Band Gap Materials for Triple Junction Solar Cells 126
5.1 Introduction . . . 126
5.2 Methodology . . . 129
5.3 Pb–Sn–S: Phase Stability . . . 130
5.4 Band Gap Analysis . . . 135
5.4.1 Orthorhombic Unit Cell Results . . . 135
5.4.2 Lowest Energy Structure Results . . . 136
5.4.3 $2 \times 2 \times 1$ Enumeration Results . . . 137
5.4.4 Thermal Averaged and Experimental Results . . . 140
5.5 Electronic Structure Analysis . . . 143
5.6 Chapter Summary . . . 148

6 Towards Understanding 2D-3D Heterostructures for Improved Perovskite Stability **150**
6.1 Introduction . . . 150
6.2 Methodology . . . 153
6.3 2D Perovskite Structures . . . 153
6.4 Phase Stability . . . 156
6.5 Electronic Structure . . . 160
6.6 Ion Migration . . . 164
6.7 Experimental Results . . . 167
6.8 Chapter Summary . . . 168

7 Conclusions and Future Work **170**
7.1 Conclusion . . . 170
7.2 Future Work . . . 172

A **193**

B **196**

C **200**

Chapter 1

Introduction

1.1 A Brief History of Perovskite Optoelectronics

Metal halide perovskites (MHP) have emerged as leading contenders for the development of next-generation optoelectronics. These technologies include perovskite solar cells, light emitting diodes (LEDs), photodetectors, and lasers.[1] While the perovskite structure has been studied since the 1950s, the field exploded with the discovery of the first perovskite solar cell in 2009 which had a power conversion efficiency (PCE) of 3.8%.[2] Since then, the dramatic increase in popularity of perovskite research has lead to ground-breaking achievements across multiple disciplines. Today, single-junction perovskite solar cells have demonstrated 26.95% PCE, all-perovskite tandems have reached 30.1% PCE, and silicon–perovskite tandems have achieved 34.85% PCE (Figure 1.1).[3]

The discovery of the perovskite solar cell quickly led to the application of perovskite halides across a wide range of research fields. This was driven by several useful features of MHPs including band gap tunability, long carrier diffusion lengths, strong optical absorptions, low defect density, and solution processability.[4] The first MHP laser was developed in 2014[5,6] along with the first MHP LED which displayed an electronic quantum efficiency (EQE) of 0.76%.[7] A few years later, the first MHP photodetectors were discovered.[7] The next perovskite breakthrough came from the development of layered per-

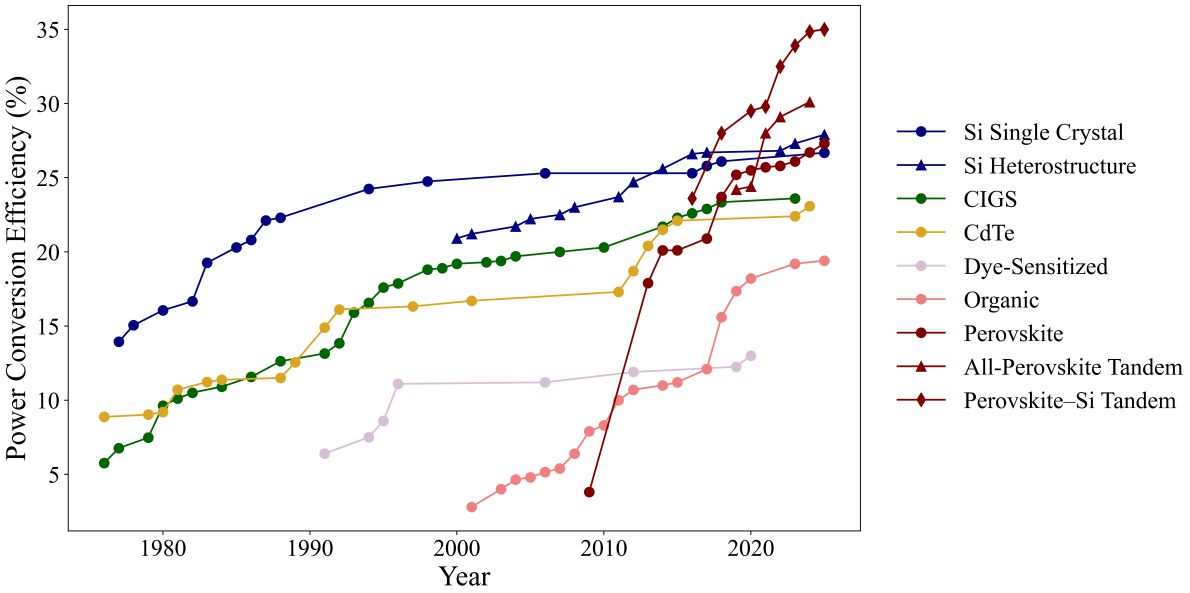


Figure 1.1: Record power conversion efficiency (PCE) measurements illustrating the remarkable rise in efficiency of perovskite solar cells from 3.81% in 2009[2] to over 25% for single-junction devices and now surpassing 30% with the introduction of tandem architectures. Data courtesy of NREL.[3]

ovskites and perovskite nanocrystals. Low-dimensionality materials have demonstrated competitive photoluminescence (PL) and electroluminescence compared to traditional 3D perovskites. These reduced-dimensionality materials include 2D perovskites, perovskite nanoplatelets (NPLs), and perovskite quantum dots. The further development of this new class of perovskite halide materials led to higher efficiency LEDs with EQEs surpassing 20% by 2018.[8–10]

The centre of this vast research field is the perovskite itself. This introduction provides an overview of the perovskite crystal structure and a few key properties of MHPs which are most relevant to the work contained in this thesis. While MHPs have been successfully applied to a wide range of optoelectronic applications, this work focuses on two types of devices: solar cells and LEDs. This introduction will also provide a brief description of these two optoelectronic devices, typical architectures and component materials, and the primary challenges each application faces in the pursuit of commercial device development.

1.2 The Perovskite Structure

Perovskites are materials of the general formula ABX_3. While various forms of perovskites exist such as the perovskite oxides, this work focuses on the metal halide perovskites where A is a large cation such as the organic cations methylammonium (MA^+) or formamidinium (FA^+) or the inorganic cation Cs^+. The B-site is a metal, often Pb^{2+} or Sn^{2+}, and the X species is one or a mixture of halides (Cl^-, Br^-, I^-). The B-site cations sit in octahedral environments coordinated by six halides. These BX_6 octahedra form a three-dimensional corner-sharing lattice with the large A-site cations held in the centre of this lattice, coordinated by twelve halides (Figure 1.2 (a)).

The stability of a perovskite structure has traditionally been represented by the Goldschmidt tolerance factor, t, which uses the radii of the elements in the compositions in relation to each other to predict phase stability with better size match between elements corresponding to higher degrees of phase stability. t is defined as

$$t = \frac{(r_A + r_X)}{\sqrt{2}(r_B + r_X)}, \tag{1.1}$$

where r_A, r_B, and r_X are the radii of the A, B, and X elements, respectively. Phase stable perovskites are considered as those for which $0.9 < t < 1.10$ for cubic structures or $0.81 < t < 0.9$ for orthorhombic structures.[11] It is worth noting that the Goldschmidt tolerance factor provides only a crude estimate of stability, as it does not account for any chemical or electronic features other than the atomic radius. This factor also does not account for the effect of multiple species occupying a single site. As detailed by Albrecht and Karttunen,[12] recent works seek to provide more accurate expressions for the tolerance factor by including features such as oxidation states and lattice orderings. In addition to phase stability, the relative sizes of the elements in these structures determines the degree of octahedral tilting. The high degree of fluxionality within the perovskite structure is also a unique feature of these materials.[11,13]

The $CsPbI_3$ material is the primary perovskite studied in this thesis; it is of particular

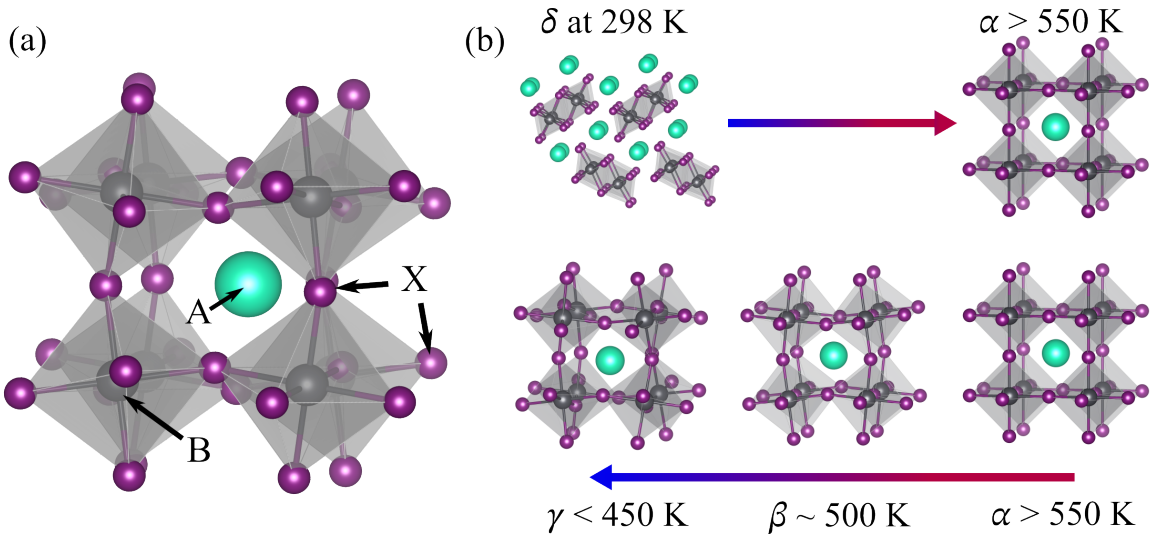


Figure 1.2: (a) Illustration of the ABX_3 perovskite crystal structure γ-$CsPbI_3$, and (b) the phase transition observed upon heating δ-$CsPbI_3$ to form the cubic α-$CsPbI_3$ structure which then transitions through the tetragonal β-$CsPbI_3$ polymorph before forming the room temperature stable orthorhombic γ-$CsPbI_3$ polymorph.[14]

interest as both a thin film material (the typical form used in solar cell applications) and as nanocrystals and nanoplatelets (the common form for LED applications). The structure adopted by $CsPbI_3$ depends on the material form and the temperature (Figure 1.2 (b)). Thin film synthesis occurs at high temperatures above 450 K which initially forms the cubic α-$CsPbI_3$ polymorph. However, upon rapid cooling, the structure transitions through the tetragonal β-polymorph to the orthorhombic γ-polymorph which is the room temperature stable photoactive phase in thin films. The γ-polymorph was not confirmed as the stable form until further characterisation work was published by Sutton *et al.* in 2018;[15] therefore, much of the previous computational work performed on this system focussed solely on the cubic structure. In contrast to thin films, the α-polymorph is the more stable form adopted in nanomaterials such as nanocrystals and nanoplatelets.[16–19]

In addition to the traditional 3D perovskite, another perovskite form is the 2D perovskite which consists of 2D sheets of corner-sharing BX_6 octahedra separated by large organic molecular spacer cations.[21] A range of quasi-2D perovskites exists as defined by the number of inorganic layers in the composition with $n = 1$ defining the pure 2D perovskite. Two structures exist: the Ruddlesden–Popper structures with 1+ molecular

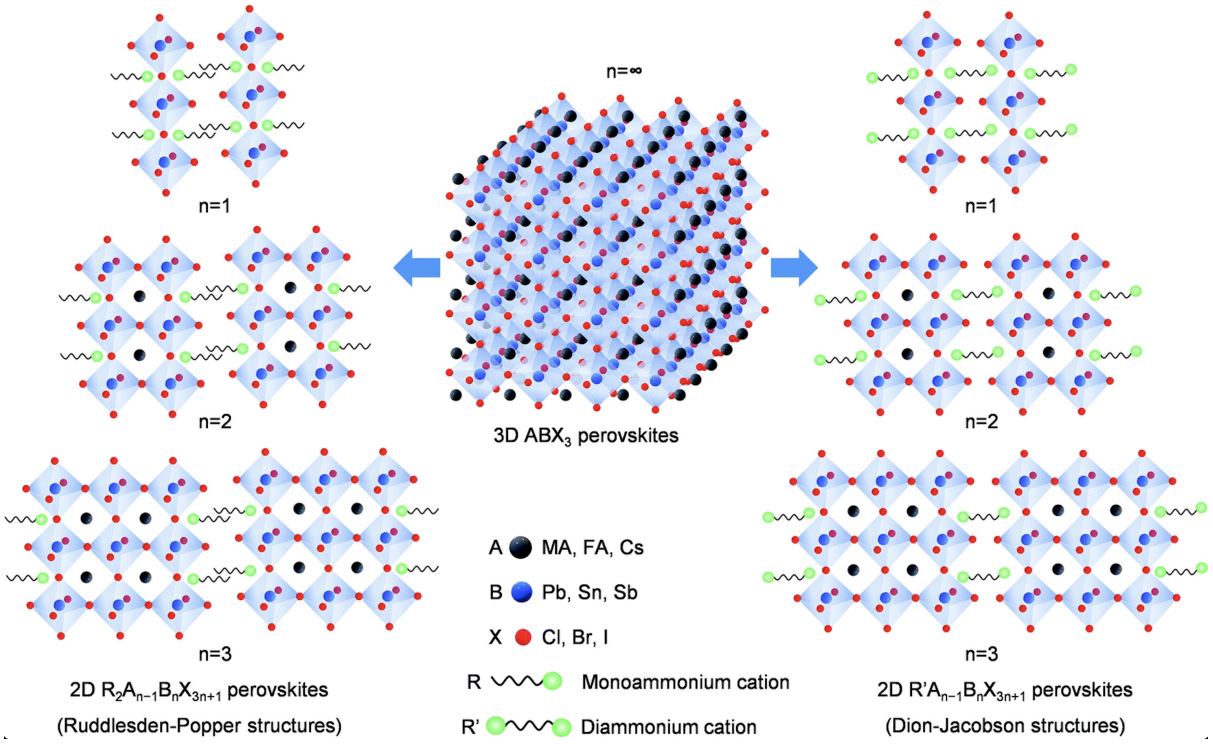


Figure 1.3: Crystal structures of the 2D Ruddlesden–Popper and Dion–Jacobson halide perovskites in comparison to the 3D ABX_3 perovskites. Figure reproduced with permission from Ghimire and Klinke, *Nanoscale*, 2021, **13**, 12394.[20] Copyright © 2021 Royal Society of Chemistry.

spacer cations and Dion–Jacobson structures with 2+ molecular spacer cations (Figure 1.3). These 2D perovskites are formed by self-assembly and present complex semiconducting properties including band-gap tunability,[22] high anisotropy,[23] high photoluminescence quantum yield (PLQY),[24] broadband light emission,[25] strongly bound excitons at room temperature,[26] and large Rashba splitting.[27,28] These materials have demonstrated applications including solar cells,[29] LEDs,[30] and photodetectors.[31] Much like the 3D perovskites, these materials benefit from earth abundant elemental compositions, low cost and low temperature synthesis strategies, and simple solution processing.[32] Notably for the work contained in this thesis, these 2D perovskites can be used to form templated heterostructures consisting of stacked 2D and 3D perovskite structures. These heterostructures have been shown to improve both the efficiency and stability of PV and LED devices. Heterostructure devices have demonstrated thousands of hours of stability in solar cells[33] and LEDs with quantum efficiency beyond 20% with high colour purity

and tunability.[34]

1.2.1 Electronic Structure and Band Gap Tunability

Understanding the electronic structure of the ABX_3 halide perovskites is key to explaining their optoelectronic properties. The band edges are mostly governed by the B–X hybridised states. X p and B s states largely comprise the valence band while X and B p states largely comprise the conduction band. The perovskite electronic structure is fairly unique in that the valence band edge is formed by antibonding states. Considering the perovskite $CsPbI_3$ as an example, the band gap is comprised of antibonding interactions between Pb 6s orbitals and I 5p orbitals at the valence band maximum (VBM) and antibonding interactions between Pb 6p orbitals and I 5p orbitals at the conduction band minimum (CBM) (Figure 1.4 (a)).[35] The high optical absorption characteristic of the MHPs is due to the high symmetry of the perovskite structure which results in a direct band gap with strong p-p transitions between the VBM and CBM.[36] The antibonding character of both the valence and conduction bands results in lower effective electron masses which increases carrier mobilities.[37,38] These features allow for strong optical transitions with high efficiencies.

Any structural changes which alter the degree of B–X overlap, such as octahedral tilting or changes in the cell volume, typically affect the valence band edge to a larger extent than the conduction band due to the valence band antibonding states being occupied. This unequal shift of the valence and conduction band edges results in a change in the band gap which is evidenced by changing the A-site cation. Increasing the effective radius of the A site cation from Cs^+ to MA^+ to FA^+ results in reduced octahedral tilting (bond angles closer to 180°). As the octahedral tilting decreases, the orbital overlap between the Pb and I atoms increases which results in smaller band gaps for $FAPbI_3$ (1.48 eV) than $MAPbI_3$ (1.55 eV) than $CsPbI_3$ (1.73 eV).[40] Another approach for tuning the band gap is via the halide composition. The band gap increases with decreasing halide radius as the energy of the valence p orbitals in the halides decreases from the I 5p orbitals to

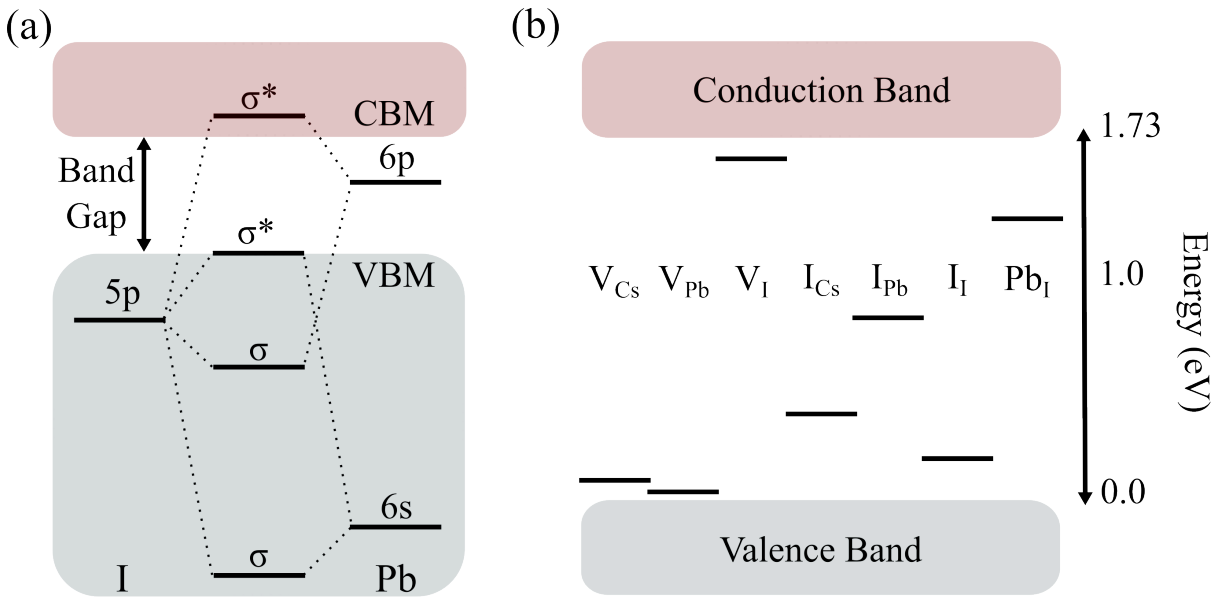


Figure 1.4: (a) Molecular orbital diagram depicting the formation of the $CsPbI_3$ band gap by the antibonding (σ^*) I 5p–Pb 6s interaction in the valence band and the I 5p–Pb 6p interaction in the conduction band. (b) The electronic states introduced into the band gap as a result of point defects in the $CsPbI_3$ perovskite as calculated by Huang *et al.* (2018).[39] The most common defects, I vacancies (V_I), do not introduce deep trap states.

the Br 4p orbitals to the Cl 3p orbitals. As the VBM lowers in energy, the band gap increases. By simply changing the halide composition, the full visible light spectrum can be emitted by perovskite LEDs.[41] These features result in the important property of band gap tunability with compositional adjustments providing fine control over the band gap of the material, making perovskites a practical choice for a wide range of optoelectronic applications.[40,42–44]

In addition to compositional changes, band gap tunability can also occur as a result of reduced dimensionality. These reduced-dimensionality materials can exhibit anisotropic electronic properties due to the introduction of quantum confinement effects which opens up a range of alternative applications.[1,45] Decreasing in dimension from the 3D to the 2D perovskites increases the band gap, introducing the potential use as wide band gap absorbers. Aside from dimensionality, the perovskite synthesis can be adjusted to form a range of nanomaterials such as 3D nanocrystals for quantum dot applications or 2D nanoplatelets for polarised light emission. Not only does changing the dimensionality

of the perovskite tune the band gap, but further tuning can be achieved by controlling the size of the materials such as the number of monolayers in 2D nanoplatelets.[46,47] The ability of the perovskites to adopt such a wide range of band gaps with a high degree of tunability via compositional and structural changes is a strong motivator for the application of perovskites to a vast range of optoelectronics.

1.2.2 Point Defect Properties

Perovskites are considered to be soft materials with a high number of intrinsic defects; although uniquely, despite the high concentration of point defects, these seem to cause relatively few electronic issues which has given rise to the common description of the perovskites as being 'defect tolerant.'[48] The majority of point defects which form in the perovskite at notable concentrations introduce states inside or near the band edges, rather than trap states deep in the band gap (Figure 1.4 (b)). Defect states near the band edges have relatively little impact on non-radiative recombination; therefore, the presence of defects in MHPs causes relatively few electronic losses.[49] The high carrier mobilities and lack of trap states both result in long diffusion path lengths with excitons able to travel long distances to the charge transport layers without recombining.[50] However, in contrast to the traditional understanding, recent computational studies suggest that in addition to the I vacancy, there are a number of defect states with low formation energies that remain accessible, including I interstitials,[51] I dimers,[51,52] and I trimers[53] which can act as non-radiative recombination centres.[54] Overall, the defect chemistry of the lead halide perovskites is a complex subject with a range of implications for device performance.

It is worth noting that this classification of 'defect tolerance' applies primarily from the perspective of the electronic structure, as point defects are linked to fairly prominent structural effects including material degradation.[13] Previous computational work[55,56] has demonstrated that ionic defects are the predominant form of disorder in the halide perovskites with low formation energies associated with Schottky-type vacancy disorder. Electrical measurements in the $MAPbI_3$ perovskite system suggest that halide vacancies

are the primary mobile species which is further supported by the presence of a significant equilibrium concentration of vacancies, calculated at or below 0.4% in $MAPbI_3$. In addition, the measured decrease in ionic conductivity with increasing iodide partial pressure also suggests that iodide vacancies, rather than interstitials, are the primary mobile defects in perovskites.[57–59] The relationship between point defects and ion migration plays an important role in the material properties of the perovskite halides which critically impacts the performance of perovskite optoelectronics and will be discussed further in both Section 1.3.1 and Chapter 3.

1.3 Optoelectronic Applications

The simplicity and affordability of processing techniques associated with perovskite synthesis have provided a substantial driving force for the application of these materials in such a wide range of devices including photodetectors, lasers, and biomarkers.[11,60] Perovskite materials can be synthesised using simple solution processing methods such as spin, spray, and blade-coating or roll-to-roll printing in contrast to the expensive manufacturing procedures required by alternative solar cell materials such as multi-crystalline silicon.[11,61–64]

The synthesis of perovskites with different dimensionalities allows further fine-tuning of the perovskite structure to a range of different applications. In addition to the traditional 3D perovskites, 2D (including quasi-2D perovskites), 1D, and 0D perovskites have all been synthesised. 2D perovskites are sheets of 3D perovskites separated by large spacer molecules. Perovskites can also be synthesised as nanoplatelets or quantum dots which extends their range of applications even further by introducing quantum confinement effects.

Solar cells or photovoltaics (PV) and LEDs are the two applications studied in this thesis. While a range of different perovskite compositions and dimensionalities have all been applied to several forms of device, this work looks at thin film perovskite PV

applications, including both 3D and 2D perovskites, and 2D nanoplatelets (NPLs) for LEDs. In both applications, $CsPbI_3$ is the primary 3D perovskite studied in this thesis.[11]

1.3.1 Perovskite Solar Cell Devices and Architectures

MHPs are leading candidates for next-generation PV materials, primarily due to their record-breaking PCEs (Figure 1.1).[3,65] Hybrid organic–inorganic perovskite solar cells have achieved efficiencies exceeding 26%,[66–68] while the all-inorganic perovskite $CsPbI_3$ has reached a record of 21.15%.[69,70] Inorganic halide perovskites are the primary perovskite studied in this thesis, as they exhibit superior thermal stability and resistance to degradation under light and humidity compared to their hybrid counterparts.[71,72] Notably, several $CsPbX_3$ (X = Cl, Br, I) compositions prepared under ambient conditions have demonstrated one to two months of stability with minimal efficiency loss, even without encapsulation.[71,73] This enhanced stability has made γ-$CsPbI_3$ a particularly attractive candidate for single-junction devices. Its band gap of 1.73 eV[15,74] is also well-suited for both silicon–perovskite and perovskite–perovskite tandem solar cells, enabling PCEs that surpass theoretical limits.[75,76]

Solar cell devices generate electricity via a three step process (Figure 1.5 (a)): (i) photons are absorbed generating charge carriers; (ii) the charge carriers are transported to the metal contacts; and (iii) the metal contacts extract the charge carriers to the external circuit.[78] The perovskite absorbs a photon typically generating an exciton: a bound electron–hole pair. The electron and hole rapidly dissociate as exciton binding energies are typically less than thermal energy at room temperature in the MHPs, resulting in an unbound electron which migrates to the electron transport layer (ETL) and an unbound hole which migrates to the hole transport layer (HTL). Following dissociation, the electrons in the ETL migrate towards the anode, and the holes in the HTL migrate towards the cathode. The collection of electrons and holes creates a current in the external circuit which generates electricity. The flow of charge carriers occurs due to the precise band alignment of these transport components. The excited electrons are held in

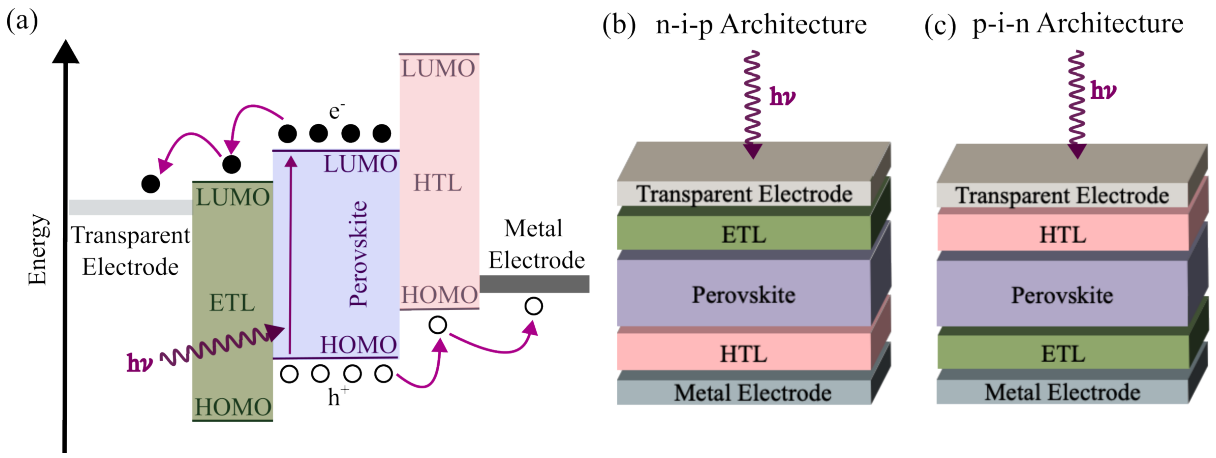


Figure 1.5: (a) Good band alignment between the perovskite absorber material, ETL, HTL, and metal contacts reduces losses. Excited electrons in the perovskite LUMO flow into the ETL LUMO before reaching the anode while the positively charged holes flow from the perovskite HOMO to the HTL before joining the external circuit at the cathode.[11] Perovskite solar cells typically take one of two architectures: (b) the traditional n-i-p architecture or (c) the inverse p-i-n architecture. While perovskite solar cells have traditionally been designed using the n-i-p architecture, the p-i-n format has become increasingly more popular. In both architectures, the devices are fabricated starting with the transparent electrode at the bottom.[77]

the perovskite's lowest unoccupied molecular orbital (LUMO) in the conduction band. These excited electrons then move into the LUMO of the ETL which must be slightly lower in energy to ensure efficient charge transport. Similarly, migration of the excitons into the anode is controlled by a slight decrease in energy compared to the LUMO of the ETL. Migrating in the opposite direction, holes move from the highest occupied molecular orbital (HOMO) of the perovskite to the HOMO of the HTL and finally into the metal electrode where they are extracted.[11,77]

Two common architectures are the n-i-p and p-i-n configurations (Figure 1.5 (b) and (c)), where n and p describe the type of charge carrier being transported: n for negative or p for positive. This terminology is a reference to the n- and p-doped silicon wafers used to transport charge in silicon solar cells. Both architectures contain an absorber layer, ETL, HTL, transparent conductive oxide, and a metal contact. The theory is the same in both, but the deposition order is inverted. Starting with the substrate on top, the n-i-p architecture begins with a transparent electrode, then an ETL layer,

followed by the perovskite, then an HTL layer, and finally the bottom metal contact. For this architecture, Spiro-MeOTAD (2,2',7,7'-tetrakis[N,N-di(4-methoxyphenyl)amino]-9,9'-spirobifluorene) is a common choice of HTL, and TiO_2 and SnO_2 are common ETLs. The p-i-n architecture begins with a transparent electrode, then deposition of an HTL layer, followed by the perovskite, then the ETL, and finally the metal electrode at the back. In the p-i-n architecture, PTAA (poly[bis(4-phenyl)(2, 6-trimethylphenyl)amine]), PEDOT:PSS (poly(3,4-ethylenedioxythiophene:poly(styrenesulfonate)), and NiO are common HTLs and C_{60} and $PC_{60}BM$ are common ETLs. Typically, fluoride-doped tin oxide (FTO) is the transparent electrode in both architectures.[11]

The n-i-p architecture has traditionally been the most common choice due to ease of process optimisation and high reported efficiencies; however, the p-i-n architecture has gained in popularity due to its improved HTL compatibility with a variety of materials and reported suppression of hysteresis. The gentler processing techniques available also make p-i-n architectures more promising for flexible electronic manufacturing. Both architectures share the disadvantages of requiring further HTL optimisation and surface passivation to stabilise the perovskite and metal electrodes (typically Ag or Au) introduce stability issues and environmental concerns.[11] Perovskite solar cell device optimisation is a broad and active research field which is not the focus of this thesis; however, it is important as a background consideration that all components within the solar cell must be considered holistically for the development of commercially viable perovskite solar cells.

Perovskite Instability

The primary challenge of the perovskites is the issue of long-term operational instability. All perovskites struggle with degradation of the photoactive black phase to the inactive yellow δ-phase. Perovskite stability is also negatively impacted by exposure to moisture, oxygen, heat, light, the external bias, and the metal contact layers.[79] The effect of light can catalyse the oxidation of halides to form molecular halogens which also enhances perovskite degradation.[80] The synthesis route of the perovskite thin film also impacts the

stability of the perovskite; for instance, increased densities of grain boundaries have been linked to accelerated degradation.[81]

Ion migration is a significant factor contributing to perovskite instability and short device lifetimes. The presence of ion migration reduces PV efficiency during operation via voltage–current hysteresis.[36] Build-up of halide ions at surfaces and grain boundaries also leads to structural degradation due to the formation of defect clusters,[82–84] and phase segregation can result in band-bending effects which reduce device performance by misaligning the electronic states involved in charge transport.[55] Furthermore, while traditional defect literature considered point defects to be relatively harmless, more recent studies have linked ion migration to the formation of halide dimers and trimers which can act as exciton recombination centres.[51,85–87] As a result of its many negative implications, ion migration has become an important field of study.

One strategy for improving perovskite stability is the introduction of dopants. A range of doping strategies have been suggested to improved grain characteristics, reduced charge recombination, and increase material stabilities.[88–97] These positive effects have often been attributed to reduced ion migration despite little experimental understanding of the precise role doping plays on ion migration in perovskites. Chapter 3 explores both the presence of ion migration in γ-$CsPbI_3$ and investigates the impact small concentrations of inorganic cation dopants have on the presence of ion migration.

Another strategy to improve stability is the mixing of 2D and 3D perovskites to create 2D-3D heterostructures. The combination of these two structures results in improved grain orientation, passivation of defects, and reduced ionic diffusion into the charge transport layers.[20,98–102] The clean interfaces displayed by these heterostructures improve charge carrier lifetimes with suppressed recombination.[98] The improved stability displayed by 2D-3D heterostructures has also been linked to longer PCE lifetimes.[33,103] Solar cell thin films capped with 2D perovskite layers demonstrates higher stability and longer lifetimes under light, heat, and moisture with some devices maintaining over 95% of their starting PCE for over 1000 hours.[104,105] While the development of 2D-3D heterostructures

remains in the early stages, the experimental results are promising. A computational investigation into the properties of these heterostructures is discussed in Chapter 6.

1.3.2 Multi-Junction Devices

All solar cells are limited in efficiency due to the physics underpinning device operation. The Shockley–Queisser limit estimates the ideal maximum efficiency possible for a material of a particular band gap.[106] This model accounts for five types of losses as demonstrated in Figure 1.6 (a) which plots the fraction of percent efficiency lost for a material given a particular band gap (E_g). The two largest forms of loss are 'below E_g' losses and thermalisation losses. 'Below E_g' loss is due to the non-absorption of photons with energies below the band gap. Naturally, this form of loss increases as the band gap also increases in energy. Thermalisation occurs when electronic energy is lost in the form of heat. This can occur as the result of energy mismatch between the photons absorbed and the band gap. When a photon with an energy larger than the band gap of the material is absorbed, the resulting exciton is formed in an excited state, higher in energy than the exciton ground state. This excited electron relaxes as it passes from the absorber to the ETL with the excess energy dissipating via phonons in the lattice. This energy released as heat is not collected, and therefore amounts to an energetic loss.

Another form of thermalisation is nonradiative recombination which occurs when an exciton and hole recombine, and the energy is released by the formation of a phonon. Electron-hole recombination occurs when an excited electron in the conduction band recombines with a hole in the valence band, resulting in the loss of a charge-carrier that could be extracted. This process often occurs due to interaction of the charge-carrier with a defect trap state or via surface recombination pathways, and it can critically decrease device performance by reducing the number of excitons harvested.[54] Boltzmann losses describe the energy lost as the result of mismatch between absorption and emission which results in entropy generation.

The final two forms of losses are by far the smallest: Carnot losses and emission.

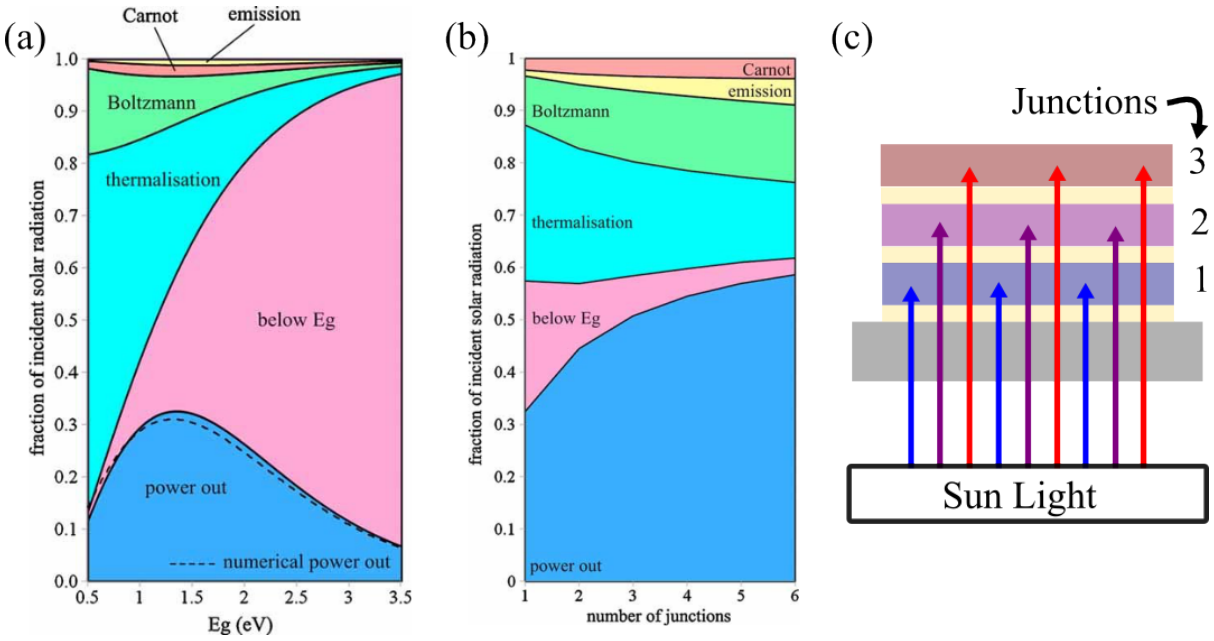


Figure 1.6: (a) The fraction of light lost via the five types of losses that contribute to the Shockley–Quiesser limit (i) 'below E_g', (ii) thermalisation, (iii) Boltzmann, (iv) Carnot, and (v) emission as a function of absorber band gap (E_g). (b) The change in efficiency limit as a function of number of absorbers. (c) A diagram illustrating how stacking absorbers of different band gaps improves efficiencies by reducing 'below E_g' losses. Figures (a) and (b) are reproduced with permission from Hirst and Ekins-Daukes, *Prog. Photovolt: Res. Appl.*, 2011, **19**, 286–293.[106] Copyright © 2010 John Wiley & Sons, Ltd..

The conversion of thermal energy into electric work inherently incurs an energy penalty (Carnot factor), and some excitons will undergo radiative recombination (emission) which again causes a loss of efficiency. The sum of these losses at a given band gap define the maximum theoretical efficiency of a solar cell (power out).

As can be seen, the two largest forms of losses are due to photons of a lower energy than the band gap not being absorbed and losses to heat following absorption. The focus of research into limiting thermalisation loss includes improved synthesis strategies for smoother grains in thin films,[61] more effective defect and surface passivation strategies,[107] and introduction of new methodologies such as hot carrier collection.[108] The second primary form of loss, 'below E_g' losses, can be tackled by introduction of multi-junction PV architectures.

Multi-junction tandem solar cells seek to improve efficiency limits by stacking multiple

absorber layers (Figure 1.6 (b)). The device architectures remain the same but combine two or more absorber materials with different band gaps. Pairing different band gap absorbers targets different regions of the solar spectrum, resulting in the absorption of more photons which reduces the 'below E_g' losses (Figure 1.6 (c)). The introduction of multiple junctions also causes a slight decrease in thermalisation losses, as fewer excitons would be formed in energetic states high above the CBM.[11,106] Typically, a low band gap absorber, either silicon with a 1.1 eV band gap[109] or a mixed Pb–Sn perovskite,[110,111] would be paired with a wide band gap perovskite such as $CsPbI_3$ to form a tandem architecture.[112] As an additional route to further improving multi-junction device efficiencies, this thesis proposes a low band gap material in the Pb–Sn–S family that can further improve device efficiency by absorbing photons in the near-IR region which has previously been neglected.

1.3.3 LEDs for Polarised Emission

Beyond PV, MHPs have also garnered attention for applications in LEDs due to their narrow emission linewidths and bright photoluminescence.[113–118] In contrast to the thin films discussed in the previous sections which are used for solar cell devices, reduced-dimension perovskites such as nanoplatelets (NPLs), nanocrystals, or quantum dots (QDs) are the perovskite form typically used in light emission applications. Semiconductor nanocrystals were discovered separately by Alexei Ekimov and Alexander Efros in the USSR and Louis Brus at Bell Laboratories in the 1980s.[119] A special 2D version of the nanocrystal called the nanoplatelet (NPL) is the material of focus in the LED work discussed in this thesis. The first NPLs reported were made of CdSe in 2011 by Ithurria *et al.*,[120] and these materials quickly gained interest due to colour conversion applications such as in liquid-crystal displays (LCDs), micro-LEDs, and quantum-LEDS (QLEDs). The modern Samsung QLED display is evidence of the technological importance of these materials. QLEDs are created out of liquid crystals which utilise optically excited QDs.[119]

The common device architecture for perovskite LEDs combines the perovskite material

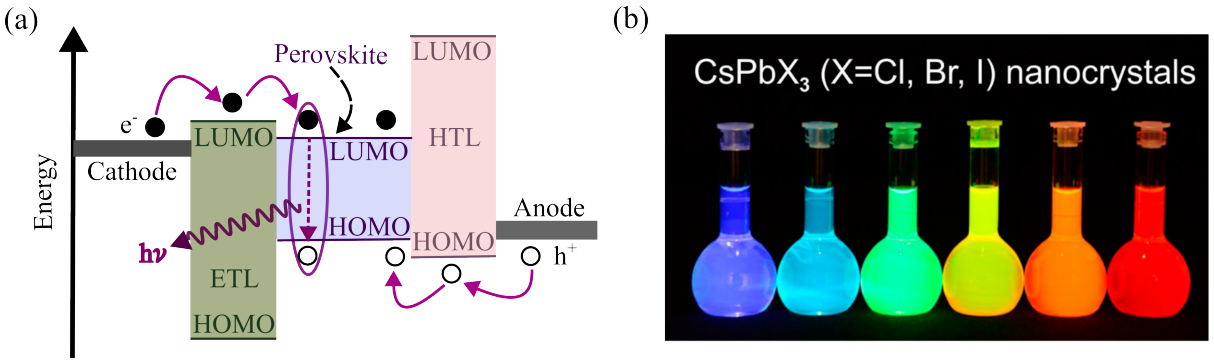


Figure 1.7: (a) Schematic of the band alignment of the charge transport layers in a perovskite LED device. (b) Range of colours emitted by tuning $CsPbX_3$ perovskite compositions. Figure reproduced with permission from Protesescu *et al.*, *Nano. Lett.*, 2015, **15**, 3692–3696.[121] Copyright © 2015 American Chemical Society.

with an n-type ETL and a p-type HTL similar to the PV devices discussed previously. However, in an LED, charge carriers are injected into the perovskite where they radiatively recombine to emit light. Just as for solar cell devices, the band alignment of the charge transport layers is critical for effective transport and efficient light emission (Figure 1.7 (a)). Several forms of perovskites are utilised for LEDs including the traditional 3D perovskite thin films as well as layered or nanostructured perovskites.[122,123] In 2015, Protesescu *et al.*[121] were the first to synthesise a $CsPbX_3$ halide perovskite nanocrystal with demonstrated emission across the entire visible spectrum. This work synthesised 'perovskite-based colloidal quantum dot materials' with dimensions ranging between 4–15 nm. Tuning of the nanocrystal composition provides fine control over the colour emitted, allowing the whole visible light spectrum to represented ($CsPbI_3$ in the red region all the way to $CsPbCl_3$ in the purple region).[124] The range of colours emitted by these nanocrystals is reproduced in Figure 1.7 (b).

The perovskite LED application studied in this work is specifically designed to emit polarised light. This is achieved by utilising 2D perovskite NPLs which introduce quantum confinement in only a single direction which produces emission preferentially in the plane of the NPL. Synthesis of these NPLs requires very fine control to produce a well-ordered superlattice as depicted in Figure 1.8 and generally involves the following growth phases: (i) reaction of the precursors leads to the initial formation of an intermediate

phase. The precursor make-up determines which orientation and phases are created. (ii) Nucleation of the crystalline material begins followed by (iii) growth of the NPL. Finally, (iv) ligands are added to quench further growth of the NPLs. In order for NPL synthesis to be suitable for technological applications, it is critical that the NPLs produced are of uniform size. This requires strict control over both the growth kinetics which occur during the initial nucleation and growth stages as well as during the quenching phase. A narrow distribution of NPL widths ensures a uniform LED emission.[124]

In addition to ligands, the inclusion of metal halide species in the precursor solution has also been linked to improved NPL synthesis properties. While these metal additives are not believed to dope into the bulk of the perovskite at high concentrations,[125,126] their presence in the precursor solution provides a driving force for the formation of ultrathin and highly monodisperse NPLs with improved PLQY (greater than 85%) which is suggested to be a result of improved short-range lattice order and reduction of intrinsic defects such as halide vacancies.[127] A recent breakthrough in the field,[128] the effects of metal halide addition into the NPL synthesis are explored further in Chapter 4.

Polarised emission occurs as a result of quantum confinement,[119,130,131] a quantum effect which increases the kinetic energy of a particle such as an electron when confined in a smaller volume.[124] Nanoplatelets are quasi-two-dimensional colloids with one dimension much smaller than the other two. Typically NPLs target monolayer widths of $\leq$3 due to dramatic increases in exciton binding energy and high PLQYs at room temperature for these narrow NPLs. Other properties displayed include intensified oscillator strength and optical non-linearities making these materials ideal for LED applications.[46,47] Figure 1.8 (b) illustrates how exciton fine structure splitting creates bright states which allows for strong polarised emission. NPL colloidal semiconductors demonstrate fluorescence lifetimes much shorter than other colloidal particles, wide tunability of narrow absorption, and PL emission via fine control over monolayer widths.[120]

The primary challenge facing NPL synthesis is that perovskite growth occurs quickly due to high ionicity and low formation energies which typically leads to the synthesis of

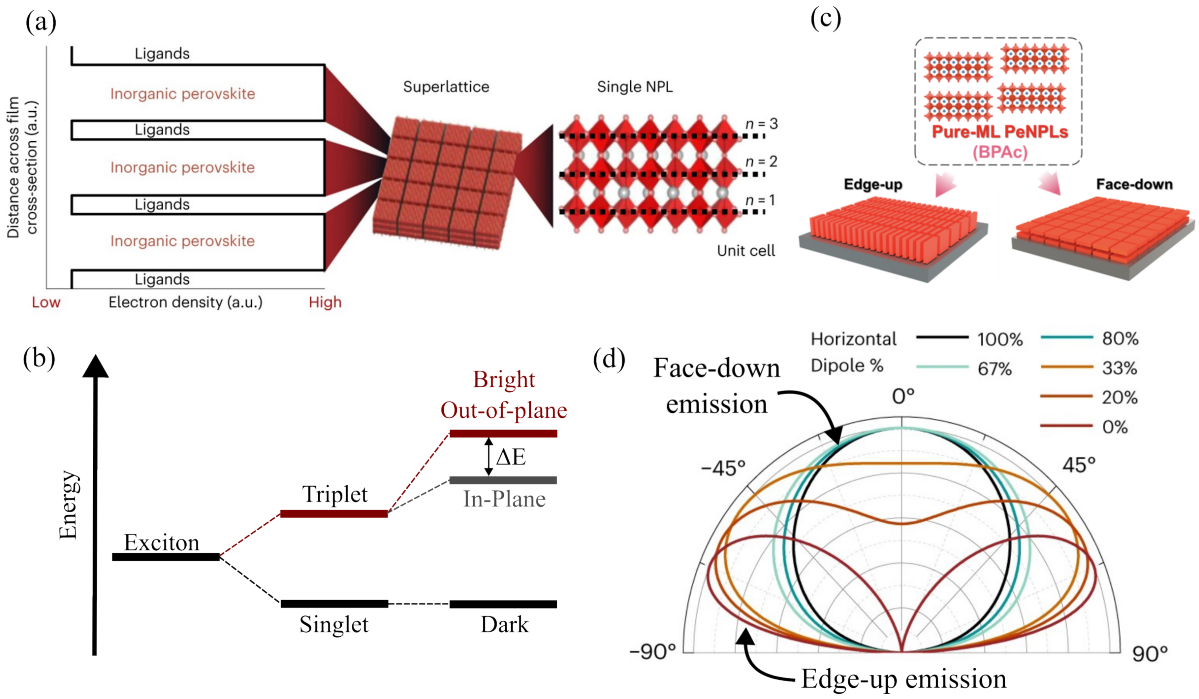


Figure 1.8: (a) Diagram of the perovskite 2D nanoplatelet superlattice synthesised for polarised LED applications demonstrating the $n = 1, 2$, and 3 monolayer widths. (b) Depiction of the exciton fine structure splitting induced as a result of quantum confinement which allows for polarised light emission. (c) Illustration of two superlattice orientations: edge-up and face-down. (d) The polarised emission patterns observed as a function of face-down down nanoplatelet percentage. Figures (a) and (d) are reproduced from Ye *et al.*, *Nat. Photonics*, 2024, **18**, 586–594[18] under the Creative Commons License: https://creativecommons.org/licenses/by/4.0/. Published by Springer Nature. Figure (c) is reproduced courtesy of Kim *et al.* (pre-print).[129]

a range of NPL widths rather than preferential synthesis of a single monolayer width.[92] This variability in size broadens the emission profile and reduces the degree of electronic and optical uniformity, thereby reducing the usefulness of the material for technical applications.[132,133] Size-mismatch also effects the superlattice ordering. Figure 1.8 (c) shows two perfectly-aligned super-lattices, one in the edge-up orientation and the other in the face-down orientation. Any degree of misalignment within the superlattice reduces the degree of polarisation achievable, as the direction of emitted light is directly determined by the orientation of the NPLs (Figure 1.8 (d)). Differently sized NPLs lead to misalignment within the superlattice which reduces the degree of polarisation of emitted light, and this misalignment also reduces the stability of the NPL superlattice. As a result, achiev-

ing high monodispersity through understanding the NPL synthesis route and stability is critical for the development of NPLs which have the degree of polarisation necessary for commercialisation. Currently, perovskite NPLs synthesised for polarised light emission struggle with low degrees of polarisability, poor quantum efficiencies, and reduced stability as a result of high thickness and poor monodispersity during synthesis.[102,134] This topic of research comprises the body of work contained in Chapter 4.

1.4 Thesis Aims and Overview

Many of the key processes governing the performance and stability of MHPs originate at the atomic scale in phenomena such as defect formation, ion migration, and surface passivation. While experimental techniques have provided significant insights into the behaviour of these materials, they often lack the ability to probe the atomistic mechanisms underpinning these key properties. As a result, computational modelling has emerged as a powerful approach for understanding and predicting the properties of MHPs. *Ab initio* modelling based on density functional theory (DFT) calculations enable the investigation of fundamental properties of the perovskites such as the electronic structure, ion migration pathways, and surface chemistry. Molecular dynamics calculations allow for longer timescales and larger systems to be modelled allowing ion diffusion pathways to be directly probed and statistical information to be derived such as migration barriers. The development of machine learning interatomic potentials has allowed molecular dynamics simulations to be theoretically performed at the same levels of accuracy as DFT simulations. The overall objectives and new science described in this thesis involves combining these multiscale modelling approaches to provide a multifaceted analysis of the perovskite properties which determine device performance and to gain atomistic insights that can guide the design of more efficient and stable perovskite optoelectronics.

The methods used in this work, including DFT, molecular dynamics, and machine learning methods, are discussed in the following chapter (Chapter 2). The first results

chapter of this thesis (Chapter 3) explores the role of ion migration in γ-$CsPbI_3$, a promising solar cell thin film material, and investigates how the introduction of cation dopants effects the presence of ion migration. The second results chapter (Chapter 4) explores the impact of ancillary ligands and dopants on the synthesis of α-$CsPbI_3$ perovskite NPLs for use in polarised light emission devices. The third results chapter (Chapter 5) seeks to improve perovskite tandem solar cell efficiencies by developing a new absorber material that targets the near-IR region of the solar spectrum. Finally, the fourth results chapter (Chapter 6) investigates 2D-3D heterostructures as another method of improving perovskite stability via the use of 2D perovskites as capping layers on 3D perovskite thin films. This body of work provides a basis for the further development of perovskite optoelectronics in the fields of multi-junction photovoltaics with improved device lifetimes and performances and LEDs for polarised light emission.

Chapter 2

Methodology

This chapter summarises the wide range of multi-scale modelling techniques used in this thesis to study material systems from the angstrom to nanometre scale over timescales ranging up to nanoseconds. The selection of research methodology is driven by the scientific question under consideration; each method is chosen to best address the phenomena of interest. The majority of work contained in this thesis is based on density functional theory (DFT) which has become a popular *ab initio* computational method for investigating and predicting materials properties due to its accuracy and transferability across a wide range of systems.[135] Several types of DFT calculations are performed in this work including nudged elastic bands, surface binding energies, and band structure calculations which are surveyed in this chapter. The specific functionals and convergence parameters relevant to each investigation are detailed in the methodology sections of each of the following results chapters with additional information provided in the Appendices. Beyond the *ab initio* methods, molecular dynamics and machine learning interatomic potentials are also discussed in addition to a variety of supporting methods such as Bader charge analysis.

2.1 Density Functional Theory

Density functional theory (DFT) is an *ab initio* simulation method meaning that it is derived from first principles and provides a quantum mechanical model of a system. This section describes the development of DFT from its derivation via the Schrödinger equation through its implementation via numerical methods in modern DFT codes.

2.1.1 Time Independent Schrödinger Equation

Quantum mechanical information is derived from the Schrödinger equation.[136] Solving this equation exactly would provide an exact description of any system; however, this equation depends on the positions and momenta of every nuclei and electron in the system. As a result, solving this equation becomes computationally prohibitive for systems containing more than a few electrons. As such, an exact solution for any crystalline material is inaccessible; therefore, approximate methods such as DFT have been developed to model these systems. The following overview of the derivations underlying modern DFT are based on the discussion contained in Giustino (2014).[135]

The time independent Schrödinger equation,

$$\hat{H}\psi = E\psi, \tag{2.1}$$

calculates the energy eigenvalue, E, corresponding to the wavefunction, ψ, via the Hamiltonian operator, $\hat{H}$. The Hamiltonian calculates the total energy of a system; therefore, intuitively, the form of the Hamiltonian consists of a sum of a kinetic energy operator and a potential energy operator in the form of

$$\hat{H} = -\frac{\hbar^2}{2m}\nabla^2(\mathbf{r}) + V(\mathbf{r}), \tag{2.2}$$

where $\hbar$ is the reduced Planck constant and ∇^2 represents the Laplacian operator,

$$\nabla^2 = \frac{\delta^2}{\delta x^2} + \frac{\delta^2}{\delta y^2} + \frac{\delta^2}{\delta z^2}. \tag{2.3}$$

$V(\mathbf{r})$ represents the potential energy, and $\mathbf{r}$ is a vector representing a point in space. For a single electron, this equation can be re-written as

$$\left[-\frac{\hbar^2}{2m_e}\nabla^2(\mathbf{r}) + V(\mathbf{r})\right]\psi(\mathbf{r}) = E\psi(\mathbf{r}), \tag{2.4}$$

where m_e is the mass of the electron. To ensure sensible probabilities, the probability density of the wavefunction is normalised such that

$$\int |\psi(\mathbf{r})|^2 d\tau = 1, \tag{2.5}$$

where $|\psi(\mathbf{r})|^2$ represents the probability of finding a single electron at a given point in space, τ.

2.1.2 Many-Body Schrödinger Equation

To expand this representation from a single electron to a system containing multiple electrons and nuclei, the many-body wavefunction, Ψ, is introduced which depends on the coordinates of N electrons: $\mathbf{r}_1, \mathbf{r}_2, \mathbf{r}_3, ..., \mathbf{r}_N$ and the coordinates of M nuclei: $\mathbf{R}_1, \mathbf{R}_2, \mathbf{R}_3, ..., \mathbf{R}_M$. In this representation, the probability of finding a particle at a single point in space, $\mathbf{r}_1$, while the location of the other particles remains unknown is given by

$$P(\mathbf{r}_1 = \mathbf{r}) = \int |\Psi(\mathbf{r}, \mathbf{r}_2, ..., \mathbf{r}_N; \mathbf{R}_1, \mathbf{R}_2, ..., \mathbf{R}_M)|^2 d\mathbf{r}_2 ... d\mathbf{r}_N d\mathbf{R}_1 ... d\mathbf{R}_M. \tag{2.6}$$

This formalism allows the electron density, $n(\mathbf{r})$, to be written as the sum of the probabilities of finding any electron at a given point in space:

$$n(\mathbf{r}) = P(\mathbf{r}_1 = \mathbf{r}) + P(\mathbf{r}_2 = \mathbf{r}) + ... + P(\mathbf{r}_N = \mathbf{r}). \tag{2.7}$$

Based on the particles being indistinguishable, the previous Eqn. 2.6 can be simplified as

$$n(\mathbf{r}) = N \int |\Psi(\mathbf{r}, \mathbf{r}_2, ..., \mathbf{r}_N; \mathbf{R}_1, \mathbf{R}_2, ..., \mathbf{R}_M)|^2 d\mathbf{r}_2 ... d\mathbf{r}_N d\mathbf{R}_1 ... d\mathbf{R}_M. \tag{2.8}$$

Given the integral of the particle density over all space must be normalised as demonstrated in Eqn. 2.5, this equation can be further reduced to

$$\int n(\mathbf{r}) d\mathbf{r} = N \tag{2.9}$$

which illustrates the intuitive result that the integral of the particle density over all space must equal the number of electrons in the system. The electron density will be discussed further in the Kohn–Sham Section 2.1.8.

To finish calculating the many-body form of the Schrödinger equation, the Hamiltonian operator must be re-written to include the contributions from all particles. The kinetic energy operator, $\hat{T}$, is broken into two sums: one each for the kinetic contributions of the electrons, $\hat{T}_e$, and the nuclei, $\hat{T}_n$, resulting in

$$\hat{T} = \hat{T}_e + \hat{T}_n = -\sum_{i=1}^{N} \frac{\hbar^2}{2m_e} \nabla_i^2 - \sum_{I=1}^{M} \frac{\hbar^2}{2M_I} \nabla_I^2. \tag{2.10}$$

The potential energy operator, $\hat{V}$, can be similarly updated to include Coulombic interactions between electrons and nuclei with the following three terms:

$$\hat{V}_{ee} = \frac{1}{2} \sum_{i \neq j} \frac{e^2}{4\pi\epsilon_0} \frac{1}{|\mathbf{r}_i - \mathbf{r}_j|} \tag{2.11}$$

representing Coulombic repulsion between electrons;

$$\hat{V}_{nn} = \frac{1}{2}\sum_{I\neq J}\frac{e^2}{4\pi\epsilon_0}\frac{Z_I Z_J}{|\mathbf{R}_I - \mathbf{R}_J|} \tag{2.12}$$

representing Coulombic repulsion between nuclei; and

$$\hat{V}_{en} = -\sum_{i,I}\frac{e^2}{4\pi\epsilon_0}\frac{Z_I}{|\mathbf{r}_i - \mathbf{R}_I|} \tag{2.13}$$

representing Coulombic attraction between electrons and nuclei.

These results allow the full many-body Schrödinger equation to be written as

$$\hat{H}\Psi = E_{total}\Psi \tag{2.14}$$

where the Hamiltonian, $\hat{H}$, is given by

$$\hat{H} = \hat{T}_e + \hat{T}_n + \hat{V}_{ee} + \hat{V}_{nn} + \hat{V}_{en} \tag{2.15}$$

or written in full as

$$\begin{aligned}\hat{H} = &-\sum_{i=1}^{N}\frac{\hbar^2}{2m_e}\nabla_i^2 - \sum_{I=1}^{M}\frac{\hbar^2}{2M_I}\nabla_I^2 \\ &+ \frac{1}{2}\sum_{i\neq j}\frac{e^2}{4\pi\epsilon_0}\frac{1}{|\mathbf{r}_i - \mathbf{r}_j|} + \frac{1}{2}\sum_{I\neq J}\frac{e^2}{4\pi\epsilon_0}\frac{Z_I Z_J}{|\mathbf{R}_I - \mathbf{R}_J|} - \sum_{i,I}\frac{e^2}{4\pi\epsilon_0}\frac{Z_I}{|\mathbf{r}_i - \mathbf{R}_I|}.\end{aligned} \tag{2.16}$$

The implementation of atomic units allows this form to be greatly simplified by calculating energy in units of Hartrees (1 Ha = 27.2114 eV), distances in units of the Bohr radius or the average radius of an electron in a hydrogen 1s orbital ($a_0 = 0.529177$ Å), and mass in atomic units (1 a.u. $= m_e = 9.10938291 \cdot 10^{-31}$ kg). The electron charge, e, is set to 1. The simplified Hamiltonian which assumes the respective summations occur

over N electrons and M nuclei is now

$$\hat{H} = -\sum_i \frac{1}{2}\nabla_i^2 - \sum_I \frac{1}{2M_I}\nabla_I^2 + \frac{1}{2}\sum_{i\neq j}\frac{1}{|\mathbf{r}_i - \mathbf{r}_j|} + \frac{1}{2}\sum_{I\neq J}\frac{Z_I Z_J}{|\mathbf{R}_I - \mathbf{R}_J|} - \sum_{i,I}\frac{Z_I}{|\mathbf{r}_i - \mathbf{R}_I|}. \tag{2.17}$$

2.1.3 Born–Oppenheimer Approximation

Under the Born–Oppenheimer Approximation, electronic and nuclear motion are considered to occur on vastly different timescales. On the ultrafast timescale within which electron motion occurs, nuclei can be considered to remain fixed in time; therefore, the kinetic energy term describing nuclear motion, T_n, can be removed from the Hamiltonian (Eqn. 2.17). Additionally, if the positions of the nuclei, $\mathbf{R}_I$, are approximated as fixed, then the Coulombic repulsion between the nuclei, V_{nn}, can be approximated as a constant value subtracted from the total energy of the system, E_{total}, such that

$$E = E_{total} - \frac{1}{2}\sum_{I\neq J}\frac{Z_I Z_J}{|\mathbf{R}_I - \mathbf{R}_J|}. \tag{2.18}$$

The new form of the Schrödinger equation becomes

$$\left[-\sum_i \frac{1}{2}\nabla^2 - \sum_{i,I}\frac{Z_I}{|\mathbf{r}_i - \mathbf{R}_I|} + \frac{1}{2}\sum_{i\neq j}\frac{1}{|\mathbf{r}_i - \mathbf{r}_j|}\right]\Psi = E\Psi. \tag{2.19}$$

In order to completely remove nuclear coordinates from this equation, the nuclear coordinates, $\mathbf{R}_I$, can be treated as external parameters. As a result, the Coulombic interactions between the electrons and nuclei, $V_n(\mathbf{r})$, can be expressed as

$$V_n(\mathbf{r}) = -\sum_I \frac{Z_I}{|\mathbf{r} - \mathbf{R}_I|}. \tag{2.20}$$

The resulting form of the Schrödinger equation under the Born–Oppenheimer approxi-

mation thus becomes

$$\left[-\sum_i \frac{1}{2}\nabla^2 + \sum_i V_n(\mathbf{r}_i) + \frac{1}{2}\sum_{i\neq j}\frac{1}{|\mathbf{r}_i - \mathbf{r}_j|}\right]\Psi = E\Psi. \tag{2.21}$$

2.1.4 Slater Determinants

The next step is finding a suitable representation of the many-body wavefunction. In keeping with the Pauli exclusion principle and the antisymmetry requirement of fermion particles,[137] the wavefunction must maintain a form whereby the sign of the wavefunction changes if two particles are exchanged. One equation which satisfies this requirement for a two-particle system, $\Psi(\mathbf{r}_1, \mathbf{r}_2)$, is

$$\Psi(\mathbf{r}_1, \mathbf{r}_2) = \frac{1}{\sqrt{2}}\left[\phi_1(\mathbf{r}_1)\phi_2(\mathbf{r}_2) - \phi_1(\mathbf{r}_2)\phi_2(\mathbf{r}_1)\right], \tag{2.22}$$

where $\phi_i(\mathbf{r})$ describe the orbitals available for occupation. Swapping $\mathbf{r}_1$ and $\mathbf{r}_2$ results in $\Psi(\mathbf{r}_2, \mathbf{r}_1) = -\Psi(\mathbf{r}_1, \mathbf{r}_2)$. Slater first proposed the writing of this wavefunction in the form of a determinant,

$$\Psi(\mathbf{r}_1, \mathbf{r}_2) = \frac{1}{\sqrt{2}}\begin{vmatrix}\phi_1(\mathbf{r}_1) & \phi_1(\mathbf{r}_2)\\ \phi_2(\mathbf{r}_1) & \phi_2(\mathbf{r}_2)\end{vmatrix}. \tag{2.23}$$

This expression of the Slater determinant[138] can be extended the many-body case as

$$\begin{aligned}\Psi(\mathbf{r}_1, \mathbf{r}_2, ..., \mathbf{r}_N) &= \frac{1}{\sqrt{N!}}\begin{vmatrix}\phi_1(\mathbf{r}_1) & \phi_2(\mathbf{r}_1) & ... & \phi_N(\mathbf{r}_1)\\ \phi_1(\mathbf{r}_2) & \phi_2(\mathbf{r}_2) & ... & \phi_N(\mathbf{r}_2)\\ \vdots & \vdots & \ddots & \vdots\\ \phi_1(\mathbf{r}_N) & \phi_2(\mathbf{r}_N) & ... & \phi_N(\mathbf{r}_N)\end{vmatrix}\\ &= \frac{1}{\sqrt{N!}}\det|\phi_1(\mathbf{r})\phi_2(\mathbf{r})...\phi_N(\mathbf{r})|.\end{aligned} \tag{2.24}$$

This form is computationally useful because it allows for the creation of trial wavefunctions for complex systems that ensure the Pauli exclusion principle and antisymmetry

requirement are met. Under this formalism, electron–electron exchange is treated exactly while correlation is neglected, as electron behaviour is approximated to be independent. The use of the determinant form also allows for easy mathematical manipulation, and the wavefunction density can be simply normalised with a factor of $\frac{1}{\sqrt{N!}}$.

2.1.5 Mean-Field Approximation

The mean-field approximation seeks to provide an approximation for the Coulombic repulsion between electrons by simplifying the many-body Schrödinger equation to a single-particle form. This approximation then represents the repulsion one electron experiences as an electrostatic potential based on the charge density. This approximate form of the electron–electron repulsion is described as the Hartree potential, V_H.[139,140] Under the mean-field approximation, the many-body Schrödinger equation can be contracted into the single-body form as

$$\left[-\frac{1}{2}\nabla^2 + V_n(\mathbf{r}) + V_H(\mathbf{r})\right]\phi_i(\mathbf{r}) = \varepsilon_i\phi_i(\mathbf{r}), \tag{2.25}$$

where $\phi_i(\mathbf{r})$ represents the single-particle wavefunction and ε_i is the particle energy. The mean-field approximation introduces self-interaction error by considering a particle's repulsion with its own charge density. This approximation is no longer used; however, it served as a good first approximation, and it paved the way for the development of better approximations of electron–electron repulsion.

2.1.6 Hartree–Fock Method

The Hartree–Fock method[139,140] was developed as a way to re-frame the Schrödinger equation in a more tractable form as a single Slater determinant. Electron–electron exchange is treated exactly while correlation is neglected. Therefore, the Hamiltonian operator can be written as the sum of three terms which contribute to the energy of the system: the kinetic energy term, the potential energy derived from an external potential, and the

energy produced by particles interacting with each other. By solving this equation, the energy of the system can be calculated as the sum of four terms: the kinetic energy, the external potential, the Coulomb energy, and the exchange energy. The Coulomb energy represents the potential of one electron interacting with the electron density of another orbital. This introduces the issue of self-interaction, as an electron is considered to interact with its own charge density. The exchange energy is the interaction between two different electrons, making it a non-local potential.

As shown previously, the many-body wavefunction can be written in the form of a Slater determinant under the approximation that Coulombic repulsion does not strongly affect the electronic behaviour in the system. The Hartree–Fock method[141] seeks to provide a solution to the single-particle wavefunctions, $\phi_i(\mathbf{r})$, defined in the Slater determinant while including electronic interaction. This approach utilises the variational principle which states that the minimum energy of a system calculated by taking a valid trial wavefunction will be greater than or equal to the true minimum energy of the system and that the calculated minimum energy can reach the true minimum energy by testing all possible valid wavefunctions. Rewriting the many-body Schrödinger equation (Eqn. 2.14) in Dirac notation allows the total energy of the system, E, to be described as

$$E = \langle \Psi | \, \hat{H} \, | \Psi \rangle \,, \tag{2.26}$$

where Ψ are the Slater determinant wavefunctions for the total system which are a normalised determinant comprised of single-particle functions as defined in Eqn. 2.24. The minimum energy of the system can be calculated by setting the first derivative of the energy with respect to the single-particle functions equal to 0,

$$\frac{\delta E}{\delta \phi_i^*} = 0. \tag{2.27}$$

The Hamiltonian operator corresponds to the energy observable; therefore, the Hamiltonian operator is Hermitian. Eigenstates corresponding to distinct eigenvalues must be

orthonormal under the condition of Hermiticity.[136] Based on the mean-field form of the Schrödinger equation (Eqn. 2.25), the energy derivative is calculated as

$$\left[-\frac{1}{2}\nabla^2 + V_n(\mathbf{r}) + V_H(\mathbf{r})\right]\phi_i(\mathbf{r}) + \int d\mathbf{r}' V_X(\mathbf{r},\mathbf{r}')\phi_i(\mathbf{r}') = \varepsilon_i\phi_i(\mathbf{r}). \tag{2.28}$$

The difference between this result and the previous expression calculated under the mean-field approximation is the addition of an extra potential energy term, V_X, which solves to

$$V_X(\mathbf{r},\mathbf{r}') = -\sum_j \frac{\phi_j^*(\mathbf{r}')\phi_j(\mathbf{r})}{|\mathbf{r}-\mathbf{r}'|}. \tag{2.29}$$

This potential is summed over all single particle states in the Slater determinant, Ψ. The result of the implementation of electron interactions in the Hartree–Fock form is this additional potential known as the Fock exchange potential, V_X. This potential introduces non-local interactions because the sum occurs over an additional location parameter, $\mathbf{r}'$, representing another point in space *i.e.* this interaction potential describes the interaction that occurs as a result of 'exchanging' one electron with another at a different location. This term arises from the Pauli exclusion principle which prevents two electrons from occupying the same point in space.

2.1.7 Hohenberg–Kohn Theorems

The Hohenberg–Kohn Theorems[142] are the foundation of modern density functional theory (DFT). The first theorem states that the electron density determines the external potential, V_n (to within an additive constant). The second theorem states that the external potential uniquely defines the wavefunction, Ψ; and therefore, for any trial density, n, such that $\int n(\mathbf{r})d\mathbf{r} = N$, the energy of the system as calculated as a function of the density must be greater than or equal to the ground state energy of the system, $E[n] \geq E_0$, which is a result of the variational principle. The final theorem states that a universal function can be defined to separate out the non-local Coulombic contributions from the local (classical) contributions. This leads to the creation of an energy–density functional.

Starting from the Hamiltonian derived under the Born–Oppenheimer approximation,

$$\left[-\sum_i \frac{1}{2}\nabla^2 + \sum_i V_n(\mathbf{r}_i) + \frac{1}{2}\sum_{i\neq j}\frac{1}{|\mathbf{r}_i - \mathbf{r}_j|}\right]\Psi = E\Psi, \tag{2.30}$$

where the kinetic energy operator and operator describing the Coulombic repulsion between electrons are now be defined as

$$\hat{T} = -\sum_i \frac{1}{2}\nabla_i^2 \tag{2.31}$$

and

$$\hat{W} = \frac{1}{2}\sum_{i\neq j}\frac{1}{|\mathbf{r}_i - \mathbf{r}_j|}, \tag{2.32}$$

respectively. This results in an expression for the energy that can be expressed in Dirac notation as

$$E = \langle\Psi|\sum_i V_n(\mathbf{r}_i)\,|\psi\rangle + \langle\Psi|\,\hat{T} + \hat{W}\,|\Psi\rangle\,. \tag{2.33}$$

Using the relationship between the electron density and the wavefunction described in Eqn. 2.8, this expression can be rewritten as

$$E = \int d\mathbf{r} n(\mathbf{r}) V_n(\mathbf{r}) + \langle\Psi|\,\hat{T} + \hat{W}\,|\Psi\rangle\,. \tag{2.34}$$

Based on these Hohenberg–Kohn theorems, the ground state energy of a system, E, can be expressed as a function of the electron density, n, such that

$$E = F[n] \tag{2.35}$$

or rather,

$$F[n] = \int d\mathbf{r} n(\mathbf{r}) V_n(\mathbf{r}) + \langle\Psi[n]|\,\hat{T} + \hat{W}\,|\Psi[n]\rangle\,. \tag{2.36}$$

This result provides an expression for the energy–density functional; however, these theorems do not explicitly define the form of this functional.

2.1.8 Kohn–Sham Equations

To provide an expression for the form of the energy–density functional, Kohn and Sham reintroduce the wavefunction in the Slater determinant form which allows the functional, $F[n]$, to be expressed as

$$F[n] = -\frac{1}{2}\sum_i \langle\psi_i|\,\nabla^2\,|\psi_i\rangle + \frac{1}{2}\int d\mathbf{r}d\mathbf{r}'\frac{n(\mathbf{r})n(\mathbf{r}')}{|\mathbf{r}-\mathbf{r}'|} + E_{XC}[n], \tag{2.37}$$

where the first term describes the kinetic energy, $T_s[n]$, with the subscript s indicating that this kinetic energy represents the kinetic energy under the non-interacting particle approximation, the second term is the Hartree potential which represents the classical Coulombic potential of an electron in a charge density, and the third term represents the energetic contributions which remain unknown.

The Hartree–Fock result includes energetic contributions arising from the kinetic energy of the electrons, the mean-field Coulombic repulsion between electrons, and a new term representing the exchange energy resulting from the interaction of one electron with the electron density of another. The final term to include is the correlation energy: the probability of finding an electron in the vicinity of another electron. This term is represented as $V_c(\mathbf{r})$. The resulting Kohn–Sham equation[143] can be represented as

$$\left[-\frac{1}{2}\nabla^2 + V_n(\mathbf{r}) + V_H(\mathbf{r}) + V_x(\mathbf{r}) + V_c(\mathbf{r})\right]\phi_i(\mathbf{r}) = \varepsilon_i\phi_i(\mathbf{r}) \tag{2.38}$$

where $-\frac{1}{2}\nabla^2$ is the kinetic energy contribution, $V_n(\mathbf{r})$ is the potential energy due to Coulombic repulsion between nuclei, $V_H(\mathbf{r})$ is the Hartree potential that results from treating electron–electron repulsion as a mean-field, $V_x(\mathbf{r})$ is the exchange energy contribution that results from swapping two electrons of the same spin, and $V_c(\mathbf{r})$ is the correlation energy which results from one electron interacting with the probability density of another electron.

The result of these theorems is that the energy of a system can be uniquely defined

by the electron density which can be calculated by integrating over the charge density in the system which is assumed to be comprised of non-interacting particles. The Kohn–Sham equations instead represent the electron–electron repulsion term as the exchange–correlation potential, V_{XC}, resulting in the form

$$\left[-\frac{1}{2}\nabla^2 + V_n(\mathbf{r}) + V_H(\mathbf{r}) + V_{XC}(\mathbf{r})\right]\phi_i(\mathbf{r}) = \varepsilon_i\phi_i(\mathbf{r}) \tag{2.39}$$

The result is an equation that specifies the energy of the system as a sum of four terms:

$$E[n] = T_s[n] + V_{ext}[n] + V_H[n] + E_{XC}[n]. \tag{2.40}$$

While the interaction between the external potential and the charge density is now trivial to solve, the kinetic energy component and the electron–electron interactions remain unknown. These two terms comprise the exchange correlation functional $E_{xc}[n] = K_{ee}[n] + T_c[n]$. In practice, this term is calculated through an approximation provided by the choice of functional.[144] The extra term introduced here, V_{xc}, is the exchange–correlation potential which is represented as

$$V_{xc}(\mathbf{r}) = \left.\frac{\delta E_{xc}[n]}{\delta n}\right|_{n(r)}. \tag{2.41}$$

If the exact form of the exchange–correlation functional were known, then the energy predicted by these equations would be the true ground state energy of the system.

2.1.9 Functionals

As the exact form of the exchange–correlation functional remains inaccessible with current computational resources, an approximation is provided by the choice of functional. Each DFT calculation requires a functional to be specified, and this choice determines the form of the exchange–correlation component of the energy. Functionals come in different families which are classified according to the order of theory (Table 2.1).[145]

Table 2.1: Classes of DFT functionals in increasing order of theory, often referred to as Jacob's ladder of functionals with ρ describing the electron density, $\nabla\rho$ describing the first order gradient of electron density, $\nabla^2\rho$ describing the Laplacian of the spin density, τ describing the local kinetic energy density (not always explicitly included), E_x^{HF} describing the exact Fock exchange energy, and E_c^{MP2} describing the MP2 correlation energy. Double hybrid functionals were not used in this work but are included here for completeness. Terms in parenthesis, ($\nabla^2\rho$ or τ), may be included if the hybrid or double hybrid functional is based on a meta-GGA functional.[145,146]

Class	Variables
LDA	ρ
GGA	$\rho, \nabla\rho$
meta-GGA	$\rho, \nabla\rho, \nabla^2\rho$ or τ
Hybrid	$\rho, \nabla\rho, (\nabla^2\rho \text{ or } \tau), E_x^{HF}$
Double hybrid	$\rho, \nabla\rho, (\nabla^2\rho \text{ or } \tau), E_x^{HF}, E_c^{MP2}$

The Local Density Approximation (LDA)[147,148] was the first functional developed to approximate the exchange–correlation energy. This functional calculates the exchange–correlation potential of a material as that of the homogeneous electron gas with the same density as the local electron density:[146]

$$V_{XC}^{LDA}(\mathbf{r}) = V_{XC}^{electron\ gas}[n(\mathbf{r})]. \tag{2.42}$$

The homogeneous electron gas is a theoretical gas consisting only of electrons which are contained within a box with the nuclear potential term treated as a constant. For this simple system, the exchange energy can be calculated exactly and the correlation energy can be calculated via numerical techniques.[135] This functional is a poor estimate of electron–electron interactions but cancellation of errors results in a surprisingly decent spherical average of the pair density.[144] Due to the assumption that the electron density behaves like the homogeneous gas, LDA often fails to accurately predict properties, especially in atomic and molecular systems with high variabilities in electron density and long-range Van der Waals interactions. Notably, LDA tends to underestimate band gaps and overestimate binding energies. As a result of the poor accuracy of this functional, LDA is rarely used in modern computational work, but it serves as the basis upon which

more advanced functionals were developed.

The next level of functional theory are the Generalized-Gradient Approximation (GGA) functionals. These functionals include additional information describing the first order gradient of the charge density:

$$V_{XC}^{GGA}(\mathbf{r}) = V_{XC}[n(\mathbf{r}), \nabla n(\mathbf{r})]. \tag{2.43}$$

Inclusion of the charge density gradient provides information about the variations of charge density within a particular region. This provides more accuracy when modelling systems by identifying regions where the charge density changes sharply for highly localised charge populations or gradually for diffuse charge regions. Prominent GGA functionals include the Perdew–Burke–Ernzerhof functional (PBE)[149] and the PBE functional revised for solids (PBEsol).[150] PBE emerged as a popular choice of functional due to its computational efficiency, numerical accuracy, and broad applicability. PBE additionally reduces the over-binding tendency introduced as a result of the local density approximation; however, PBE also has a tendency to overestimate lattice constants and demonstrates inaccuracies for other bulk material properties. As a result, Perdew *et al.* later developed the modified functional PBEsol which demonstrates better performance predicting lattice parameters and bond lengths as well as other bulk structural properties such as bulk moduli. The improvements to the PBEsol functional are largely due to altering two parameters in the gradient expansion to fit the homogeneous electron gas surface exchange–correlation energy.[150]

The next class of functionals are the meta-GGA functionals which add additional terms including the Laplacian of the spin density, $\nabla^2 n(\mathbf{r})$, or the local kinetic energy density, $\tau(\mathbf{r})$:

$$V_{XC}^{meta-GGA}(\mathbf{r}) = V_{XC}[n(\mathbf{r}), \nabla n(\mathbf{r}), \nabla^2 n(\mathbf{r}) \; or \; \tau(\mathbf{r})] \tag{2.44}$$

The local kinetic energy density, $\tau(\mathbf{r})$, is calculated via

$$\tau(\mathbf{r}) = \frac{1}{2} \sum_{\substack{occupied \\ states}} |\nabla \phi_i(\mathbf{r})|^2. \tag{2.45}$$

Both the local kinetic energy density and the Laplacian of the spin density contain similar information, so different meta-GGA functionals may use one over the other.[146]

The final class of functionals used in the work are the hybrid functionals which estimate the exchange–correlation energy as a weighted sum of the Fock exchange energy and the exchange–correlation energy of a GGA functional. Eqn. 2.46[144] provides an exact representation of the exchange–correlation energy if the value of λ is known:

$$E_{XC}^{Hybrid}[\rho] = \frac{1}{2} \int d\mathbf{r} d\mathbf{r}' \int_{\lambda=0}^{1} d\lambda \frac{\lambda e^2}{|\mathbf{r} - \mathbf{r}'|} [\langle \rho(\mathbf{r}) \rho(\mathbf{r}') \rangle_{\rho,\lambda} - \rho(\mathbf{r}) \delta(\mathbf{r} - \mathbf{r}')]. \tag{2.46}$$

$\lambda = 0$ returns the Hartree–Fock result (which assumes fully non-interacting electrons), and $\lambda = 1$ returns the result for a fully-correlated system: the same system that the LDA and GGA functions seek to approximate. In contrast to the functionals previously described, hybrid functionals introduce non-locality into the system by directly considering the exact Hartree–Fock exchange which depends on two positional variables, $\mathbf{r}$ and $\mathbf{r}'$. Hybrid functionals are typically considered to provide high levels of accuracy as they combine elements of the exact exchange, the electron density, and the first order electron density gradient; however, they also increase the computational cost of calculations in comparison to functionals from lower levels of theory.[144]

2.1.10 Plane-Wave DFT

In order to solve the Kohn–Sham equations as described in the previous section, a mathematical model must be developed to numerically model the electron density as described by Scholl and Steckel (2009).[146] This work considers solid state materials which have periodic boundary conditions, meaning that each unit cell is repeated periodically in

three-dimensional space. DFT calculations in this thesis are performed using the Vienna *Ab initio* Simulation Package (VASP) which is a plane-wave code. Localised basis sets have also been used successfully implemented in DFT codes for modelling solid states systems; however, these methods are beyond the scope of this thesis. Solving the Schrödinger equation for such a periodic system requires that the solution observe Bloch's theorem. The fundamental argument of this theory is that the solution to Schrödinger's equation in periodic systems can be expressed as a sum of terms in the form

$$\phi_k(\mathbf{r}) = e^{i\mathbf{k}\cdot\mathbf{r}} u_{\mathbf{k}}(\mathbf{r}), \tag{2.47}$$

where $u_{\mathbf{k}}(\mathbf{r})$ matches the periodicity of the cell. This representation is referred to as the plane-wave representation because functions of the form $e^{i\mathbf{k}\cdot\mathbf{r}}$ are plane waves. To ensure periodicity, $u_{\mathbf{k}}(\mathbf{r}+n_1\mathbf{a}_1+n_2\mathbf{a}_2+n_3\mathbf{a}_3) = u_{\mathbf{k}}(\mathbf{r})$, where n_1, n_2, and n_3 are any integers and $\mathbf{a}_1$, $\mathbf{a}_2$, and $\mathbf{a}_3$ are the lattice vectors of the cell. As a result, the Schrödinger equation can be solved for any value of $\mathbf{k}$ under the plane-wave representaiton.

In the plane-wave representation, $\mathbf{k}$ vectors represent reciprocal space in contrast to the real space representation discussed previously in terms of $\mathbf{r}$. Using reciprocal space allows for efficient solving of plane-wave equations. This space is defined by a set of reciprocal lattice vectors described as follows:

$$\begin{aligned}
\mathbf{b}_1 &= 2\pi \frac{\mathbf{a}_2 \times \mathbf{a}_3}{\mathbf{a}_1 \cdot (\mathbf{a}_2 \times \mathbf{a}_3)} \\
\mathbf{b}_2 &= 2\pi \frac{\mathbf{a}_3 \times \mathbf{a}_1}{\mathbf{a}_1 \cdot (\mathbf{a}_2 \times \mathbf{a}_3)} \\
\mathbf{b}_3 &= 2\pi \frac{\mathbf{a}_1 \times \mathbf{a}_2}{\mathbf{a}_1 \cdot (\mathbf{a}_2 \times \mathbf{a}_3)}.
\end{aligned} \tag{2.48}$$

This set of $\mathbf{b}$ vectors defines reciprocal space in terms of three vectors which are orthogonal to each of the three planes defined by pairs of the three real-space $\mathbf{a}$ vectors. Each of the reciprocal space vectors are normalised by 2π divided by the volume of the cell as calculated by the triple product in the denominator. The use of reciprocal space means

that longer lattice vectors in real space correspond to shorter lattice vectors in reciprocal space, which is also known as k-space.

The importance of the k-space representation, lies in the computational simplification that it allows. Instead of solving complex integrals exactly, the plane wave functions can be much more simply integrated in reciprocal space using numerical methods which evaluate the function at a set of discrete points, known as k-points, and then the integral can be calculated by summing over the k-points with appropriate weighting. Increasing the number of k-points increases the accuracy of the calculation, and additionally, the choice of location of the k-points can alter the accuracy of the calculations. Typically, k-meshes are centred around a point at k=0 which is known as the gamma point, Γ, which allows substantial reduction in computational cost as a result of the reduction of k-points considered due to symmetry. The choice of k-point density and location are critical to reaching convergence. In addition, implementation of the Fast Fourier Transform allows for quick transformation between real and reciprocal space.

Another key feature of plane-wave calculations is the cut-off energy, a parameter which defines the number of place waves considered in each calculation. The plane-wave expression given in Eqn. 2.47 contains a periodic expression for the wavefunction amplitude in the term $u_{\mathbf{k}}(\mathbf{r})$. Due to the periodicity of this term, it can also be expanded as a sum of plane waves as

$$u_{\mathbf{k}}(\mathbf{r}) = \sum_{\mathbf{G}} c_{\mathbf{G}} e^{i\mathbf{G}\cdot\mathbf{r}}, \tag{2.49}$$

where $\mathbf{G} = m_1\mathbf{b}_1 + m_2\mathbf{b}_2 + m_3\mathbf{b}_3$. This sum acts over all reciprocal space vectors, $\mathbf{b}$. Using this result, the Bloch equation can be re-written as

$$\phi_{\mathbf{k}}(\mathbf{r}) = \sum_{\mathbf{G}} c_{\mathbf{k}+\mathbf{G}} e^{i(\mathbf{k}+\mathbf{G})\mathbf{r}}. \tag{2.50}$$

As these functions are solutions to the Schrödinger equations, they are also solutions with a kinetic energy,

$$E = \frac{\hbar^2}{2m}|\mathbf{k}+\mathbf{G}|^2. \tag{2.51}$$

Using this result allows the kinetic energy to be calculated for each of the plane waves which comprise the Bloch solution. DFT is a ground-state energy methodology, meaning that low energy plane waves are more relevant for predicting electron density than high energy plane waves. For a given cut-off energy, E_{cut}, the infinite sum described in Eqn. 2.50 can be reduced to the finite sum

$$\phi_{\mathbf{k}}(\mathbf{r}) = \sum_{|\mathbf{G}+\mathbf{k}|<G_{cut}} c_{\mathbf{k}+\mathbf{G}} e^{i(\mathbf{k}+\mathbf{G})\mathbf{r}}. \tag{2.52}$$

All plane-waves included in this sum correspond to energies below E_{cut} as calculated by

$$E_{cut} = \frac{\hbar^2}{2m} G_{cut}^2. \tag{2.53}$$

Reducing this infinite sum to a finite sum greatly increases the computational efficiency without substantial loss of accuracy assuming a suitable choice of cut-off energy, E_{cut}.

Pseudopotentials

Another computational development designed to improve calculation efficiency was the implementation of pseudopotentials. Instead of explicitly considering the density of all electrons in the system, pseudopotentials replace the density attributed to core electrons with a smooth density function carefully chosen to represent the core properties of each element. In many circumstances, core electrons need not be directly included in the plane-wave model because they do not form chemical bonds and have little impact on other chemical and physical properties of the system. Additionally, core electrons exhibit high place-wave oscillation frequencies in real space; therefore, high energy cut-offs are required for accurate mapping. Replacing these plane waves with pseudopotentials greatly reduces the computational cost of the simulation. In addition to the choice of k-point sampling density and plane-wave cut-off energy, the pseuodopotentials must be suitably chosen to ensure the accuracy of the calculation.

The DFT code employed in this work is VASP,[151–154] a plane-wave DFT code util-

ising projector-augmented-wave (PAW) pseudopotentials.[155,156] This approach has been extensively used for modelling solid state materials.[156] Previous pseudopotential forms, such as the ultrasoft pseudopotentials (US-PPs) developed by Vanderbilt, demanded a high degree of computational expense to accurately model first-row elements, transitions metals, and rare-earth elements and were also difficult to implement accurately due to the large degree of parameters that had to be specified by the user. The development of the PAW pseudopotentials by Blöchl[155] solved several of these issues by constructing potentials that work directly with full all-electron wavefunctions and potentials. Kresse and Joubert[156] re-worked Blöchl's PAW pseudopotentials allowing them to be easily integrated into commercial DFT codes such as VASP.

2.1.11 Self-Consistent Field Calculations

Following the derivation of the Kohn–Sham equations and the development of a suitable choice of functional, the ground state energy of a system can be calculated using DFT. This process is described as a self-consistent field (SCF) calculation based on iteratively solving the Kohn–Sham equations using the following method:

1. The atomic coordinates of the system are used to calculate the nuclear potential energy term, $V_n(\mathbf{r})$, where $V_n(\mathbf{r}) = -\sum_I \frac{Z_I}{|\mathbf{r}-\mathbf{R}_I|}$.

2. A guess is provided for the electron density, $n(\mathbf{r})$, which can be made by considering the electron densities for isolated atoms arranged according to the atomic coordinates in the system, as $n(\mathbf{r}) = \sum_i |\phi_i(\mathbf{r})|^2$.

3. The electron density, $n(\mathbf{r})$, is used to calculate the Hartree potential, $V_H(\mathbf{r})$, which represents the background electron mean-field and the exchange–correlation potential, V_{xc}, which is calculated via the choice of functional.

$$\begin{aligned} \nabla^2 V_H(\mathbf{r}) &= -4\pi(\mathbf{r}) \\ V_{xc} &= \frac{\delta E_{xc}[n]}{\delta n}(\mathbf{r}) \end{aligned} \tag{2.54}$$

4. The total potential, V_{total}, can now be calculated by summing the nuclear potential, the Hartree potential, and the exchange–correlation potential: $V_{total} = V_n(\mathbf{r}) + V_H(\mathbf{r}) + V_{xc}(\mathbf{r})$.

5. The energy can now be calculated using numerical methods such as the plane-wave method described previously. This result yields a value of the ground state energy for this system solved from the Kohn–Sham equation, $\left[-\frac{1}{2}\nabla^2 + V_{total}(\mathbf{r})\right]\phi_i(\mathbf{r}) = \varepsilon_i\phi_i(\mathbf{r})$.

6. Using the results of this equation, new wavefunctions, ϕ_i, can be estimated. These are used to construct a new electron density, $n(\mathbf{r})$, and a new potential, V_{total}. This process is repeated until the new energy is within a certain convergence threshold of the previously calculated energy, hence the ground state energy provides a self-consistent solution to the Kohn–Sham equations.

2.1.12 Electronic Structure

Following a geometry optimisation, analysis of the electronic structure may be performed. The SCF cycle calculates the relaxed electron density as a function of plane waves. The energy of these relaxed electronic density states can be calculated as

$$E = \frac{(\hbar\mathbf{k})^2}{2m}. \tag{2.55}$$

Integrating the relaxed electron density in k-space allows a density of states (DOS) to be calculated which represents the density of electronic states at a given energy.

In order to calculate partial contributions to the DOS, such as the contributions of a single atom or orbital, requires that the plane-wave density be decomposed onto local functions. In VASP, this decomposition occurs via the use of projector functions specified by the PAW pseudopotentials.[157] Specification of the l- or lm- decomposition allows the plane-wave electron density to be projected onto spherical harmonics which

means that in addition to the total and elemental density of states, it is possible to identify contributions from specific orbitals (l) and even spin states (m). Furthermore, it is even possible to decompose change density by electronic bands. For instance, the partial charges associated with the valence band can be calculated by setting the LPARD tag in VASP. Charge densities, often written to the CHGCAR or ELFCAR files, can be visualised on top of an atomic structure to provide additional analysis about the localisation of charge within the system. The structural and charge density visualisations included in this thesis were largely performed in VESTA.[158]

A band structure can be similarly constructed from a self-consistent electronic relaxation; however, while a density of states may be plotted from relaxing the electronic structure on a k-mesh grid, a band structure requires the k-points are specified to map the high-symmetry path through the Brillouin zone in reciprocal space. Despite covering three-dimensional space, band structures are traditionally plotted in two-dimensions to improve readability. The high-symmetry path is plotted between unique symmetry points along the edges of the irreducible Brillouin zone.[135] This ensures that the band structure maps all important electronic features within the primitive cell, regardless of the space group. Especially important for optoelectronic materials, these electronic characterisation methods provide critical information about the magnitude and nature of the band gap.[135]

Introducing Spin

Spin plays an important role in modelling electronic structure properties. Spin is introduced into DFT by considering that the total energy now depends on both the electron density and on the spin density.[159] This result leads to the introduction of an additional term in the exchange–correlation matrix which can now be expressed as

$$V_{xc}^{\alpha\beta}(\mathbf{r}) = V_{XC}(\mathbf{r})\mathbf{1} + \mu_B \boldsymbol{\sigma} \cdot \mathbf{B}_{XC}(\mathbf{r}). \tag{2.56}$$

This allows the Hartree-Fock expression to be rewritten as

$$\left[-\frac{1}{2}\nabla^2 + V_n(\mathbf{r}) + V_H(\mathbf{r}) + V_{XC}(\mathbf{r}) + \mu_B \boldsymbol{\sigma} \cdot \mathbf{B}_{XC}(\mathbf{r})\right] \Psi_i(\mathbf{r}) = \varepsilon_i \Psi_i(\mathbf{r}) \tag{2.57}$$

where $\boldsymbol{\sigma}_{\alpha\beta}$ represents the Pauli spin matrix with spins α and β, μ_B is the Bohr magneton which provides the units of the magnetic moment of an electron, and $\mathbf{B}_{XC}(\mathbf{r})$ represents the effective magnetic field produced due to the presence of electron spins in the system.

Spin polarised non-collinear DFT calculations require two separate spatial wavefunctions to model spin-up and spin-down electrons which increases the cost of such a calculation by a factor of $\sim 4^3$. As a result of the expense associated with such calculations, spin effects are only included where they are considered to provide a substantial impact on the outcome of the calculations. Notably, the presence of spin-orbit coupling becomes especially important when investigating band gaps and other electronic properties in materials containing heavy atoms with relativistic properties such as Pb.

Bader Charge Analysis

For further analysis of charge localisation, Bader charge analysis provides a method of mapping electronic density onto atoms. This method uses zero flux surfaces to attribute regions of space to specific atoms. These zero flux surfaces are two-dimensional surfaces upon which the charge density is at a minimum perpendicular to the surface. As the charge density naturally reaches a minimum in between atoms, these surfaces provide a chemically intuitive way of separating the charge associated with one atom from its neighbours. By integrating over the charge density in each region, an effective charge can be calculated for each atom. Bader charge analysis may be effectively performed with the codes developed by the Henkelman group[160–162] which are based on the Bader theory developed by Richard Bader.

2.2 Numerical Energy Minimisation Algorithms

The calculations performed in this thesis require optimisation or energy minimisation algorithms to effectively search for local minima. In the case of DFT calculations, a trial electron density is constructed based on the atomic positions in the starting geometry; however, these positions are unlikely to be in the lowest energy configuration. Between iterations of the SCF cycle, the atomic positions are adjusted to minimise the energy of the total system. Additionally, depending on the type of simulation, the lattice parameters and cell angles may also be adjusted. A numerical optimisation algorithm guides this relaxation, choosing how to update the ionic coordinates at each ionic step. This process occurs iteratively until the forces calculated on each atom are converged to within a predetermined convergence criterion. Several methods are utilised in this work depending on the nature of the calculation and the key properties required for the minimisation. A brief overview of these algorithms is provided below.

Two common algorithms implement in VASP for this purpose are the conjugate-gradient (CG) method and the Residual Minimization Method with Direct Inversion in the Iterative Subspace (RMM-DIIS) algorithm. The CG method[146] calculates the gradient of the potential energy surface and selects an initial movement along the direction of steepest decline which can be calculated as $d_1 = -\nabla E(\mathbf{x})$. Following the first step, the CG algorithm performs a second search in a direction orthogonal to the first step as calculated via

$$d_2 = -\nabla E(\mathbf{x}_2) + \frac{(\nabla E(\mathbf{x}_2) \cdot \mathbf{d}_1)}{(\mathbf{d}_1 \cdot \mathbf{d}_1)}\mathbf{d}_1. \tag{2.58}$$

Additional steps follow this same procedure, with the direction of subsequent steps being defined as orthogonal to the previous two steps. The CG algorithm is considered a highly robust and stable optimisation method, but it can be slow to converge, especially if the starting geometry is far from a minimum.

The RMM-DIIS algorithm[163] calculates the direction of descent by taking linear combinations of previous positions. This method has been found to be faster than other

methods, including the CG algorithm, as it uses previous steps to extrapolate where the minima is located; however, this algorithm struggles when the starting geometry is far from a minima and also may fail to reach convergence.

The Multi-ACE (MACE) nudged elastic band (NEB) calculations (detailed below in Section 2.3) were performed using the Broyden–Fletcher–Goldfarb–Shanno (BFGS) optimiser as implemented in the Atomic Simulation Environment (ASE).[164,165] The BFGS algorithm is a quasi-Newtonian method for solving unconstrained non-linear optimisation problems iteratively. It determines the search direction by incorporating curvature information through an approximation to the Hessian matrix, a square matrix of second-order partial derivatives, which is updated using gradient evaluations. Compared to full Newtonian methods, BFGS is computationally efficient, with a per-iteration computational complexity that scales as $\mathcal{O}(n^2)$, where n is the number of degrees of freedom.[166] This algorithm is typically faster and more accurate than CG; however, it also requires higher computational memory which can be problematic for expensive calculations.

In addition, the Henkelman group implemented a set of Variational Transition State Theory (VTST) optimisers designed to improve the efficiency of performing NEB calculations in VASP (see Section 2.3). Due to the presence of the spring force between images, the calculated energy of the system does not reflect the force being optimised. As a result, many of the optimisers implemented in VASP which utilise the energy for structure optimisations are therefore not suitable for NEB calculations. To solve this problem, the Henkelman group developed a set of optimisers designed to only optimise the forces in the system. Optimiser testing[167] has demonstrated the efficiency of the Fast Inertial Relaxation Engine (FIRE)[168] optimiser and the Limited-memory Broyden–Fletcher–Goldfarb–Shanno (LBFGS)[169] optimisers which were the two chosen for the NEB calculations in this thesis. The FIRE optimiser employs a variable time step algorithm, and it only projects the velocity component in the same direction as the force while maintaining momentum in all other directions. The velocities are reset if the force and velocity are in opposite directions. This methodology was shown to improve error sensitivity compared

to other methods due to its ability to smooth out errors during convergence,[168] therefore, this algorithm is considered a strong choice for noisy systems despite being less formally rigorous. Meanwhile, the LBFGS optimiser is based on the BFGS optimiser; however, this version is designed for large systems requiring high memory usages. This optimiser efficiently updates the quasi-Newtonian matrix at each iteration by replacing the oldest information with new updates. While slightly less accurate than original BFGS, the reduced memory cost allows for computationally efficient handling of expensive NEB calculations. The FIRE optimiser was the primary optimiser used in this work due to its slightly improved efficiency compared to the LBFGS optimiser, as determined by testing of both algorithms.

In summary, the DFT and MD simulations performed in this work utilise a range of standard optimisers including CG, RMM-DIIS, and BFGS. CG is considered a slow but robust algorithm for finding a minima. RMM-DIIS improves efficiency compared to CG but at the cost of stability. The BFGS quasi-Newtonian method is used for MD calculations, as it improves efficiency compared to CG but at the cost of increased memory usage which is prohibitively expensive for DFT calculations. NEB calculations, which require force-based optimisers, are performed using FIRE which was found to be the most stable and efficient option or the LBFGS algorithm as an alternative.

2.3 Nudged Elastic Band Calculations

Nudged elastic band (NEB) calculations search the potential energy surface to find the minimum energy pathway between a reactant and a product. In this work, these calculations are used to derive ion migration barriers. After performing a full geometry relaxation of the starting and end points, a series of intermediate images are created that map the transition evenly between the two. The images are developed such that the migrating species moves an equal distance between each image. While performing the calculation, the potential energy surface is searched by simultaneously relaxing the

intermediate images. The elastic band refers to the implementation of a spring force in between each image. During relaxation, only the perpendicular component of the force is considered which prevents the images from collapsing onto the endpoints. The parallel component of the spring force is only considered to maintain spacing between images along the band. The Climbing Image Nudged Elastic Band (CI-NEB) variation forces the image at the saddle point into the highest energy possible in order to avoid under-estimating the activation barrier. This is achieved by inverting the parallel component of the force during relaxation which allows the image to 'climb' to the peak energy. The perpendicular component of the force is still minimised to keep the image on the path. The energy difference between the highest-energy transition state image and the reactants represents the activation barrier which can be used to calculate the migration energy for an atom moving through a crystalline lattice. The codes provided within the VTSTToolkit were used to set up the intermediate images for each CI-NEB calculation performed in this thesis.[170,171]

2.4 Surface Calculations

This work includes several instances where DFT relaxations are performed on a solid surface. For surface relaxations, a vacuum region is introduced into the simulation cell. Surface simulations are still periodic in all three dimensions, so the vacuum must be suitably sized to reduce any interactions between periodic images. Achieving a sufficiently large vacuum can be determined by calculating the planar-average potential which should reach a constant value across the vacuum.

When molecular species are included in the vacuum, dipole corrections must be included. Using a simulation box that allows for a plateau in the planar-average between periodic surface images also ensures that the molecule is able to relax onto the surface without being affected by interactions with the periodic image of the surface. Additionally, while all bulk DFT geometry optimisations include the full relaxation of all atomic

coordinates, several surface calculations include one or more layers of fixed atomic positions which act as a representation of the bulk perovskite. The upper layers of the surface were allowed to relax and interact with any molecules added to the simulation box. In addition, van der Waals interactions were implemented for any simulation including molecules to ensure proper representation of long range dispersion forces.

Surface energies represent the energy required to cleave a slab from the bulk. The process of cleaving a slab from the bulk results in the formation of two surfaces; therefore, this energy must be halved. The surface energy, σ, is calculated via the following formula

$$\sigma = \frac{E_{slab} - nE_{bulk}}{2A}, \tag{2.59}$$

where E_{slab} is the DFT energy of the surface, n is the number of formula units in the surface slab, E_{bulk} is the DFT energy of the bulk material per formula unit, and A is the surface area of the slab. When working with non-stoichiometric surfaces, chemical potentials were subtracted from the slab energy to account for the energy of the elements appearing in excess. A is doubled in the denominator to reflect the formation of two surfaces.

To calculate surface binding energies, a molecule is fully relaxed onto a surface slab. Following relaxation, two single point calculations are performed on the isolated surface and isolated molecule in the exact same configurations. These single point energies are then subtracted from the total energy of the relaxed surface to provide a binding energy.

$$E_{Binding} = E^{Geomtry\ Optimised}_{Surface\ +\ Molecule} - E^{Single\ Point}_{Surface} - E^{Single\ Point}_{Molecule} \tag{2.60}$$

2.5 Cluster Expansions

For solid solutions or significant ion mixing, the cluster expansion method is used to predict the energy of a structure as a function of local clusters within that structure. This prediction is based on the creation of a cluster space that contains information

about the primitive cell, the cut-off radii for each element, and the types of elements in the compositions. This section describes the cluster expansion formalism as implemented in the integrated cluster expansion toolkit (ICET).[172]

The cluster space is comprised of a set of configurations that represent a distribution of M species arranged over N sites which are written as a vector $\boldsymbol{\sigma}$.[173] The property of interest, in this case the total energy of the system, can be represented as a function of these clusters such that $Q = f(\boldsymbol{\sigma})$, where Q is the total energy, $\boldsymbol{\sigma}$ are the clusters, and f represents a cluster function which calculates the cluster energy. Based on this, an orthonormal basis of cluster functions $\Gamma_\alpha(\boldsymbol{\sigma})$ can be constructed to describe the total energy, Q,[173,174] in the form $Q = \Sigma_\alpha m_\alpha J_\alpha \langle \Gamma_{\alpha'}(\boldsymbol{\sigma}) \rangle_\alpha$[175] where α represent the symmetry equivalent clusters with a given multiplicity, m_α, and J_α describes the effective cluster interactions (ECIs). The $\langle \Gamma_{\alpha'}(\boldsymbol{\sigma}) \rangle_\alpha$ term takes the average over the cluster functions belonging to symmetry equivalent clusters.

The cluster expansion can then be trained as $\bar{\mathbf{\Pi}}\boldsymbol{J} = \boldsymbol{Q}$ where $\bar{\mathbf{\Pi}}$ is a matrix formed by stacking vectors representing each structure in the training set, $\boldsymbol{J}$ are the vector representations of the ECIs, and $\boldsymbol{Q}$ is a vector of the structure energies which is the property being targetted in this training. This training is a complex minimisation where the clusters, each associated with an energy, are minimised via a given cost function. The resulting optimal set of ECIs for a given training set and cluster space are found by minimising the geometric norm of the training equation such that

$$J_{opt} = \arg\min_J \{||\bar{\mathbf{\Pi}}\boldsymbol{J} - \boldsymbol{Q}||_2\}. \tag{2.61}$$

The generated cluster expansion must then be validated. The validation method performed in this work is the k-fold cross validation which is considered best for limiting over-fitting within the model. This method retains 10% of the training set to use for validation. A good model is considered one for which the RMSE of the training and validation sets are similar.[175] This training produces a cluster expansion Hamiltonian that

can then be used to predict the total energy of new structures. The cluster expansion methodology is useful for studying mixed compositions where the ordering of elements on the lattice effects the energy and dynamics of the system.

2.6 Molecular Dynamics

Molecular dynamics (MD) is a framework for studying the dynamic motion of a system based on updating atomic positions by iteratively solving Newton's equations of motion. The simulations performed in this work sample the canonical ensemble which includes states of fixed values of the number of atoms, N; the volume of the simulation box, V; and the system temperature, T. To keep the energy of the system constant, the total momentum must also be conserved. Here, atomic velocities are determined by a Maxwell–Boltzmann distribution for a given temperature.[146]

Based on Newton's equations of motion, the Verlet algorithm solves a system of equations iteratively over a small timestep (Δt). As the positions and velocities of the atoms are updated, new forces are calculated which in turn are used to correct the initial prediction. The cycle then repeats with a new iteration such that the equations can be solved self-consistently both backwards and forwards in time. The basis for the Verlet algorithm is Newton's equation of motion $F = ma$. Acceleration is a second order derivative of the position, and expanding this differential equation as a Taylor series provides:

$$r_i(t + \Delta t) = r_i(t) + \frac{dr_i(t)}{dt}\Delta t + \frac{1}{2}\frac{d^2 r_i(t)}{dt^2}\Delta t^2 + \frac{1}{6}\frac{d^3 r_i(t)}{dt^3}\Delta t^3 + \mathcal{O}(\Delta t^4) \tag{2.62}$$

which is equivalent to writing

$$r_i(t + \Delta t) = r_i(t) + v_i(t)\Delta t + \frac{1}{2}a_i(t)\Delta t^2 + \frac{1}{6}\frac{d^3 r_i(t)}{dt^3}\Delta t^3 + \mathcal{O}(\Delta t^4). \tag{2.63}$$

Taking the sum between two versions of this expression, one with a positive step and one

with a negative step, results in

$$\begin{aligned} r_i(t+\Delta t) + r_i(t-\Delta t) &= r_i(t) + v_i(t)\Delta t + \frac{1}{2}a_i(t)\Delta t^2 + \frac{1}{6}\frac{d^3 r_i(t)}{dt^3}\Delta t^3 + \mathcal{O}(\Delta t^4) \\ &\quad + \left[r_i(t) - v_i(t)\Delta t + \frac{1}{2}a_i(t)\Delta t^2 - \frac{1}{6}\frac{d^3 r_i(t)}{dt^3}\Delta t^3 + \mathcal{O}(\Delta t^4) \right] \\ &= 2r_i(t) + a_i(t)\Delta t^2 + \mathcal{O}(\Delta t^4) \end{aligned} \tag{2.64}$$

which can be rearranged to achieve the result:

$$r_i(t+\Delta t) = 2r_i(t) - r_i(t-\Delta t) + \frac{F_i(t)}{m_i}\Delta t^2. \tag{2.65}$$

The time step, Δt, is chosen such that it is on the order of the fastest motion with the system, and for sufficiently small time steps, this algorithm provides an accurate approximation of trajectories.[146] In this work, a 5 fs time step was used, which was made possible by the relatively slow motion exhibited by the heavy atoms present in the $CsPbI_3$ system.

The MD calculations contained in this thesis were performed in LAMMPS (Large-scale Atomic/Molecular Massively Parallel Simulator)[176] using the NVT canonical ensemble (meaning the number of particles, N; volume, V; and temperature, T, are held constant).

In keeping with the constraints of the given ensemble, a thermostat must be chosen to specify how the equations of motion are obeyed. The NVT simulations performed in this work utilise two different thermostats: the Langevin thermostat and the Nosé–Hoover thermostat. The Langevin thermostat maintains a constant temperature by introducing a friction coefficient into Newton's equations of motion. This method also includes a random force which mimics the effect of particle motion damping as a result of friction. This random force is chosen according to a Gaussian distribution. As a stochastic thermostat, the Langevin thermostat provides a computationally efficient method for performing expensive AIMD simulations (see Subsection 2.6.1).[146,177] The Nosé–Hoover thermostat maintains the simulation at a specified temperature by introducing two terms

to the Langevin thermostat: a friction term and an additional equation which provides feedback to control the temperature at a constant value. As a result, the Nosé–Hoover thermostat couples the system to a heat bath which provides more accurate trajectories at a greater cost. This thermostat is utilised for the MD diffusion simulations described in Chapter 3, as it provides a more realistic model of transport properties.[146,177]

Within classical molecular dynamics simulations, potential energy contributions arising due to interactions between atoms are calculated using an interatomic potential which contains a set of coefficients describing the type and strength of interactions between the various species in the simulation. The method used to calculate the energy and forces fed into the MD framework is the distinguishing feature which separates classical MD, *ab initio* MD, and MLIP MD.

2.6.1 *Ab Initio* Molecular Dynamics

Ab Initio Molecular Dynamics (AIMD)[178] is a method which incorporates *ab initio* simulation calculations of forces and energies into the molecular dynamics framework. Within an AIMD simulation, ion positions are updated using classical equations of motion as determined by the chosen time-propagation algorithm and the choice of thermostat as described in the previous section.[146,177] Following each ionic step, an *ab initio* calculation is performed to generate the forces and energy of the system which makes these calculations expensive to run on long timescales. However, AIMD can be useful for high-accuracy simulations such as modelling molecular interactions at a crystal surface. In addition, AIMD-generated trajectories can be sampled to create training datasets for machine learning interatomic potentials.

2.7 Machine Learning Interatomic Potentials

Machine Learning Interatomic Potentials (MLIPs) promise molecular dynamics simulations with the accuracy of *ab initio* methods while retaining the efficiency of classical

methods. Machine learning techniques have been developed to generate new force fields of higher accuracy which can replace the classical force fields traditionally used in MD simulations. In contrast to classical force fields which are difficult to develop and are not available for all systems; machine learning algorithms provide a means of training highly accurate force fields, MLIPs, for many chemical systems given a high-accuracy training dataset.

The MLIP used in this thesis is MACE (Multi-ACE), a higher order equivariant message passing neural network which builds on the framework developed in the Atomic Cluster Expansion (ACE) descriptors which are detailed below.[179,180] MLIPs are trained on a dataset of structures containing information about the system including atomic coordinates, energies, forces, and species labels. During training, the MLIP learns the energy of the total system as well as the atomic forces and stresses in the structure as calculated by DFT. The goal of training is to develop an MLIP that can accurately predict the potential energy and atomic forces of a structure with the same level of accuracy as DFT. MLIPs are trained on short-range interactions within a particular cut-off. These models are short range which removes the size-dependency of the calculation in order to achieve the desired efficiency. As a result, the total energy of the system is calculated based on local atomic environments.[181]

The model learns local environments by creating a set of descriptors, P, based on a set of symmetry conditions. First, these descriptors must be invariant with respect to translation.[182] Translating atoms in space does not change their energy, so this transformation cannot change the descriptors, $P(x_i) = P(x_i + T)$. Rotations, while not changing the energy of an atom, do effect other properties such as dipole moments. As a result, descriptors must be equivariant with rotation: $P(x_i \times R) = P(x_i) \times R$. Descriptors must also be invariant to permutations because swapping two identical atoms in space does not change the energy of the system: $P(x_i) = P(x_{\sigma(i)})$. The result of this training is the creation of a descriptor space that is much larger than real space with many descriptors, P, that do not map onto real sites, x_i; however, all real sites, x_i, must map onto a

descriptor, P. Descriptors are also associated with a particular body order: second order descriptors describe two-body interactions (bonds), third order descriptors describe three-body interactions (angles), and higher-body descriptors include higher-order geometric correlations (e.g. dihedrals). As energy transitions should be smooth, it is also important that descriptor representations and their derivatives are also slowly varying with small changes in real space corresponding to small changes in descriptor space.[181]

2.7.1 Descriptor Frameworks

ACE

ACE was developed by Ralf Drautz in 2018.[183] The goal of developing these descriptors was to create a complete and systematically improvable descriptor of local atomic environments that scale efficiently with the size of the system and with the number of elements in the system, which earlier methods did not. The energy of a system can be described as a many-atom expansion,

$$E = V_0 + \sum_i V^{(1)}(\mathbf{r}_i) + \frac{1}{2}\sum_{ij} V^{(2)}(\mathbf{r}_i, \mathbf{r}_j) + \frac{1}{3!}\sum_{ijk} V^{(3)}(\mathbf{r}_i, \mathbf{r}_j, \mathbf{r}_k) + \frac{1}{4!}\sum_{ijkl} V^{(4)}(\mathbf{r}_i, \mathbf{r}_j, \mathbf{r}_k, \mathbf{r}_l) + ..., \tag{2.66}$$

where $\mathbf{r}_i$ is the position of atom i and the variables V are potentials such that V_0 is a constant which can be set to zero, $V^{(1)}$ is the chemical potential, and the higher-order potentials $V^{(2)}$, $V^{(3)}$, etc. are symmetric and uniquely defined potentials describing many-body interactions. These system-wide potentials can be separated into atomic contributions to define the atomic energy E_i as

$$E_i = V^{(1)}(\mathbf{r}_i) + \frac{1}{2}\sum_{j} V^{(2)}(\mathbf{r}_i, \mathbf{r}_j) + \frac{1}{3!}\sum_{jk} V^{(3)}(\mathbf{r}_i, \mathbf{r}_j, \mathbf{r}_k) + \frac{1}{4!}\sum_{jkl} V^{(4)}(\mathbf{r}_i, \mathbf{r}_j, \mathbf{r}_k, \mathbf{r}_l) + ... \tag{2.67}$$

A complete set of orthogonal basis functions, $\phi_v(\mathbf{r})$, that depend on a single bond, $\mathbf{r}$, are constructed by the product of radial functions, R_{nl}, and spherical harmonic functions,

Y_l^m, as

$$\phi_v(\mathbf{r}) = \sqrt{4\pi} R_{nl}(r) Y_l^m(\hat{\mathbf{r}}), \tag{2.68}$$

where $v = (nlm)$, $r = |\mathbf{r}|$, and $\hat{\mathbf{r}} = \mathbf{r}/r$ meaning that the radial functions depend on the distance from the atom and the spherical harmonics depend on the direction of the bond. n, l, and m take the same meaning as understood from atomic orbitals with n describing the number of nodes in the radial function, l describing the shape of the orbital via the angular momentum, and m describing the orientation of the spherical harmonic in space.

ACE achieves linear scaling with the number of site neighbours by defining an atomic base, A_{iv}, which is the projection of single-bond basis functions onto the local atomic density such that

$$A_{iv} = \sum_j \phi_v(\mathbf{r}_{ij}). \tag{2.69}$$

This allows the site energy to be written as a function of the atomic base, A_{iv}, as

$$E_i(\boldsymbol{\sigma}) = \sum_v c_v^{(1)} A_{iv} + \sum_{v_1 v_2}^{v_1 \geq v_2} c_{v_1 v_2}^{(2)} A_{iv_1} A_{iv_2} + \sum_{v_1 v_2 v_3}^{v_1 \geq v_2 \geq v_3} c_{v_1 v_2 v_3}^{(3)} A_{iv_1} A_{iv_2} A_{iv_3} + ..., \tag{2.70}$$

where $c_v^{(K)}$ are expansion coefficients symmetric to permutation of the indices v_1, v_2, ... which are defined for a given configuration $\boldsymbol{\sigma} = (\mathbf{r}_{1i}, \mathbf{r}_{2i}, ..., \mathbf{r}_{Ni})$ for atom i.

The basis functions, $B^{(K)}$, are rotationally invariant descriptors constructed from tensor products of the atomic base. These basis functions are constructed by coupling the angular momenta of the spherical harmonics comprising the atomic basis functions with Clebsch–Gordan coefficients which provide a systematic method of decomposing products of spherical harmonics into components with well-defined total angular momentum. The products of these couplings transform equivariantly under rotations. Rotational invariance is obtained only for couplings with total angular momentum $l = 0$, which corresponds to scalar quantities. For two-body terms, only radial functions can contribute because Y_{00} is the only spherical harmonic that is invariant under rotation. For higher-body terms, products of angular basis functions are recursively coupled via Clebsch–Gordan coeffi-

cients, and only coefficients that yield a total angular momentum of $l = 0$ contribute to rotationally invariant features. These rotationally invariant basis functions, $B^{(K)}$, can be used to construct an expression for the energy that is invariant with respect to translation, rotation, and inversion,

$$E_i(\boldsymbol{\sigma}) = \sum_n c_n^{(1)} B_{in}^{(1)} + \sum_{n_1 n_2 l}{}' c_{n_1 n_2 l}^{(2)} B_{in_1 n_2 l}^{(2)} + \sum_{n_1 n_2 n_3 l_1 l_2 l_3}{}' c_{n_1 n_2 n_3 l_1 l_2 l_3}^{(3)} B_{in_1 n_2 n_3 l_1 l_2 l_3}^{(3)} + ... \quad (2.71)$$

Notably, the basis functions described here, $B^{(K)}$, are invariant, meaning that directional information is lost from the model. As described previously, descriptors should retain equivariance with respect to rotation in order to accurately describe properties such as dipoles.

MACE

MACE builds on the advances developed within the ACE framework with two notable distinctions. First, MACE, a message passing neural network, utilises a graph neural network framework of environmental descriptors in contrast to the linear description utilised by ACE, and second, MACE achieves equivariance in the definition of its higher-order feature descriptors. Message passing neural networks (MPNNs) are a form of graph neural network (GNN). For a crystal structure, the nodes of the graph represent atoms and the edges of the graph represent bonds. In this framework, all atoms within a certain cut-off radius are considered to be bonded regardless of chemical intuition. A node can be represented as $\sigma_i^{(t)} = (\boldsymbol{r}_i, z_i, \boldsymbol{h}_i^{(t)})$ where $\boldsymbol{r}_i$ is the position of that atom, z_i is the chemical element, and $\boldsymbol{h}_i^{(t)}$ are the learnable features. Each iteration of the MPNN includes three stages: message construction, update, and readout. The following description of this process follows the outline of MACE as derived in Batatia *et al.* (2023).[179]

First, a message, $\boldsymbol{m}_i^{(t)}$, is created for each node by gathering information from its neighbours within a certain cut-off in the graph: $\boldsymbol{m}_i^{(t)} = \bigoplus_{j \in \mathcal{N}(i)} M_t(\sigma_i^{(t)}, \sigma_i^{(t)})$ where M_t is the learnable message function and $\bigoplus_{j \in \mathcal{N}(i)}$ represents the pooling function over all

neighbours of atom i. In MACE, the edges of the graph are embedded with radial basis functions, spherical harmonics, and embeddings of the weighted averages of the previous node features. During pooling, MACE retains two-body features with full directional information which creates a full representation of the atomic environment,

$$A^{(t)}_{i,kl_3m_3} = \sum_{l_1m_1,l_2m_2} C^{l_3m_3}_{l_1m_1,l_2m_2} \sum_{j\in\mathcal{N}(i)} R^{(t)}_{kl_1l_2l_3}(r_{ij}) Y^{m_1}_{l_1}(\hat{\boldsymbol{r}}_{ji}) \sum_{\tilde{k}} W^{(t)}_{k\tilde{k}l_2} h^{(t)}_{j,\tilde{k}l_2m_2}, \tag{2.72}$$

where $C^{l_3m_3}_{l_1m_1,l_2m_2}$ are the standard Clebsch–Gordan coefficients which ensure the proper equivariance, $R^{(t)}_{kl_1l_2l_3}$ are the radial descriptors formed by Bessel functions, and r_{ji} is the interatomic distance between nodes with the relevant unit vector $\hat{\boldsymbol{r}}_{ji}$.

The critical feature of MACE is the construction of higher-order features from these atomic environment descriptions as tensor products of the atomic features as

$$\boldsymbol{B}^{(t)}_{i,\eta_\nu,kLM} = \sum_{\boldsymbol{lm}} C^{LM}_{\eta_\nu,\boldsymbol{lm}} \prod_{\xi=1}^{\nu} \sum_{\tilde{k}} w^{(t)}_{k\tilde{k}l_\xi} A^{(t)}_{i,\tilde{k}l_\xi m_\xi}, \tag{2.73}$$

where $\boldsymbol{lm} = (l_1m_1, ..., l_\nu m_\nu)$. $C^{LM}_{\eta_\mu,\boldsymbol{lm}}$ represent the generalised Clebsch–Gordan coefficients to ensure equivariance and $w^{(t)}_{k\tilde{k}l_\xi}$ are the weights of the relative channels. ν represents the correlation order which is defined as the body order minus 1 for a descriptor. Generalised Clebsch–Gordan coefficients are products of standard Clebsch–Gordan coefficients which reduce reducible representations of tensor products into irreducible representations (labelled by L).

Crucially, this step ensures the higher-order features, $\boldsymbol{B}^{(t)}_{i,\eta_\nu kLM}$, are L-equivariant meaning they transform as tensors of rank L. This ensures that internal features and messages transform consistently under the O(3) symmetry group which describes rotations and reflections of atomic positions in 3D Euclidean space. It is this feature which allows MACE to describe an atomic system at a high accuracy with relatively few layers. Another notable feature of MACE is that tensor products are evaluated on edges only once to create 2-body A-features. The initial edge embeddings are expensive, so higher-order

equivariant tensor products are performed on nodes (fewer nodes than edges) to keep the model efficient, and generalised Clebsch–Gordan coefficients are summed via loop tensor contraction with learnable weights instead of an expensive tensor product while maintaining higher-order accuracy. The loop tensor contraction builds higher-body-order (up to 4 body messages) information into a single layer; therefore, only 2 message passing layers are required to reach accuracy which other models require 5 or 6 layers to achieve.

Following construction, the message can then be written as a linear expansion

$$m_{i,kLM}^{(t)} = \sum_{\nu} \sum_{\eta_\nu} W_{z_i kL,\eta_\nu}^{(t)} \boldsymbol{B}_{i,\eta_\nu kLM}^{(t)} \tag{2.74}$$

where $W_{z_i kL,\eta_\nu}^{(t)}$ is the learnable weight matrix. This results in a message that is linear combination of higher order features $\boldsymbol{B}_{i,\eta_\nu kLM}^{(t)}$.

Second, the message is updated by transforming it into new features: $\boldsymbol{h}_i^{(t+1)} = U_t(\sigma_i^{(t)}, \boldsymbol{m}_i^{(t)})$ where U_t is a learnable update function. In MACE, this update function can be written as

$$\boldsymbol{h}_{i,kLM}^{(t+1)} = \sum_{\tilde{k}} W_{kL,\tilde{k}}^{(t)} m_{i,\tilde{k}LM} + \sum_{\tilde{k}} W_{z_i kL,\tilde{k}}^{(t)} h_{i,\tilde{k}LM}^{(t)}. \tag{2.75}$$

Third, after a specified number of construction and update steps, T, the learnable readout function maps the node states to the energy as $E_i = \sum_{t=1}^{T} \mathcal{R}_t(\sigma_i^{(t)})$. In MACE, these readout functions appear as:

$$E_i = E_i^{(0)} + E_i^{(1)} + ... + E_i^{(T)} \tag{2.76}$$

where

$$E_i^{(T)} = \mathcal{R}_t(\boldsymbol{h}_i^{(t)}) = \begin{cases} \sum_{\tilde{k}} W_{readout,\tilde{k}}^{(t)} h_{i,\tilde{k}00}^{(t)} & \text{if} \quad t < T \\ MLP_{readout}^{(t)}\left(\left\{h_{i,k00}^{(t)}\right\}\right) & \text{if} \quad t = T \end{cases}. \tag{2.77}$$

Following update, the internal messages and updates are equivariant, but the site energy must be invariant to rotation. In the readout phase, only the invariant part of

the node feature ($L = 0$) is mapped to the energy which ensures that the energy of the system does not change if the structure is rotated in space.

Finally, chemical elements are embedded into a fixed-size vector space instead of being treated as a rigid dimension. This ensures that the B-features do not include an extra species dimension, so the basis set does not increase in size with the number of elements. Instead, element information is passed through the message construction phase where the learnable weight matrices W depend on the chemical element, z_i, meaning that the complexity of the model does not scale with the number of species in the system. This makes MACE ideal for training systems with multiple elements such as doped systems. This high degree of training efficiency and demonstrated accuracy, especially with regard to the number of elements in the system,[184] was a key reason for the choice of MACE as the MLIP model used in this thesis.

Chapter 3

Ion Migration and Dopant Effects in the γ-$CsPbI_3$ Thin Film Solar Cell Material

3.1 Introduction

$CsPbI_3$ remains one of the most highly studied perovskite solar cell materials due to its thermal stability and suitable band gap. As an all-inorganic material, $CsPbI_3$ derives a higher thermal stability and degradation resistance due to the absence of organic A-site cations whose volatility can drive degradation when exposed to heat and light.[71,72] In addition to the improved thermal stability, $CsPbI_3$ has a band gap of 1.73 eV[15,74] which is suitable for both single- and multi-junction devices, including both silicon–perovskite and perovskite–perovskite tandem architectures.[43,44] The current record efficiency for an all-inorganic $CsPbI_3$ module has reached 21.41%,[185] making it a promising next-generation PV material.

Despite the many strengths of the perovskites, this class of material suffers from a high concentration of intrinsic point defects ($\sim 10^{14}$ cm^{-3}),[186,187] primarily consisting of halide vacancies. Perovskites are soft materials that distort easily under pressure,[188,189] and they

are also ionic-electronic conductors with some experimental measurements demonstrating that ionic conductivities exceed electronic conductivities.[190] The high concentrations of defects in perovskites are intrinsically linked to iodide (I) migration.[82] Historically, perovskites were considered to be 'defect tolerant'[54] because I vacancies, the most common defects, do not introduce trap states, electronic states deep in the band gap.[22,56,191–195] For reference, trap densities are measured to be between $\sim 10^{11}$–10^{16} cm^{-3} for single crystals and polycrystalline samples which is comparable to the traditional semiconductor polycrystalline silicon at 10^{13}–10^{14} cm^{-3}.[196]

The presence of point defects in perovskites is inherently linked to ion migration which presents a host of issues in perovskite semiconductors with voltage-current hysteresis being the most commonly discussed.[55,58,197–199] Voltage-current hysteresis (often referred to as simply hysteresis) describes the mass anisotropic migration of ions as the result of the electric field applied in the solar device during operation. This results in the build-up of ions near interfaces.[200] When the local composition varies throughout the perovskite as a result of this build-up, a band bending effect can be observed.[55] This is especially problematic in mixed-halide compositions where de-mixing occurs quickly under light conditions, reducing the device's absorption efficiency and creating I rich regions that can act as trap centres for non-radiative recombination.[201,202] Band bending reduces the electronic overlap between the thin film and the charge transport layers, reducing the efficiency of the device. This build-up has been linked to 'ionic losses,' the loss in PCE due to hysteresis during the first moments of device performance. Hysteresis has historically been considered a reversible effect with experiments demonstrating that the ions return to an even distribution across the thin film when illumination is removed.[203]

In addition to hysteresis, point defects and ion migration also reduced device performance by promoting degradation. Defect clusters have been shown to form at the interfaces and grain boundaries of thin films[82] where these defect clusters can lead to formation of the stable but photo-inactive precursor PbI_2.[83,109,204] In addition, grain boundaries have been shown to act as ion conduction channels.[205,206] Here, clustering of I defects

in high concentrations can again lead to structural degradation.[83] Once secondary phases form, the whole material will begin to irreversibly degrade back into its precursors. In contrast to the 'ionic losses,' this poses a much more substantial issue for long-term device stability.

Previous computational work has focused on the cubic α-$CsPbI_3$[82,207] structure with comparatively few studies investigating other polymorphs.[208–212] However, the α-polymorph is not stable in thin films at room temperature.[213] Instead, it is the orthorhombic γ-polymorph that is the stable room-temperature phase in thin films.[15,40,213] This structure is distinct from the cubic phase due to its tilted octahedra which introduce two distinct I sites as detailed in Section 3.3.1. These sites introduce additional I migration pathways which must be studied to provide a comprehensive picture of ion migration in γ-$CsPbI_3$ thin films. The impact of dopants on these pathways and migration barriers must also be investigated to understand the relationships between inorganic doping and material stability.

In the attempt to improve the various stability concerns associated with perovskite solar cell devices, recent experimental studies[16,89,91,93–97,208,214–225] posit that the inclusion of inorganic dopants improves device lifetimes and efficiency. However, these studies often neglect in-depth characterisation of the synthesised materials to discern what role these dopants are playing, or even if the dopants are being incorporated into the bulk of the perovskite. In the absence of experimental characterisation, it has been hypothesized that these dopants were improving perovskite stability by reducing ion migration. This effect could be due to steric or electronic effects: dopant introduction can cause structural distortions that affect the I migration pathways and the associated activation energies. This work seeks to answer exactly these questions: what effect do dopants have on I migration and are there any overarching trends that suggest which dopants would be most effective?

This chapter provides a comprehensive investigation into the role inorganic dopants and ion migration play in the γ-$CsPbI_3$ perovskite solar cell material as published by

Arber *et al.* in *ACS Chemistry of Materials* (2025).[226] First, *ab initio* DFT models are developed to simulate the crystalline lattice and electronic structure of γ-$CsPbI_3$. Second, climbing image nudged elastic band (CI-NEB) calculations were performed to model ion migration via distinct pathways in the pristine material. These results are then compared to CI-NEB calculations performed in the presence of nine inorganic dopants. Finally, for the first time for γ-$CsPbI_3$, a machine learning interatomic potential (MLIP) was trained with MACE[180] to model ion migration over longer timescales ($\sim$80 ns), beyond the capability of traditional *ab initio* techniques. Analysis of these long-timescale trajectories provides a more realistic picture of ion migration that represents the dynamics observed during device operation and shows whether doping strategies can successfully improve device performance by reducing ion migration.

3.2 Methodology

3.2.1 *Ab initio* Simulations

All density functional theory (DFT) calculations were performed in the Vienna Ab Initio Simulation Package (VASP)[151,152,154,156] with the generalized gradient approximation (GGA) exchange–correlation functional PBEsol,[150] as introduced in Chapter 2. A plane-wave cut-off energy of 500 eV was applied, along with a k-point mesh defined by a k-spacing of $0.2/2\pi$Å^{-1}. Structural optimisations were performed until all atomic forces converged to below 0.01 eV Å^{-1}. The choice of the PBEsol functional reflects its well-established balance between computational cost and accuracy, particularly in predicting lattice parameters. All calculations incorporated spin polarisation to account for possible contributions from unpaired electrons, which can be especially relevant in systems containing defects;[227] however, no signs of charge localisation were observed in any of the defect structures examined. The band structure and density of states figure was plotted using the Python Materials Genomics code (Pymatgen),[228] and the CI-NEB images were created and analysed with the assistance of VASP Transition State Theory Tools

(VTSTTools).[170,171]

Ion migration, which is the focus of this study, is primarily governed by the lattice geometry and local defect environment. While spin-orbit coupling strongly influences the electronic structure of $CsPbI_3$, previous work has shown that its inclusion has only a minor effect on the atomic forces calculated while relaxing iodide vacancy structures, which are the key quantities required for CI-NEB calculations and MLIP training.[229] Consequently, spin-orbit coupling was omitted to enable the large number of CI-NEB calculations and reference structures required for MLIP development at a computationally feasible cost. Similarly, although the higher-order exchange–correlation functional HSE06 was examined, the substantially higher computational expense of employing hybrid functionals in VASP would have made the present study prohibitively expensive. The use of GGA functionals and the neglect of spin-orbit coupling is consistent with previous first-principles investigations of ion migration in lead-halide perovskites, which have successfully employed a similar methodology for migration-barrier calculations.[55,58] For further details of functional testing, see Appendix A.

Ion migration processes were examined using the climbing-image nudged elastic band (CI-NEB) method[170,171] as implemented in VASP. These calculations were performed on $2\times2\times2$ supercells containing 159 atoms and a single I vacancy which ensured that periodic image interactions were minimized. Both the initial and final states were fully relaxed to ensure an accurate determination of the transition state energy profile. Activation energies for individual migration pathways were determined by taking the average energy difference between the saddle point and the initial and final configurations along the minimum energy pathway. The supercell employed is sufficiently large for describing ion migration in the dilute-defect limit and avoids interactions between periodically repeated vacancies. This general approach has been used reliably in several previous studies of ion migration.[55,214,230]

Table 3.1: Composition of the training dataset for MLIP development. All structures are $2 \times 2 \times 2$ supercells of γ-$CsPbI_3$.

	Pristine			**Sn-Doped**		
Source	NEB	AIMD	MD	NEB	AIMD	MD
# Structures	238	2375	1274	361	213	90

3.2.2 Machine Learning Methods

To probe long-range I transport beyond DFT-accessible timescales, a machine learning interatomic potential (MLIP) was trained using the MACE framework as described in Chapter 2.[179,180] The MLIP was constructed and trained on a dataset of approximately 4,000 structures (Table 3.1). This dataset consisted of configurations obtained from *ab initio* molecular dynamics (AIMD) simulations as well as single-point calculations on structures obtained during the CI-NEB migration pathway relaxations. All training data was generated at the same GGA level of theory used for the DFT calculations. The dataset included both pristine and defect configurations, including those containing vacancies and dopants in order to provide broad structural and chemical coverage for model training. Analysis of the dataset energy vs density distribution and of the dataset Smooth Overlap of Atomic Positions (SOAP) descriptors was performed to ensure an appropriately diverse training set (Figure 3.1).

The MLIP development was carried out using the MACE framework,[179,180] which is a higher order equivariant message passing neural network approach for constructing interatomic potentials. The model employed a maximum equivariance order of 2, 256 chemical channels, and 2 layers with a local environment cut-off radius of 5 Å. A single model was trained from scratch and demonstrated sufficient transferability across the pristine and Sn-doped compositions investigated in this work.

The MACE model trained in this chapter was developed before the existence of foundational models. As a result, this model was entirely trained from scratch using DFT data generated specifically on this γ-$CsPbI_3$ system. The dataset used for training contains

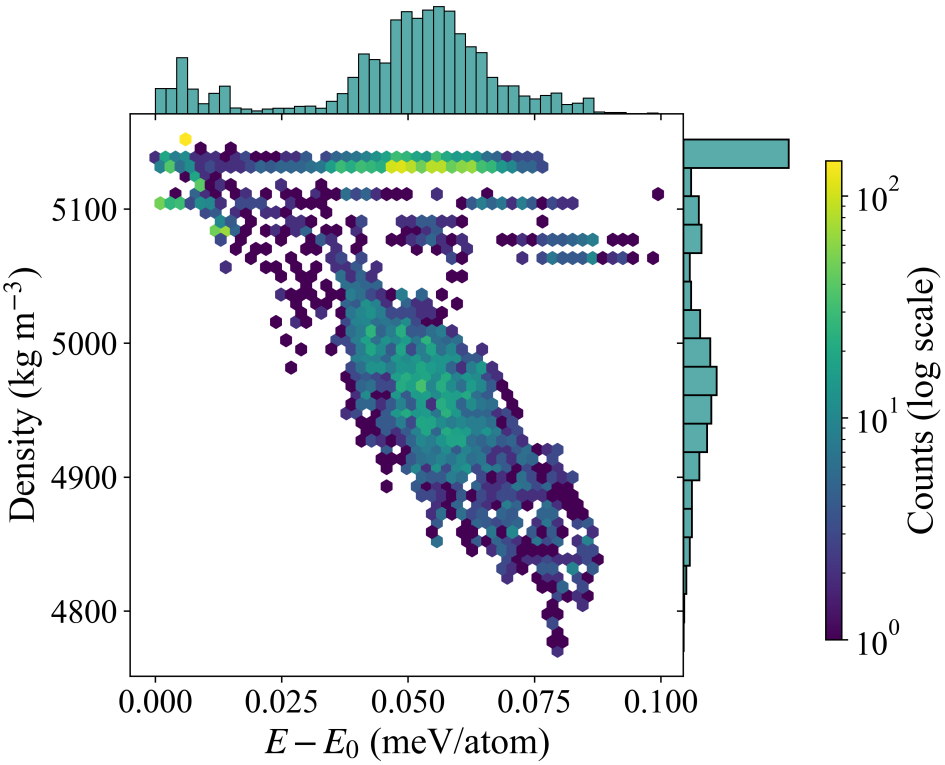


Figure 3.1: Depiction of the training data showing the variation of density with relative energy.

∼4,000 structures (Table 3.1) obtained from geometry relaxations, CI-NEB calculations, and AIMD simulations spanning 300 K–600 K. AIMD calculations were performed for a range of cell volumes and biasing was introduced into the simulations to generate a diverse set of local configurations in the training data. By trial-and-error, it was discovered that the most efficient way to select structures from this dataset for training was to choose the most distinct structures by performing a Furthest Point Sampling (FPS) analysis. SOAP descriptors were used to create a vector representation of each structure in the dataset. These vector representations were then reduced into a two-dimensional representation via a Kernal Principal Component Analysis (PCA), upon which the FPS sampling could be performed. The trained model achieved a mean absolute error (MAE) of 0.503 meV/atom for energies and 1.06 meV/Å for forces (Figure 3.2).

While low MAE values for the energies and forces are a crucial test for model validity, these values do not guarantee an accurate or stable potential. Additional validation of

the model against DFT and experiment where possible is necessary to ensure accuracy. In this case, the trained model was validated against the DFT CI-NEB calculations which show good agreement, as discussed in Section 3.3.3. Additional validation comes from demonstration of stable energies during production MD runs and lattice parameters consistent with experiment at room temperature.

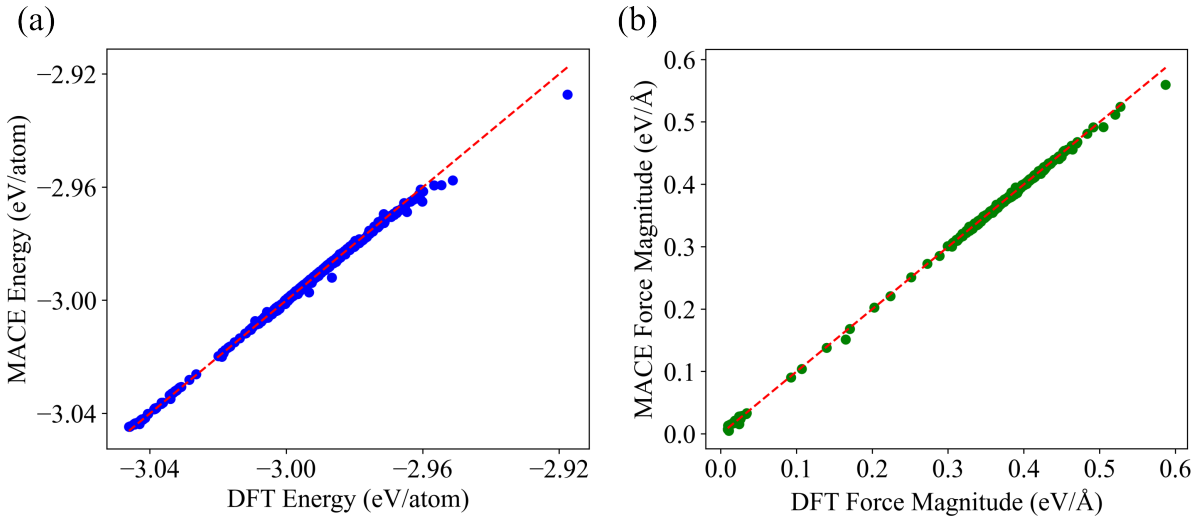


Figure 3.2: Performance of the MACE-trained MLIP model. Mean absolute error in (a) total energy (0.695 meV/atom) and (b) atomic forces (0.895 meV/Å).

The MACE NEB calculations were performed using the BFGS optimisation algorithm as implemented in ASE and discussed in Chapter 2.[164,165] In the NEB procedure, the endpoint structures were first fully optimised after which the intermediate images were relaxed while constrained to the band, thereby minimising the total energy along the reaction pathway.

MD simulations were then performed on $4\times4\times3$ supercells containing 960 atoms with ∼1% I vacancies (Figure 3.10). Vacancy sites were randomly distributed to reproduce the target concentration of 1%, in agreement with the DFT CI-NEB relaxations. MD simulations were conducted at constant volume and temperature over ∼80 ns, far exceeding typical AIMD timescales which are generally limited to durations below 100 ps. I diffusivities were evaluated from MD trajectories at four temperatures chosen to be linearly spaced on an inverse-temperature scale between 300 K and 500 K. A 10 ns equilibration

period was removed from the beginning of the trajectory to ensure converged dynamics.

Mean-squared displacement (MSD) plots (Figure 3.11) and associated diffusion coefficients were extracted using the kinisi package (v1.0.0).[231,232] The diffusion coefficients, D, were obtained from the MSD according to the Einstein relation where x is position and t is time:

$$\text{MSD} = \langle [x(t) - x(0)]^2 \rangle = 6Dt \tag{3.1}$$

The activation energy (E_a) for I diffusion was determined by examining the temperature dependence of D based on the Arrhenius expression:

$$\ln D = -\frac{E_a}{RT} + \ln D_0, \tag{3.2}$$

where R is the gas constant, T is the absolute temperature, and D_0 is the pre-exponential factor. The value of E_a was obtained from the slope of $\ln D$ plotted against $1/T$.

3.3 Results and Discussion

3.3.1 Ion Migration in Pristine γ-$CsPbI_3$

First, an accurate DFT model of the pristine γ-$CsPbI_3$ perovskite was developed. Lattice parameters and electronic structure properties were modelled to ensure good agreement with experimental data. Lattice parameters were calculated to within 2% of the values measured via a Rietveld refinement of neutron powder diffraction data[15] and the band gap to within 0.13 eV of the value measured via PL studies (Table 3.2).[44]

Table 3.2: Comparison of experimental[15,44] and calculated structural parameters and band gap of γ-$CsPbI_3$.

Parameter	**Experiment**	**Calculated**	**Difference (%)**
a (Å)	8.86	8.71	-1.69
b (Å)	8.58	8.68	1.17
c (Å)	12.47	12.44	-0.24
Mean Angle (°)	90.0	90.0	0.00
Cs–I Bond (Å)	4.42	4.43	0.23
Pb–I Bond (Å)	3.18	3.18	0.00
Band Gap (eV)	1.72	1.60	-6.98

The electronic structure of γ-$CsPbI_3$ was characterised through band structure and density of state calculations (Figure 3.3) which shows the recognizable features of a perovskite: the B-site element (Pb) and the halide (I) contribute to the electronic states near the band edges while the A-site cation (Cs) has no direct impact on the band gap. As a result, the band gap of the perovskite is determined by the Pb–halide bonding interactions. However, the A-site cation does influence the band gap indirectly via octahedral tilting. As the PbI_6 octahedra tilt in the perovskite due to either steric or Coulombic effects from the large A-site cation, the degree of orbital overlap changes within the Pb–I bonds, resulting in a narrowing of the band gap for higher degrees of tilting.[40] As a result, the γ-$CsPbI_3$ perovskite has a narrower band gap (1.72 eV[15]) than the α-$CsPbI_3$ perovskite (1.92 eV[15]).

The two types of intrinsic point defects are Schottky defects and Frenkel defects. A Schottky defect refers to an empty lattice site (a vacancy) while a Frenkel defect describes an atom that has been moved off its lattice site to create an interstitial, thereby forming a vacancy-interstitial pair. The full Schottky defect (Eqn. 3.3) describes the creation of one formula unit of vacancies. In the $CsPbI_3$ material, this equates to one Cs vacancy, one Pb vacancy, and three I vacancies. The creation of a Frenkel vacancy-interstitial defect pair is described for the I Frenkel defect in Eqn. 3.4. These expressions are the

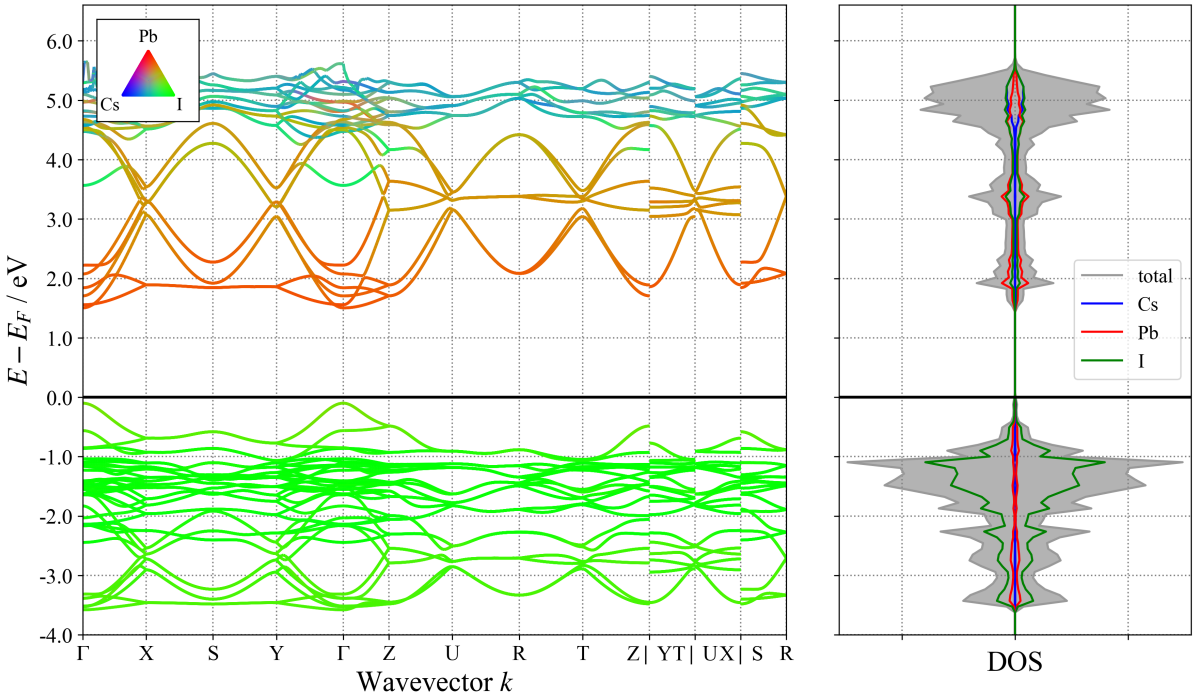


Figure 3.3: Band structure (left) and density of states (right) of γ-$CsPbI_3$ calculated with PBEsol. The valence band is primarily comprised of I states, and the lower energy conduction band states belong to Pb with the Cs A-site contributing little near the band edges.

basis for calculating the formation energies for the two types of defect disorder.

$$\text{nil} \rightarrow V'_{\text{Cs}} + V''_{\text{Pb}} + 3V^{\bullet}_{\text{I}} \quad \text{(Full Schottky defect)} \tag{3.3}$$

$$\text{nil} \rightarrow V^{\bullet}_{\text{I}} + I'_i \quad \text{(I Frenkel defect)} \tag{3.4}$$

Calculation of these two defect formation energies demonstrates that the $CsPbI_3$ Schottky defect is more favourable (0.18 eV per defect) than the I Frenkel defect (0.58 eV per defect), a result that agrees with previous computational defect studies of the halide perovskites.[56] Both the Schottky and I Frenkel energies were calculated by placing all defects in a single supercell, and as a result, these values include the binding energy for the various point defects. The vacancy formation energies for the 8*d* and 4*c* I sites were found to be 0.118 and 0.119 eV per defect, respectively, which confirms that both vacancies would exist in approximately equal concentrations. This finding also reinforces the

understanding that vacancy-type disorder dominates these systems. Ionic conductivity measurements as a function of I_2 partial pressure confirm that I vacancies are the primary mobile ionic species[57] and that it is the I vacancies which facilitate ion diffusion through the lattice.[57,233–235]

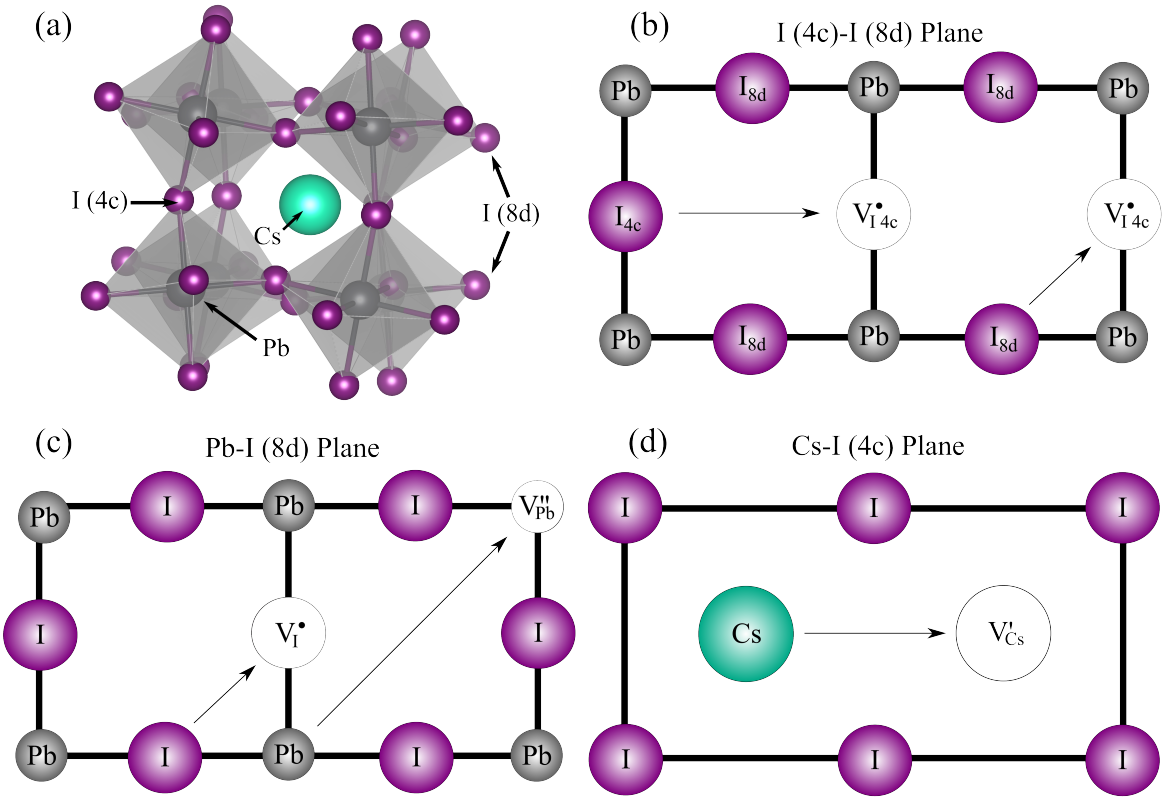


Figure 3.4: Illustrations of (a) the γ-$CsPbI_3$ perovskite lattice with Wyckoff site labels distinguishing the 8*d* and 4*c* I sites and (b)–(d) the five migration pathways investigated using CI-NEB calculations. Figure adapted from Arber *et al.*, *Chem. Mater.*, 2025, **37**, 4416–4424[226] under the Creative Commons License: https://creativecommons.org/licenses/by/4.0/. Published by the American Chemical Society.

After confirming the dominant type of defect disorder in the perovskite structure, the next step was to develop a DFT model of ion migration. This process began by identifying the possible migration pathways through the γ-polymorph. The tilting of the PbI_6 octahedra lowers the symmetry of the γ-polymorph relative to the α polymorph. This lowering of symmetry also impacts the availability of migration pathways through the lattice. In the perfectly cubic α structure, each I–I hop can be treated equivalently, but

that is no longer the case in the orthorhombic structure. The octahedral tilting creates two inequivalent I symmetry sites (8*d* and 4*c*) allowing for three distinct hopping pathways (Figure 3.4). As the 8*d* and 4*c* Wyckoff sites are in different planes, the differing symmetry also raises the possibility that diffusion could be anisotropic if there is a substantial difference between activation energies which could impact device performance if the perovskite grains are aligned incorrectly.

Ion migration is considered to occur via a traditional vacancy-mediated hopping mechanism and has been observed in similar perovskite systems.[57,233–235] Based on this understanding, CI-NEB calculations were performed to model this hopping migration mechanism. To begin, all distinct migration pathways were mapped on the orthorhombic lattice. Figure 3.4(a) illustrates the γ-$CsPbI_3$ lattice and the distinct I symmetry sites 4*c* and 8*d*. Figure 3.4(b)–(d) depict the five migration pathways investigated in this work. Figure 3.4(b) depicts a slice through the perovskite in the xz or yz planes. These planes contain migrations across the face of the unit cell between neighbouring 4*c* sites and migrations between neighbouring 8*d* and 4*c* sites along the edge of a PbI_6 octahedron. Orthogonal to these planes is the xy slice shown in Figure 3.4(c) which holds migrations along the PbI_6 octahedral edge between adjacent 8*d* sites and Pb migrations across the diagonal of the unit cell to a nearby B-site vacancy. Figure 3.4(d) depicts a parallel xy plane in which a Cs moves to a neighbouring A-site vacancy.

CI-NEB calculations were used to calculate the activation barriers and minimum energy pathways (Figure 3.5) for the five migrations depicted in Figure 3.4. In all cases, the average of the forward and reverse barriers is reported with only the I8*d*-I4*c* profile showing a small degree of asymmetry (∼0.03 eV) (Figure 3.6). As can be expected, the longest migration pathways produce the highest activation barriers. This includes the Cs–Cs, Pb–Pb, and I4*c*–I4*c* pathways. The high barriers for the cation migrations is consistent with our understanding that the cation species are largely immobile in these perovskite systems. Out of the I migration pathways, the 8*d*-8*d* and 8*d*-4*c* pathways are lowest in energy with barriers of 0.34 eV and 0.36 eV, respectively. These pathways

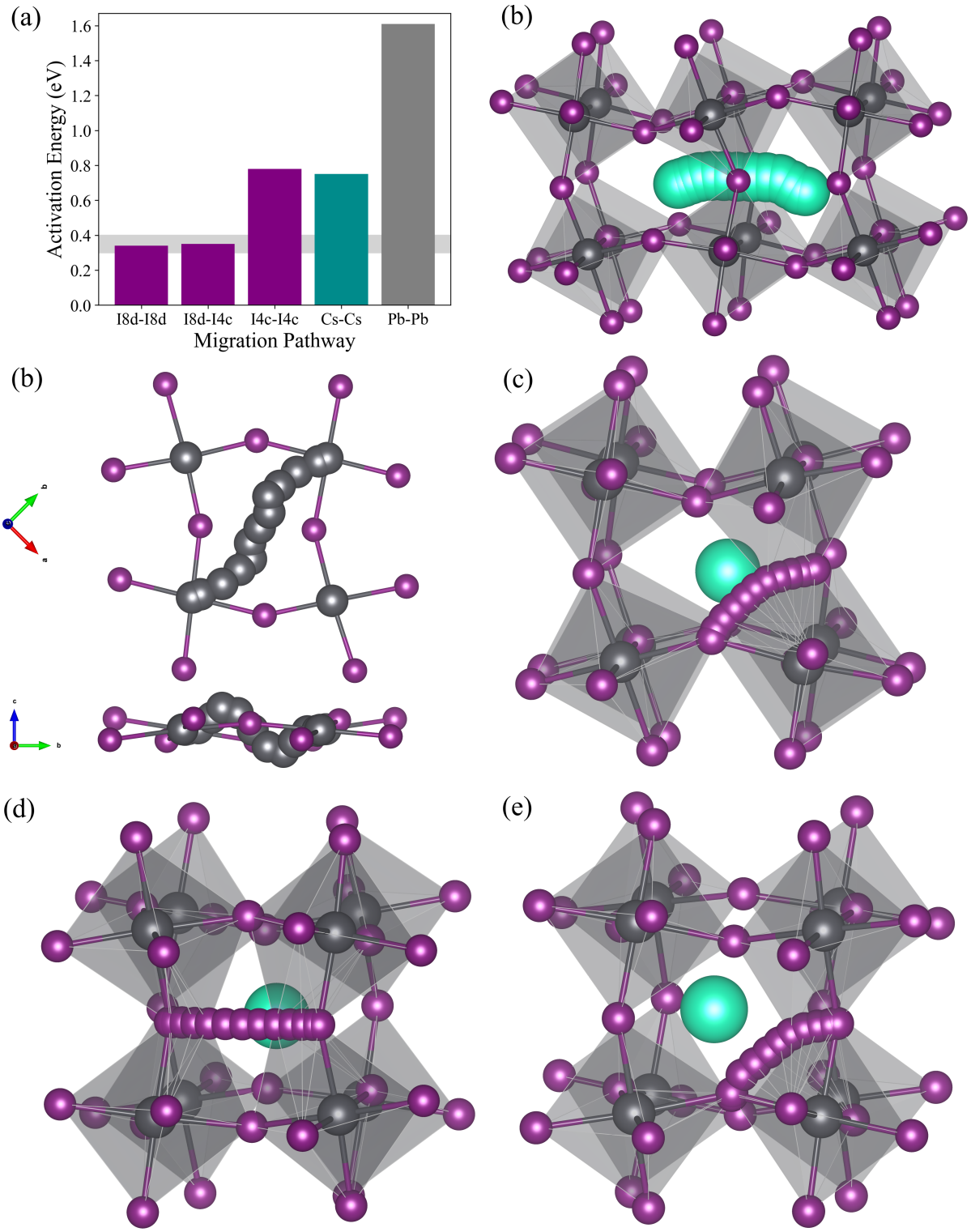


Figure 3.5: (a) Calculated activation energies for the five migration pathways investigated in γ-$CsPbI_3$ with the range of typical literature values shaded behind in grey and (b)–(e) the minimum energy pathways calculated for the Cs–Cs, Pb–Pb, I8*d*–I8*d*, I4*c*–I4*c*, and I8*d*–I4*c* migrations, respectively (Cs, aqua; Pb, grey; I, purple). Figure adapted from Arber *et al.*, *Chem. Mater.*, 2025, **37**, 4416–4424[226] under the Creative Commons License: https://creativecommons.org/licenses/by/4.0/. Published by the American Chemical Society.

correspond to I migrations along the edge of PbI_6 octahedra, and these barriers are consistent with I diffusivity measurements in related halide perovskite systems (Table 3.3). The similarity in the 8*d*–8*d* and 8*d*–4*c* pathways suggests that both will be easily accessible for migration and therefore, will create a three dimensional network of ion diffusion through the lattice.

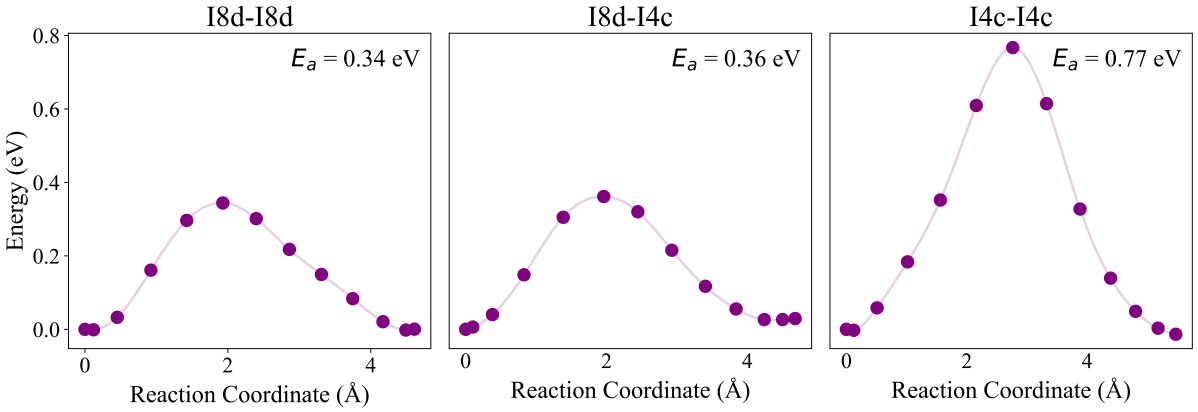


Figure 3.6: NEB energy profiles for the I8*d*–I8*d*, I8*d*–I4*c*, and I4*c*–I4*c* migration pathways.

Notably, the minimum energy pathway observed in these low energy I migration curves around the PbI_6 octahedral edge (Figure 3.5), shifting the transition state away from the Pb atom at the centre of the octahedron. The curvature observed in this migration pathway is the result of the bonding interactions between the Pb and I atoms. Throughout the migration, the Pb–I bond is maintained at a nearly constant length which optimises the stability gained from the bonding overlap of these two atoms and ensures that the Pb atom does not become further under-coordinated. This result replicates the finding of previous computational studies on the perovskites $MAPbI_3$[55] and $LaGaO_3$[236] where similar curved paths were observed. These simulations are also backed up by experimental neutron diffraction maximum entropy methods which illustrate the presence of similar curved migration pathways.[237]

It is worth noting that CI-NEB calculations are limited in their capacity to capture lattice dynamics, as these are static calculations performed along a specified pathway. These calculations do not allow for substantial structural rearrangements or correlated

motion that might occur in a dynamic system, which are addressed below through MD simulations.

Table 3.3: Experimental and calculated activation energies for halide ion migration in a range of inorganic halide perovskites from previous studies and this work. Previous computational work has either relied on DFT-NEB calculations or barriers derived from classical MD performed with a classical force field fitted to DFT data (DFT-CMD); in both cases, these calculations were performed on the high temperature α polymorph.

Compound	**Activation Energy (eV)**	**Technique/Reference**
$CsPbCl_3$	0.29	Expt: AC impedance spectroscopy[233]
$CsPbBr_3$	0.25	Expt: AC impedance spectroscopy[233]
$KMnCl_3$	0.39	Expt: AC impedance spectroscopy[233]
$CuCdCl_3$	0.36	Expt: AC impedance spectroscopy[238]
$CsPbCl_3$	0.17	Expt: DC conductivity measurement[234]
$CsPbBr_3$	0.17	Expt: DC conductivity measurement[234]
$KMnCl_3$	0.65	Expt: DC conductivity measurement[239]
$CsCdCl_3$	0.73	Expt: DC conductivity measurement[239]
$CsSnBr_3$	0.23	Expt: DC conductivity measurement[239]
$CuPbI_3$	0.29	Expt: DC conductivity measurement[235]
$CsPbI_3$	0.38	Expt: selective blocking method[240]
α-$CsPbI_3$	0.36	Calc: DFT-NEB[58]
α-$CsPbBr_3$	0.44	Calc: DFT-CMD[241]
α-$CsPbBr_2I$	0.33	Calc: DFT-CMD[241]
α-$CsPbBrI_2$	0.49	Calc: DFT-CMD[241]
α-$CsPbI_3$	0.53	Calc: DFT-CMD[241]
γ-$CsPbI_3$	0.34	Calc: DFT-NEB (this work)
γ-$CsPbI_3$	0.42	Calc: MLIP (this work)

3.3.2 Inorganic Dopant Effects on Ion Migration Activation Energies

To understand the impact dopants have on the lowest energy I migration pathway in γ-$CsPbI_3$, a wide array of inorganic B-site dopants cited in experimental studies[16,89,91,93,95–97,208,214–225] were, for the first time, investigated computationally: Cu, Zn, Ge, Ag, Cd, Sn, Sb, Ba, and Bi. This set of nine dopants was chosen to represent a wide range of available inorganic dopants because these elements cover a range of ionic radii, valence states, and bonding character which allows a broad analysis of the

key criteria for dopant selection. These dopants span a Shannon ionic octahedral radius difference of 0.73 Å–1.35 Å compared to the Pb Shannon radius of 1.19 Å.[242] These dopants also have different valence character with the majority likely acting as isovalent dopants in the 2+ charge state (Cu, Zn, Ge, Cd, Sn, Ba) but with a few others likely doping aliovalently in either the 1+ charge state (Ag) or the 3+ charge state (Sb, Bi). To ensure consistency between the calculations, all dopants were considered to adopt the 2+ charge state and all supercells were treated as charge neutral under the assumption that in a real system, any charges would be neutralised by the introduction of additional iodide vacancies or interstitials. While charge balancing could be explicitly included in the supercell by the addition of these point defects, this would introduce an element of inconsistency between the calculations which could result in unique behaviours in the migration pathways. However, while assuming neutrality maintains a consistent comparison of the migrations through the lattice, it does eliminate any electronic effects that may be impacting the migration energies for dopants that are unlikely to adopt the 2+ charge state.

The size and electronic character of these dopants determine the hardness and therefore the strength and polarisability of the dopant–I bonding interactions. Additionally, these dopants span the period table covering the alkaline earth metals, the transition metals, and the post-transition metals. In particular, the post-transition metals are associated with stereoactive lone pairs which can induce asymmetric local distortions that could affect migration pathways. Preceding this investigation, it was hypothesised that dopant activation barriers might be determined by the ionic radius with larger dopants providing increased steric hindrance and therefore increasing the activation barriers. Another hypothesis was that a stronger dopant–I bond could suppress migration by tightly binding the I to its lattice site. A third consideration was that migration could be suppressed by introducing dopants that increase the rigidity of the lattice.

In order to benchmark the migration pathways and energy barriers for each doped system, a CI-NEB calculation is performed with the dopant located at the B-site around

which the migration is occurring. The 8*d*–8*d* pathway along the PbI_6 octahedral edge was chosen, as it was shown to be the lowest energy pathway in the pristine γ-$CsPbI_3$. All dopants were studied at 3% substitution to eliminate the possibility of phase segregation which can occur at high doping levels.

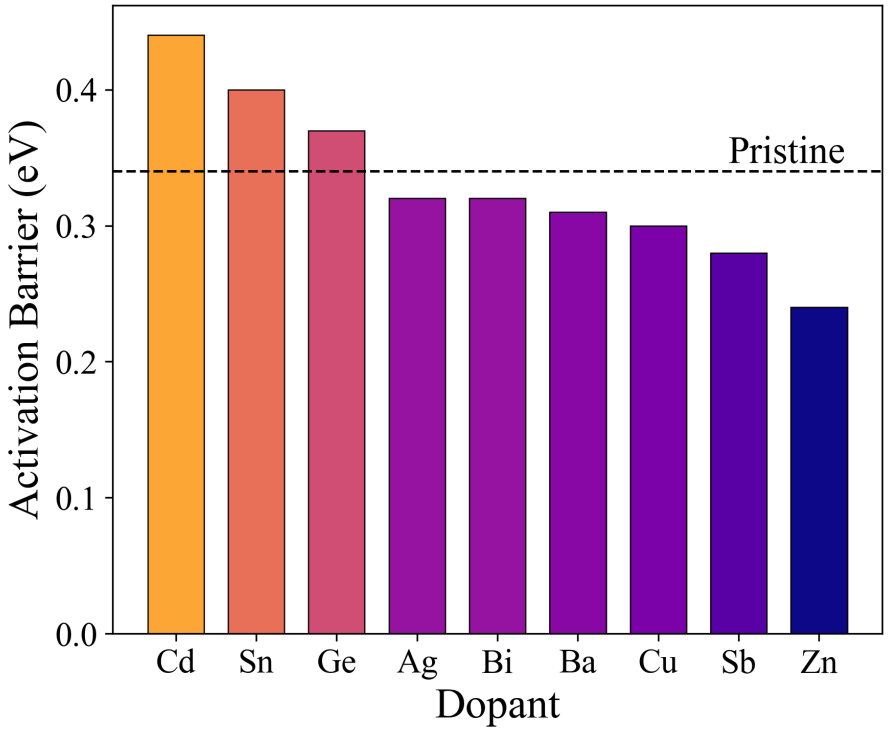


Figure 3.7: CI-NEB activation barriers calculated for the nine dopants investigated compared to the I8*d*-I8*d* barrier in the pristine γ-$CsPbI_3$ system. Figure adapted from Arber *et al.*, *Chem. Mater.*, 2025, **37**, 4416–4424[226] under the Creative Commons License: https://creativecommons.org/licenses/by/4.0/. Published by the American Chemical Society.

The resulting activation energies are plotted in Figure 3.7, and the migration energy profiles are provided in Figure 3.8. From these results, three main comments can be made. First, none of the dopants substantially increase the activation barrier. In fact, several dopants reduce the activation barrier as compared to the pristine system. This suggests that dopants such as Zn would not substantially reduce the levels of ion migration in γ-$CsPbI_3$.

Second, analysis of the migration pathways shows that the doped compositions with the highest barriers (Cd, Sn, Ge) are rigid throughout the migration with little rear-

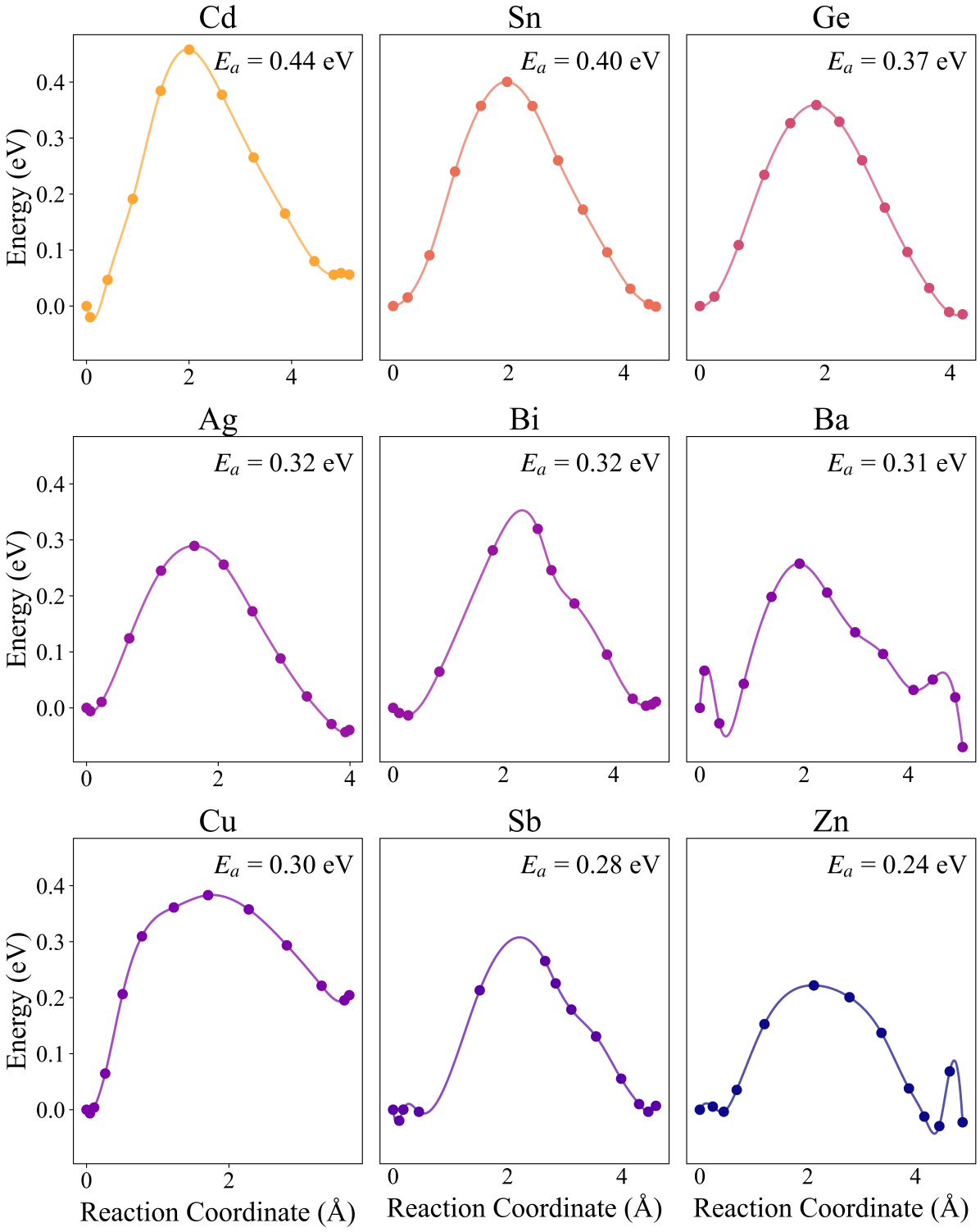


Figure 3.8: NEB energy profiles for the nine dopants investigated.

rangement occurring within the lattice as the I migrates. The migration energy profiles (Figure 3.8) show that the energy profiles for the higher energy migrations around Cd, Sn, and Ge are very similar to the I migrations simulated in the pristine system. The profiles are broadly symmetric with little structural rearrangement occurring before or after the migration. During these migrations, the migrating I is the only ion moving in the system. In contrast, the compositions with reduced migration barriers show a high degree of fluxionality with substantial reorganization occurring as the I migrates. This fluxionality is most clearly observed in the Zn, Sb, and Cu compositions. Notably, the dopant–I bond is ∼0.3 Å smaller in the Zn-doped composition's transition state than in the same image of the Cd and Sn composition migrations. Other structural features were analysed such as dopant radius; however, there are not any apparent design rules that can be used to predict the activation energy trends. This can be attributed to the fact that the barrier differences are all fairly small in comparison.

Third, the dopants Cd and Sn do affect a small increase in activation barrier, as does Ge to a lesser extent. To create a dynamic model of ion transport, longer time scales, larger system sizes, and higher temperatures must be investigated. Sn was chosen for further investigation with an MLIP due to its positive effect on the activation barrier. Additionally, mixed Pb–Sn perovskites have gained increasing interest due to their improved carrier mobility and stronger optical absorption due to a reduced band gap, which allows these materials to be used in either single or multi-junction perovskite thin films.[243] Previous experimental and computational studies on a 50%–50% Pb–Sn perovskite have also shown Sn to be effective at suppressing ion migration (largely related to the oxidised Sn^{4+} species).[90] Cd was not chosen for further investigation due to its high toxicity which makes it an undesirable dopant.[244] Concerns have previously been raised about the toxicity of the perovskite elements, including Pb. The partial substitution of Pb with Sn has been proposed as a method of reducing toxicity concerns associated with the lead halide perovskites, in addition to the improved optoelectronic properties.[243]

3.3.3 Machine Learning MD Model of Ion Diffusion in γ-$CsPbI_3$

Modelling long-range diffusion is critical for understanding how transport flux occurs within a perovskite thin film absorber. A MACE[180] model was trained which could be used to produce simulations of the time and length scales necessary to observe low temperature ion transport. Both numeric and dynamical insights can be derived from MD that are more statistically accurate than what can be extracted from static *ab initio* methods alone. The use of a MLIP for the MD simulations theoretically produces results at the accuracy of *ab initio* calculations but with the reduced computational efficiency of classical MD. The longer timescale becomes increasingly important when studying statistically rare events such as ion hops. MD also provides information relating to hopping correlations and thermal disorder which only become apparent in large systems over long timescales. In essence, MD conveys information of the free energy landscape of the entire simulation, not simply a local migration barrier.

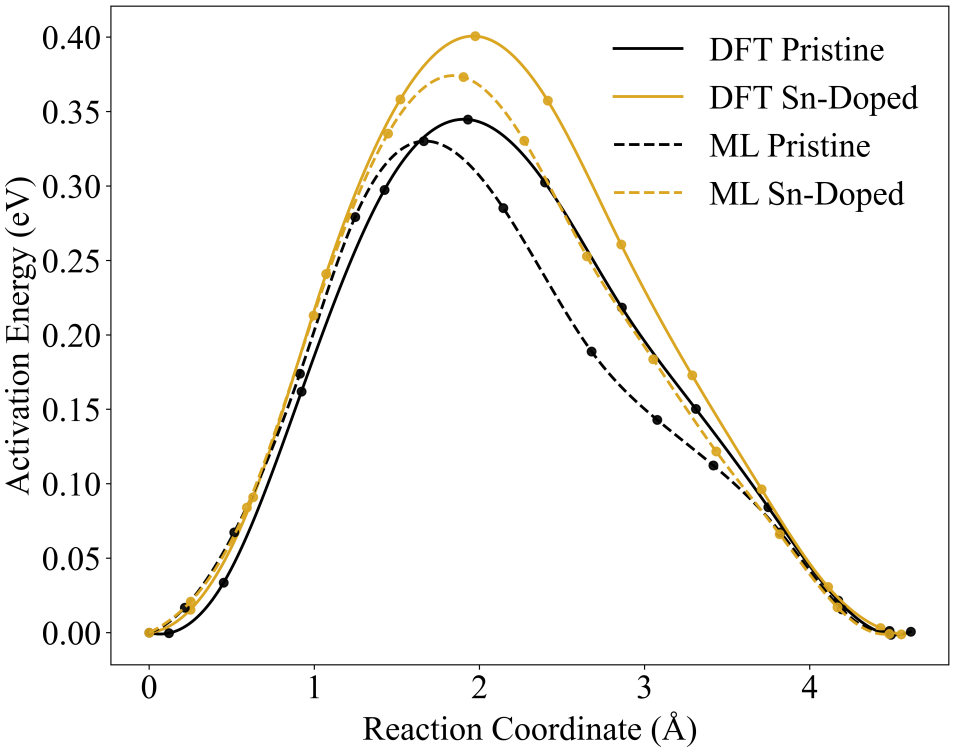


Figure 3.9: Comparison of the DFT (solid) and ML (dashed) CI-NEB energy profiles in the pristine γ-$CsPbI_3$ (black) and Sn-doped (gold) compositions.

Here, a single MLIP is trained on both the pristine and 3% Sn-doped γ-$CsPbI_3$ compositions. As mentioned previously, the Sn dopant was chosen for further investigation due to its positive effect on the I migration barrier as well as increasing interest in mixed Pb–Sn perovskites for single- and multi-junction solar cell applications. The MACE model was first validated against the DFT CI-NEB barriers. Figure 3.9 depicts the energy profiles for both the DFT and MACE CI-NEB calculations. All pathways show a largely symmetric I migration pathway with activation energies between 0.33 eV and 0.40 eV. In both the DFT and the ML calculations, the I barrier in the pristine composition is lower in energy than the Sn-doped composition and in both cases, the increase in barrier upon the addition of Sn is $\sim$0.05 eV. Both pristine compositions display a slight shoulder compared to the Sn-doped NEB in support of the hypothesis that Sn-doping increases the rigidity of the system. The MACE barriers are slightly higher than the DFT barriers. It is typical for MLIPs to underestimate activation barriers and overestimate diffusion due to the lack of electrostatics in these models.

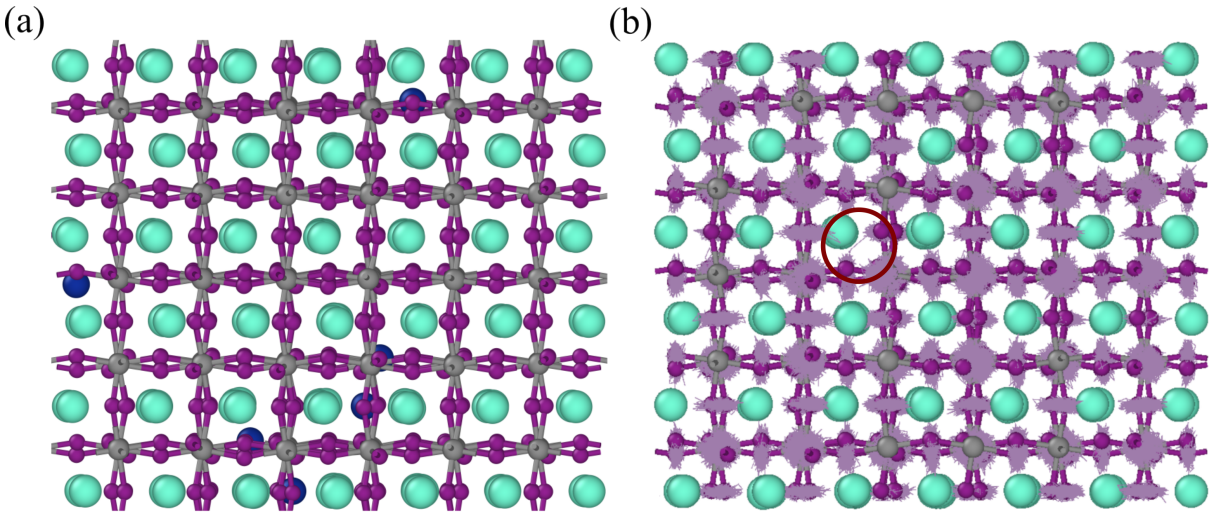


Figure 3.10: (a) Initial configuration of the MD simulation for pristine γ-$CsPbI_3$ (Cs, aqua; Pb, grey; I, purple). Blue spheres indicate randomly distributed I vacancies corresponding to a 1% concentration. (b) Trajectories of all species over a time period of 0.1 ns at 300 K. Evidence of an I hop is shown inside the maroon circle. Clearly, the movement of the mobile I ions dominates the Cs and Pb atoms in agreement with the MSD and RDF plots (Figure 3.11 (c) and Figure 3.13, respectively.)

For the first time, long-timescale MD simulations were performed on pristine and Sn-

doped γ-$CsPbI_3$ compositions between 300 K–500 K, the temperature region within which perovskite synthesis occurs. The inclusion of 1% I vacancies (visualised in Figure 3.10 (a)) and 3% Sn provides a direct comparison with the CI-NEB simulations which included a similar concentration of each species. The 1% I vacancy concentration here ($\sim 10^{20}$ cm^{-3}) is higher than observed experimentally ($\sim 10^{14}$ cm^{-3});[186,187] however, this is necessary to improve the statistical sampling of migration events which occur infrequently, especially at the relatively low temperatures being investigated.

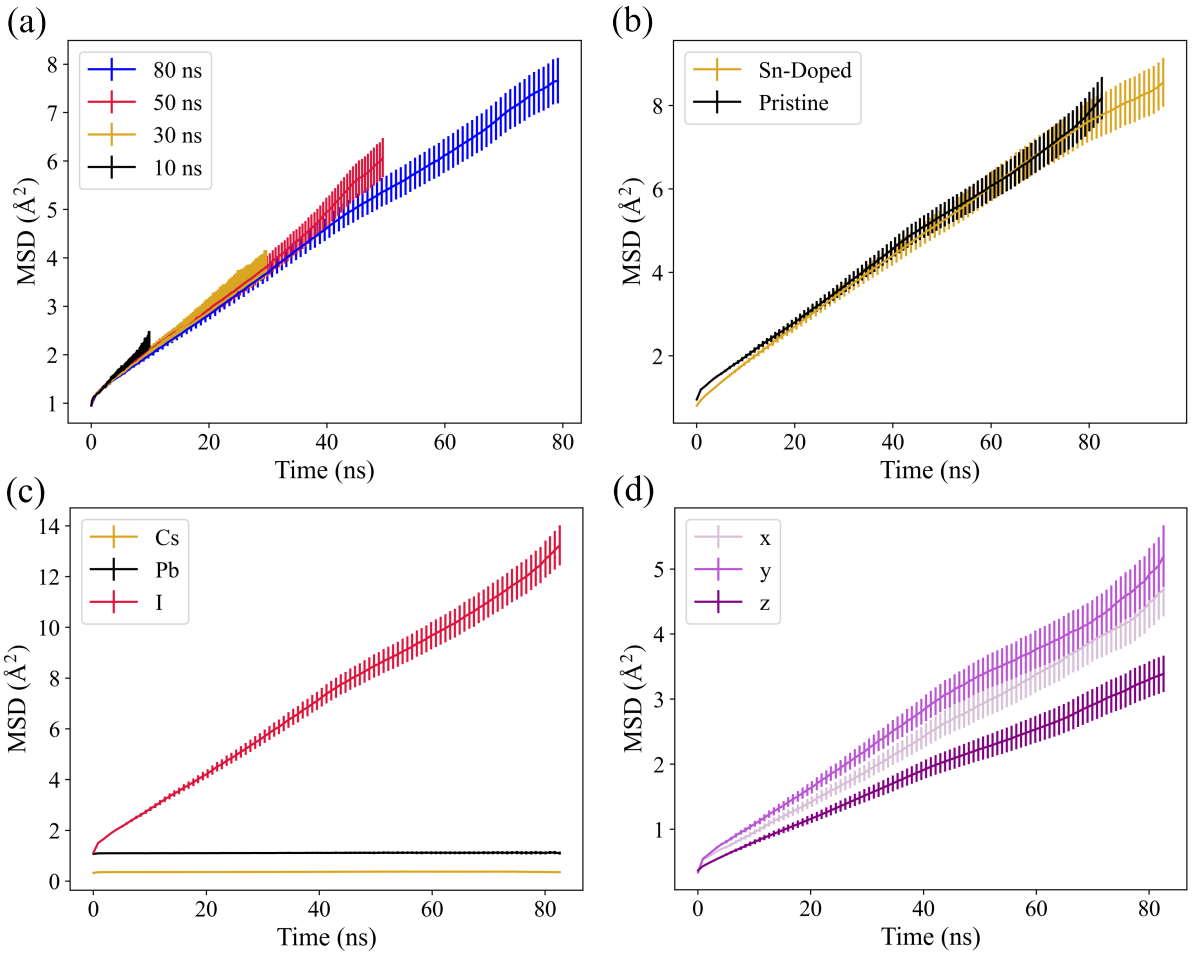


Figure 3.11: MSD plots demonstrating (a) convergence of I diffusion over 80 ns trajectories, (b) I ion diffusion for pristine and Sn-doped γ-$CsPbI_3$ at 500 K, (c) the dominance of I migration in the diffusivity calculation, and (d) the x, y, and z components of I diffusion in the pristine composition at 500 K.

Previous studies have looked at higher temperature scales to increase the sampling frequency, but this approach runs the risk of altering the hopping mechanisms observed.

The perovskite degrades at high temperatures, so the simulations should be kept at low enough temperatures to safely observe the dynamics occurring during device function (250 K–360 K).[245,246] In order to reach statistically significant results at relatively low temperatures, these calculations ran over a timescale of at least 80 ns, which compares favourably to typical AIMD simulations of only 50–100 ps. This time was demonstrated to be sufficiently converged by analysing the MSDs plotted for a range of simulation lengths (Figure 3.11 (a)) which confirm linear diffusion behaviour is achieved within the 80 ns trajectory.

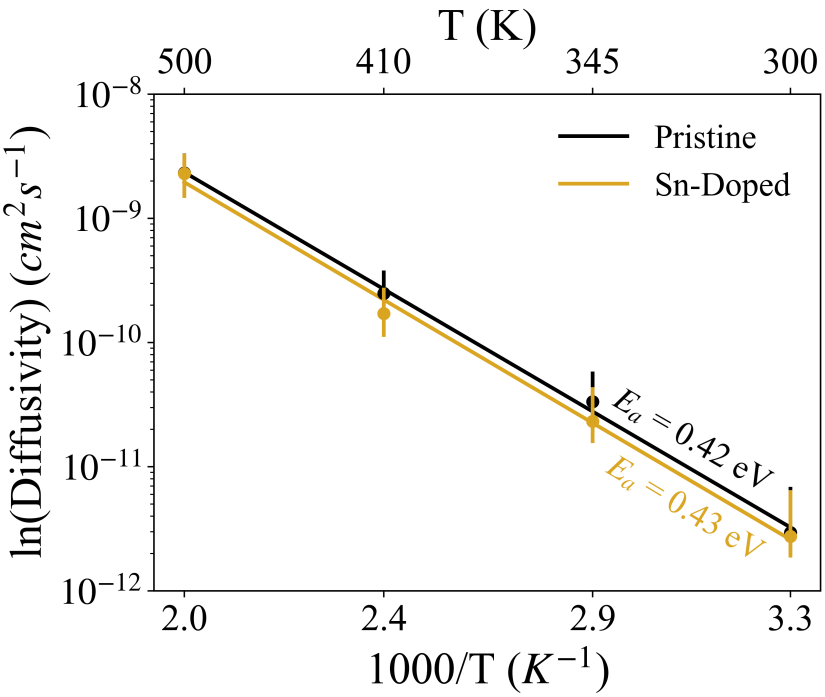


Figure 3.12: Arrhenius plot depicting the linear relationship between ln$D$ and 1/T in the MACE MD simulations for both the pristine γ-$CsPbI_3$ and 3% Sn-doped compositions. The corresponding activation energy can be derived from the slope. Figure adapted from Arber *et al.*, *Chem. Mater.*, 2025, **37**, 4416–4424[226] under the Creative Commons License: https://creativecommons.org/licenses/by/4.0/. Published by the American Chemical Society.

Diffusion coefficients (D) act as a metric for the ionic conductivity within the system. The method requires the assumption that the van Hove coefficient is 1, thereby enforcing that all ionic hops are fully decorrelated within the system. This approximation is used as the field standard for estimating trends in conductivities in similar systems. The

Arrhenius plot of ln$D$ versus 1/T provides an estimation of the activation barrier for each hop in the system. Direct comparison with experimental D values can be difficult, as they are not straightforward to measure for complex perovskites. Experimental D values for the perovskite $MAPbI_3$ range between 10^{-11}–10^{-6} cm^2s^{-1} at room temperature.[190,247]

The diffusivity values determined from the slope of the MSD curves were used to construct an Arrhenius plot (Figure 3.12) which displays the relationship between the ionic diffusivities and temperature. The derived activation barriers of 0.42 eV and 0.43 eV for the pristine and Sn-doped systems (Figure 3.12), respectively, are in good agreement with experimental values and with the CI-NEB results (Table 3.3). Despite the small difference in activation energies between MD and DFT-NEB, these values are still within the range of energy barriers experimentally found in similar inorganic perovskite systems and show consistent trends with temperature and composition.

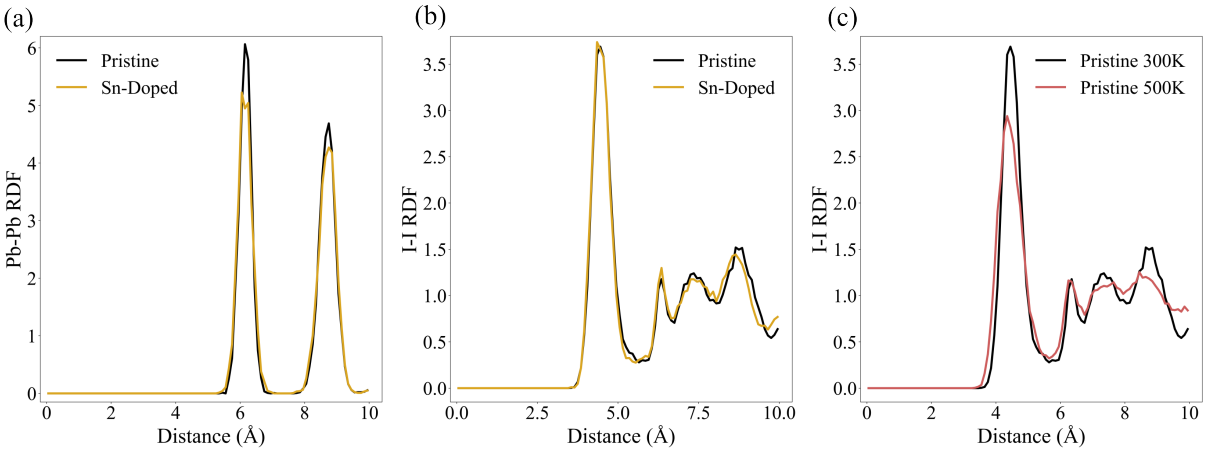


Figure 3.13: RDFs for (a) Pb–Pb in pristine and Sn-doped γ-$CsPbI_3$ at 300 K; (b) I–I in pristine and Sn-doped γ-$CsPbI_3$ at 300 K; and (c) I–I at 300 K and 500 K in pristine γ-$CsPbI_3$. Figure adapted from Arber *et al.*, *Chem. Mater.*, 2025, **37**, 4416–4424[226] under the Creative Commons License: https://creativecommons.org/licenses/by/4.0/. Published by the American Chemical Society.

The radial distribution function (RDF) provides additional structural insights into the long-range ordering of perovskite materials. The RDFs for Pb–Pb (Figure 3.13 (a)) reveal a series of sharp peaks for both compositions, with the first coordination shells clearly resolved, in agreement with the observed ordered crystal structure of γ-$CsPbI_3$. In contrast, the RDF for I–I (Figure 3.13 (b)) shows a broader, more diffuse structure

for separations greater than nearest-neighbour, indicative of greater ion mobility in the I sublattice. Additional analysis of the visualised trajectories for all elements, as well as the elemental MSDs, confirms that I mobility dominates (Figure 3.10 and Figure 3.11 (c)). This effect is more pronounced at higher temperatures with lower maxima in the RDF (Figure 3.13(c)).

Further atomistic insights into the mechanistic features of I transport can be gained from visualising the ion jumps or trajectories from the MD simulations. Figure 3.10 illustrates the significant movement of I ions in the pristine and Sn-doped structures. The line trajectories also confirm that I diffusion primarily occurs via conventional hops between I lattice sites along the Pb–I octahedral edges for both systems, in agreement with the DFT CI-NEB simulations (Figure 3.5). In addition, the diffusivities can be broken down into directional components. Plotting the x, y, and z MSDs for a given simulation shows that the diffusions in each direction are similar, indicating that the high degree of fluxionality in the perovskite lattice sufficiently ensures that while diffusivity is slightly higher in the x and y directions, there is no substantial anisotropic bias (Figure 3.11 (d)).

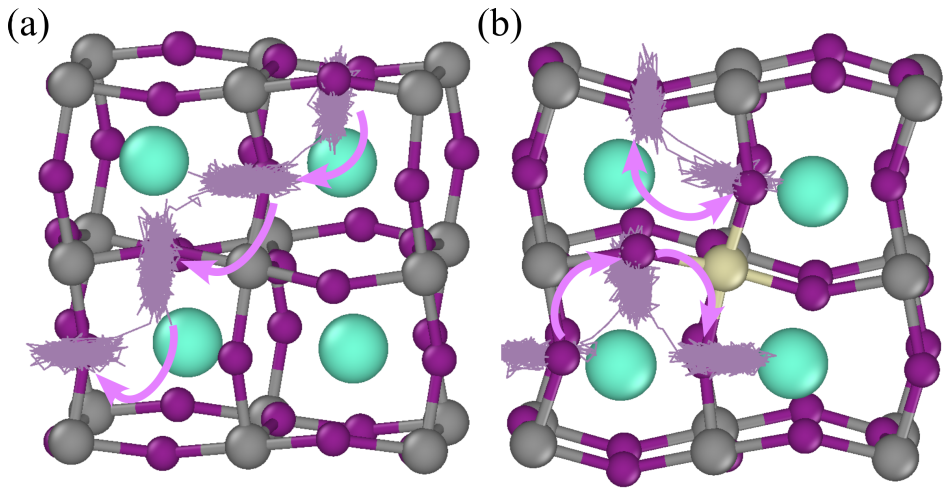


Figure 3.14: Molecular dynamics trajectory (lilac) of an I vacancy migrating through the (a) pristine and (b) Sn-doped γ-$CsPbI_3$ supercells (Cs, aqua; Pb, grey; I, purple). Figure adapted from Arber *et al.*, *Chem. Mater.*, 2025, **37**, 4416–4424[226] under the Creative Commons License: https://creativecommons.org/licenses/by/4.0/. Published by the American Chemical Society.

Figure 3.14 depicts the trajectories of I atoms moving through the perovskite lattice

(marked by pink arrows) in both the pristine and Sn-doped compositions. As I ions hop between neighbouring lattice sites, I vacancies move through the lattice in the opposite direction. The trajectories demonstrate that in both compositions, the migrations follow the same curved pathway along the PbI_6 octahedral edge between both 8*d* and 4*c* Wyckoff sites. These hopping trajectories occurred over a time period of 2.5 ps–6 ps. The vast majority of observed migrations occur via this traditional vacancy mediated hopping mechanism; however, in a few cases, the migration was observed to occur via a different pathway. In one example, an I4*c*–I4*c* migration was observed to occur via a long-lived transition state (Figure 3.15). This migration occurred over the span of ∼10 ps with the transition state intermediate surviving for ∼3 ps. It is clear that while alternative pathways, such as those which occur via longer-lived transition states, are accessible, they comprise a small minority of total migrations. This is supported by experimental measurements of ionic conductivity as a function of I_2 partial pressure that indicate I vacancy migration dominates.[57]

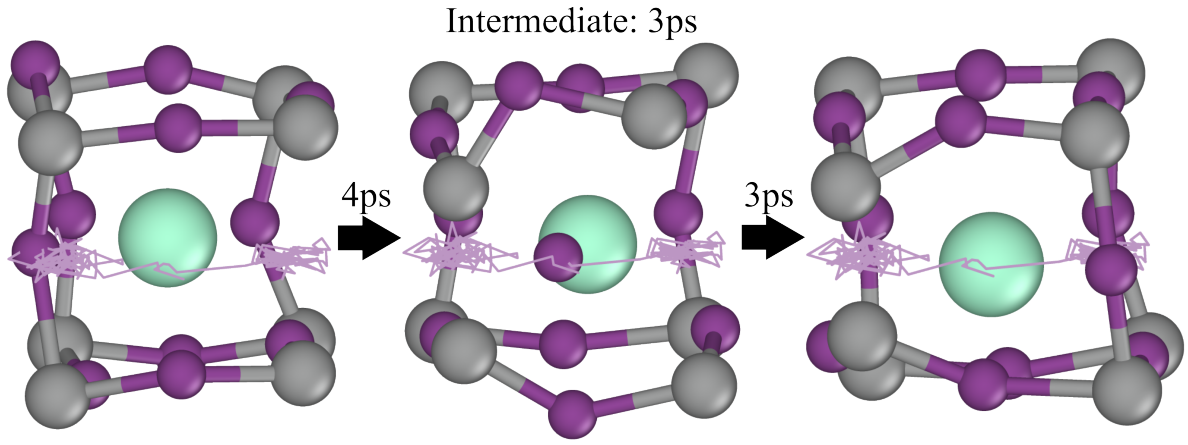


Figure 3.15: Visualisation of an I4*c*–I4*c* migration that occurs via a long-lived transition state. The total migration occurs over a 10 ps time period with the interstitial transition state existing for ∼3 ps.

3.4 Chapter Summary

This chapter combines first-principles calculations with machine learning molecular dynamics simulations to provide a comprehensive understanding of the effect of dopants on migration barriers and long-timescale ion transport behaviour in the orthorhombic γ-$CsPbI_3$ perovskite. Such atomic-scale understanding of ion migration is key to the further development of perovskite optoelectronic devices.

An *ab initio* model of the pristine γ-$CsPbI_3$ material exhibits good agreement with the structure and electronic properties that are experimentally observed which provides a reliable basis for further investigation. The octahedral tilting in the γ-polymorph's lattice creates two unique I Wyckoff sites which allows for five symmetrically-inequivalent I migration pathways. Out of these pathways, the I–I migrations along the edges of the PbI_6 octahedra were shown to be most energetically favourable. These pathways create a three-dimensional network for ion diffusion through the perovskite lattice with activation barriers consistent with both experimental measurements and previous computational studies on $CsPbI_3$ and other inorganic halide perovskites.

Investigation into the effect of partial B-site doping on ion migration shows that doping does not substantially increase the activation barriers for I migration. However, in several cases, such as Zn and Cu, dopants were found to decrease the activation barrier. This was associated with tighter binding between the dopant and migrating I which led to a substantial increase in structural rearrangement throughout the migration. This contrasts with the migrations with higher activation barriers where no structural rearrangements were observed. These results suggest that any relationship observed in experimental literature between the addition of inorganic dopants and improved device lifetimes would likely be due to another mechanism such as stability gained from surface passivation or improved growth kinetics.

An MLIP model was trained to perform MD simulations on the nanosecond timescale. This MLIP provides MD simulations at the accuracy of an *ab initio* simulation but on

larger simulations and over longer timescales than are accessible using traditional methods. These MD simulations demonstrate that I migrations occur via the same vacancy-mediated hopping mechanism along the PbI_6 octahedral edges predicted by DFT. The Cs and Pb sublattices do not display any correlated motion and are largely immobile. The activation barriers derived from Arrhenius plots for both the pristine and Sn-doped system largely agree with those calculated via CI-NEB and again fall within values reported previously in literature for similar perovskite systems. More broadly, these results highlight the importance of considering ion migration as a structural feature that requires the sort of dynamic, long-timescale analysis performed in this work to understand its nature.

In conclusion, this work enhances our understanding of the presence of ion migration and the effect of inorganic dopants in the γ-$CsPbI_3$ thin film material and provides a framework for guiding future ion diffusion and doping studies in inorganic perovskite materials.

Chapter 4

Ancillary Ligand and Dopant Effects in α-$CsPbI_3$ Nanoplatelets for Polarised Light Emission

4.1 Introduction

Colloidal semiconductor nanocrystals have a wide range of applications in the fields of optics and photonics such as LEDs, luminescent tags for biomarkers, and lasers.[17,248–250] Nanocrystals derive their unique optoelectronic properties from quantum confinement which is introduced through the reduction of all three dimensions. In contrast, nanoplatelets (NPLs) represent a unique class of nanomaterial in which quantum confinement is introduced through the reduction of only one dimension. Lead halide perovskites such as $CsPbI_3$ are particularly attractive candidates for NPL design due to their band gap tunability, narrow emission linewidths, defect tolerance, high luminescence quantum yields, and ease of solution processability.[121,251–256] Unique to the NPL, the directional dependence of the quantum confinement drives out-of-plane exciton fine-structure splitting, thereby raising the energy of the exciton states with dipole moments aligned in this direction. This effect produces linearly polarised emission preferentially in the in-

plane directions,[18,257,258] making NPLs interesting candidates for applications requiring polarised light such as optical communications devices, 3D displays, and bio-imaging instruments.[132,133]

In order to target polarised light emission, strong one-dimensional confinement is critical. The exciton Bohr radius in the $CsPbX_3$ (X = Cl, Br, I) perovskites is ~6 nm.[121] Inducing confinement requires NPLs with widths of at least half this radius which corresponds to roughly five monolayers. Previous studies have demonstrated that ultrathin NPLs (defined as fewer than three monolayers wide) display the strongest polarised light emission due to strong confinement which maximises the fine structure splitting.[18,259–261] In addition to the monolayer width, a high degree of uniformity in NPL size is crucial. The high shape anisotropy provides a driving force for orientational ordering and superlattice assembly in NPL films, but even slight degrees of size variance can reduce the overall polarisation response.[262] Therefore, linearly polarised light emission applications require precise synthesis of ultrathin NPLs with a high degree of monodispersity.

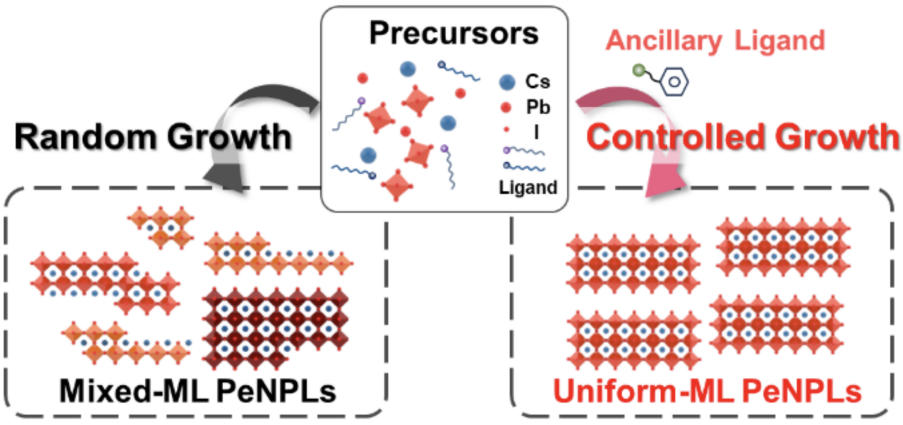


Figure 4.1: Schematic of the NPL synthesis procedure reproduced from Kim *et al.* (2026).[129]

For $CsPbI_3$, the perovskite NPL synthesis involves mixing a precursor solution of CsI, PbI_2, and ligands (Figure 4.1). In contrast to thin films, $CsPbI_3$ NPLs adopt the cubic α polymorph which is the form studied in this chapter. The ligands prevent formation of a three dimensional thin film by binding to the surface of the NPLs, halting growth

in the reduced dimension. Oleic acid, $C_{18}H_{34}O_2$, and oleylamine, $C_{18}H_{35}NH_2$, are commonly used ligands in this synthesis.[19,263,264] In addition to controlling the monolayer width, these ligands also help stabilise the NPLs by passivating surface defects such as halide vacancies and under-coordinated Pb atoms. However, weak binding of the ligands can lead to desorption which results in poor colloidal stability due to combination of neighbouring NPLs and degradation via unpassivated surface defects.[265–267]

Furthermore, recent investigations have pointed towards an additional route to achieving highly ordered, monodisperse NPLs through the inclusion of metal halide additives in the NPL precursor solution.[128] As a recent breakthrough in the field, little is understood about the precise mechanism underpinning this observation. As introduced in Chapter 1, developing NPLs suitable for device integration requires precise understanding and control over the nucleation and growth mechanisms governing thickness formation which can be achieved by carefully selecting the ligands and metal halide additives included during synthesis.[92,268–271]

Experimental investigations undertaken by our collaborators led by Prof. Robert Hoye in Oxford Chemistry (detailed in Sections 4.3.3 and 4.5) discovered two routes for improving monodispersity and thickness control during NPL synthesis. First, our collaborators observed that the addition of certain ancillary acid ligands to the original oleic acid and oleylamine mixture resulted in a dramatic improvement in NPL uniformity and optical performance. Ancillary ligands are ligands which participate in the synthesis but do not form part of the reaction. Second, our collaborators observed that the addition of 30% ZnI_2 to the precursor solution provided a strong driving force for the preferential synthesis of n=2 monolayers and improved NPL stability. However, in both cases, the precise mechanistic role of the ancillary ligands and the Zn additive remained unclear.

The computational work described in this chapter first provides atomistic insights into the interactions between the ligands and the perovskite surface which play a critical role in determining the outcome of the synthesis. Four candidate ligands are studied alongside the reference oleic acid to highlight the key properties of a successful ancillary ligand. The

results of this investigation are published by Kim *et al.* in *Advanced Materials* (2026).[129] Second, to understand the impact of Zn as an additive, a computational investigation was performed on the stability of the bulk α-$CsPbI_3$ and α-$CsPbI_3$ NPLs when doped with varying concentrations of Zn. Furthermore, this chapter explores the role that may Zn play in a surface passivating complex formed in conjunction with an ancillary ligand. By developing an atomistic understanding of these interactions, this work aims to provide guidelines for the design of further synthesis strategies for the production of ultrathin, highly monodisperse perovskite NPLs for polarised light emission.

4.2 Methodology

VASP[151,152,154,156] with the PAW method[155] was employed for all DFT calculations which were performed using the VASP-supplied PAW pseudopotentials and the PBE exchange–correlation functional as described in Chapter 2.[149] The functionals and cut-offs used in this chapter were chosen based on previous investigations performed within the group on similar perovskite and molecular passivation systems and are in agreement with published literature.[83,84,107]

The surface slabs used to investigate the interactions between ancillary ligands and the $CsPbI_3$ NPL were constructed from a geometry optimised cubic α-$CsPbI_3$ structure. Bulk structure relaxations were performed using a k-point grid of $6 \times 6 \times 6$ corresponding to a reciprocal k-spacing of $0.2/2\pi$Å^{-1}. The (001) surface was chosen, as this surface has been experimentally observed to be the most prominent.[74,272] The surface energy of this surface was calculated to be 0.18 Jm^{-2} which is typical of stable perovskite surfaces.[273] This surface slab is stoichiometric. The (001) Pb–I terminated surface was chosen for this investigation due to X-ray photoelectron spectroscopy (XPS) measurements indicating higher relative concentrations of Pb than Cs in the NPLs. Surface slabs with dimensions of $2 \times 2 \times 4$ were constructed with a 30 Å vacuum with the coordinates of the bottom layer fixed to replicate a bulk-like structure. These slabs can be considered the equivalent of a

stoichiometric $n = 4$ NPL which is a typical width observed experimentally. Structural optimisation was performed until the total energy was converged to within 10^{-5} eV and the atomic forces were converged to within 10^{-2} eV Å^{-1}. A 500 eV plane-wave cut-off and a Γ-centred $3 \times 3 \times 1$ k-mesh, maintaining a k-spacing $0.2/2\pi$Å^{-1}, were used for all surface relaxations. Long-range van der Waals dispersion interactions were accounted for by including Grimme's DFT-D3 correction[274] which is required to accurately represent the surface–molecule interactions. Dipole corrections were additionally included to ensure convergence of the planar-averaged electrostatic potential. Strong agreement between the DFT and experimental lattice parameters was achieved with the calculated parameters $a = b = c = 6.25$ Å producing an error of 0.6% compared to the experimental parameters $a = b = c = 6.29$ Å.[275]

After introduction of the ligand, a second geometry relaxation was performed. Ligands were placed to bind to a Pb atom on the NPL surface. The binding interaction between the ligands and Pb was chosen as the focus of this study, as under-coordinated Pb sites are known to be a primary source of instability in perovskites and previous passivation work has highlighted Pb passivation as a key route to improved perovskite stability.[83,103,107,276–279] For each surface, multiple random binding configurations around the Pb site were tested, and the lowest energy site was chosen for further analysis as discussed in this chapter. Binding energies were calculated by taking the difference in energy between the bound surface–molecule structure and the sum of the isolated molecule and isolated surface. For structures containing surface I vacancies, the I interstitials were introduced sufficiently far from the surface to maintain charge neutrality and suppress spurious magnetic moments arising from unpaired electrons. Ligands were also investigated in their deprotonated form. In these simulations, a uniform compensating background charge was introduced as implemented in VASP to ensure appropriate charge balancing.

Bader charge analysis[162,280] was carried out to quantify charge transfer between the molecule and the perovskite surface. This method is based on high-precision DFT single-

point calculations which use a fine Fast Fourier Transform (FFT) mesh of $260 \times 260 \times 1400$ points. Similar *ab initio* computational techniques have been applied to recent studies of molecular passivation of perovskite halide surfaces.[107,281,282]

For the Zn investigation, surface slabs were relaxed using the same convergence thresholds, Gimme DFT-D3 dispersion correction, and dipole correction described above. The $n = 2$ slabs were generated from $2 \times 3 \times 2.5$ supercells with a 20 Å vacuum. Typically, these slabs are comprised of an integer multiple of formula units; however, XPS measurements showed that the relative concentration of Pb in the NPLs was higher than Cs, suggesting that the NPLs are PbI_2 terminated on both sides. To create a slab with a double PbI_2 termination, an additional PbI_2 layer was added to form what is technically an $n = 2.5$ slab thickness. For simplicity, these slabs will be referred to as $n = 2$. The surface energies were calculated via the equation:

$$\gamma = \frac{E_{slab} - nE_{bulk}}{2A} \tag{4.1}$$

where n denotes the number of formula units in the slab and A is the surface area of the slab. The slab energy, E_{slab}, is the DFT energy of the surface slab, and the energy of the bulk, E_{bulk}, is the energy of the α-$CsPbI_3$ bulk with elemental potentials added to account for non-stoichiometric slabs.

Zn-doped bulk structures were generated using the ICET[172] enumeration function which provides a representation of symmetry inequivalent structures in a given composition. 58 structures of mixed compositions that cover a range of Pb–Zn ordering within the lattice were geometry optimised. The mixing energies plotted for the Pb–Zn solid solution were calculated via the following formula:

$$\Delta E_{mix} = \frac{1}{N}\left(E_{total} - \sum_i n_i Ei\right) \tag{4.2}$$

where E_{total} is the DFT energy of a mixed structure in the solid solution, E_i is the energy of the pure end-members, n is the number of formula units of pure component in the

mixed structure, and N is the total number of formula units.

The surface binding analysis was again performed using the same methodology as described above. Surface slabs with an ancillary ligand were relaxed in a 30 Å vacuum to prevent interactions between periodic images.

4.3 Nanoplatelet Surface Passivation

4.3.1 Ligand–Surface Binding Energies

To investigate the impact different ancillary ligands have on the synthesis of the $CsPbI_3$ perovskite NPLs, the binding energies between the NPL surface and ligand were first investigated. These energies provide a metric representing the strength of the interaction between the two species. Perovskite crystallisation occurs quickly in solution, and it is the addition of the ancillary ligands which prevents further growth in the reduced dimension to create the desired NPL shape and properties. This work hypothesises that varying the strength of the ligand–surface interactions impacts the growth kinetics, and therefore, the growth rate can be finely tuned according to the choice of ligand. Stronger binding represents quicker quenching of the growth phase which favours the synthesis of ultrathin, highly-ordered NPLs capable of achieving the desired high degree of polarisability.

A range of four ancillary ligands (Figure 4.2) were investigated to provide a comparison of the impact of changing both the functional group and the backbone of the ligand. These ligands include benzene sulphonic acid (BSAc), benzoic acid (BAc), benzyl phosphonic acid (BPAc), and diphenyl phosphoric acid (DPPAc). Oleic acid is one of the ligands commonly used in the perovskite NPL synthesis and is included here as a reference point for comparison with the other ancillary ligands investigated.

Acids were chosen as the class of the ancillary ligand studied due to the strength of Pb–O bonds. The functional group, or the head of the binding molecule, determines the coordination chemistry of the ligand including which atom or atoms bind to the perovskite surface, the polarisability of the bond, and the degree of electron donation.

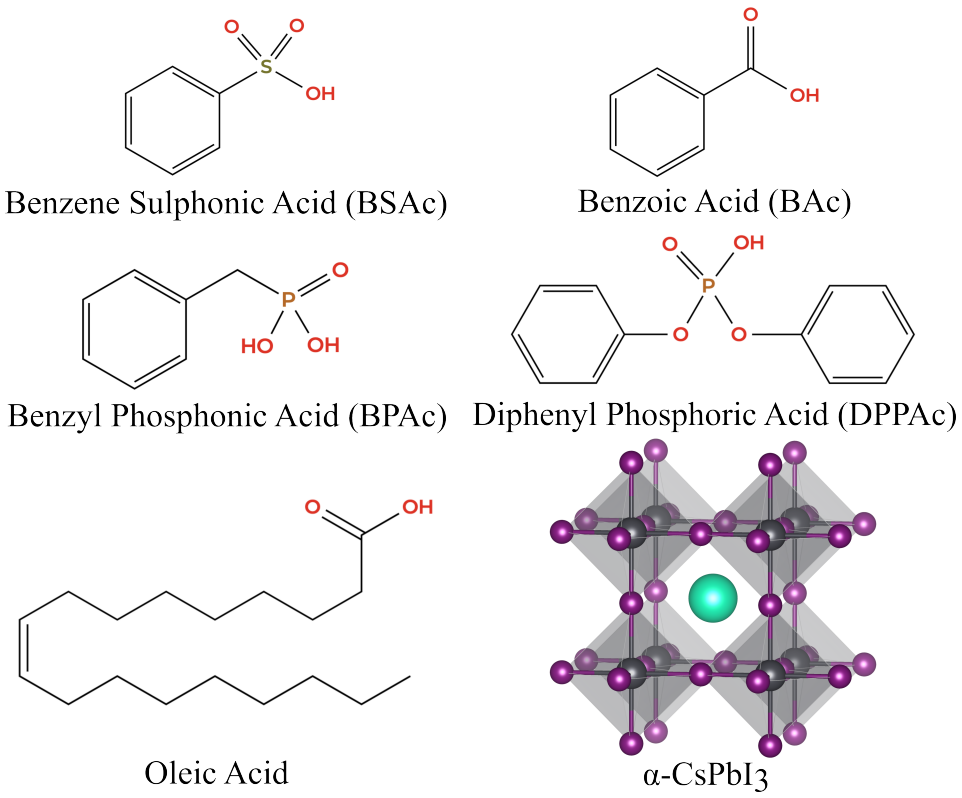


Figure 4.2: Diagram of the four ancillary ligands investigated in this work alongside the reference oleic acid and the α-$CsPbI_3$ perovskite structure (Cs, aqua; Pb, grey; I, purple). Molecular structures were produced using MolView.

The elements in the functional group determine the strength of the bonds and whether any deprotonation occurs will also impact the binding interactions. The set of ligands investigated here covers a range of carboxylic, sulphonic, and phosphorus acid groups, each of which have different electronic characters, different number of bonding groups, and different levels of protonation. The backbone of the ligand, either a carbon chain or benzyl groups, determines whether there will be any mesomeric or inductive electronic donation. These chains also experimentally will have the impact of steric hindrance or more broadly determining any solvent interactions. These atomic-scale features are difficult to investigate and isolate experimentally. Calculation of the ligand–surface binding energies provides a representation of the cumulative effect of these interactions which can be linked to an overall impact on the NPL synthesis.

Figure 4.3 depicts the relaxed (100)-$CsPbI_3$ NPL surface when bound to each of the

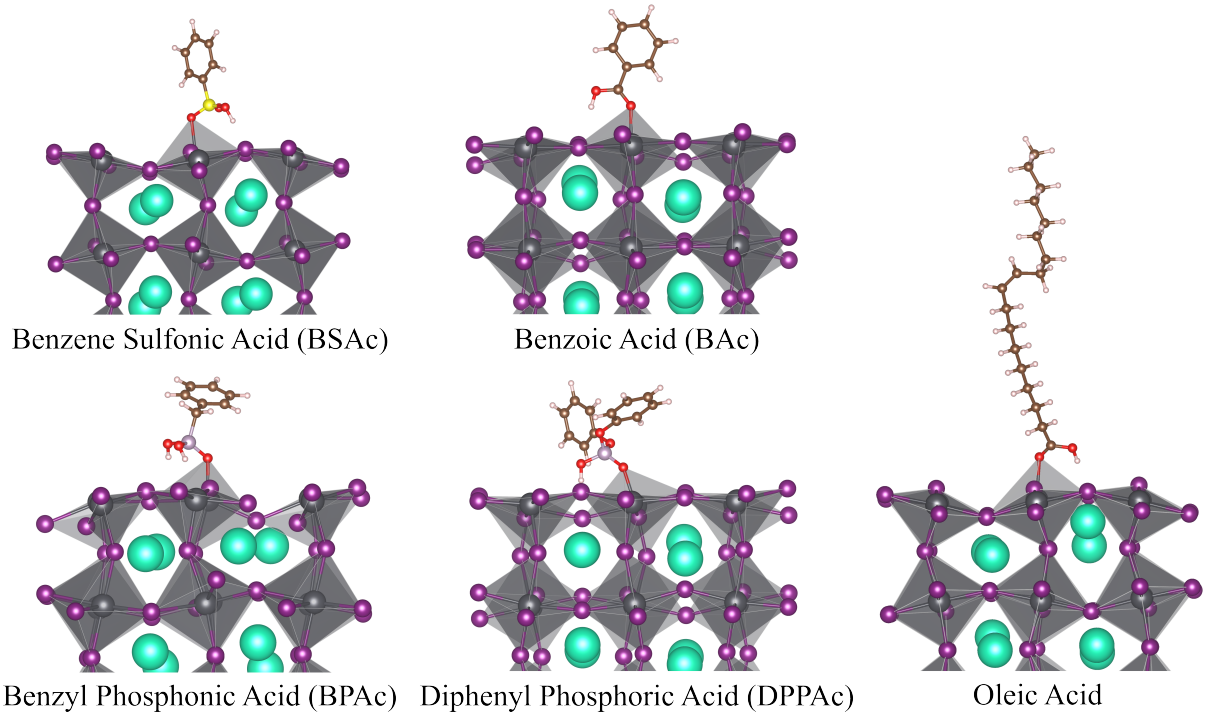


Figure 4.3: Relaxed α-$CsPbI_3$ surfaces for all four of the ancillary ligands and the reference oleic acid. Stronger binding interactions induce higher degrees of octahedral tilting (Cs, aqua; Pb, grey; I, purple; C, brown; S, yellow; P, silver; O, red; H pink).

four ancillary ligands and oleic acid. In each case, the functional group of the ligand is bound to an under-coordinated Pb on the perovskite surface. Previous studies[103,277–279] show that the under-coordination of Pb atoms on the surface is a critical route to perovskite degradation, so the addition of ligands which can passivate Pb by increasing the coordination from five to six is crucial for improving NPL stability. For each of the ligands, the molecule is bound to the perovskite surface via an O atom in the functional group. The O atoms which preferentially bind are those which are not protonated in the acid. It can be seen that the protonated O atoms are oriented such that they form H–I hydrogen bonds with surface I atoms. It can also be observed that the surface binding interactions result in PbI_6 octahedral distortions within the perovskite surface.

The binding energies calculated for these five surface–ligand interactions (Figure 4.4 (a)) demonstrate that the two phosphorus acids (DPPA and BPAc) bind most strongly to the $CsPbI_3$ surface. Visually, these ligands both induce the largest degree of PbI_6 octahedral distortions in the top-most layer of the surface slabs (Figure 4.3). In addition,

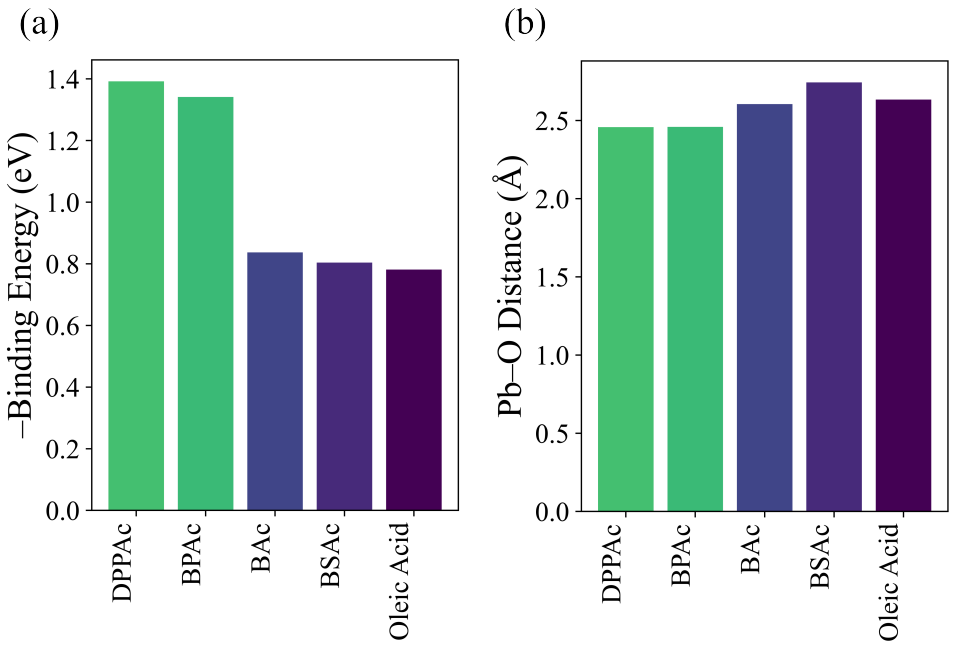


Figure 4.4: Calculated results for (a) the ligand–surface binding energy and (b) the molecule–Pb bond length demonstrating correlation between both calculated values.

analysis of the Pb–O bond lengths (Figure 4.4 (b)) demonstrates a similar trend as the binding energies. The bond length between the ligand and surface Pb provides a representation of the strength of that bond with shorter bonds typically correlating to stronger binding interactions. The phosphorus acids exhibit the shortest Pb–O bond lengths due to the high electronegativity difference between P and O which means more electron density is available for donation from the O atom. Oleic acid is the only ligand that does not follow the binding energy trend directly; this result is likely due to the difference in the long carbon chain backbone which has a slight positive inductive effect, and is therefore likely contributing more electronic character to the surface. In conclusion, the phosphorus acid ligands are characterised by the strongest binding energies which also correlate to higher degrees of octahedral distortions induced in the perovskite surface and shorter Pb–O bond lengths. Both effects are related to higher degrees of electron donation to the surface.

The binding energies of BPAc and oleic acid are further investigated under a variety of conditions that could occur during the synthesis such as binding in the presence I

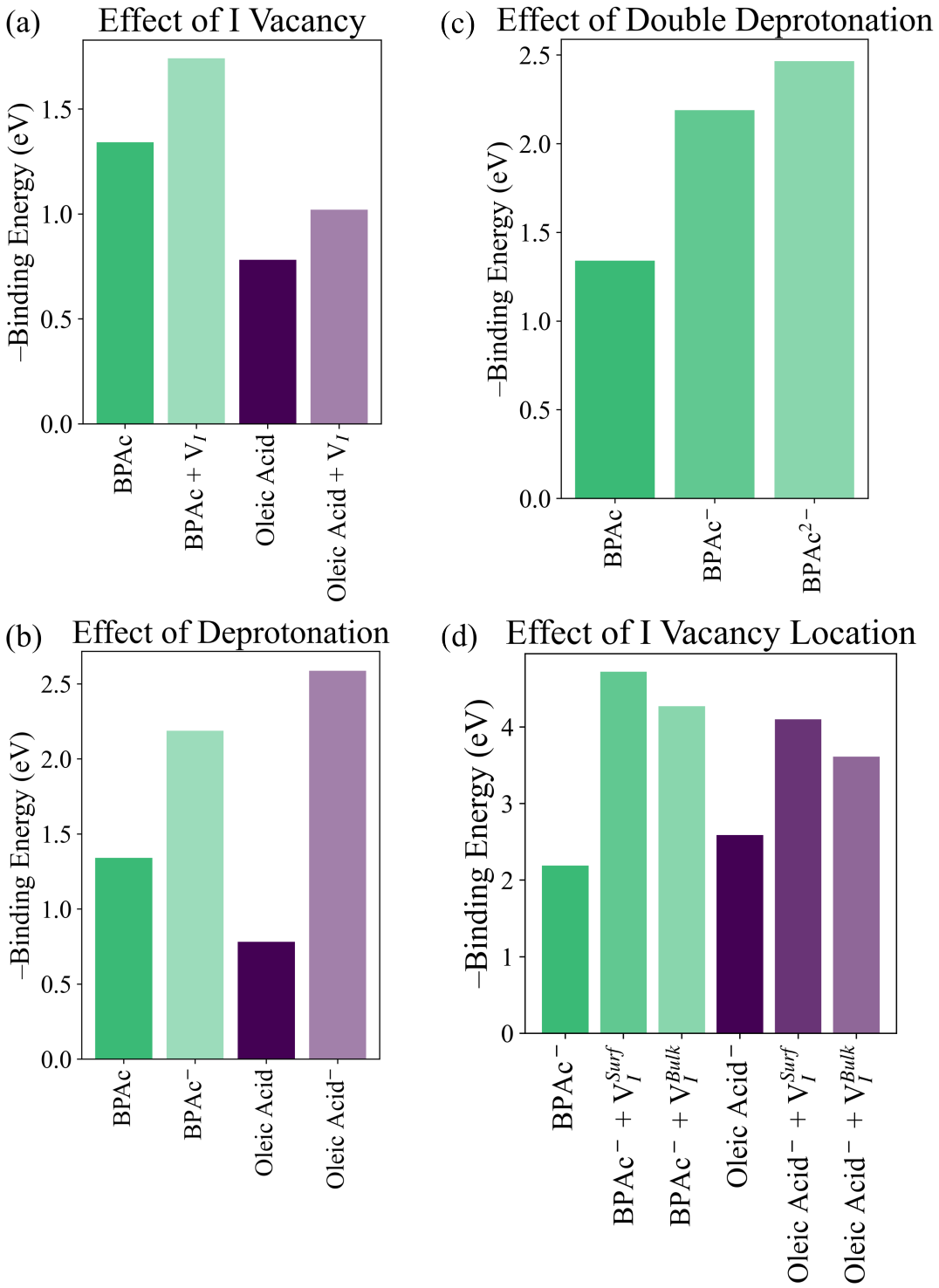


Figure 4.5: Binding energies of BPAc and oleic acid under various surface and ligand conditions: (a) in the presence of a surface I vacancy (V_I); (b) following ligand deprotonation; (c) after single (-) and double deprotonation (2-); and (d) deprotonated ligands in the presence of an I vacancy placed either in the outer-most surface layer (V_I^{Surf}) or in the third layer (V_I^{Bulk}).

vacancies or after deprotonation of the ligand (Figure 4.5). An I vacancy is created by removing an I atom from the outer-most layer of the surface slab. When the ligands bind to the I vacancy surface, the functional group binds in place of the vacancy site on the surface. This placement allows the ligand to bind to both of the neighbouring Pb atoms which are only four-coordinated following introduction of the I vacancy (Figure 4.6). Inspection of the I vacancy surfaces shows that the binding strength for both ligands increases due to the under-coordination of Pb and the introduction of secondary bonding interactions through both O atoms in the acid functional group. The increase in binding strength for both ligands demonstrates how these molecules effectively act as surface passivators. Additionally, the overall binding strength of BPAc is stronger both on the pristine surface and I vacancy surface than either of the oleic acid configurations; this result supports the understanding that the P–O bonds have more favourable orbital overlap with the surface Pb atoms. Furthermore, the phosphonic acid group has three O atoms: two of which bind to the under-coordinated Pb atoms and the third forms a hydrogen bond (H–I) to an under-coordinated I on the surface. This bidentate interaction increases the binding strength even further compared to the oleic acid ligand.

In addition to the I vacancies, which are common defects in perovskite structures, the acid ligand could bind either in its fully-protonated or deprotonated states. Figure 4.5 (b)–(d) illustrates binding energy trends in the case of deprotonation. In the instance of the first deprotonation of BPAc and oleic acid, the binding strength of both ligands increases noticeably. Both ligands when deprotonated bind to the surface Pb atom but now as a bidentate ligand (Figure 4.7 (e) and (f)). In the oleic acid case, both acid O atoms lack a proton and bind to the same Pb on the surface. In the case of BPAc, two out of the three O atoms lack a proton and these two O atoms bind to the same surface Pb atom while the third protonated hydroxyl group again forms a hydrogen bond (H–I) to a surface I. In both cases, the loss of a proton allows the ligand to bind more strongly to the surface by introducing an extra binding site which turns the monodentate ligands into bidentate ligands. In contrast to the I vacancy results, the deprotonated oleic acid

binding is stronger than either the BPAc or deprotonated BPAc results. This is likely because oleic acid is a weaker acid and therefore, is less stable in its deprotonated state making it a stronger binding agent. However, due to oleic acid being a weak acid, it is unlikely to be deprotonated under experimental conditions. Due to the higher acidity of BPAc, this ligand was chosen to investigate the effect of single vs double deprotonation. As would be expected, the removal of a second proton from the acid further increases the binding energy of the molecule. The doubly deprotonated BPAc ligand binds to the surface in a similar bidentate configuration to the singly deprotonated form, and Bader charge analysis indicates the charge on the bound Pb atom is slightly higher under double deprotonation indicating stronger binding.

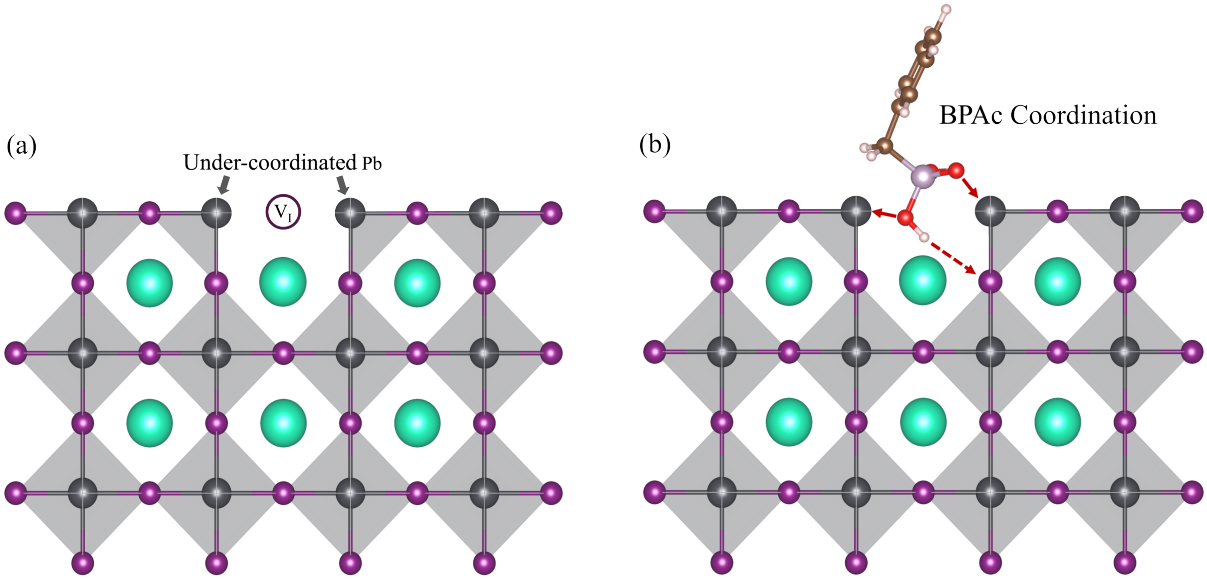


Figure 4.6: (a) $CsPbI_3$ surface with an I vacancy resulting in under-coordinated neighbouring Pb sites, and (b) BPAc passivates the under-coordinated Pb sites by forming two Pb–O bonds (solid arrows) as well as an OH–I hydrogen bond (dashed arrow).

For completeness, the joint effect of deprotonation and inclusion of an I vacancy were investigated (Figure 4.5 (d)). Here, two I vacancy sites were investigated: a I vacancy in the outer-most surface layer (V_I^{Surf}) and an I vacancy in the bulk (V_I^{Bulk}) of the NPL. It can be seen that for both ligands, the inclusion of an I vacancy in either location increases the binding energy. This suggests that there may be a charge compensation effect which allows the ligand to passivate defects deeper in the surface than expected. For

both ligands, the binding energy increases when the vacancy is on the surface relative to the bulk by ∼0.5 eV; this result quantitatively correlates well with the increase in binding strength shown in Figure 4.5 (a). It is clear that the ligand is binding strongly to defect surfaces regardless of the location which would provide a stabilising interaction. BPAc binds slightly more strongly to the defect surfaces than the oleic acid which again supports the observation that BPAc is more effective in passivating the NPL surface.

4.3.2 Ligand–Surface Electronic Effects

Electronic analysis of the ligand-bound surfaces illustrates how binding results in redistribution of the electron density around the surface. Figures 4.7 (a) and (b) illustrate this effect with BPAc and oleic acid, respectively, binding to the NPL. The larger isosurfaces shown on the BPAc surface correlate to a higher degree of electronic redistribution which can be correlated to a stronger binding interaction. Additionally, hydrogen bonds formed between the hydroxyl groups and the surface I atoms can be observed in both plots. The lack of charge density changes on either ligand backbone demonstrates that neither of these carbon backbones provides significant electronic contributions to the binding interactions.

Inclusion of a surface I vacancy changes the binding configuration of the ligands (Figure 4.7 (c) and (d)). Here, the ligands take the place of the I vacancy site and bind to both neighbouring Pb sites via two O atoms. The largest degree of electronic redistribution is observed between the double bonded O and the surface Pb, and both ligands also demonstrate hydrogen bonding between the hydroxyl groups and I atoms in the Cs–I layer immediately below the surface. The hidden hydroxyl group in the BPAc ligand is again forming a hydrogen bond to an I atom on the surface. This additional bonding interaction and increased electronic redistribution correlates to stronger binding for the BPAc ligand compared to oleic acid.

Finally, the introduction of a deprotonated ligand (Figure 4.7 (e) and (f)) results in the highest degree of electronic redistribution out of the three scenarios. Now, both de-

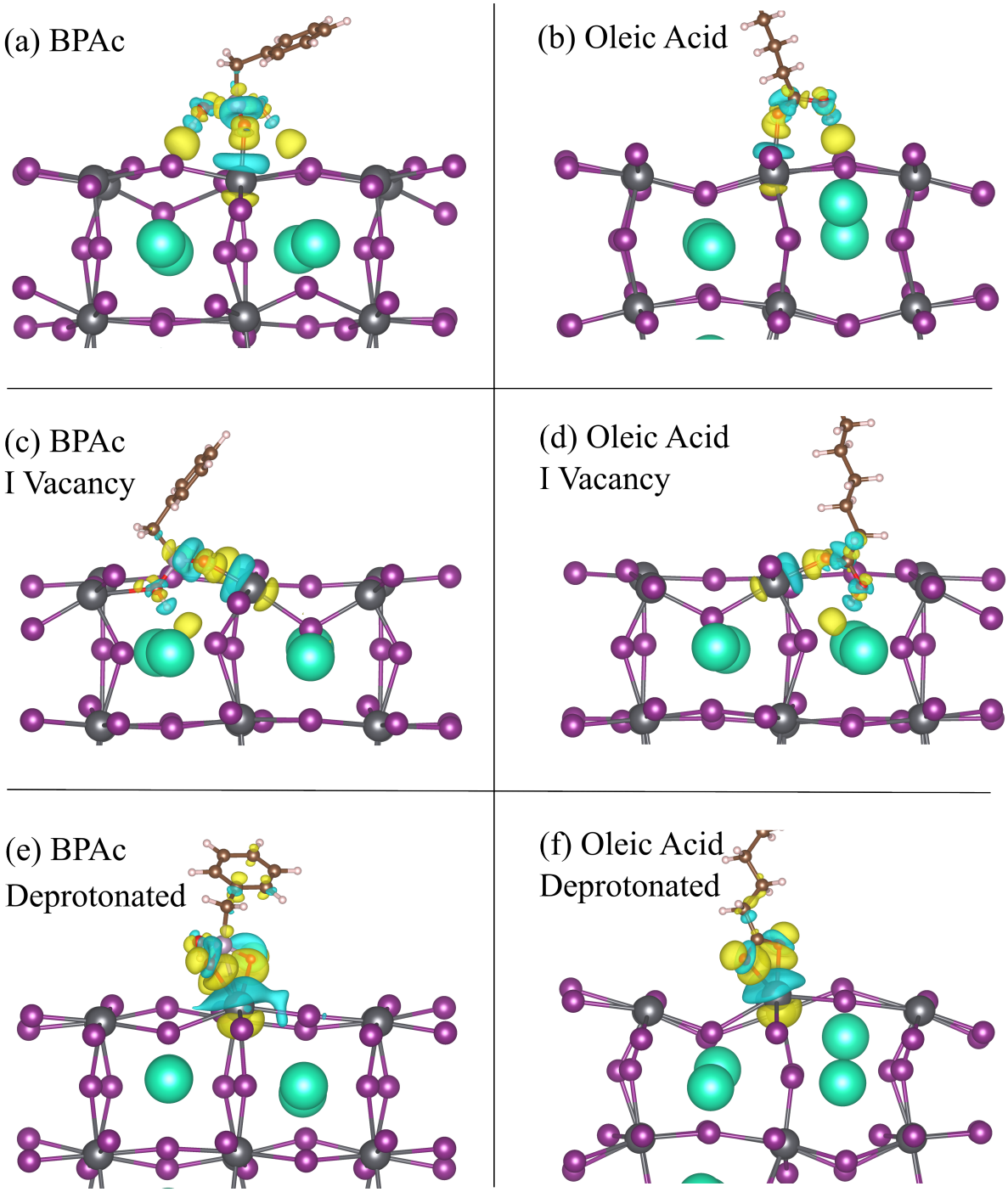


Figure 4.7: Visualisation of the charge build-up resulting from binding of ligands to the $CsPbI_3$ perovskite surface. Blue isosurfaces reflect a decreased charge density, and yellow isosurfaces reflect a positive change in charge density. The size of the isosurface provides a measure of the degree of charge redistribution that occurs as a result of binding. The images depict BPAc and oleic acid bound to pristine surfaces (a) and (b); BPAc and oleic acid bound to I vacancy surfaces (c) and (d); and deprotonated BPAc and deprotonated oleic acid bound to pristine surfaces (e) and (f).

protonated ligands bind in a bidentate manner with both O atoms coordinating to the surface Pb. Again, charge density is shifted, but in both cases, the electronic redistribution now spreads further up the backbone of the ligands. The introduction of charge increases the strength of the binding interaction in both cases with deprotonated oleic acid demonstrating slightly stronger binding strength; although, both structures display larger degrees of redistribution in the electron density which corresponds to increased binding energies.

To provide further evidence of the electronic interactions between the ancillary ligands and the surface, a site specific density of states (DOS) is plotted for the BPAc surface (Figure 4.8). The grey shaded partial DOS corresponds to the 6p orbitals on the ligand-bound Pb site on the perovskite surface, and the red shaded partial DOS corresponds to the BPAc O site 2p orbitals. Pb atoms in the perovskite are in the 2+ charge state, meaning that their 6p orbitals should be empty in the valence band; however, here, it can be seen that there is substantial electron density in the Pb 6p orbitals near the valence band edge. In addition, the shape of these filled orbitals mirrors that of the filled O 2p orbitals in the BPAc ligand.

From the decomposition of the plane-wave charge density into these orbitals, it can be seen that there is a degree of hybridisation occurring between the BPAc O 2p orbitals and the perovskite Pb 6p orbitals. This result again correlates to the strength of the Pb–O bonding between BPAc and the perovskite surface and suggests that BPAc stabilises the perovskite surface by acting as a Lewis base, donating electron density to passivate the under-coordinated Pb atoms. The improved bonding in the phosphorus acids compared to the sulphonic or carboxylic acids can be explained by the bonding character of the P–O bonds which are the most ionic in character due to the larger electronegativity difference between P and O. This means the O in these phosphorus acid molecules will be more negative, and therefore has more electronic density available to donate to the surface Pb.

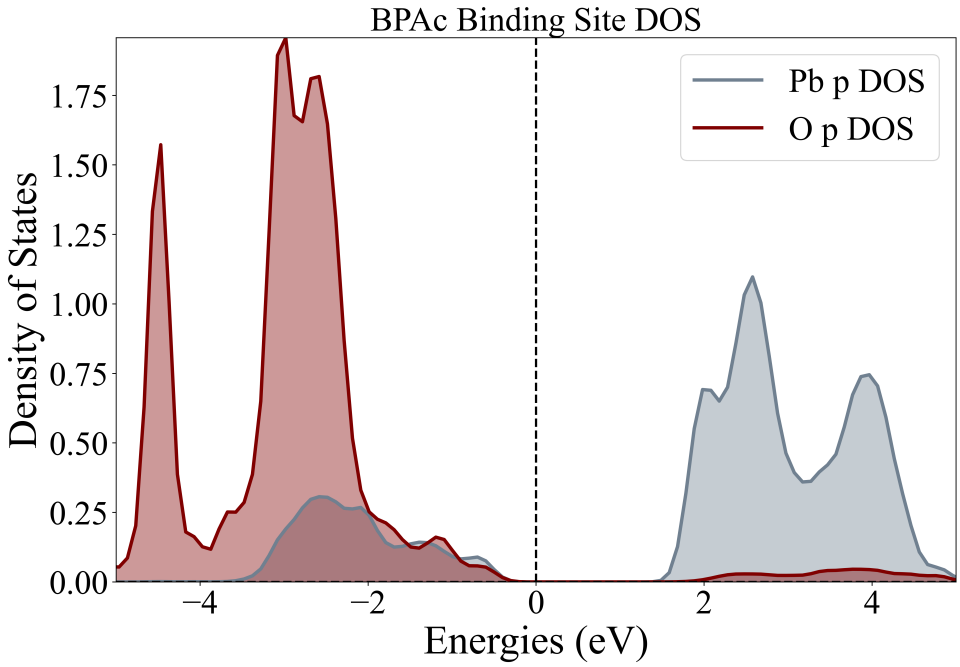


Figure 4.8: Site density of states for the BPAc O and bound perovskite surface Pb site shows evidence of hybridisation between the Pb 6p orbitals and the O 2p orbitals.

4.3.3 Experimental Results and Calculated Charge Analysis

Experimental investigations were performed by our collaborators in Prof. Robert Hoye's group in the Oxford Department of Chemistry, Prof. Myoung Hoon Song's group at the Department of Materials Science and Engineering at the Ulsan National Institute of Science and Technology, and Prof. Bo Ram Lee's group in the School of Advanced Materials Science and Engineering at Sungkyunkwan University. The experimental work was primarily carried out by Jongbeom Kim in Prof. Song's group and Dr. Woo Heon Jeong and Dr. Junzhi Ye in Prof. Hoye's group.

Figure 4.9 (a) demonstrates the monolayer dispersity observed when different ancillary ligands are used in the NPL synthesis. As can be seen, the stronger binding ligands show higher monodispersity and a preference for thinner NPLs, both of which improve the degree of polarisation exhibited. BPAc displays better experimental performance than both DPPAc and the pristine synthesis route which refers to the oleic acid and oleylamine synthesis without the inclusion of any ancillary ligands. Despite DPPAc demonstrating slightly stronger binding strength than BPAc, it does not perform quite as well which

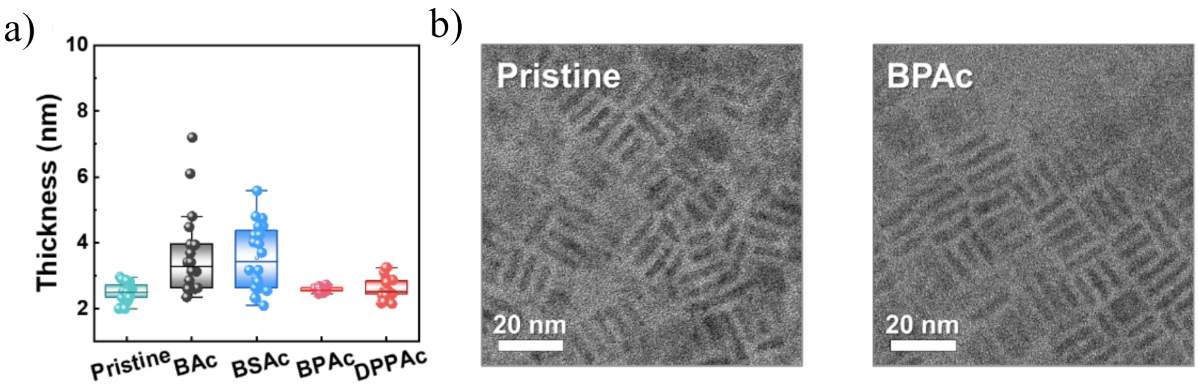


Figure 4.9: Experimental results illustrating (a) the improved monodispersity observed with the BPAc ancillary ligand compared to other ligands investigated and (b) TEM images illustrating the improved NPL ordering observed after BPAc addition. Figures reproduced from Kim *et al.* (2026).[129]

could be a result of the increased steric hindrance as a result of the additional phenyl group that may repel neighbouring ligands. Figure 4.9 (b) illustrates how the improved monodispersity directly links to the formation of a highly ordered NPL superlattice which is ideal for producing highly polarised light.

To provide additional characterisation of the interactions occurring during the synthesis process, ^{207}Pb NMR spectra were measured in the PbI_2 precursor solution with and without ancillary ligands being present (Figure 4.10 (a)). The BPAc and DPPAc ligands both induce chemical shifts to higher levels of deshielding compared to the pristine solution (from 1943.4 ppm (pristine) to 1953.2 ppm (BPAc) and 1949.7 ppm (DPPAc)). Bader charge analysis (Figure 4.10 (b)) was performed on the ligand-bound Pb atoms on the $CsPbI_3$ surface to support the NMR observations. The charges calculated represent the charge localised around the surface Pb atom which is bound to the ligand. These charges are referenced with respect to the charge on the same Pb atom in the unbound surface. These results support the ^{207}Pb NMR findings which show an increase in Pb charge (deshielding effect) upon binding with both BPAc and DPPAc ligands showing increased Pb charge compared to the other ligand-bound surfaces.

As observed by my experimental collaborations, the addition of ancillary ligands greatly impacts the growth kinetics of NPLs. Based on my computational investigation,

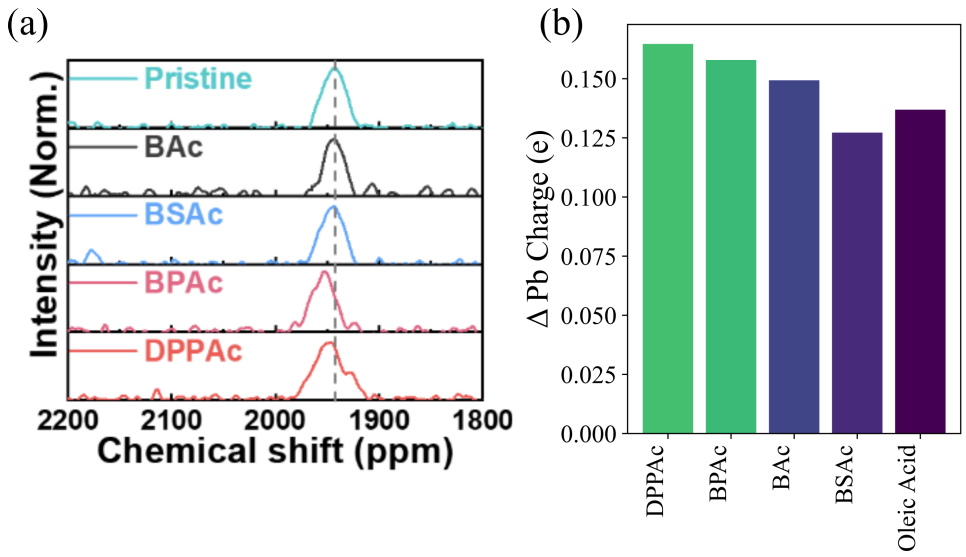


Figure 4.10: (a) Observed ^{207}Pb NMR spectra reproduced from Kim *et al.* (2026),[129] and (b) the change in bound Pb charge as calculated via Bader charge analysis.

I propose that the strength of the binding interactions between the ligand and the perovskite surface is the key feature controlling the synthesis outcome. As a result, I propose that the use of ancillary ligands which demonstrate strong binding to the $CsPbI_3$ NPL surface will result in the synthesis of highly ordered monodisperse NPLs which are ideal for emitting polarised light. Additionally, this work illustrates why further experimental studies should utilise computational investigations of ligand–surface binding energies as a guide for rational synthesis design.

4.4 Effects of Zn Addition

Following the previous experimental investigations, it was additionally observed by our collaborators, lead by Ashish Gaurav in Prof. Robert Hoye's group, that the addition of ZnI_2 to the NPL precursor solution further improved the monodispersity and provided a driving force for the preferential synthesis of ultrathin $n = 2$ NPLs (Figure 4.11). Our collaborators found that the addition of 5% Zn increased the reaction rate in the precursor solution and drove a preference for the $n = 3$ and $n = 4$ monolayers. The addition of 10% Zn slightly increased the reaction rate compared to the 5% result but still produced

a range of monolayer widths. However, increasing the Zn concentration to 30% was found to further increase the rate of reaction while also increasing monodispersity with a strong preference for the ultrathin $n = 2$ monolayer. Despite the dramatic improvement in synthesis outcome upon the addition of 30% Zn, the mechanistic role that Zn played during the synthesis remained unclear. This modelling work explores the overall stability of Zn incorporation into the α-$CsPbI_3$ bulk and ultrathin monolayers. Additionally, Zn was investigated as part of a coordinating surface complex that modulates NPL energies without incorporating into the bulk.

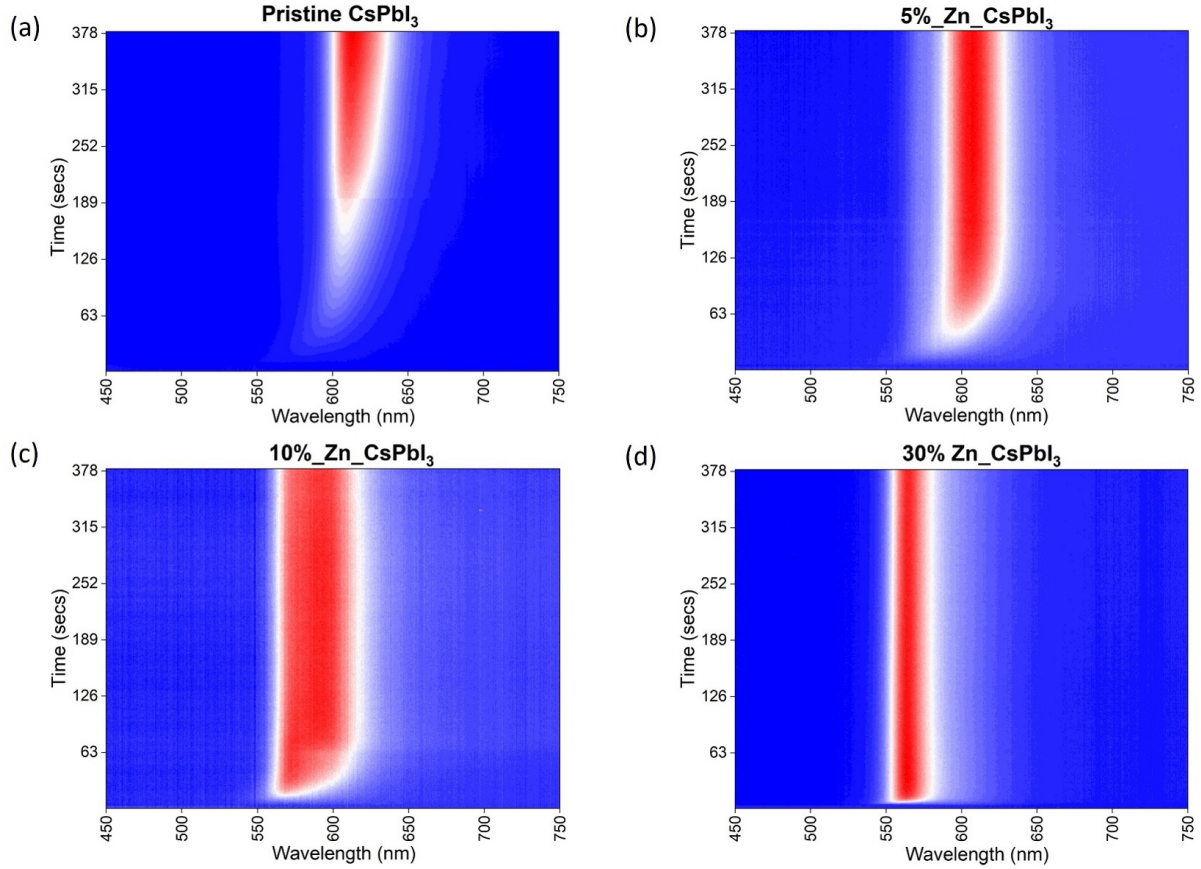


Figure 4.11: *In-situ* PL spectra recorded during synthesis of $CsPbI_3$ NPLs in solutions containing (a) 0%, (b) 5%, (c) 10%, and (d) 30% ZnI_2 precursor. Increasing the concentration of ZnI_2 in the precursor solution increases the reaction rate, but only the 30% Zn solution preferentially forms monodisperse and ultrathin $n = 2$ NPLs. Spectra provided by Ashish Gaurav in Oxford Chemisty.

4.4.1 Zn-Doping Investigation

First, the stability of Zn incorporation into the bulk α-$CsPbI_3$ perovskite was investigated. Zn and Pb atoms were placed on B-sites in the perovskite lattice in different orderings. The energies of these relaxed structures are plotted as mixing energies (Figure 4.12 (a)) to demonstrate the stability across the full solid solution, $CsPb_{1-x}Zn_xI_3$. The points on the gold convex hull identify that mixed compositions are only predicted to be stable for Zn concentrations greater than 40%. Any of the structures where Zn was doped in at low concentrations (<0.4 Zn) are not predicted to be stable. This can be attributed to the size mismatch between Pb^{2+} and Zn^{2+} which introduces large distortions into the perovskite lattice, especially at low concentrations as illustrated in Figure 4.12 (b). Previous experimental studies[125–127] on Zn incorporation into perovskite nanoparticles found that low concentrations of doping were accessible. The solubility limit was found to decrease with increasing halide radius from $CsPbCl_3$ (<11.6% Zn) to $MAPbI_3$ (<2.0% Zn), suggesting that the greater size mismatch between the large I anions and the small Zn cation leads to instability in the structure.

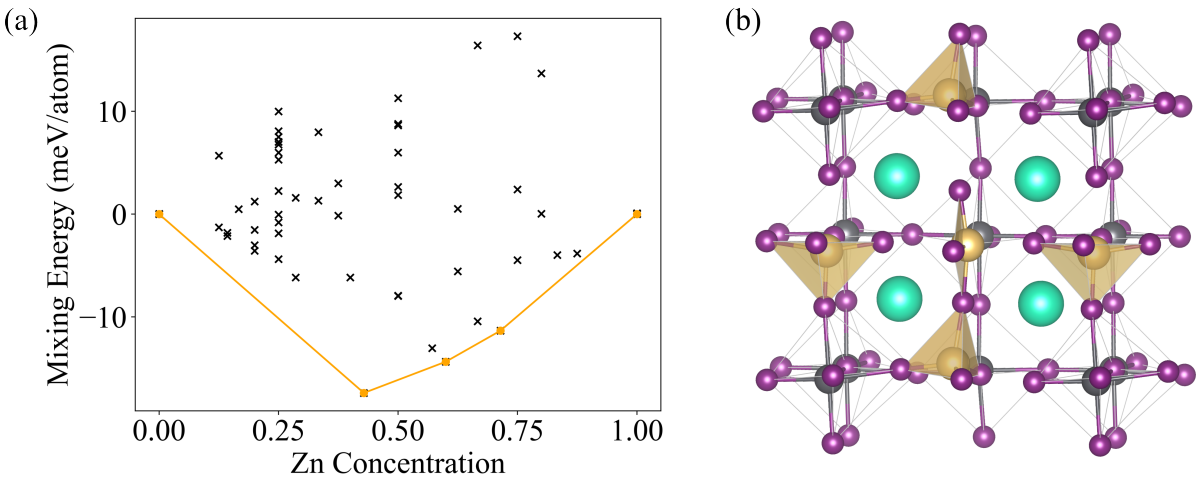


Figure 4.12: (a) The mixing energies for the Pb–Zn solid solution in $CsPb_{1-x}Zn_xI_3$ demonstrate that Zn doping only becomes favourable for Zn concentrations greater than $x = 0.4$. (b) A slice of a Zn-doped α-$CsPbI_3$ supercell illustrating how the Zn atoms preferentially shift off the octahedral B-sites to form ZnI_4 tetrahedra, resulting in the miscibility gap observed.

These calculated findings and the reported literature suggest that the improved monodis-

persity is unlikely a result of Zn directly doping into the NPL. However, the energetics of ultrathin NPLs may differ from the bulk as the lattice strain introduced by Zn doping could be accommodated by surface reconstructions. To study this further, the surface energies of Zn-doped $n = 2$ NPLs were also investigated. A set of $n = 2$ surface slabs were constructed in the pristine $CsPbI_3$ composition as well as including 5% Zn and 30% Zn. For the 5% and 30% Zn-doped compositions, several different arrangements of Zn were investigated in the lattice to asses whether the Pb–Zn orderings significantly impacted the surface energy.

Six doping configurations were investigated in the $n = 2$ monolayer (Figure 4.13). Surfaces A and B were both doped with a single Zn atom in the surface and interior layer, respectively. Surfaces C–F were all doped at 30% Zn with C and D illustrating fully ordered configurations with all Zn atoms placed on the surface or interior. Surface E maximised the disorder by placing all Zn atoms as far apart as possible within the slab, and surface F provided a disordered structure but with all Zn atoms spread across the two surface layers.

Analysis of the $n = 2$ surface energies shows two main trends. First, there is only one Zn-doped configuration that is lower in energy than the pristine surface which is the structure that has one Zn atom (5%) on the surface of the slab. The other 5% Zn-doped slab holds the Zn atom in the middle layer and has a surface energy above that of the pristine. This result suggests that at low levels of Zn doping in the $n = 2$ monolayer, there will be a preference for Zn to sit at the surface where structural reconstruction can more easily reduce lattice strain. Second, the surface energies for the 30% Zn-doped $n = 2$ slabs are all substantially higher in energy than the pristine, suggesting that higher levels of Zn doping are inaccessible in this thin monolayer.

These findings, in conjunction with the mixing energies calculated for Zn doping in the α-$CsPbI_3$ bulk, suggest that while it may be energetically accessible for small concentrations of Zn to dope into the NPL, it is generally unfavourable. It can certainly be understood that the full 30% Zn is not doping into the bulk. These calculated results are

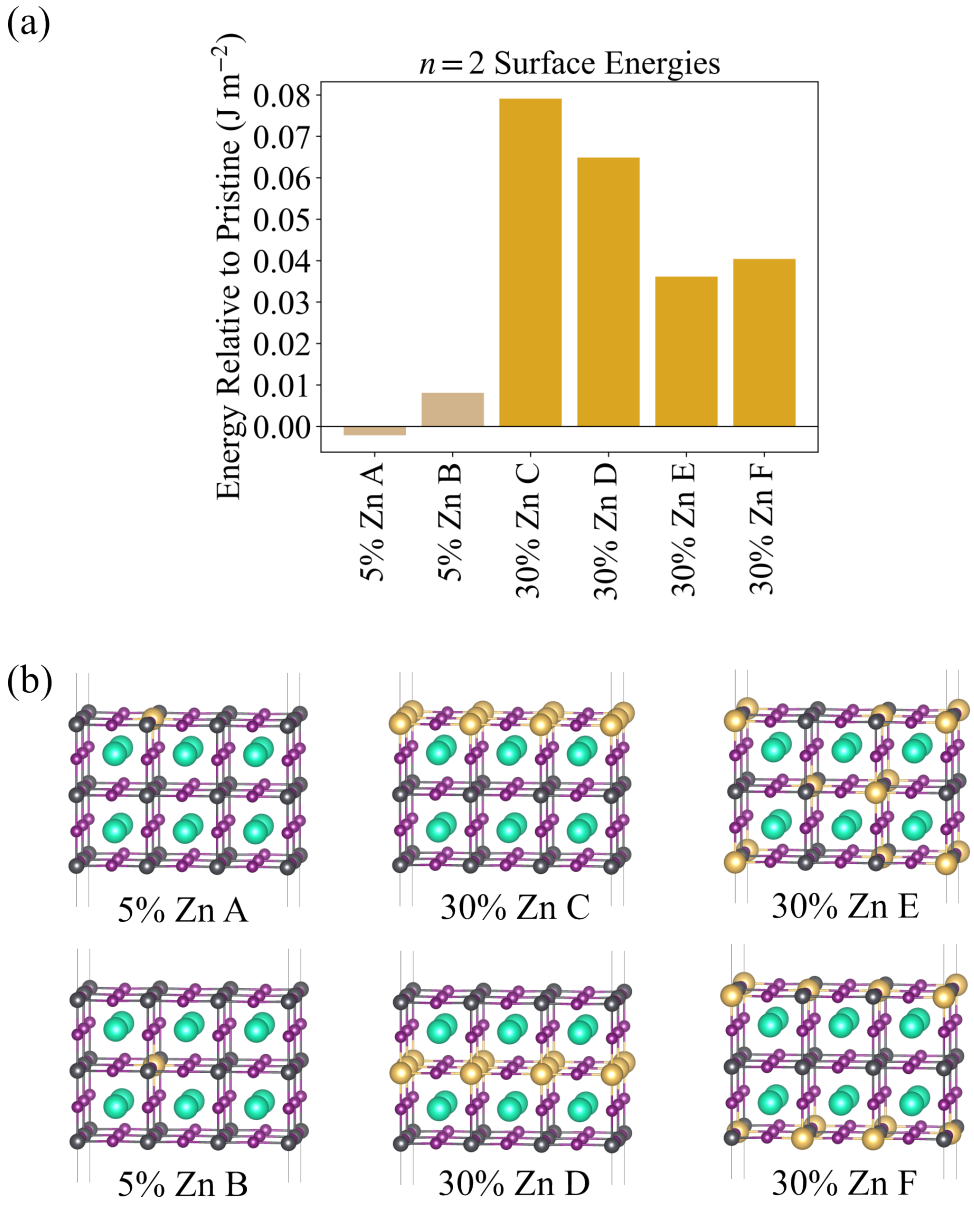


Figure 4.13: (a) Calculated surface energies of Zn-doped $n = 2$ slabs referenced to the energy of the pristine $n = 2$ slab. Six different dopant configurations across the 5% and 30% Zn concentrations were investigated. (b) The corresponding surface slabs are pictured with the Zn dopants marked by large yellow spheres for clarity and the slab are periodic in a, b with the (001) PbI_2 termination oriented along the c axis.

further supported by NMR and PES experiments which do not observe any Zn signature in the NPL product.

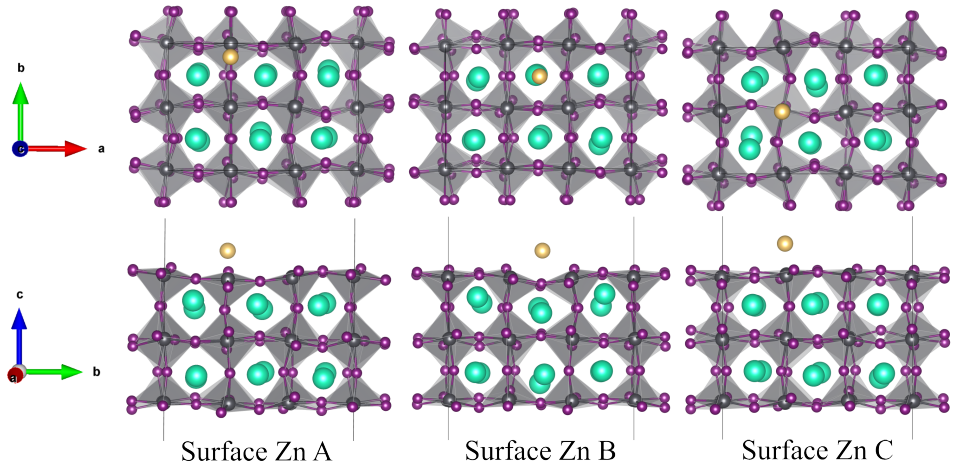


Figure 4.14: Three $n = 2$ NPL surfaces relaxed with a Zn atom placed in distinct locations above the surface.

4.4.2 Zn Surface Passviation Investigation

Based on the conclusion that Zn does not dope into the NPL but is experimentally observed to impact the growth kinetics of the product, the next step was to investigate how Zn interacts with the NPL surfaces. Three $n = 2$ slabs were relaxed with Zn placed in different locations above the surface: above an I (Surface Zn A), above an interstitial site (Surface Zn B), and above a Pb (Surface Zn C). The relaxed surfaces are shown from the side (100) and top (001) directions in Figure 4.14. Using three different surface configurations provides an estimate of the degree to which the surface energies fluctuate based on the placement of Zn.

Following relaxation of the three surface Zn configurations, each of these surfaces was then relaxed again in the presence of either an oleic acid or oleate ligand. The surface energies of all nine surfaces, including the ligand-free Zn surface, are plotted in Figure 4.15 (a). These energies are referenced to the energy of the pristine $n = 2$ NPL surface. It can be seen that all of the slabs with Zn sitting on the surface are similar in energy, and all are more stable than either the Zn-doped surfaces or the pristine surface.

The surfaces relaxed in the presence of the oleic acid and oleate ligands are depicted in Figure 4.15 (b). First considering the oleic acid surfaces, it can be seen that the oleic acid only binds to the Zn atom in one of the three surfaces. Despite the difference in bonding coordination between the oleic acid, the Zn atom, and the perovskites observed between the three structures, the surface energies are very similar. This suggests that the oleic acid interacts weakly with the Zn atom. While the introduction of oleic acid stabilises the Zn surfaces, the Zn-free $n = 2$ NPL surface with oleic acid is more stable than either the Zn-oleic acid surfaces or the Zn-only surfaces.

Compared to the oleic acid surfaces, the oleate ligand demonstrates a much stronger effect. The oleate ligand binds to the surface in two configurations: binding either in a bridging coordination with one O bound to Pb and the other O bound to Zn or as a bidentate ligand doubly bound to Pb. In the presence of oleate, the Zn atom can be observed to migrate towards the perovskite surface and appears to incorporate by interacting with I atoms on the surface. The oleate surfaces are all more stable than any of the previous configurations with the bridging coordination being the most favourable. Despite the stability of the oleate-Zn surfaces, the Zn-free oleate surface remains the most stable.

To further support these results, the binding energies of the oleic acid and oleate ligands were calculated on the pristine and Zn surfaces (Figure 4.16). The binding energy of the oleic acid is very similar whether or not Zn is present on the surface. The binding energy of oleate is stronger than oleic acid across all surfaces with the strongest binding energy corresponding to the pristine surface. These results suggest that while the Zn-oleate interactions are highly favourable, the most stable surface and therefore, the most stable form of the NPLs is likely a Zn-free, oleate-passivated surface.

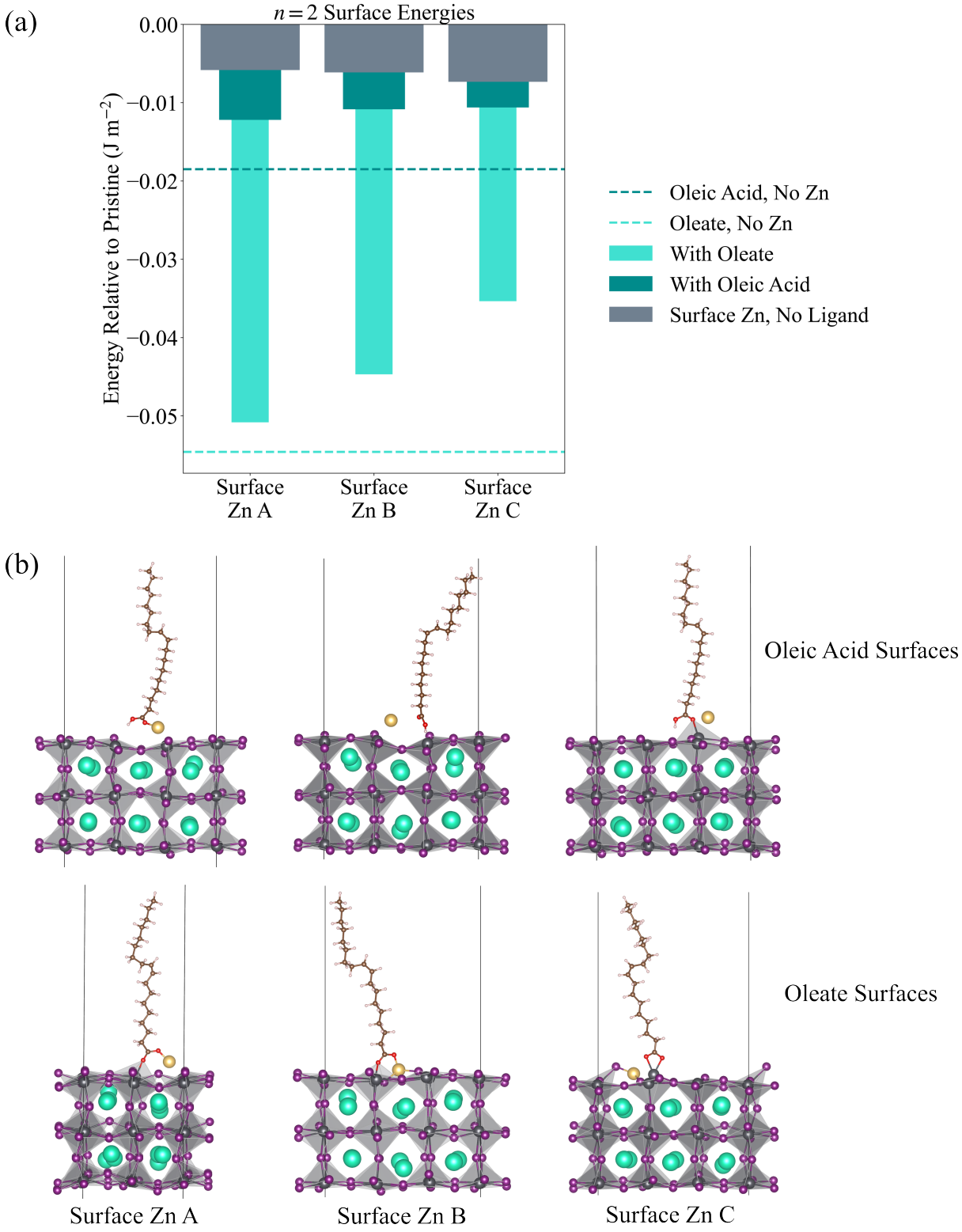


Figure 4.15: (a) Calculated surface energies relative to the pristine $n = 2$ surface for the three Zn-configurations depicted in Figure 4.14 in isolation, in the presence of oleic acid, and in the presence of oleate. (b) The relaxed structures with oleic acid and oleate ligands bound to the $CsPbI_3$ surface in the presence of Zn.

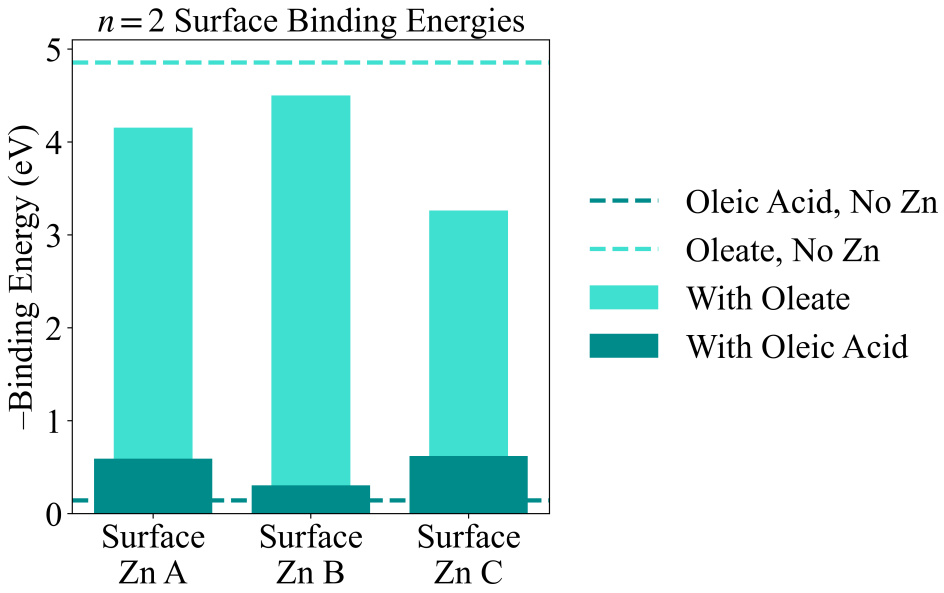


Figure 4.16: The binding energies calculated for oleic acid and oleate bound to the pristine and Zn $n = 2$ surfaces.

4.5 Proposed Mechanism and Supporting Experimental Results

The results of this computational investigation support the experimental observations that Zn is not incorporating into the NPLs. Instead, the calculated increased stability and observed monodispersity of the Zn surfaces compared to the pristine surface suggests that as the NPLs begin to form from the precursors, Zn quenches growth by sitting on top of the perovskite surface, lowering the surface energy. Increasing the concentration of Zn to 30% in the precursor solution increases the quenching rate and provides a high enough concentration to prevent further growth, resulting in a strong preference for the synthesis of the ultrathin $n = 2$ monolayer.

The increased interaction calculated between Zn and the oleate ligand compared to oleic acid suggests that the Zn prefers to form complexes with the oleate ligands, binding them to the NPL surface. This hypothesis is further supported by experimental ^{1}H NMR spectra. These spectra show that the oleic acid Hs exist in similar environments in all precursor solutions (Figure 4.17 (a)). After formation of the NPLs, the ligand H

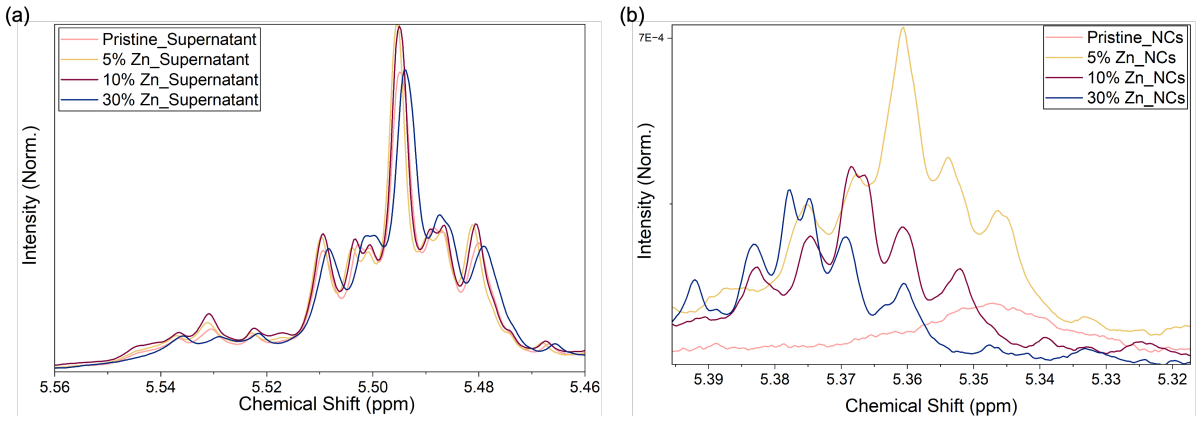


Figure 4.17: (a) The ^{1}H NMR spectra of the precursor solution before reaction shows the BPAc ligands exist in similar environments before reaction occurs across all solutions. (b) The ^{1}H NMR spectra of the NPL solution following reaction shows that deshielding increases with Zn concentration and that H environments are evolving in the 10% and 30% Zn solutions, as indicated by the presence of peak splitting. NMR spectra provided by Ashish Gaurav in Oxford Chemistry.

environments are furthest deshielded in the 30% Zn solution, and there is a peak splitting effect observed in the 10% and 30% Zn solutions which indicates the presence of different H symmetry environments (Figure 4.17 (b)). These spectra support the hypothesis that the oleic acid ligands do not play a role in the initial NPL growth quenching as there is no change in environment with Zn concentration. However following NPL synthesis, the ligands are increasingly deshielded with increasing Zn concentration, indicating that the Zn atoms are withdrawing electron density from the ligands. This effect could aid in deprotonation of the oleic acid ligands by other solvent molecules. The appearance of peak splitting in the 10% and 30% Zn solutions may reflect formation of the bridging surface binding configuration in which an oleate ligand is bound simultaneously to Pb and Zn, introducing additional H couplings in the NMR spectra.

The DFT-relaxed surfaces show the formation of a bridging surface complex with an oleate ligand bound simultaneously to Zn and Pb. The formation of this intermediate complex is further supported by experimental Fourier Transformed Infrared (FTIR) spectra (Figure 4.18) which presents an asymmetric carboxylic acid stretching peak. The intensity of the peak increases in the 30% Zn solution as compared to the pristine solu-

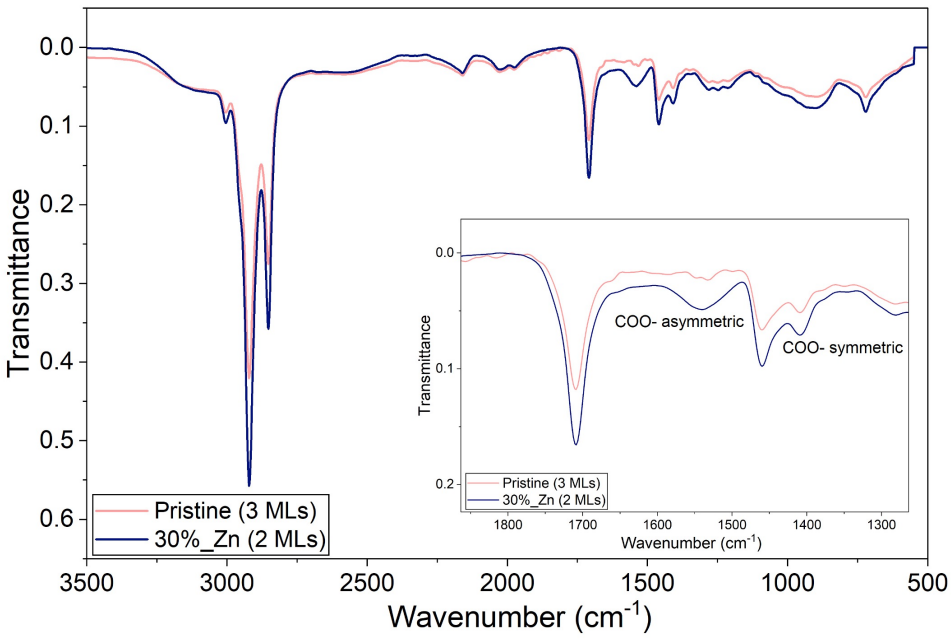


Figure 4.18: An FTIR spectrum demonstrating the increased intensity of the asymmetric carboxylic acid stretching peak in the 30% Zn NPL solution compared to the pristine NPL solution. This asymmetry can be attributed to the formation of the bridging oleate complex on the NPL surface. FTIR spectrum provided by Ashish Gaurav in Oxford Chemistry.

tion indicating that additional asymmetric oleate binding occurs in the 30% Zn solution. This feature supports my proposed mechanism that formation of the asymmetric oleate bridging complex is intrinsically linked to the presence of Zn.

Finally, the DFT calculations find that the most stable surface is the Zn-free, oleate-passivated surface. Based on this finding, I propose that the oleate ligands complexed to the Zn atoms on the perovskite surface migrate to bind as bidentate ligands to the NPL. The unbound-Zn is washed off the perovskite surface resulting in the most stable configuration: a Zn-free NPL surface passivated by an oleate ligand. The formation of a symmetrically bound oleate ligand is further supported by experimental FTIR measurements (Figure 4.18) which also show an increase in the symmetric carboxylic acid stretching intensity in the 30% Zn solution compared to the pristine. This result supports my proposed mechanism in which Zn aids in the deprotonation of oleic acid to form oleate ligands which bind in a symmetric bidentate fashion to the NPL surface. As shown previously in Figure 4.5 (b), the calculated binding strength of the oleate ligand

is even stronger than the deprotonated BPAc ligand which reinforces my conclusion that these oleate-passivated NPL surfaces will display high degrees of stability as observed experimentally. A schematic of my proposed mechanism is depicted in Figure 4.19.

While the experimental component of this work is still on-going, this mechanism provides a basis for understanding how metal iodide precursors can be utilised to form monodisperse ultrathin NPLs. Further work investigating other metal iodide additives is underway which seeks to elucidate exactly why Zn performs better than other metals additives such as Ca and also aims to identify any metal candidates that can further improve synthesis outcomes.

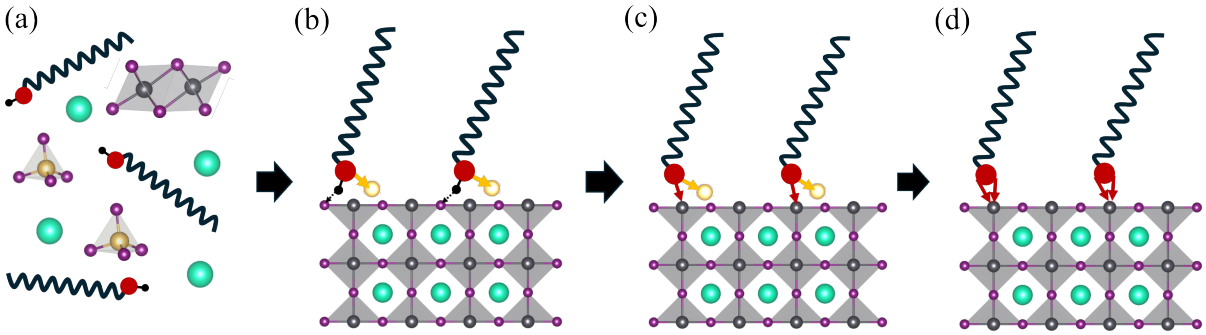


Figure 4.19: Schematic of the proposed role of Zn in the NPL growth synthesis: (a) precursors including the atoms Cs (aqua), Pb (grey), I (purple), and Zn (yellow) and the oleic acid ligand with the carboxylic acid head group (red); (b) Zn quenches growth of the $n = 2$ NPL surfaces and binds to the passivating oleic acid ligands which form hydrogen bonds to the surface; (c) while bonded to Zn, oleic acid ligands are more easily deprotonated by solvent molecules, allowing formation of bridging Pb–O–C–O–Zn complexes; and (d) Zn is washed away in solution leaving behind highly stable bidentate oleate ligands passivating the perovskite surface.

4.6 Chapter Summary

In this study, two routes for stabilising $CsPbI_3$ NPLs for polarised emission LEDs have been explored. The first route is via the addition of ancillary ligands into the NPL synthesis, primarily those with phosphorus acid functional groups and phenyl ring backbones. The two such acids modelled, benzyl phosphonic acid (BPAc) and diphenyl phosphoric acid (DPPAc), both demonstrate very strong binding to the $CsPbI_3$ perovskite surface

which enables the necessary fast quenching of NPL growth to ensure high monodispersity and strong ordering of the NPLs. This is critical for achieving the desired degree of polarisability and stability necessary for commercial LED and optoelectronic applications.

The computational investigation described here provides a template for predicting the success rate of ancillary ligands based on calculated properties. Good candidate ligands for future work include those with phosphoric acid head groups and smaller backbones which do not provide too high a degree of steric hindrance. It is likely that this steric hindrance effect is why BPAc outperforms DPPAc, despite demonstrating slightly weaker binding energies and associated properties.

The computational investigation into Zn additives demonstrates the relative instability of Zn-inclusion directly in the NPL structure; the results rather support the experimental evidence that the Zn is likely sitting on the NPL surface where it forms a complex with the oleic acid. From this intermediate complex, the oleic acid ligands are deprotonated and transferred to the perovskite surface. Zn performs two critical functions: Zn stabilises the $n = 2$ surface to quickly quench NPL growth and Zn complexes with oleic acid ligands, acting as an intermediary which enables the ligands to be deprotonated and transferred to the perovskite surface, producing the highly stable ultrathin NPLs experimentally observed.

Future work should investigate not only the interactions between the ligands and the surface but also ligand–ligand interactions given the high concentrations with which these ligands sit upon the NPL surface. Furthermore, if an MLIP model could be trained to investigate these surface interactions, it would be interesting to see how these ligands dynamically interact with the perovskite surface at larger length scales. Additionally for the Zn investigation, developing an MLIP model of the fast crystallisation that occurs would provide unique insights into the precise mechanism via which the Zn-oleic acid complexes form and would also shed light on the mechanism via which the Zn atoms are removed from the surface.

Overall, the two studies presented in this chapter provide new atomistic insights into

the complex mechanisms underpinning perovskite NPL synthesis and point to design guidelines for further enhancement of the experimental methodologies required to synthesise NPLs suitable for commercial applications.

Chapter 5

Pb–Sn–S-Based Low Band Gap Materials for Triple Junction Solar Cells

5.1 Introduction

Increasing solar cell efficiency is a key route to further reducing the cost of electricity production.[283,284] Crystalline silicon modules have now exceeded 27% PCE[285] but are quickly approaching the practical efficiency limit of 29.4%,[65] meaning there is little capacity for further efficiency improvements in single-junction silicon architectures. As an alternative, multi-junction PV architectures have increasingly attracted attention as these devices surpass the efficiency limits of single-junction cells by reducing thermal losses.[106,286] Metal halide perovskites have emerged as leading candidates for tandem PV due to their tunable bandgaps, high absorption coefficients, and compatibility with silicon processing.[287,288] Currently, the silicon–perovskite tandem architecture record efficiency has reached 34.85%,[3] and these devices are now commercially available from companies such as Oxford PV.[289]

Up until now, most research efforts have focused on improving silicon efficiencies

by adding wide band gap perovskite sub-cells which capture higher energy photons as demonstrated by Figure 5.1. Perovskites such as $CsPbI_3$ and $MAPbI_3$ with band gaps between 1.5 eV[44] and 1.7 eV[290] complement the 1.1 eV silicon band gap and produce devices with a theoretical efficiency limit of 43%.[109] In addition, the cheap manufacturing costs of the perovskite[62] ensure that the gain in PCE offsets the cost increase due to additional material production. As perovskite–silicon tandem efficiencies continue to improve, attention has turned to triple-junction architectures which are commonly of the perovskite–perovskite–silicon form.[69,243,281]

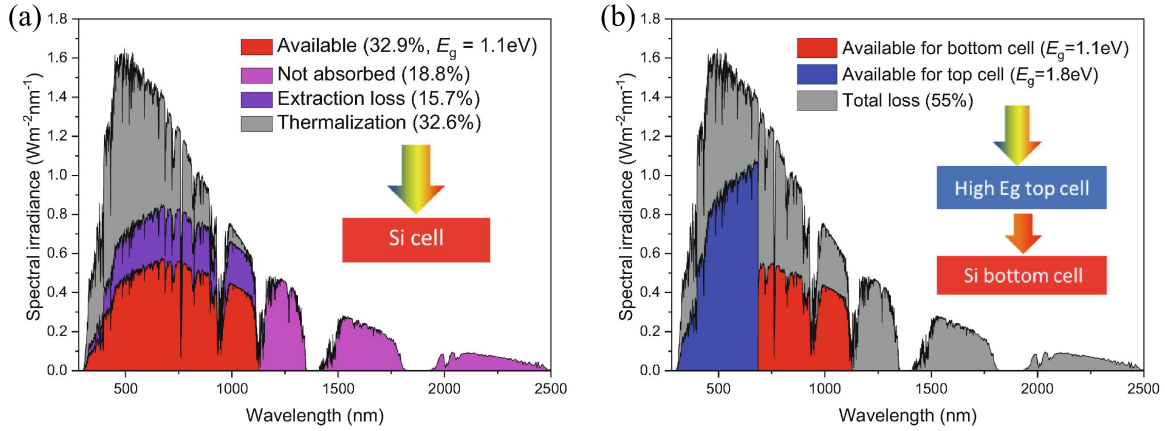


Figure 5.1: Comparison of the region of the solar spectrum available for absorption by (a) a silicon single-junction solar cell and (b) a perovskite–silicon tandem solar cell. The region highlighted in pink in (a) between the ∼1200–1400 nm wavelengths is the near-IR region targetted by the Pb–Sn–S material proposed in this chapter. Figure reproduced with permission from Zhu *et al.*, *J. Energy Chem.*, 2021, **58**, 221.[291] Copyright © 2021 Elsevier.

Within these triple-junction tandems, most research efforts have focused on adding wide band gap sub-cells in tandem architectures which neglect the low energy near-IR region of the solar spectrum.[292] Silicon–perovskite tandems absorb light at wavelengths between 250–1200 nm, leaving the region between 1200–1400 nm unabsorbed (Figure 5.1).[292] A triple-junction tandem solar cell could be designed such that these lower energy photons are also absorbed by a lower band gap material. Incorporating a sub-1 eV band gap absorber would target this previously ignored region of the solar spectrum; therefore, the identification of a material suitable for this purpose represents a critical opportunity

for further efficiency gains.

In the halide perovskite field, the alloying of Pb and Sn has commonly been used to create a class of materials that demonstrate band gap tunability as function of composition. For instance, the hybrid organic-inorganic $MAPb_xSn_{1-x}I_3$ perovskites show band gap variability between 1.7 eV and 1.1 eV. Additionally, an anomalous band bowing effect is observed whereby intermediate compositions demonstrate band gaps smaller than either of the pure end-members.[40,293] Despite these results, no perovskite has been observed with a sufficiently low band gap to act as a sub-1 eV absorber.

Instead, our collaborators, led by George Morgan in Prof. Henry Snaith's group in Oxford Physics, considered the chalcogenides PbS and SnS due to their respective band gaps of 0.4 eV[294–297] and 1.05–1.4 eV.[298–302] Our collaborators hypothesised that by mixing these two compositions, a material with the desired 0.8–0.9 eV band gap could be created. In addition to their band gaps, PbS and SnS possess favourable optoelectronic properties. Cubic PbS is characterised by a direct band gap, high absorption coefficient ($>10^4$ cm^{-1}), and good hole mobilities (30–60 $cm^2V^{-1}s^{-1}$).[294–297,303,304] Meanwhile, orthorhombic SnS has an indirect band gap at ∼1.05 eV and a direct band gap between 1.2–1.4 eV along with similar absorption coefficients and reasonable hole mobilities (10–40 $cm^2V^{-1}s^{-1}$).[298–301,305] Although these materials have been previously studied for thermoelectric and energy storage applications, mixed Pb–Sn–S systems have been largely ignored as low band gap absorbers.[305–307]

The work in this chapter explores the $Pb_xSn_{1-x}S$ solid solution produced by the mixing of PbS and SnS, including bulk stability and electronic properties. Band gaps are calculated for mixed phases within the predicted stability region, and electronic structure analysis characterises the structural properties which drive the band bowing effect commonly observed in mixed Pb–Sn systems. In addition, carrier mobility trends are predicted from electronic structure properties. Finally, these results are compared to experimental findings which establish the Pb–Sn–S system as a promising candidate for integration into triple-junction PV architectures that feature enhanced near-IR absorp-

tion. Experimental work was carried out by George Morgan and Dr. Brian Wieliczka in Prof. Henry Snaith's group in Oxford Physics, Dr. Harry Sansom at the University of Bristol, and Dr. Dmitry R. Maslennikov in Prof. Laura Herz's group in Oxford Physics.

5.2 Methodology

DFT calculations were carried out using the plane wave code Vienna *Ab initio* Simulation Package (VASP) with the projector-augmented-wave (PAW) pseudopotential framework as detailed in Chapter 2.[151–154] A plane wave cut-off energy of 500 eV was employed for all calculations along with an electronic convergence criterion of 10^{-4} eV. Reciprocal space was sampled with a k-point spacing of $0.2/2\pi$ Å^{-1}. Both lattice parameters and ionic positions were fully relaxed until all atomic forces were below 0.01 eV Å^{-1}. Geometry relaxations were performed using the exchange–correlation meta-generalised gradient approximation (meta-GGA) functional regularized-restored strongly constrained and appropriately normed (r^{2}SCAN).

The r^{2}SCAN functional was selected based on its ability to accurately reproduce the lattice parameters and bandgap for the pure end-members, SnS and PbS. Functional testing included a range of GGA, meta-GGA, and hybrid functionals to demonstrate that r^{2}SCAN provided the best approach to maximise computational accuracy and efficiency. See Appendix B for additional details. Spin-orbit coupling was included for the bandgap calculations to account for relativistic contributions arising from the heavy Pb atoms.

Cluster expansion models were constructed using the Integrated Cluster Expansion Toolkit (ICET) as described in Section 2.5.[172] Two distinct cluster expansions were developed: one based on the cubic rock salt PbS crystal structure (space group 225) and another on the orthorhombic SnS crystal structure (space group 62). The rock salt cluster expansion was fitted using 414 structures relaxed using the DFT methodology described previously. These structures ranged in size up to a $3 \times 3 \times 3$ supercell. The DFT energies were then plotted with reference to the energies of the pure end-members as mixing en-

ergies. The mixing energies plotted for the Pb–Sn solid solution were calculated via the following formula:

$$\Delta E_{mix} = \frac{1}{N}\left(E_{total} - \sum_i n_i Ei\right) \tag{5.1}$$

where E_{total} is the DFT energy of a mixed structure in the solid solution, E_i is the energy of the pure end-members, n is the number of formula units of pure component in the mixed structure, and N is the total number of formula units. The orthorhombic cluster expansion was similarly fitted to 3,304 DFT-relaxed structures. In both cases, the cluster expansions were fitted by considering pair interactions up to a cut-off of 13.5 Å, triplet interactions up to 6.5 Å, and quadruplet interactions up to 6.0 Å. The validation RMSE of each cluster expansion was calculated to be 5.04 and 0.41 meV/atom for the cubic and orthorhombic structures, respectively.

Following the structural stability investigation, a band gap analysis was performed across the $Pb_xSn_{1-x}S$ solid solution, focusing on the region with Pb concentration less than $x = 0.5$. Several functionals were again tested on the r^{2}SCAN-relaxed structures to ensure that the results reported are not unique to the functional of choice. The trends observed are not substantially changed by the choice of functional. In order to accurately replicate the band gap values measured experimentally, electronic single points were performed with the GGA functional PBE and spin-orbit coupling which presented the same trends as band gaps calculated from r^{2}SCAN band structures. Band gap values were extracted from single points performed with a standardised k-mesh. Conduction band maxima and valence band minima were plotted with reference to the energies of core-like non-bonding states in Sn and Pb which were held at constant energies. Electronic structure analysis was performed using Pymatgen.[228]

5.3 Pb–Sn–S: Phase Stability

Investigating the crystalline lattice of the mixed-composition phase was the first step to understanding the $Pb_xSn_{1-x}S$ solid solution. The pure end-members of this compositional

space, SnS and PbS, adopt two distinct structures: the orthorhombic structure of space group 62 and the cubic rock salt structure of space group 225. Figure 5.2 illustrates these two lattices with the SnS structure on the left displaying its signature two-dimensional layers and the cubic PbS structure displaying the high symmetry of the three-dimensional rock salt lattice. Both crystal structures were used to investigate the energetic dependence of each lattice on the Pb–Sn orderings. A DFT model of this system was developed to accurately reproduce both the lattice parameters of the end-members and the band gaps (Table 5.1). The bar chart in Figure 5.2 shows the comparison between the experimental (striped) and DFT-calculated (solid) band gaps of 1.07 eV[302] and 1.12 eV for SnS and 0.4 eV[294–297] and 0.36 eV for PbS. In addition to the values displayed, the direct band gap of SnS was also calculated at 1.45 eV which again shows good agreement with experimental values that range between 1.2–1.4 eV.[298–301]

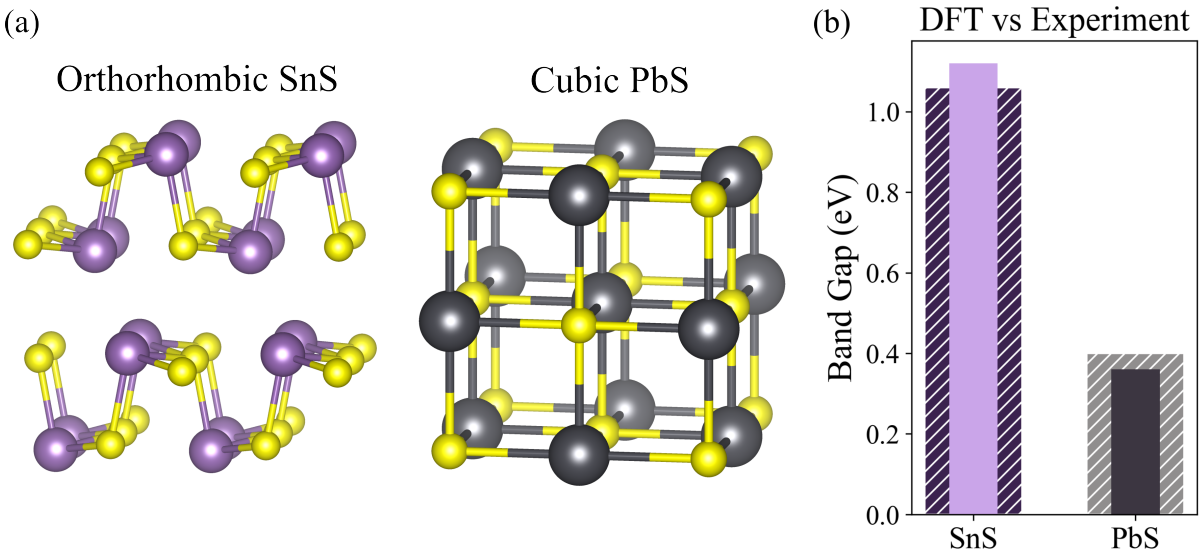


Figure 5.2: (a) The crystalline lattices of the two structures investigated in this work: the orthorhombic SnS crystal structure (space group 62) and the cubic rock salt PbS structure (space group 225) (Sn, lilac; Pb, grey; S, yellow). (b) The experimental (striped) and calculated (solid) band gaps for the SnS and PbS end-members show good agreement.

Table 5.1: Comparison of experimental[308,309] and calculated structural parameters and band gap of PbS and SnS.

Composition	Parameter	Experiment	Calculated	Difference (%)
PbS	$a = b = c$ (Å)	5.91	5.97	0.98
	Mean Angle (°)	90.0	90.0	0.0
SnS	a (Å)	4.34	4.53	4.42
	b (Å)	3.97	3.96	0.22
	c (Å)	11.14	11.33	0.52
	Mean Angle (°)	90.0	90.0	0.0

Using this DFT model, a total of 3,718 structures were generated between both crystal structures across the entire $Pb_xSn_{1-x}S$ composition range. The mixing energies calculated for this very large number of structures provide a metric representing the relative stability of the mixed phases. In Figure 5.3, the mixing energies of the cubic and orthorhombic structures are plotted in dark grey and lilac, respectively. The shaded region represents the structures with energies considered to be thermally accessible at room temperature which are calculated as those within 1 kT/atom or ∼25 meV/atom within the convex hull. It can be seen that the cubic structures are only lower in energy than the orthorhombic ones at very high Pb concentrations ($x > 0.9$). In addition, it is only at these high Pb concentrations that the mixing energies fall to within 1 kT of the convex hull. Most of the structures fall along a linear path of increasing energy with decreasing Pb concentration; however, there are a few structures which fall in energy below this inverse trend. There are no visible distortions in the relaxed structures, so no clear conclusions can be drawn regarding any structural cause for these deviations.

In contrast, the vast majority of the orthorhombic structures fall within 1 kT/atom of the hull with a shallow hull minimum located at a Pb concentration of $x = 0.25$, and there are dozens of structures sitting within a few meV/atom of the hull (Figure 5.3). These results suggest that the mixed compositions with Pb concentrations (x) less than 0.9 are likely to adopt the orthorhombic structure over the cubic structure. Furthermore, the fact that the mixing energies of many orthorhombic structures are within a few

meV/atom of the hull suggests that a wide range of compositions between $x = 0.0$ and $x = 0.5$ should be stable and therefore experimentally accessible. However, the number of thermally accessible configurations suggests there is a possibility that several competing phases could form within the thin film.

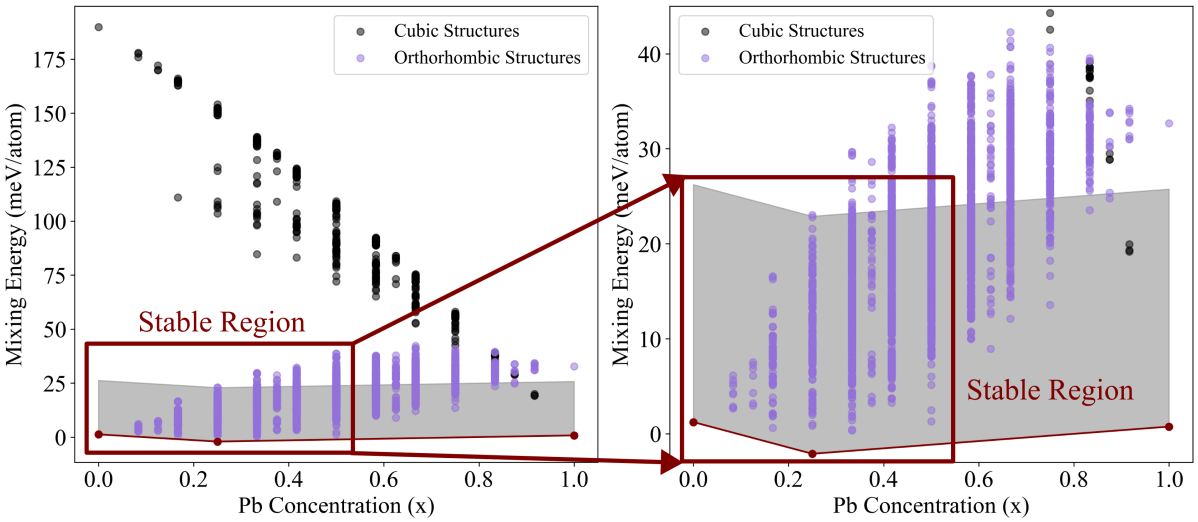


Figure 5.3: Mixing energies of $Pb_xSn_{1-x}S$ structures across the full solid solution range. Energies for structures with the cubic rock salt lattice are plotted in dark grey, and energies for structures with the orthorhombic lattice are plotted in lilac. The convex hull, plotted in maroon, shows a minimum at the $x = 0.25$ composition. The grey shaded region marks energies within 1 kT/atom of the convex hull demonstrating that the majority of orthorhombic structures fall within 1 kT/atom for compositions with less than $x = 0.5$.

Additionally, the large number of orthorhombic configurations with very similar mixing energies suggests that the relative ordering of Pb and Sn atoms on the lattice has very little effect on the overall structure energy. The lowest and highest energy structures in the orthorhombic lattice at $x = 0.25$ are depicted in Figure 5.4. It can be seen that the Pb atoms are alternating with Sn throughout the lattice in the lowest energy structure (Figure 5.4 (a)). In contrast, Pb atoms form a pattern of two-dimensional chains through the lattice in the highest energy configuration (Figure 5.4 (b)). This result illustrates that there is a slight preference for disordered Pb–Sn over clustered Pb chains within the orthorhombic lattice; however, both of these structures are within 1 kT/atom of each other which again shows that there is only a slight energetic bias due to different Pb–Sn

configurations.

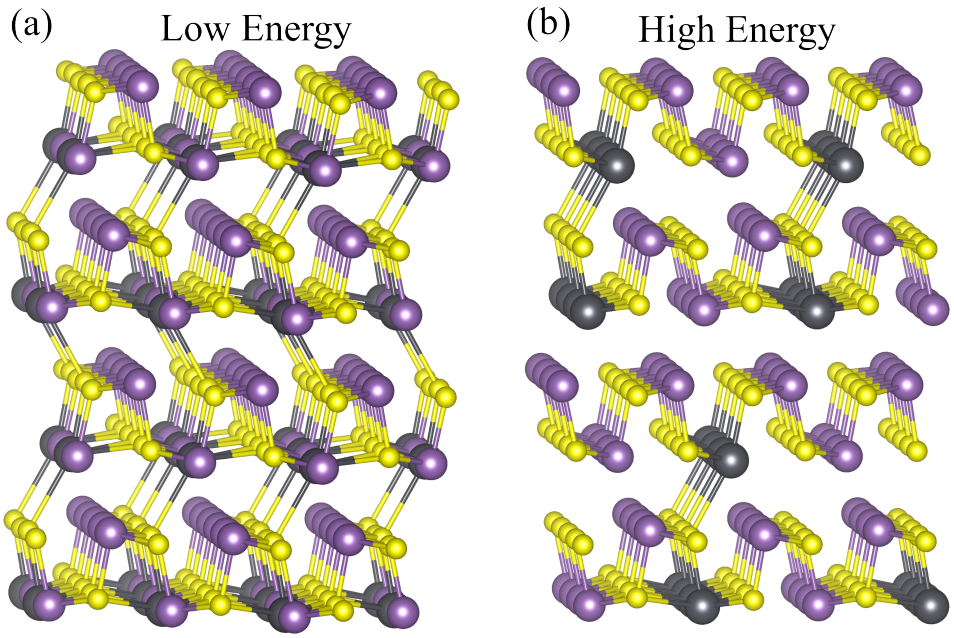


Figure 5.4: The (a) lowest and (b) highest energy structures in the $Pb_{0.25}Sn_{0.75}S$ composition in the orthorhombic crystal structure (Sn, lilac; Pb, grey; S, yellow). The low energy structure contains an alternating Pb–Sn configuration while the high energy structure contains 2D chains of clustered Pb atoms demonstrating a slight energetic preference for disordered Pb–Sn configurations; although, both structures are within 1 kT/atom.

These results are supported by the previous experimental investigations of Lebedev *et al.* (2001)[310] which suggests that SnS is only soluble in PbS up to 10% while PbS is soluble in SnS up to 50%. The mixing energies calculated here support these experimental findings. Furthermore, the number of accessible low energy phases also provides an explanation for why other studies[310] have reported slightly different structures or solubility regions, as slight variations in synthesis technique or thermal history can easily alter the thin films. In conclusion, the large number of low energy structures for $Pb_xSn_{1-x}S$, especially between $x = 0.0$ and $x = 0.5$ supports the further analysis of this solid solution as a potential low band gap thin film material.

5.4 Band Gap Analysis

5.4.1 Orthorhombic Unit Cell Results

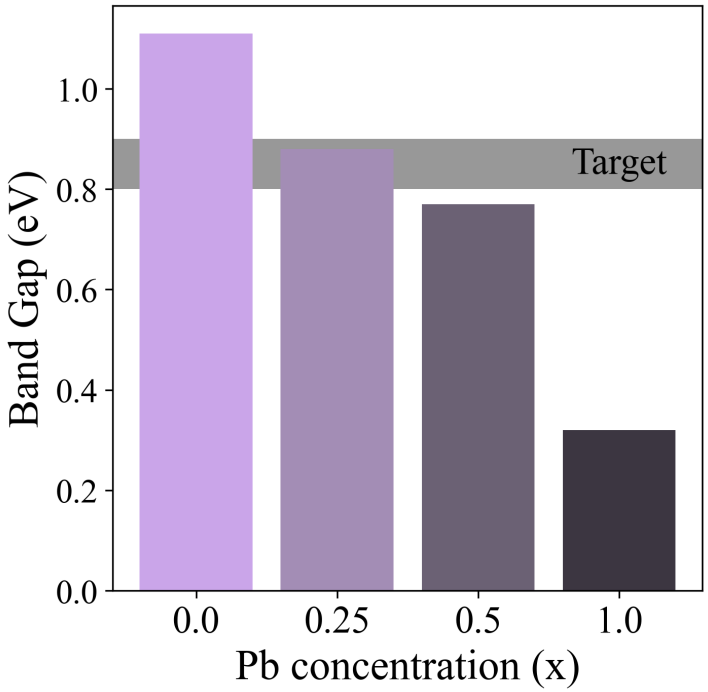


Figure 5.5: The band gaps calculated by randomly substituting Pb atoms into the orthorhombic structure to provide a prediction of the compositional dependence of the band gaps.

Based on the results of the mixing energy analysis, it is clear that there is a stability region between the $x = 0.0$ and $x = 0.5$ compositions. To develop a low band gap absorber, these materials must also have a suitable band gap in addition to being stable. An initial test was performed to calculate the band gap for the $Pb_{0.25}Sn_{0.75}S$ and $Pb_{0.5}Sn_{0.5}S$ compositions. Using the orthorhombic unit cell, Pb atoms were substituted randomly to represent a configurationally averaged structure which provides an estimate of the compositional dependence of the band gap. The calculated band gaps, which were derived from band structure calculations including spin-orbit coupling, are shown in Figure 5.5. Band gap values typically vary with composition,[40] and these results demonstrate this trend. Importantly, the target range for the low band gap absorber was between 0.8–0.9 eV which these calculations predict will be achieved for compositions around $x = 0.25$.

This is a promising result, as the compositions around $x = 0.25$ are also predicted to be the most stable. These findings provide the basis for further analysis of the electronic structure of this compositional space.

5.4.2 Lowest Energy Structure Results

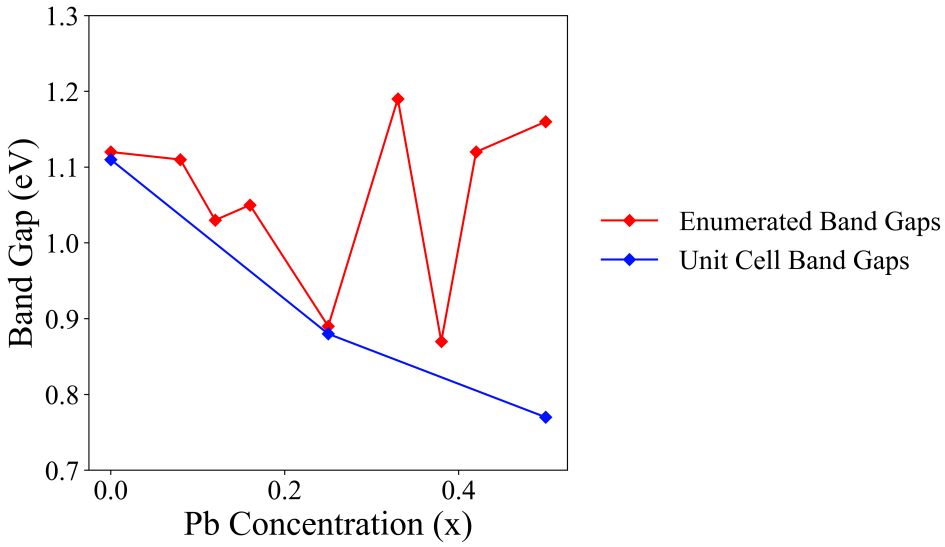


Figure 5.6: Comparison of band gaps calculated via band structure calculations performed with the functional r^{2}SCAN and spin-orbit coupling. The band gap trend observed in the randomly substituted unit cell structures (blue), shown previously in Figure 5.5, does not match the trend observed in the lowest energy enumerated structures (red) which shows a high degree of variability.

The initial band gap predictions were based on band structure calculations performed on the orthorhombic unit cell. However, the structures used for the mixing energy analysis were produced via an enumeration function and are therefore comprised of a wide range of cell sizes and shapes which are not integer multiples of the unit cell, making calculation of band structures difficult due to the altered symmetry. High symmetry paths were calculated using Pymatgen[228] for the lowest energy structures at a range of compositions. Because the orthorhombic structure was predicted to be stable for $x < 0.5$, these calculations focus on the band gaps within that region. The band gaps calculated for these structures via band structure calculations do not follow the trends predicted based on the unit cell band structure calculations, especially for Pb concentrations higher than

$x = 0.25$ (Figure 5.6). Notably, the band gaps calculated for the lowest energy structures demonstrate a high degree of variability which does not correlate with the composition.

5.4.3 $2 \times 2 \times 1$ Enumeration Results

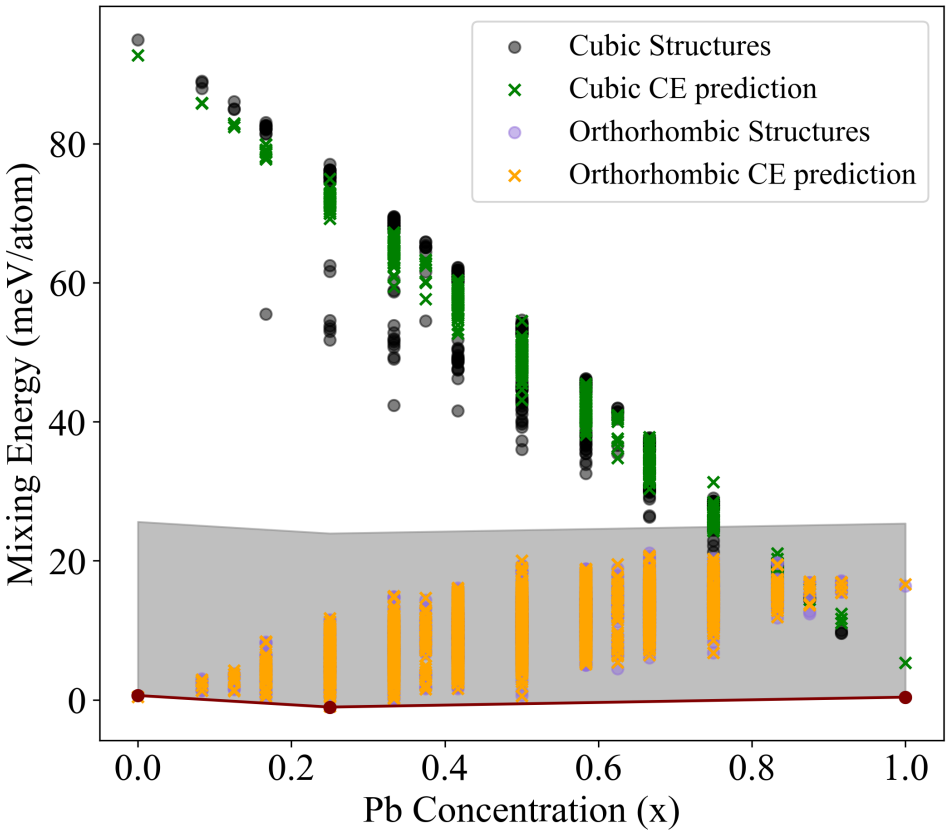


Figure 5.7: Comparison of the calculated DFT mixing energies and the predicted cluster expansion energies for the orthorhombic cluster expansion (reference in lilac and predicted in yellow) and the cubic cluster expansion (reference in grey and predicted in green), both of which appear to show good agreement.

To investigate the source of this discrepancy further, another structure enumeration was performed to create a set of $2 \times 2 \times 1$ supercells across the composition region. Fully orthorhombic cells were chosen for additional band gap calculations in order to eliminate any source of error introduced as a result of the low symmetry present in the initial enumerated set of structures. The trained cluster expansion predicted energies for the enumerate $2 \times 2 \times 1$ supercells, and the lowest energy structure at each composition was selected for further electronic structure analysis. At first, the orthorhombic cluster

expansion was thought to be suitably accurate because the training produced an RMSE of 0.41 meV/atom (Figure 5.7).

A series of single point calculations were performed on this set of r^{2}SCAN-relaxed $2 \times 2 \times 1$ supercells to investigate the electronic character of these structures as well as the variability of different functionals and k-spacings (Figure 5.8). r^{2}SCAN, HSE06, and PBE were the three functionals tested. The effect of spin-orbit coupling was also investigated with both the r^{2}SCAN and PBE functionals, and two k-spacings were used: $0.2/2\pi$ Å^{-1} (the same k-spacing as used for the geometry relaxations) and $0.1/2\pi$ Å^{-1}. In each case, the band gap was extracted from the density of states. The band gaps derived from band structures calculated on the initial cluster expansion lowest energy structures are also plotted for reference (red diamonds), labelled as the r^{2}SCAN + SOC band structure (B.S.) results.

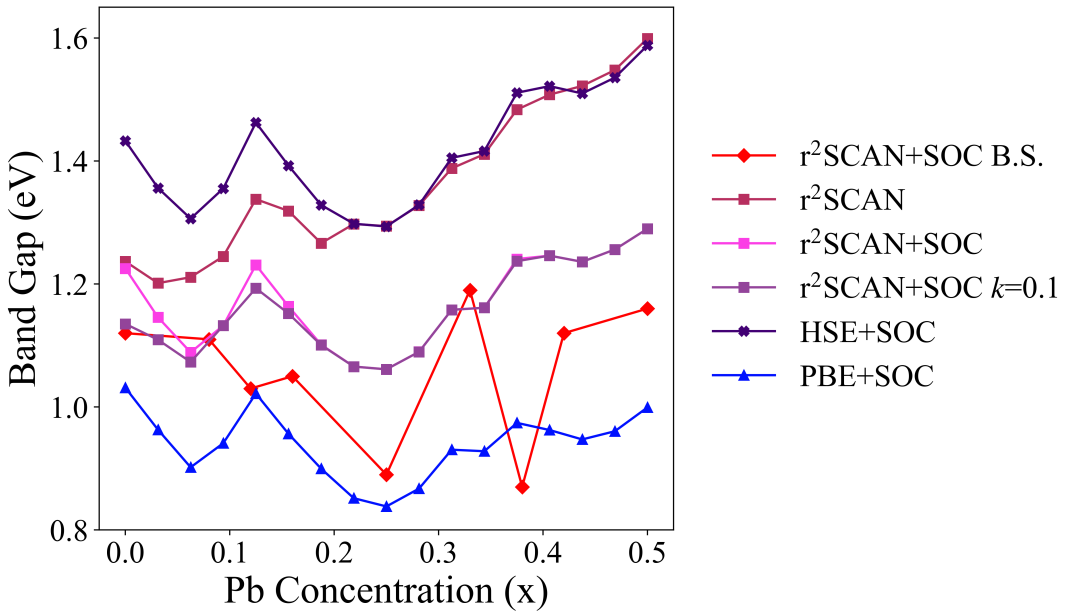


Figure 5.8: Band gap values calculated on $2 \times 2 \times 1$ supercells predicted to be the lowest energy configurations of $Pb_xSn_{1-x}S$ by the trained cluster expansion. All three functionals investigated display the same trends in band gap when spin-orbit coupling is included. PBE is selected for further analysis as the trends and magnitudes of the band gap values show the best agreement with experimental values. The trend observed for these $2 \times 2 \times 1$ supercell band gaps does not align with the band gaps calculated for the initial enumerated structures (red diamonds) which warrants further investigation.

It can be clearly seen that the band gap trend calculated for the lowest energy

$Pb_xSn_{1-x}S$ structures from the initial enumeration (red) does not demonstrate the same pattern as any of the $2 \times 2 \times 1$ supercell results. However, all band gaps derived from the $2 \times 2 \times 1$ supercells broadly demonstrate the same trend with a peak around $x = 0.15$ and a general increase in band gap for $x > 0.25$ which appears to be the location of roughly the minimum band gap. While the variation of band gap as a function of Pb concentration does not match the trends predicted in Figure 5.5, there are several features of note. First, the increase in k-spacing does not dramatically affect the predicted band gap. Spin-orbit coupling reduces the predicted values for the band gap, and the inclusion of spin-orbit coupling becomes increasingly important as the concentration of the heavier Pb element increases, although the trends stay broadly the same. The higher order hybrid functional, HSE06, and the GGA functional PBE both display the same trend in band gap as the r^{2}SCAN functional with spin-orbit coupling due to the probable cancellation of errors, as commonly reported in the literature.[311] PBE with spin-orbit coupling displays the best agreement in magnitude with the experimental values predicted for these compositions. Since these results deviate from the trends expected based on the initial band gap calculations, a further analysis was performed on the DFT energies of these enumerate supercell structures.

The DFT energies of this set of $2 \times 2 \times 1$ supercells are plotted as mixing energies on top of the initial mixing energy dataset in Figure 5.9. These energies plotted in blue clearly do not line up with those of the lowest energy structures. This result demonstrates that despite the very low RMSE of the trained cluster expansion, it is not nearly accurate enough to predict low energy structures. This may be the result of over-fitting of the model; however, attempts at adjusting the training cut-offs did not demonstrate any improvements.

The discrepancy in energy explains why the band gap trends for the $2 \times 2 \times 1$ supercells do not agree with the trends displayed by the band gaps calculated on the lowest energy structures. This result also suggests a high degree of band gap fluctionality within each composition depending on the relative ordering of Pb and Sn atoms on the lattice. The

complexity of this system requires further analysis to understand the true nature of the band gap variability with composition.

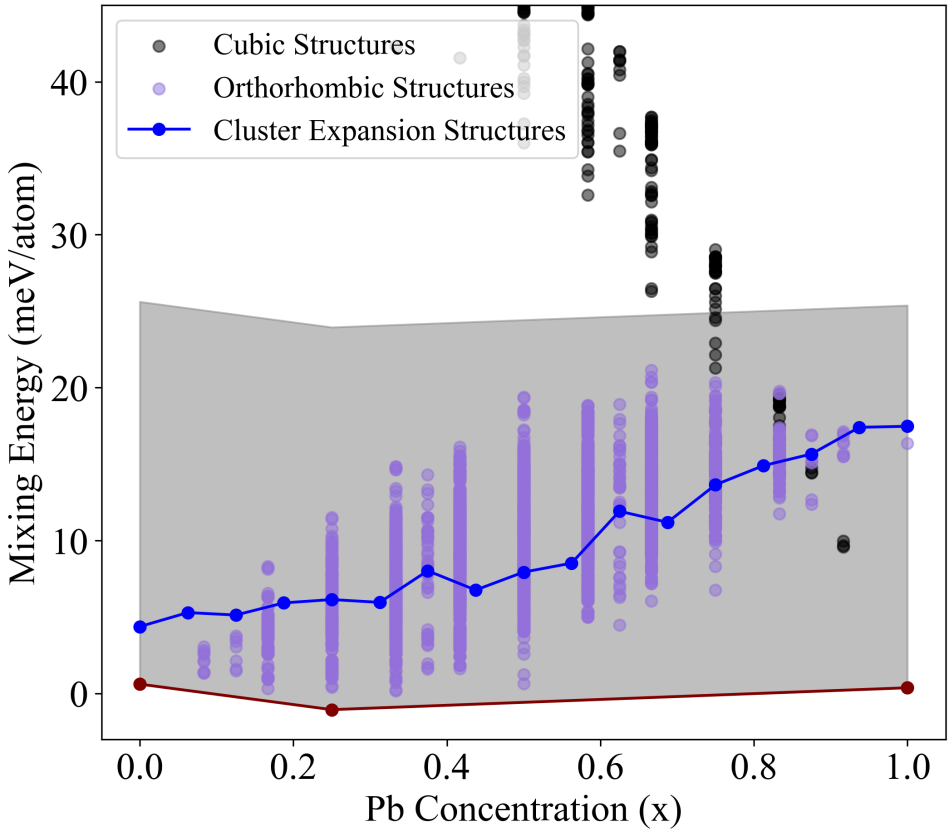


Figure 5.9: The mixing energies of the supercells predicted to be lowest in energy by the trained cluster expansion (blue) compared to the mixing energies of the orthorhombic structures initially studied (lilac).

5.4.4 Thermal Averaged and Experimental Results

As the cluster expansion was not suitable for accurately predicting low energy structures, the initial set of enumerated structures was instead used to predict the configurationally averaged electronic behaviour. Based on the functional testing, PBE with spin-orbit coupling was selected to perform the additional electronic relaxations (Figure 5.10). Each point represents a structure with the band gap plotted versus the Pb concentration. The colour mapping represents the relative energy of the structure with deep purple corresponding to lower energy structures and yellow to higher energy ones. There are

higher concentrations of yellow points towards higher concentrations of Pb due to these structures being generally higher in energy; however, there is no clear trend between the energies of the structures and their band gaps. This result supports the previous observation that small changes in structural configuration and mixing energy have large effects on the band gap.

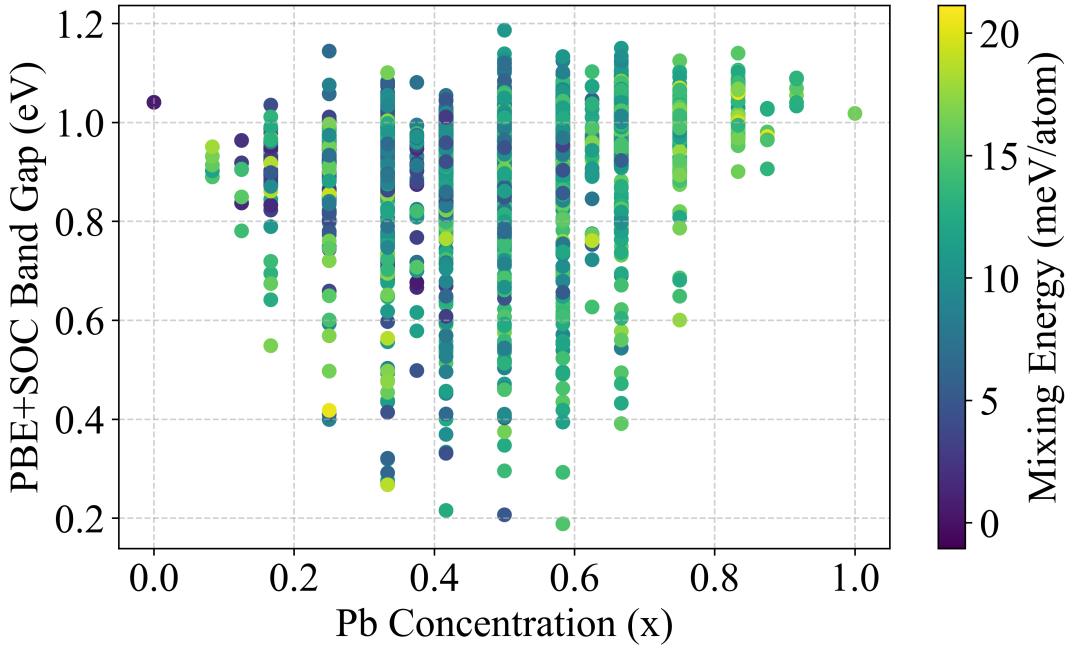


Figure 5.10: Band gaps calculated with PBE and spin-orbit coupling plotted as a function of Pb concentration (x) for $Pb_xSn_{1-x}S$. The energies of the structures are represented by the colour map with the lower energy structures in purple and the higher energy structures in yellow.

To provide a quantitative analysis of the trends, band gaps were calculated for the range of structures initially enumerated focussing on the $x < 0.5$ region, the compositional region predicted to be stable. First, an average of the band gaps at each concentration was plotted (Figure 5.11 (black)). This result shows a fairly smooth trend with an initial decrease between $x = 0.0$ and $x = 0.15$ that flattens out to a band gap of ~0.9 eV between $x = 0.15$ and $x = 0.5$. The error bars on these mean values are substantial, making it difficult to make a strong prediction of the band gap across these concentrations. The second result plotted takes a weighted average of the band gaps by using a Boltzmann coefficient to prioritise the band gaps of the lowest energy structures (Figure 5.10 (lilac)).

The Boltzmann coefficient is calculated at a temperature of 60°C, the temperature under which the PbI_2 and SnI_2 precursors are annealed. These results show higher variability with relatively low error bars. The average band gap results better fit the trend observed in the experimental band gaps measured by George Morgan which display a general decrease in band gap up to $x = 0.25$.

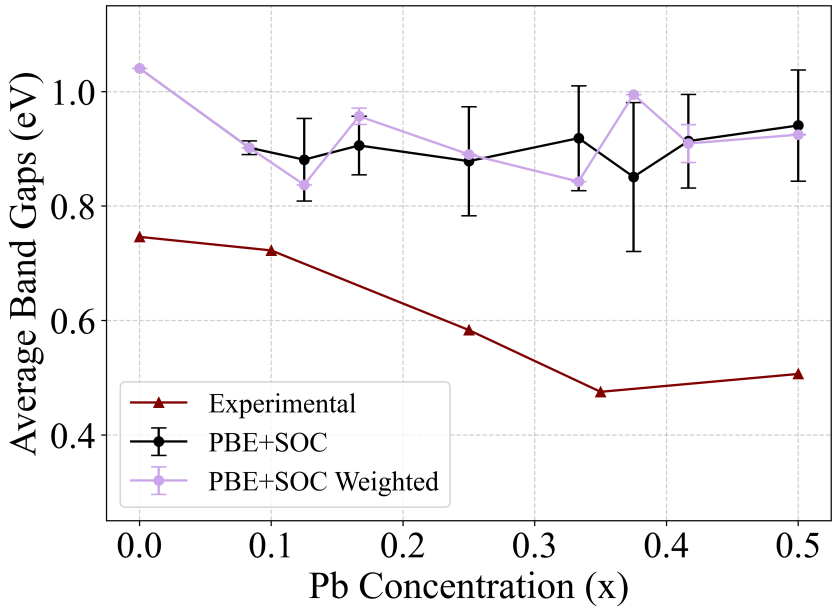


Figure 5.11: Representation of the average band gap for $Pb_xSn_{1-x}S$ ($x = 0.0$–0.5) (black), the Boltzmann weighted average band gap (lilac), and the experimental values measured by George Morgan (maroon).

XRD measurements (Figure 5.12) across the solid solution demonstrate the successful sulphurisation of the Pb–Sn–I precursor and the partial formation of a mixed Pb–Sn–S orthorhombic phase. However, additional peaks also point to the presence of impurities including a cubic phase and an unknown secondary phase, likely related to oxidised Sn^{4+}. Despite the presence of secondary phases in the experimental samples, there is clear evidence that the phases that are computationally predicted to be stable in the orthorhombic form are at least partially synthesised in the $x = 0.25, 0.35$, and 0.5 compositions. Our collaborators attribute the shifting of the experimental band gaps to energies lower than expected across the full compositional region to the presence of oxidised Sn^{4+} species as well as other competing phases such as $PbSnS_3$ that are introduced into the thin film via

air exposure which occurs throughout the sulphurisation process.

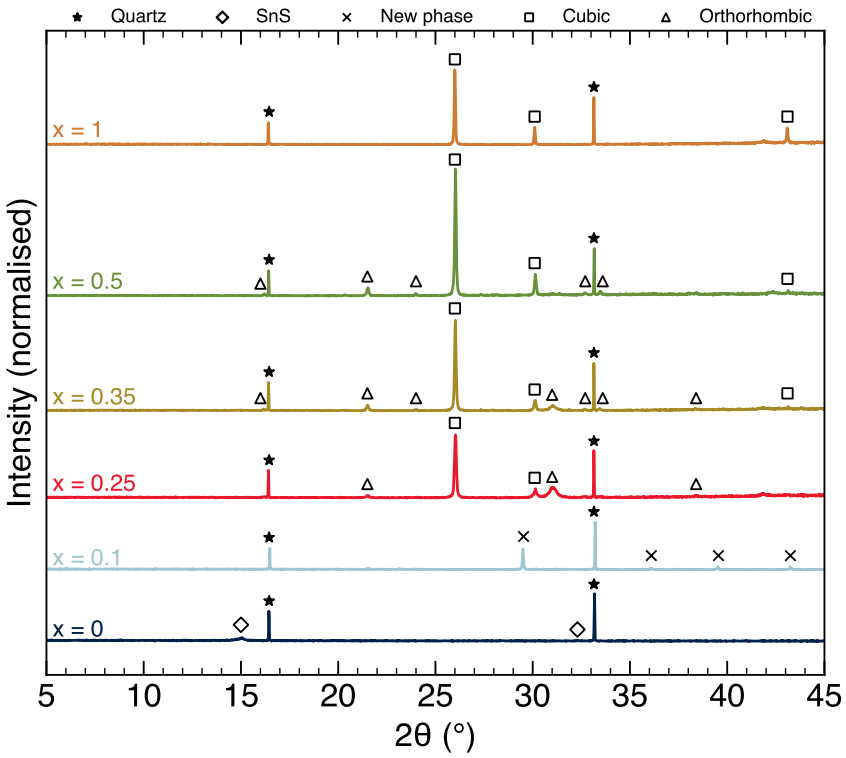


Figure 5.12: XRD measurements performed by George Morgan in Oxford Physics demonstrating the sulphurisation of annealed Pb–Sn–I. The presence of additional peaks such as those corresponding to the cubic PbS phase and those associated with an unknown phase indicate that the thin films currently being produced are not uniform; however, the presence of orthorhombic peaks across the intermediate compositions $x = 0.25, 0.35$, and 0.5 suggests that the compositions computationally predicted to be stable are at least partially being synthesised.

5.5 Electronic Structure Analysis

Further analysis of the electronic structures of $Pb_xSn_{1-x}S$ was performed to determine the cause of the high degree of band gap variability as a function of composition. First, the partial density of states (PDOS) decomposed into orbital contributions were plotted for each of the minimum energy structures at the compositions $x = 0.125, 0.25, 0.375$, and 0.5 as well as the pure end-members SnS and PbS (Figure 5.13).

In the pure SnS composition ($x = 0.0$), the valence band is primarily comprised of S p orbitals, and the conduction band is mostly comprised of Sn p orbitals, although in both

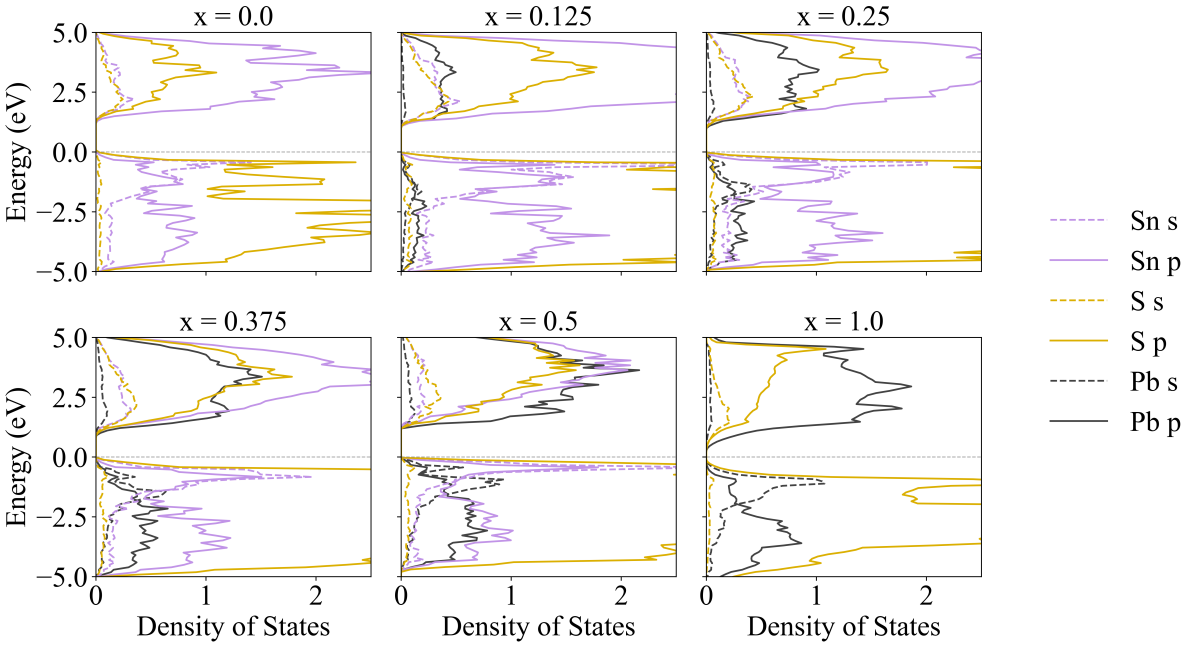


Figure 5.13: Partial density of states (PDOS) plotted for the DFT minimum energy structures at the compositions $x = 0.125, 0.25, 0.375$, and 0.5 of $Pb_xSn_{1-x}S$ as well as both of the pure end-members SnS and PbS.

bands there are notable contributions from both sets of p orbitals. As the concentration of Pb increases, contributions from Pb s and p orbitals in the valence band slowly increase; however, the valence band is dominated by the S p orbitals across all mixed-compositions. The contributions of Pb in the conduction band are much more notable with Pb p orbitals contributing equally to S p orbitals for concentrations of $x > 0.33$, and the Pb p orbitals contribute equally to the Sn p orbitals in the $x = 0.5$ composition. In pure PbS, Pb p and S p orbitals both contribute to both bands with S p orbitals dominating the valence band and Pb p orbitals dominating the conduction band. Compositions between $x = 0.5$ and $x = 1.0$ were not investigated due to their relative instability.

The valence band orbital composition can be further investigated by plotting isosurfaces of the localised charge density on a crystal structure at specific energies (Figure 5.14). As can be seen in the PDOS (Figure 5.13), the valence band in SnS is comprised of primarily Sn and S orbitals. With the increase of Pb concentration to $x = 0.5$, the charge density remains predominantly focussed around the Sn and S atoms, and in PbS, the charge density is fully localised around S.

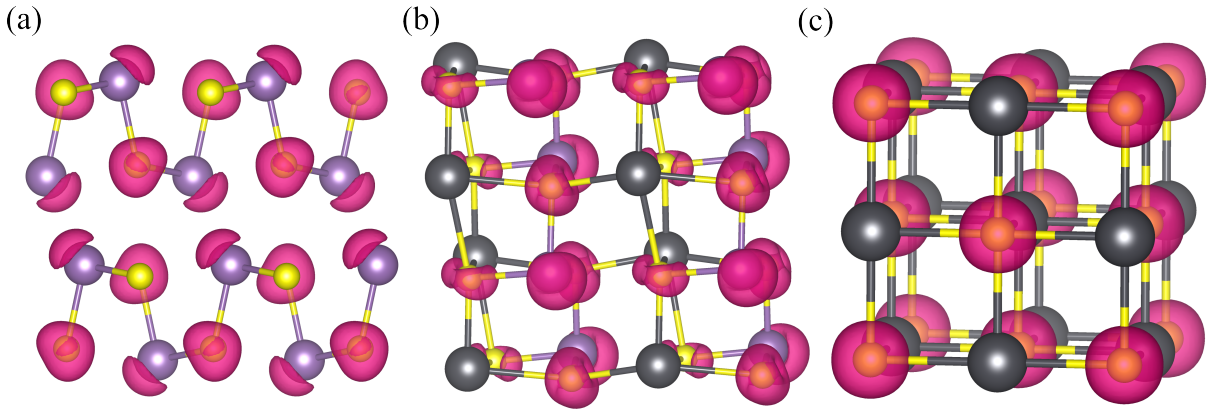


Figure 5.14: Charge density near the valence band edge (magenta) illustrated as an isosurface on the (a) SnS, (b) $Pb_{0.5}Sn_{0.5}S$, and (c) PbS compositions (Pb, grey; Sn, lilac; S, yellow).

Figure 5.15 (a)–(c) illustrates the change in lattice parameters and cell volume for Pb concentrations up to 0.5. These values were calculated from the $2 \times 2 \times 1$ enumerated supercells. First, it can be clearly seen that the a and b parameters fluctuate while the c parameter, defined as the direction separating the 2D sheets, steadily increases with Pb concentration. The overall effect on cell volume is a steady expansion. As the concentration of Pb increases and the cell generally expands, the overlap of Sn and S orbitals decreases. It is known that the valence band edge of SnS is comprised of Sn–S antibonding orbitals.[312] As a result, expansion of the lattice parameters reduces the antibonding overlap, lowering the energy of the valence band edge as is shown in Figure 5.15 (d).

In contrast, the Pb p orbitals increasingly contribute to the conduction band edge as the concentration of Pb increases. As a heavy element with relativistic effects, the impact of spin-orbit coupling becomes increasingly important, reducing the energy of the conduction band as the concentration of Pb increases. This effect competes with the lowering in energy of the valence band, resulting in a small and inconsistent decrease in band gap with increasing Pb concentration. As a result, the variability in band gap trends observed in this system may be attributed to the small fluctuation in the a, b cell parameters (Figure 5.15 (a)) which is ultimately related to the specific ordering of Pb and

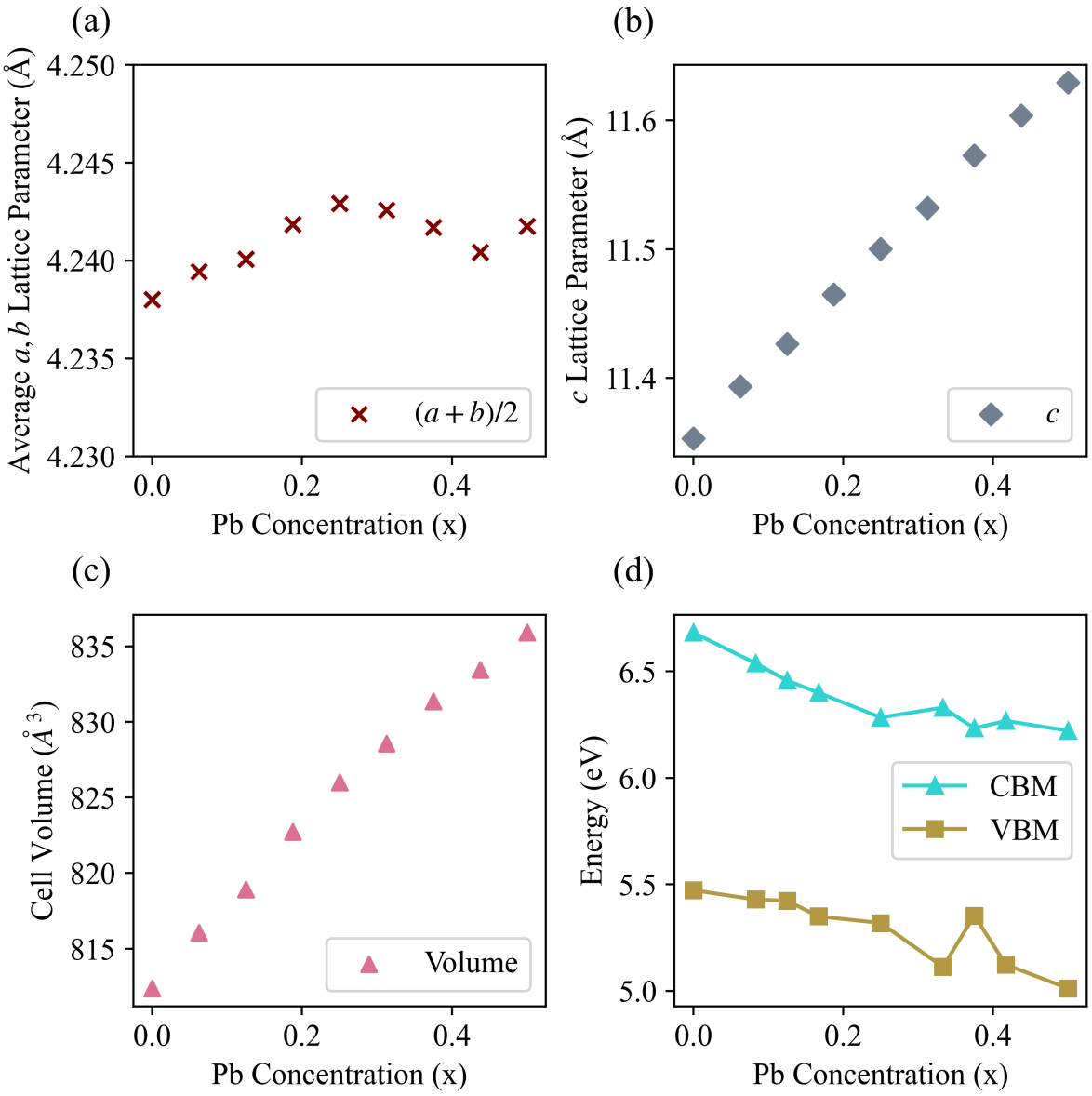


Figure 5.15: (a) The average change in a and b lattice parameters is very slight but non-linear with Pb concentration. (b) The c lattice parameter (the direction between 2D sheets) varies linearly with Pb concentration. (c) The cell volume varies linearly with c lattice parameter and Pb concentration. (d) The energies of the CBM and VBM vary non-linearly, following the trend in average a, b lattice parameter.

Sn atoms on the a, b lattice. As there is little energetic preference for specific orderings, many different configurations will likely exist in a thin film, resulting in the observed band gap fluctuations.

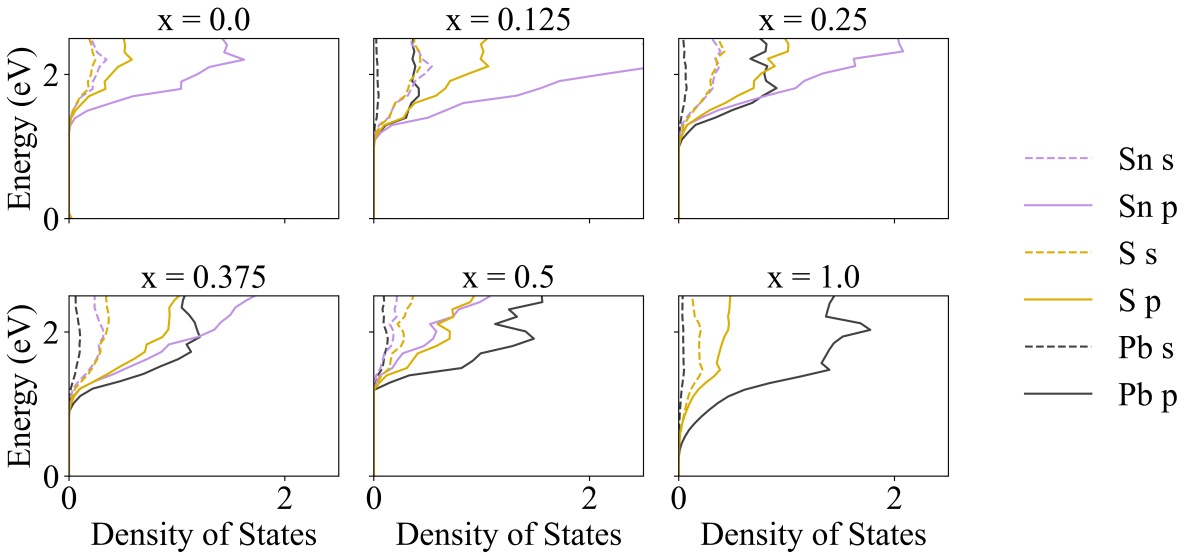


Figure 5.16: The same PDOS plots displayed in Figure 5.13 zoomed in to highlight the slope at the conduction band minima.

Finally, Figure 5.16 displays the same PDOS results as shown previously in Figure 5.13 with the plots zoomed onto the conduction band edges which are comprised of the Sn p orbitals and the Pb p orbitals. As the concentration of Pb increases, the Pb p orbitals become the predominant contribution to the conduction band edge. Additionally, the slope of the Pb p orbitals is sharper than that of the Sn p orbitals. As the Pb concentration increases and the effect of spin-orbit coupling becomes more pronounced, the conduction band edge is lowered in energy and the slope is solely determined by the slope of the Pb p states. The sharpening of the slope on the conduction band edge correlates to lower carrier mass and therefore higher mobilities. This result is in agreement with experimental THz spectroscopy measurements performed by Dr. Dmitry Maslennikov in Prof. Laura Herz's group in Oxford Physics (Figure 5.17).

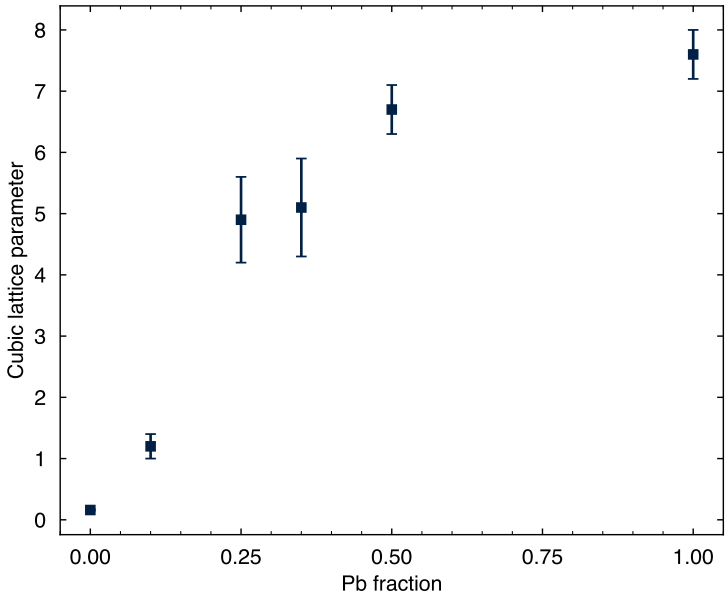


Figure 5.17: Carrier mobilities in $Pb_xSn_{1-x}S$ measured via THz spectroscopy by Dmitry Maslennikov in Prof. Laura Herz's group in Oxford Physics. The carrier mobilities increase with increasing Pb concentration.

5.6 Chapter Summary

In conclusion, we have identified a composition in the $Pb_xSn_{1-x}S$ family which has promising properties as a sub-1 eV sub-cell absorber in perovskite-tandem triple-junction solar cells. A paper on this subject is in preparation with George Morgan, Prof. Henry Snaith, Prof. Laura Herz, Dr. Harry Sansom, and others in Oxford Physics. Compositions around the $x = 0.25$ region are predicted to be stable and to have band gaps of $\sim$0.9 eV, ideal for a PV material targetting the near-IR region of the solar spectrum. Analysis of the mixing energies suggests that there is little preference for a particular Pb–Sn configuration on the orthorhombic lattice and that a range of meta-stable phases exist which could lead to difficulties in synthesising a single pure phase. Additionally, while the target band gap is achievable, different orderings of Pb and Sn cause substantial deviations in the calculated band gaps. The introduction of secondary phases and impurities during the synthesis leads to experimental band gaps which vary from those predicted by DFT, as the DFT-calculated band gaps are based on a purely orthorhombic SnS lattice which assumes that all Sn will exist in the 2+ oxidation state. The variability in band gap due

to different Pb–Sn orderings demonstrates the importance of thoroughly investigating a range of structures when performing similar computational investigations.

Further analysis of the electronic structure indicates that the change in band gap with $Pb_xSn_{1-x}S$ composition is largely a result of energy mismatch between the elements with Sn and Pb orbitals largely comprising the valence band and the conduction band, respectively. As a result, the band gap narrows as the higher energy Pb orbitals populate the conduction band. Overall, these results highlight the possibility of further increasing tandem device efficiencies and reducing the cost of solar electricity by utilising sub-1 eV band gap absorber materials such as $Pb_{0.25}Sn_{0.75}S$ to target the near-IR region of the solar spectrum.

Chapter 6

Towards Understanding 2D-3D Heterostructures for Improved Perovskite Stability

6.1 Introduction

The stability issues associated with perovskite thin films remain one of the primary limitations to the production of commercially viable perovskite devices. Exposure to heat, light, moisture, and oxygen have all been linked to the promotion of degradation in perovskite thin films.[313–317] Thermal degradation occurs quickly at temperatures above 85°C[318] which falls within the range of temperatures typically experienced during device operation.[245,246] Under exposure to any of these conditions, several degradation pathways become viable. Thermal degradation typically leads to formation of the precursor PbI_2 which can undergo further redox to form metallic Pb, while organic cations may evaporate in a gaseous molecular form such as methylamine.[314] The presence of water and light further act as catalysts for these degradation pathways with both water and superoxide, O_2^-, acting as bases which deprotonate the A-site cations leading to quick formation of the volatile neutral amine in addition to the volatile acid HI and precursor

PbI_2.[315] Therefore, methods for improving perovskite stability are critical for the design of commercial devices.

2D perovskites are a class of wide band gap semiconductor with large organic spacer cations separating layers of inorganic PbI_6 octahedra (detailed in Section 6.3).[319] There exist two distinct forms of 2D perovskites: the Ruddlesden–Popper (RP) phase and the Dion–Jacobson (DJ) phase, both of which generally display higher stabilities than the 3D perovskites. This observation is primarily attributed to the inclusion of organic spacer cations with long alkyl chains which form hydrophobic layers within the perovskite that repel water, protecting the bulk thin film.[320]

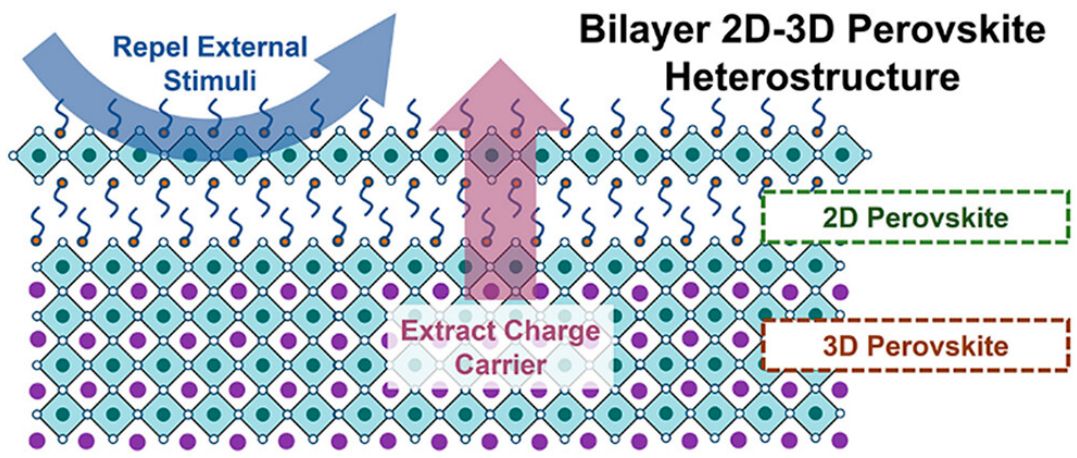


Figure 6.1: Illustration of a 2D-3D heterostructure depicting how the more stable 2D perovskite protects the 3D perovskite layer by repelling external stimuli such as water and prevents halides from migrating into the charge transport layers while maintaining efficient charge carrier extraction. Figure reproduced from Chen *et al.*, *ACS Nano.*, 2023, **18**, 67–88.[321] Copyright © 2023 American Chemical Society.

Due to the higher stabilities displayed by the 2D perovskites, one method for improving 3D perovskite stability is the introduction of a 2D perovskite capping layer on the surface of the thin film in between the 3D perovskite and the charge transport layer (Figure 6.1). The integration of 2D perovskite capping layers onto 3D perovskite thin films results in the formation of a 2D-3D heterostructure, also referred to as a heterojunction. Experimental studies of device lifetimes and performances demonstrate that the stability of these 2D-3D heterostructures is greater than that of the isolated 3D perovskite, for

both RP and DJ 2D phases.[322–329]

This improved stability is due to two features. First, the application of the 2D perovskite onto the thin film surface acts as a passivating layer. By reducing surface defects that act as charge recombination centres, charge transport between the perovskite and neighbouring interface is improved.[98,321,330] Second, a leading cause of degradation is the accumulation of halide ions at surfaces and grain boundaries.[82,83,109,204] While the effects of hysteresis cannot be entirely removed, the incorporation of large spacer molecules prevents halide ion migration to the interface and into the charge transport layer.[98,321,331,332] These effects not only improve the device lifetime but have also been shown to increase the power conversion efficiency (PCE) for lead halide perovskite devices.[103–105,333,334]

Despite the improved stability displayed by the 2D-3D heterostructures compared to pure 3D thin films, thermal stress and ageing under light still result in degradation which is thought to occur via a secondary phase. Experimental investigations suggest that organic spacer cations migrate into the 3D bulk when exposed to heat and light.[335–338] The exact nature of the secondary phase formed as a result of these migrations has yet to be elucidated;[336] however, ion migration studies on both RP and DJ phases observe mixing of spacer cations into the bulk perovskite.[269,339,340]

Our collaborator, Dr. Krishanu Dey in Prof. Henry Snaith's group in Oxford Physics, observed that when annealing the RP and DJ 2D perovskites, BA_2PbI_4 ($BA{=}CH_3(CH_2)_3NH_3^+$) and $BDAPbI_4$ ($BDA{=}NH_3(CH_2)_4NH_3^{2+}$), onto a 3D $CsPbI_2Br$ thin film, the DJ phase demonstrated higher stability. In contrast, the RP heterostructure formed an unknown secondary phase as identified by the presence of an additional peak in the PL spectra while undergoing annealing. As 2D-3D perovskite heterostructures comprise a relatively new class of material, little is understood about the fundamental properties underlying the 2D perovskite, and the lack of standardised testing and ageing protocols makes it difficult to compare reported studies investigating different heterostructures.[336] With the goal of developing a deeper understanding of 2D perovskite behaviour and stability in 2D-3D heterostructures, this work provides computational insights into

the relative stabilities of the RP and DJ phases as well as examining potential sources of the unassigned peaks observed in the PL spectra.

6.2 Methodology

VASP[151,152,154,156] was employed for all DFT calculations which were performed using the VASP-supplied PAW pseudopotentials[155] and the PBE exchange–correlation functional as detailed in Chapter 2.[149] Structural relaxations were performed using a reciprocal k-spacing of $0.2/2\pi$ Å^{-1}. The convergence criterial for the total energy and atomic forces were 10^{-5} eV and 10^{-2} eV Å^{-1}, respectively. Long-range van der Waals dispersion interactions were accounted for by including Grimme's DFT-D3 correction[274] which is required to accurately represent interaction between the organic spacer molecules and the inorganic perovskite layers. Additional electronic structure calculations were performed with a range of functionals including PBE with spin-orbit coupling and r^{2}SCAN.

Formation energies are calculated as the DFT energy of the composition with respect to the DFT energy of the precursors: CsI, PbI_2, $PbBr_2$, BAI ($CH_3(CH_2)_3NH_3I$), and $BDAI_2$ ($NH_3(CH_2)_4NH_3I_2$). The formation energies are plotted in units of meV/site in order to accurately compare the RP and DJ phases which contain different numbers of atoms. Using this method, each organic spacer cation is counted as one site along with each of the inorganic atoms in the composition. In the surface calculations, dipole corrections were additionally included to ensure convergence of the planar-averaged electrostatic potential.

6.3 2D Perovskite Structures

The reduced dimensionality characteristic of the 2D perovskite is due to the inclusion of large organic spacer cations. The perovskites investigated in this chapter are pictured in Figure 6.2. 2D perovskites are characterised by the number of inorganic layers stacked

in between the spacer molecules. The pure 2D phase ($n = 1$) has only a single layer of inorganic PbI_6 octahedra. The quasi-2D ($n \geq 2$) perovskite is formed by combining two or more layers of PbI_6 octahedra, separated by large organic cations. Within the inorganic layer Cs, MA, or FA take the traditional place of the A-site cation. In this work, Cs is the A-site cation in all structures.

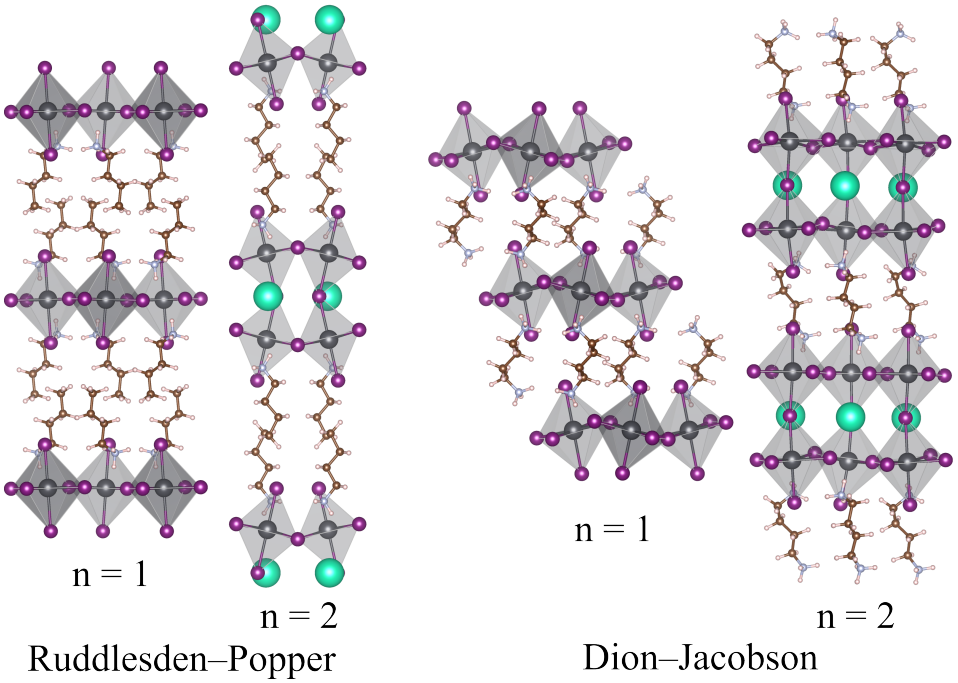


Figure 6.2: Ruddlesden–Popper (RP) and Dion–Jacobson (DJ) 2D perovskite structures in the $n = 1$ and $n = 2$ forms. The compositions of the RP $n = 1$ and $n = 2$ phases are BA_2PbI_4 and $BA_2CsPb_2I_7$, respectively, where BA=$CH_3(CH_2)_3NH_3^+$, and the compositions of the DJ $n = 1$ and $n = 2$ phases are $BDAPbI_4$ and $BDACsPb_2I_7$, where BDA=$NH_3(CH_2)_4NH_3^{2+}$ (Cs, aqua; Pb, grey; I, purple; C, brown; N, light blue; H, pale pink).

In this work, the two spacer cations investigated are butyl ammonium, $CH_3(CH_2)_3NH_3^+$ or BA^+, and 1,4-butyldiammonium, $NH_3(CH_2)_4NH_3^{2+}$ or BDA^{2+}. Different forms of the 2D structure can be achieved depending on the charge of the spacer cation. The Ruddlesden–Popper (RP) perovskites, with the general formula $A'_2A_{n-1}B_2X_{3n+1}$, are formed by including two 1+ spacer cations, A′, to balance the charges of the inorganic PbI_6 layers, producing chemical formulas of BA_2PbI_4 and $BA_2CsPb_2I_7$ for the $n = 1$ and $n = 2$ forms, respectively. In the $n = 1$ structure, the A' site is filled by the charged

ammonium heads of the spacer cations. In contrast to the 3D perovskites, the inorganic layers are not stacked directly on top of each other but rather are offset due to steric hindrance between the spacer cations that bind to each of the adjacent inorganic layers. The organic layers are held together by van der Waals interactions. In the $n = 2$ structure, each inorganic layer is comprised of two PbI_6 octahedra in width with Cs cations in the traditional A site. The DFT model of this $n = 1$ RP perovskite accurately replicates the lattice parameters to within 3% of the experimental values (Table 6.1 (a)).[341] The errors in mean angle and average Pb–I bonds and angles are negligible, and the band gap value is reproduced to within 0.1 eV demonstrating strong agreement.

Table 6.1: Comparison of DFT calculated parameters with experimental values[341,342] for (a) the $n = 1$ Ruddlesden–Popper perovskite, $(CH_3(CH_2)_3NH_3)_2PbI_4$ and (b) the $n = 1$ Dion–Jacobson perovskite, $NH_3(CH_2)_4NH_3PbI_4$.

(a)

$n = 1$ Ruddlesden–Popper			
Parameter	**Experiment**	**Calculated**	**Difference (%)**
a (Å)	8.88	8.70	-2.00
b (Å)	8.69	8.51	-2.08
c (Å)	27.62	28.23	2.23
Mean Angle (°)	90.0	90.0	0.0
Band gap (eV)	2.30	2.36	7.39
Pb–I Bond (Å)	3.19	3.18	-0.31
Pb–I–Pb Mean Angle (°)	155.02	149.13	-3.80

(b)

$n = 1$ Dion–Jacobson			
Parameter	**Experiment**	**Calculated**	**Difference (%)**
a (Å)	8.48	8.41	-0.83
b (Å)	8.79	8.78	-0.15
c (Å)	11.06	11.06	0.00
α (∘)	76.65	76.85	0.27
β (∘)	70.20	70.39	0.27
γ (∘)	89.24	89.21	-0.03
Band gap (eV)	2.36	2.12	-10.17
Pb–I Bond (Å)	3.18	3.20	0.63
Pb–I–Pb Mean Angle (°)	146.39	143.45	-2.01

The Dion–Jacobson (DJ) perovskites with the general formula $A'A_{n-1}BX_{3n+1}$ are

formed by spacer cations with a 2+ charge, in this case BDA^{2+}. The formulas for the $n = 1$ and $n = 2$ DJ 2D perovskites are $BDAPbI_4$ and $BDACsPb_2I_7$, respectively. In the $n = 1$ DJ perovskite, each spacer cation binds to both adjacent inorganic layers with each of the two ammonium head groups. This double-binding interaction keeps the PbI_6 octahedra stacked directly on top of each other and has the secondary effect of reducing the lattice parameter across the organic layer. A similar effect is observed in the $n = 2$ DJ perovskite with direct stacking observed between each adjacent inorganic layer and a smaller separation between inorganic layers compared to the RP phase. Again, Cs takes the A-site position within the inorganic layer.

The DFT model of the $n = 1$ DJ perovskite replicates the lattice parameters, cell angles, and average Pb–I bond lengths to within 1% of the experimentally measured values.[342] The band gap is measured to within 0.25 eV of the experimental value, a 10% deviation. It can be seen that the DJ structure has a higher degree of octahedral tilting than the RP structure which is due to stronger hydrogen bonding between the charged diammonium heads and the I atoms in the inorganic layer than the hydrogen bonds formed by the RP ammonium head.

6.4 Phase Stability

First, the relative stabilities of the RP and DJ compositions were investigated. The heterostructure initially formed during synthesis is comprised of a 2D perovskite, either the $n = 1$ Ruddlesden–Popper perovskite, BA_2PbI_4, or the $n = 1$ Dion–Jacobson perovskite, $BDAPbI_4$, stacked on a 3D perovskite, $CsPbI_2Br$. $CsPbI_2Br$ is used experimentally instead of $CsPbI_3$ due to its improved stability which is required for the synthesis of these heterostructures. Previous heterostructure investigations have demonstrated that the migration of cations under annealing can lead to the transformation of an $n = 1$ structure into an $n = 2$ structure.[338] In addition, while halide migration is reduced between interfaces,[321] halide mixing has been shown to occur between stacked compositions,[337]

in this case that would mean the Br ions in the 3D perovskite may migrate into the 2D perovskite. As the exact concentration of Br migration that occurs is unknown, a range of Br concentrations are investigated: 0%, 6%, 12%, and 25%. Comparing the relative formation energies provides insights into the phases most likely to be formed under annealing.

Figure 6.3 shows the formation energies for the range of pure and mixed-halide 2D compositions investigated. From this data, three key trends are found. First, the formation energies of the $n = 1$ structures (navy) are all substantially lower than the formation energies of the $n = 2$ perovskites (aqua), indicating that the $n = 1$ perovskites display a higher degree of stability and are more likely to be formed during synthesis, as observed experimentally. It can be extrapolated that as the number of inorganic layers increases towards infinity, the formation energy approaches that of the 3D phase which is known to be less stable than the 2D phase. Second, there is less energetic loss transitioning from the RP $n = 1$ to $n = 2$ phases than for the equivalent transition in the DJ phase, suggesting that the DJ compositions are more resistant to formation of $n = 2$ phases.

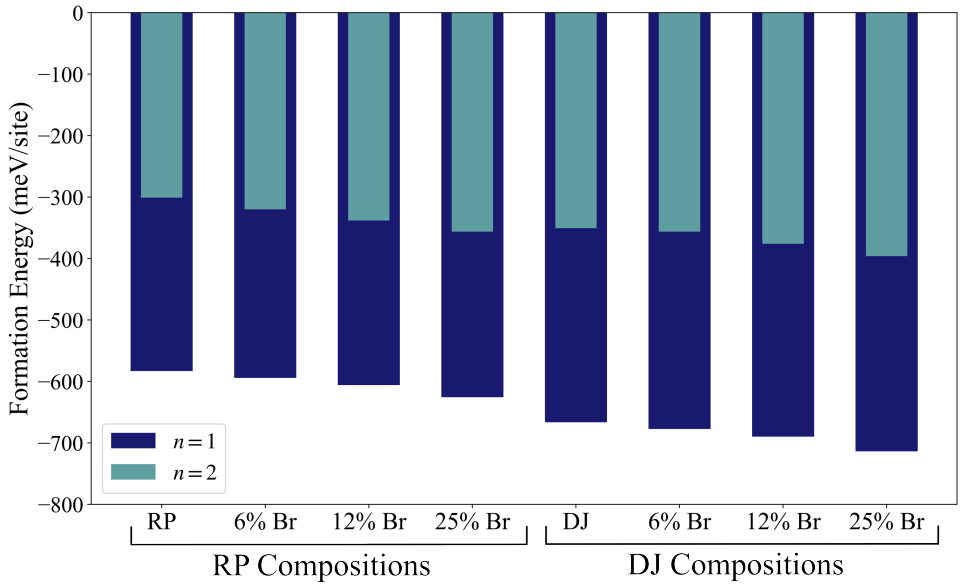


Figure 6.3: Formation energies for the $n = 1$ (navy) and $n = 2$ (aqua) RP and DJ compositions with 0%, 6%, 12%, and 25% Br doping. The compositions of the RP $n = 1$ and $n = 2$ phases are BA_2PbI_4 and $BA_2CsPb_2I_7$, respectively, where BA=$CH_3(CH_2)_3NH_3^+$, and the compositions of the DJ $n = 1$ and $n = 2$ phases are $BDAPbI_4$ and $BDACsPb_2I_7$, where BDA=$NH_3(CH_2)_4NH_3^{2+}$.

Third, comparing the RP and DJ formation energies shows that within the $n = 1$ phase, all DJ compositions are more stable than RP. Within the $n = 2$ phases, this stability difference is reduced with the DJ phase again displaying slightly lower formation energies than the respective RP composition. The lower formation energies for the DJ phase compared to the RP phase agree with experimental results[331] which suggest the DJ heterostructures are more stable. This effect is typically attributed to the inorganic layers being held together by stronger electrostatic forces in the DJ phase in contrast to weaker van der Waals interactions in the RP phase.[343] The shorter interlayer separation in the DJ phase has been shown to have the additional effect of improved dielectric screening and reduced quantum confinement of charge carriers.[328,329,343]

Br doping, which was investigated at 0%, 6%, 12%, and 25%, with Br sites being preferentially chosen in the equatorial positions which have previously been demonstrated to be the more favourable location for inclusion of halides with radii smaller than I.[344] Across both the RP and DJ compositions, the formation energies decrease steadily with increasing Br composition; this result again agrees with experimental observations that, similar to the 3D perovskites,[44,345] mixed-halide perovskite compositions have higher stabilities than the pure halide compositions.[334] The energetic gain from introducing Br is small in both $n = 1$ and $n = 2$ perovskites but is notably more prominent in the $n = 1$ phase. This suggests that the interactions between the organic spacer cation and the Br ion are the driving force behind the increased stability. The larger size of I compared to Br reduces the strength of the ammonium–I bond with respect to ammonium–Br. In the $n = 1$ phase, all Br atoms are doped in positions coordinated to the spacer cations while in the n=2 phase, some Br atoms are randomly distributed into the middle of the inorganic layer where they only interact with Pb and Cs. The increased stability with increasing Br concentration in the $n = 2$ phase, therefore, indicates that the increased stability occurs regardless of site-specific selectivity. The lowering of the formation energy for both RP and DJ compositions as a function of Br concentration is similar as the interactions between the BA and BDA ammonium spacer cations and Br are also similar.

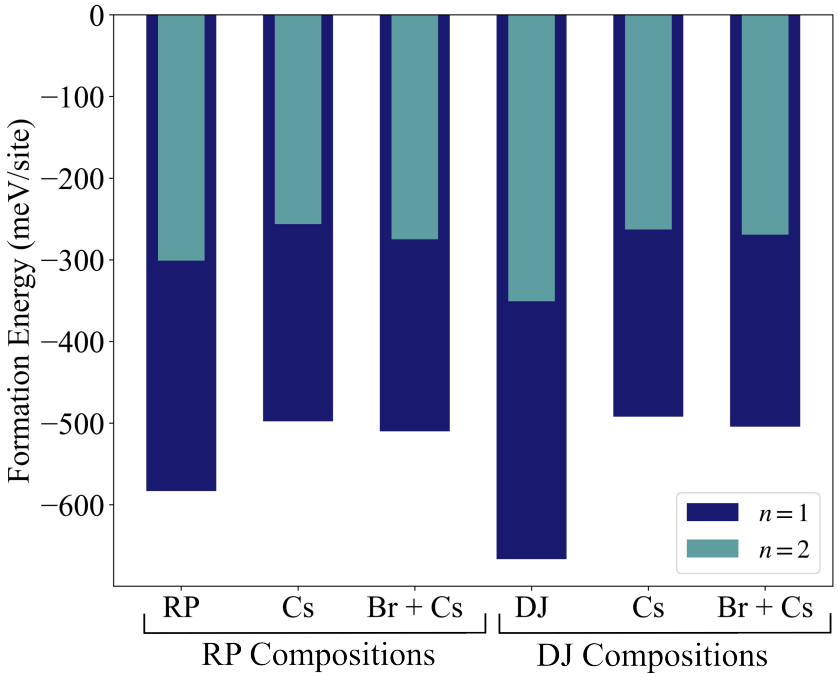


Figure 6.4: Formation energies for the $n = 1$ (navy) and $n = 2$ (aqua) RP and DJ compositions including the pristine 2D phases (RP, DJ), Cs doped into the organic layers to form a secondary phase (Cs), and Cs doped into the organic layers along with addition of 6% Br (Br + Cs). The compositions of the RP $n = 1$ and $n = 2$ phases are BA_2PbI_4 and $BA_2CsPb_2I_7$, respectively, where BA=$CH_3(CH_2)_3NH_3^+$, and the compositions of the DJ $n = 1$ and $n = 2$ phases are $BDAPbI_4$ and $BDACsPb_2I_7$, where BDA=$NH_3(CH_2)_4NH_3^{2+}$. Cs is doped into the organic layer in a concentration of 12.5% in the RP structures and 25% in the DJ structures.

Our experimental collaborators in Oxford Physics observed that annealing the 2D perovskites onto the 3D $CsPbI_2Br$ thin film resulted in the observation of an unknown peak in the PL spectrum around 560 nm (2.21 eV). It was hypothesised that this peak could be the result of Cs migration into the organic layers of the 2D perovskite, resulting in a new phase referred to here as a secondary phase. In order to achieve charge balanced structures, this doping occurred as one Cs^+ substituting a BA cation in the RP structures ($BA_{1.75}Cs_{0.25}PbI_4$ and $BA_{1.75}Cs_{1.25}Pb_2I_7$ for $n = 1$ and $n = 2$, respectively) and two Cs^+ in place of a BDA cation in the DJ structures ($BDA_{0.75}Cs_{0.25}PbI_4$ and $BDA_{0.75}Cs_{1.25}Pb_2I_7$ for $n = 1$ and $n = 2$, respectively) (Figure 6.4). Analysis of the formation energies shows that in both structures, doping Cs into the inorganic layer is notably less favourable, although the formation energies are still low enough to be thermodynamically accessible.

Despite the DJ compositions demonstrating lower formation energies in the pure and Br-doped structures, the Cs-doped structures are similar in energy between the RP and DJ compositions. This suggests that the energy penalty of Cs migrating into the organic layer is higher in the DJ phase than in the RP phase.

The secondary phases with Cs are slightly more stable in the presence of Br; however, these formation energies remain higher than that of the pure phases. This suggests that if Br ions are present in the 3D perovskite of a 2D-3D heterostructure, they may migrate into the 2D layer following formation of a Cs-doped secondary phase. This effect would promote further exchange of ions leading to destabilisation of the interface. Similar trends are found in the $n = 1$ and $n = 2$ forms, although the doped $n = 2$ structures are much more similar in energy to the pure compositions than is observed in the $n = 1$ structures.

Overall, the most important feature is likely the energy difference between the secondary phases and the pure phase. While both RP and DJ Cs-doped phases are similar in energy, the pure DJ phase is more stable than the pure RP phase; therefore, the proposed migration of Cs^+ into the organic layer of the DJ causes a more substantial gain in energy making formation of the quasi-2D DJ phases less likely, consistent with experimental observations. This feature could be a reason why the DJ compositions display higher degrees of degradation resistance compared to the RP phases.

6.5 Electronic Structure

The PL spectra measured during annealing demonstrate a gradual shift in the 2D and 3D perovskite peaks which can be attributed to the change in composition over time. Additionally, the introduction of an additional peak in the RP heterostructure under annealing remains unidentified. To investigate the cause of the PL peak shifts and find the phase responsible for the introduction of the secondary peak observed during annealing of the RP phase, the band gaps and partial density of states were calculated. The band gaps for the RP $n = 1$ and $n = 2$ (BA_2PbI_4, $BA_2CsPb_2I_7$) and DJ $n = 1$ and $n = 2$

($BDAPbI_4$, $BDACsPb_2I_7$) phases are plotted in Figure 6.5. In addition to the pure phases, compositions with doping of 25% Br, doping of Cs into the organic layers, and doping of both 6% Br and Cs are considered. As can be seen from the results, the band gaps for all $n = 1$ phases are wider than those of the $n = 2$ structures. It is known that as the inorganic composition of the 2D perovskite grows with increasing n, the band gap shrinks approaching the value of the 3D perovskite band gap (equivalent to $n = \infty$).[346]

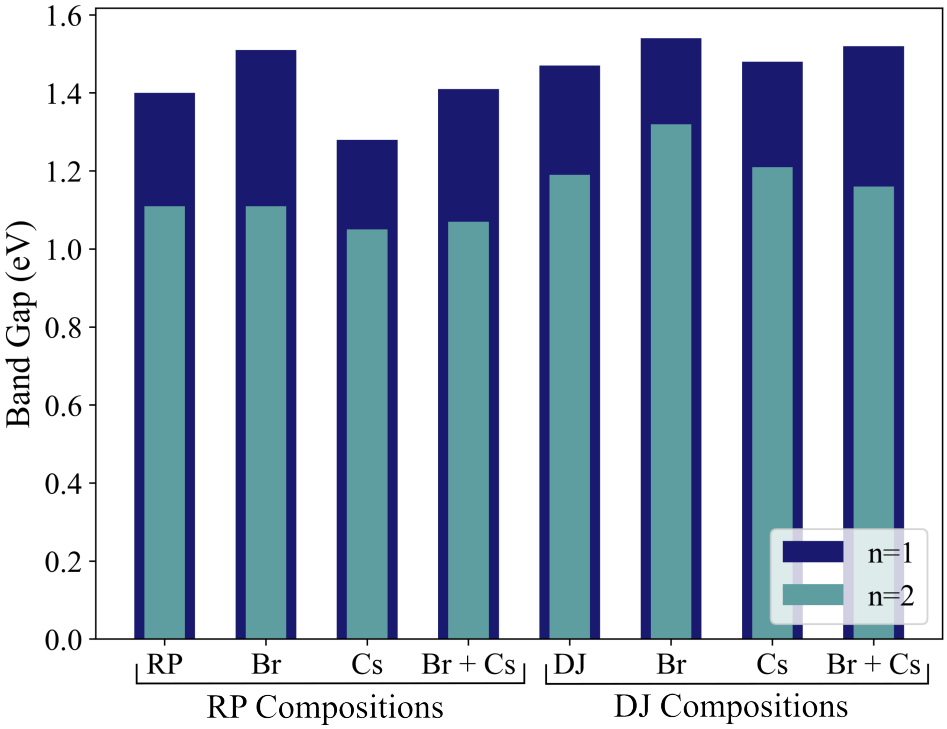


Figure 6.5: Band gaps calculated for the $n = 1$ and $n = 2$ RP and DJ phases in the pristine compositions as well as considering the effects of 25% Br (Br), doping of Cs into the organic layers (Cs), and doping of both 6% Br and Cs (Br + Cs).

First considering the $n = 1$ compositions, introduction of Br into the perovskite widens the band gap across both RP and DJ compositions. This calculated effect of Br addition is in agreement with reported experimental and computational data[347] and serves here as an additional validation of the computational model used. However, the effect of Cs doping into the organic layers has not been investigated previously. The results reported here show that the inclusion of Cs in the organic layers decreases the band gap of the RP phase but has little effect on the DJ phase. Inclusion of both halide mixing and

Cs-doping results in little change to the overall band gap in either the RP or DJ phases. In all cases, the significance of the compositional change on the band gap is greater in the $n = 1$ RP compositions with the $n = 1$ DJ structures showing less band gap variability.

Regarding the $n = 2$ compositions, the RP structures now show far less variability in band gap with only minor changes as a result of Br and Cs addition. In contrast, the DJ structures show a greater band gap fluctuations in the $n = 2$ than $n = 1$ phase. Interestingly, in both the $n = 1$ and $n = 2$ DJ compositions, the band gaps only increase or stay the same as a result of compositional changes with neither Br nor Cs inducing substantial shrinking of the band gap.

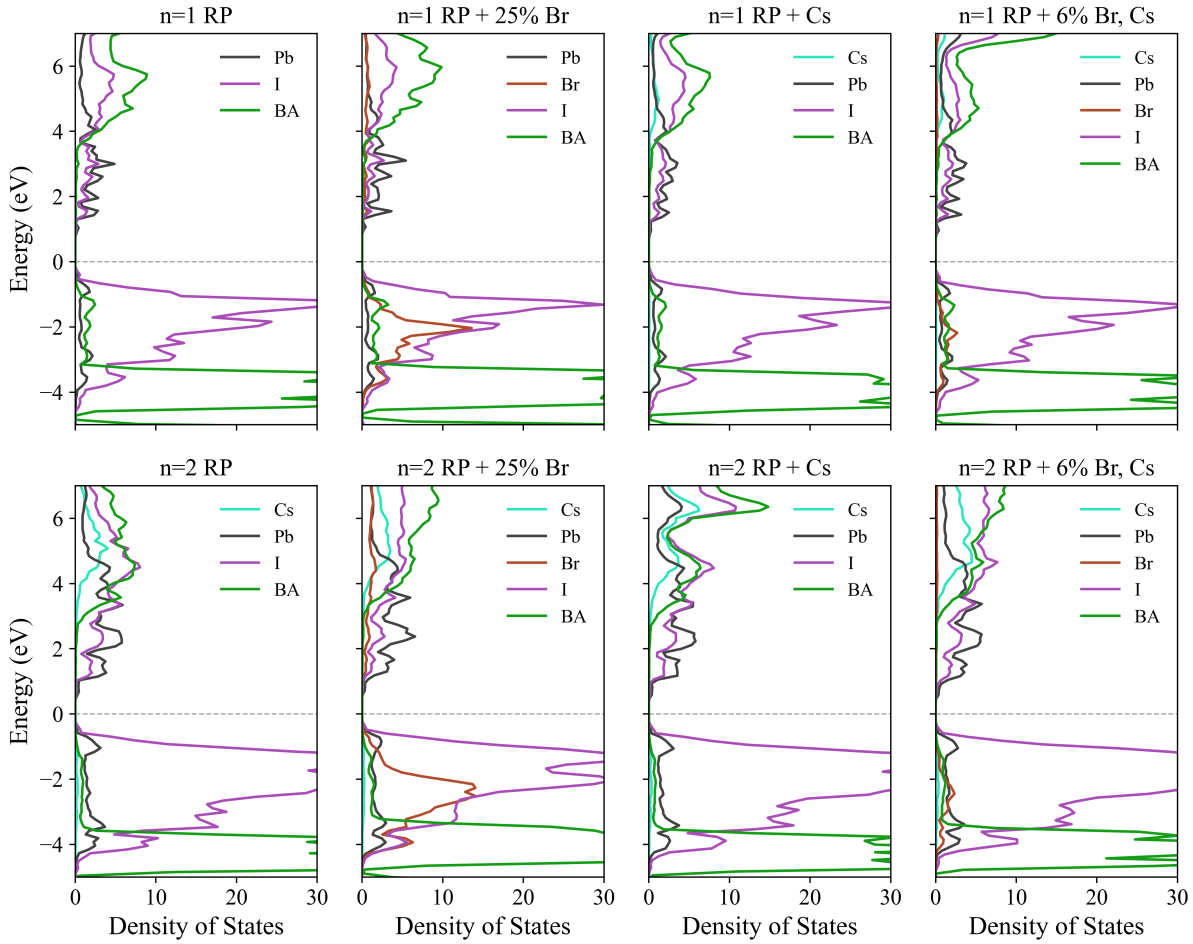


Figure 6.6: Partial density of states decomposed into the relative contributions of the elements Cs, Pb, I, and Br and the spacer molecule BA for the RP compositions investigated.

To further investigate the structural features influencing these band gap changes, the

partial density of states (PDOS) are plotted for each of the structures investigated (Figure 6.6). Considering the $n = 1$ RP structures first, comparison of the $n = 1$ RP PDOS to the $n = 1$ Br-doped PDOS shows that the band gap increases largely due to depopulation of the I PDOS near the valence band maximum. Replacement of longer Pb–I bonds with shorter Pb–Br bonds would be expected to result in the raising of the valence band energy due to increased orbital overlap; however, the Br 4p orbitals involved in bonding are lower in energy than the I 5p orbitals which results in a lowering of the valence band energy. Therefore, doping with Br results in a larger band gap. In contrast, introduction of Cs results in a reduction of cell volume as the Cs atoms replace the large spacer cations. Reducing the cell volume results in a greater Pb–X overlap which raises the antibonding orbitals in energy resulting in a higher valence band edge. Therefore, Cs doping into the inorganic layers shrinks the band gap. Doping of both Br and Cs have contrary effects which results in little change to the band edges in the PDOS. By comparing the density of the Br states in the 6% and 25% doped states it is found that there is a notable difference depending on the concentration of Br in the composition with higher levels of doping resulting in stronger effects on the band gap. The conduction band states are similarly comprised of Pb–X orbitals across all compositions. The $n = 2$ band gaps show very little variation with composition, and in keeping with that result, there is little change in the appearance of the $n = 2$ PDOS plots. Experimentally, it is not known exactly how much Br migrates from the 3D $CsPbI_2Br$ perovskite into the 2D perovskite; nevertheless, comparison of the expected band gap trends can shed light on the compositional changes that occur during annealing.

In the PDOS for the DJ compositions (Figure 6.7), it is found that the states comprising the valence and conduction bands are the same as those in the RP PDOS figures (Figure 6.6). The primary difference between the DJ band gaps and the RP band gaps is that the DJ band gaps vary little with composition. Only Br doping appears to have any impact on the band gap. Due to the 2+ charge of the BDA spacer cation, two Cs^+ atoms are substituted in place of the spacer molecule to ensure appropriate charge balancing.

As a result, Cs doping has less impact on the cell volume and therefore limited influence on the band gap.

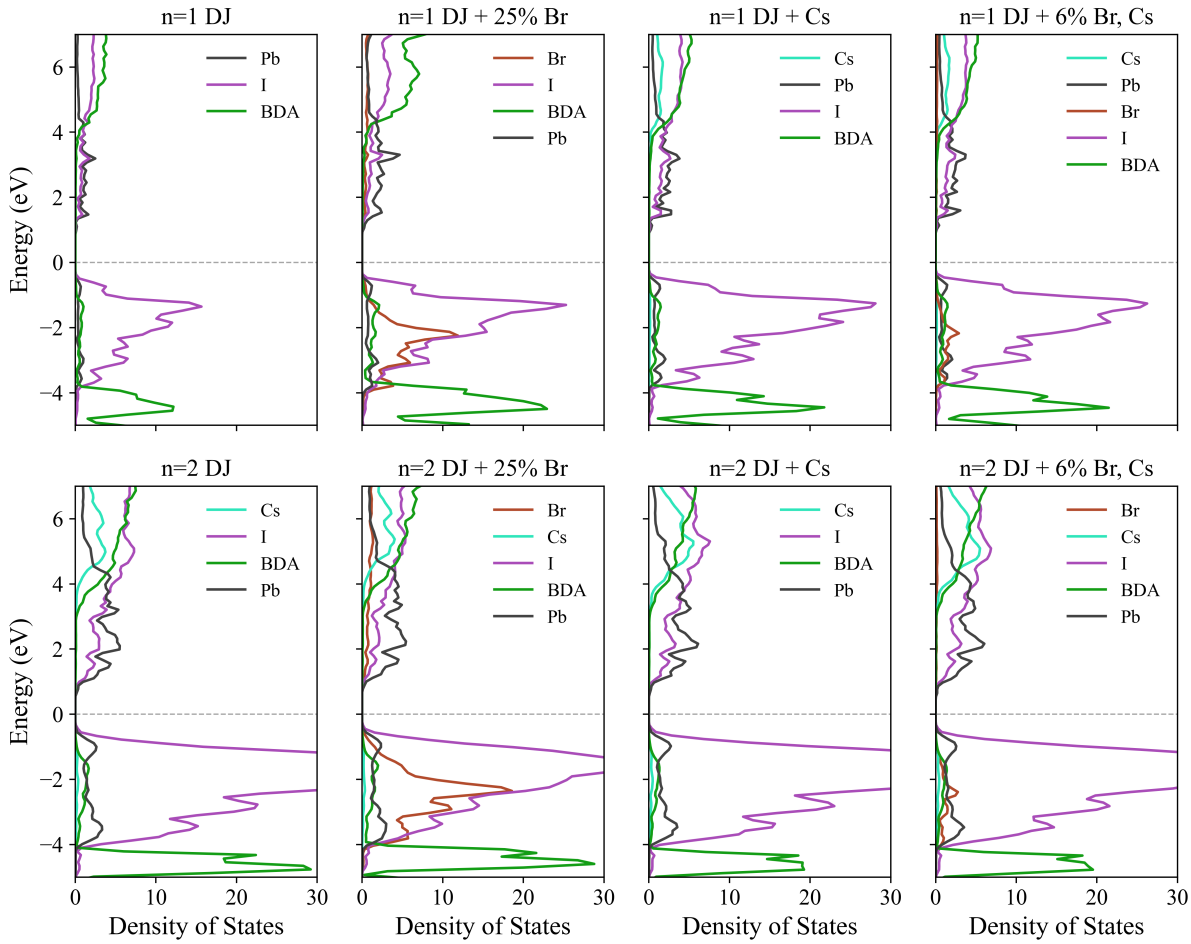


Figure 6.7: Partial density of states decomposed into the elements Cs, Pb, I, and Br as well as the organic spacer cation BDA.

6.6 Ion Migration

Experimental reports suggest that organic spacer cations migrate into the 3D bulk when exposed to heat and light,[335,336] and this cation diffusion has been linked to structural degradation.[338] Ion migration studies on both RP and DJ phases observe mixing of spacer cations into the bulk perovskite,[269,339,340] although the DJ phases are reported to be more resistant to degradation.[331] To investigate the mechanism by which this cation exchange occurs and understand the improved stability of the DJ phase, two preliminary

computational models were tested to attempt to calculate the activation barrier associated with migration of BA and BDA spacer cations into the 3D perovskite bulk. We note that there are no computational studies of spacer cation migration across a 2D-3D interface.

The first approach used biased AIMD simulations as implemented in VASP. In these calculations, a spacer cation, either BA or BDA, was placed several angstrom above a γ-$CsPbI_3$ surface containing a Cs vacancy. During the AIMD simulation, a biased potential was used to move the centre of mass of the spacer cation towards the surface. An example starting structure is depicted in Figure 6.8 (a), and the centre of mass in the z direction is plotted for one of the attempted simulations in Figure 6.8 (b). However, in every biased AIMD simulation attempted, the spacer molecule never crossed the surface threshold into the bulk, likely due to the high activation barrier associated with such a migration. The reverse simulation was also attempted with the molecule beginning in the bulk with a bias to push the molecule out of the surface; however, again these calculations failed to model the migration path of a spacer molecule crossing the surface threshold.

The second approach involved setting up a series of images with the spacer molecule placed at different z coordinates relative to the perovskite surface. The images were then relaxed with the central atom in the molecule only being allowed to relax in the x and y directions while being held at a fixed z. These energies are plotted with reference to the energy of the starting structure furthest above the surface as a function of centre of mass. Two key results emerge. First, in the RP relaxed images (Figure 6.8 (c)), the energies of the z-fixed images increase as the BA spacer cation moves into the surface as expected; however, upon fully relaxing the geometry of the final image with the molecule furthest inside the surface, the energy dramatically decreases compared even to the starting point. This change in energy suggests that despite allowing the molecule to relax fully in x and y, only a local minimum in the geometry is reached resulting in unfeasible energies. Second, in contrast, the DJ image energies (Figure 6.8 (d)) decrease as the BDA spacer cation moves into the surface. These energies better reflect the energy of the final, fully-relaxed structure; however, interestingly, there is no apparent activation barrier associated with

this migration through the surface. In conclusion, these attempts at modelling an energy barrier for a migrating spacer cation do not fully capture the physics of these interactions and cannot provide any trustworthy information about the energetics of cation migration within this system. This was the first reported attempt of performing such a calculation, and this result provides a basis for further mechanistic investigations.

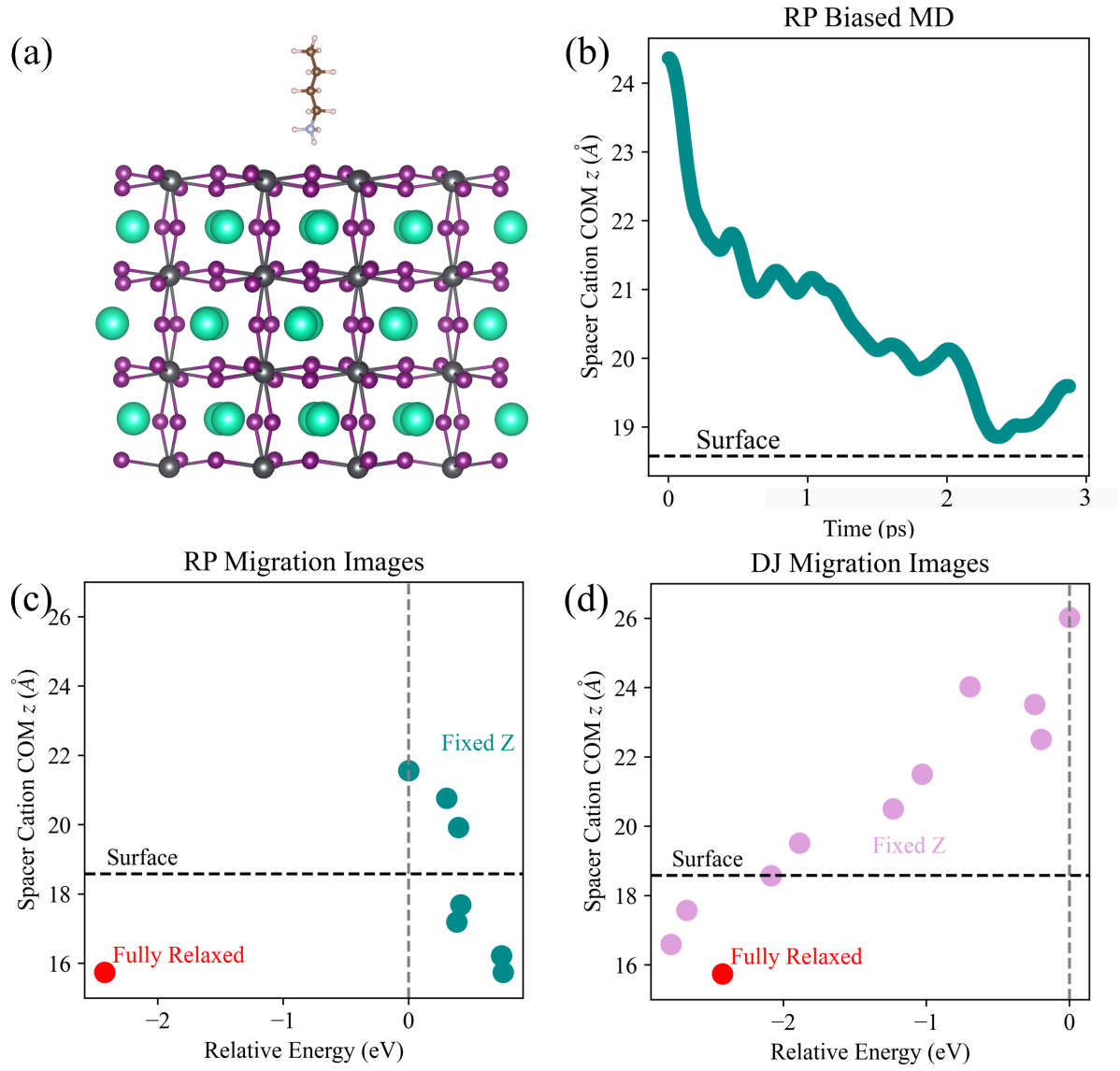


Figure 6.8: (a) Starting point for a sample biased AIMD simulation with a BA spacer cation placed ∼3 Å above a $CsPbI_3$ surface containing a Cs vacancy; (b) the z centre of mass of the BA spacer cation during an AIMD trajectory; and (c,d) energies of partially and fully relaxed structures taken from trajectory images with the BA and BDA spacer cations, respectively.

6.7 Experimental Results

Experimental band gaps were measured via PL spectra of the RP (BA_2PbI_4) and DJ ($BDAPbI_4$) 2D-3D heterostructures synthesised by Dr. Krishanu Dey in Oxford Physics (Figure 6.9). There are slight variations in the band gaps derived as a result of the heterostructure synthesis and the side of the heterostructure upon which the PL spectra are measured. The 3D perovskite is the same composition ($CsPbI_2Br$) in both heterostructures, and so the starting band gap should be identical. Considering only the trends, it can be observed that upon annealing of the RP heterostructure, the band gap of the 2D phase shrinks slightly while the band gap of the 3D perovskite expands.

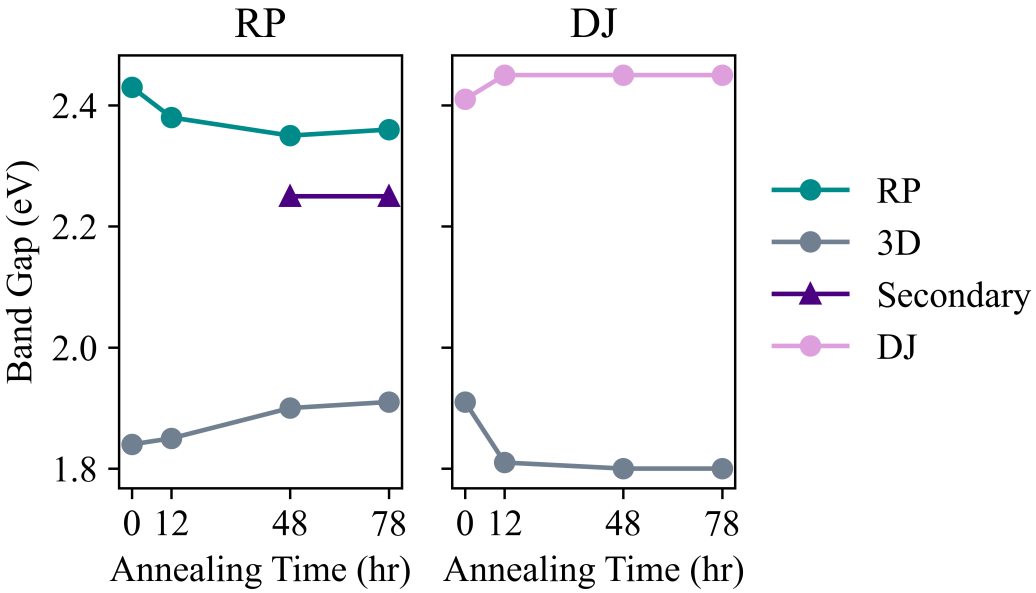


Figure 6.9: Experimental band gaps of the RP (BA_2PbI_4) and DJ ($BDAPbI_4$) 2D-3D ($CsPbI_2Br$) heterostructures measured via PL spectra. The indigo triangles represent the appearance of an unknown secondary phase during annealing of the RP heterostructure. (Unpublished data provided by Dr. Krishanu Dey in Prof. Henry Snaith's group in Oxford Physics.)

At around 48 hrs, an unknown peak in the PL spectrum appears with a band gap around 2.21 eV, about 0.2 eV smaller than the band gap of the starting $n = 1$ RP composition and about 0.1 eV smaller than the band gap of the annealed RP phase. Based on the band gaps calculated in Figure 6.5, this shrinking effect could be due to

Cs doping into the RP phase, or due to the formation of a quasi-2D $n = 2$ RP phase, or it could be the result of both. The calculated band gaps and formation energies suggest that the shrinking of the RP band gap by 0.1 eV upon annealing can be attributed to doping of Cs atoms into the organic layer in the 2D perovskite. Cs vacancies have previously been demonstrated to slightly increase the band gap in γ-$CsPbI_3$ due to the increased Pb–I overlap resulting in the CBM antibonding states being raised in energy slightly more than the VBM antibonding states.[348] Migration of Cs atoms from the 3D perovskite into the 2D perovskite could explain these two observed band gap shifts. The secondary phase peak appears around 0.2 eV below the band gap of the initial RP phase, suggesting that this peak could be a quasi-2D $n = 2$ phase that is formed by loss of volatile spacer cations during annealing.

In the DJ heterostructure, the observed trends are reversed in which the shifts in band gap only occur shortly after annealing begins, and the structures appear stable over time with no additional peaks appearing in the PL spectra. The increase in the 2D band gap and decrease in the 3D band gap could be the result of Br migration from the 3D structure into the 2D layers. Loss of Br from the 3D perovskite would reduce the band gap, while introduction of Br into the 2D phase would simultaneously raise the band gap. The stronger interactions between the doubly charge diammonium cations which bind tightly to adjacent inorganic layers prevents evaporation more effectively than in the ammonium-based RP phase. The lower formation energies of the DJ phase with respect to both the Cs-doped compositions and the $n = 2$ compositions help to explain why there are no secondary phases formed in this system.

6.8 Chapter Summary

This work on 2D-3D materials provides new insights into the relative stabilities of the RP (BA_2PbI_4) and DJ ($BDAPbI_4$) compositions as well as identifying potential sources of the unassigned quasi-2D peaks observed in the PL spectra. The simulation results

suggest that the degradation of the RP phase can be attributed to the migration of Cs atoms from the 3D perovskite structure into the organic layers of the 2D perovskite in response to loss of volatile spacer cations. The lower formation energies of the DJ phase, and the higher energetic penalty for Cs-doping or formation of $n = 2$ phases provide an explanation for the higher stability demonstrated by the DJ heterostructure.

To further investigate these novel 2D-3D systems, biased MD methods should be developed to model dynamic migration of cations in large systems. MLIP models could also be trained to simulate the complex interfaces and degradation pathways which occur in these systems. In addition, previous work suggests that octahedral tilting configurations can be related to electronic effects observed in these systems.[341] Further study of these effects requires the development of computationally efficient models that capture the unique features of these systems. In summary, this work provides a basis for further computational and experimental studies into the use of 2D capping layers for the improved stability of perovskite devices.

Chapter 7

Conclusions and Future Work

7.1 Conclusion

Metal halide perovskites are exciting candidates for the development of next-generation optoelectronics; however, the commercialisation of perovskite devices is currently limited by issues relating to the performance and stability of perovskite materials. Understanding atomistic-scale features such as point defects, ion migration, and surface chemistry is critical for improving device stability and efficiency. Experimental methods are limited in their capacity to provide these atomistic insights; therefore, this thesis employs a range of multiscale computational modelling techniques including DFT, molecular dynamics, and machine learning interatomic potentials (MLIPs) to study a variety of perovskite systems which cover a range of optoelectronic device applications. The materials investigated in this work include $CsPbI_3$ in the γ-polymorph observed in solar cell thin films and the α-polymorph observed in nanomaterials for LEDs, a Pb–Sn–S material to be paired with perovskite tandem PV devices, and 2D-3D perovskite heterostructures.

First, a computational model of ion migration in the solar cell material γ-$CsPbI_3$ was developed using *ab initio* methods and an MLIP. The orthorhombic structure, band gap, and activation barriers calculated are in good agreement with experimental data. I migration along the PbI_6 octahedral edge is predicted to be the lowest in energy. Additionally,

a range of inorganic B-site dopants were investigated and none were found to appreciably increase the activation energy of I migration. Rather, certain dopants such as Zn actually lead to decreased migration barriers as a result of introducing local structural distortions. The results of this study suggest that partial B-site doping with inorganic cations does not significantly suppress I migration in γ-$CsPbI_3$. Furthering the *ab initio* investigation, an MLIP model was developed for the first time to run long timescale simulations beyond 80 ns in the pristine and Sn-doped materials. These simulations provide mechanistic insights into the vacancy-mediated pathways via which diffusion occurs in the lattice. I ion mobility dwarfs that of the Pb and Cs sublattices which do not display any evidence of correlated motion to the I hops. Overall, this study enhances our understanding of ion migration in γ-$CsPbI_3$ and provides guidelines for future doping and migration work on the development of metal halide perovskites for solar cell materials.

Second, the role of ancillary ligands and Zn dopants was investigated in the complex growth mechanisms driving perovskite nanoplatelet synthesis. Benzyl phosphonic acid (BPAc) and diphenyl phosphoric acid (DPPAc) were identified as the ligands with the strongest binding energies to the perovskite surface in agreement with experimental evidence demonstrating that these two ligands produced NPLs with the strong ordering and high monodispersity necessary for commercial LED applications. Additionally, Zn was investigated as both a dopant and a surface passivator. Mixing energies calculated in the bulk perovskite and surface energies calculated for the formation of Zn-doped NPLs support the experimental observation that Zn does not incorporate into the NPL bulk. Rather, Zn likely sits on the NPL surface, quenching NPL growth quickly to achieve the high monodispersity observed. Zn also likely forms complexes to oleic acid ligands in the solution, and these complexes mediate deprotonation of the oleic acid and transfer of the oleate ligands to the perovskite surface, improving the NPL surface stability. These two findings provide design rules for further experimental advancements in the development of commercial polarised light NPL applications.

Third, this work proposes a composition in the Pb–Sn–S family, $Pb_{0.25}Sn_{0.75}S$ as a low

band gap sub-cell absorber in perovskite-tandem triple-junction solar cells. Compositions around this proposed material are predicted to be stable and to have band gaps suitable for targetting the near-IR region of the solar spectrum. The orderings of Pb and Sn on the orthorhombic lattice have little impact on the mixing energy of the material but have a substantial impact on the band gap. This poses a challenge in synthesising a single pure phase. Despite this challenge, our experimental collaborators have synthesised several compositions with band gaps in agreement with the calculated trends. The results of this study provide a starting point for the further development of near-IR absorbers which would increase the achievable efficiencies of multi-junction tandem solar cell devices.

Finally, a fundamental investigation into 2D-3D perovskite heterostructures provides insights into the relative stability of the Ruddlesden–Popper (RP) perovskite, $(CH_3(CH_2)_3NH_3)_2PbI_4$, compared to the Dion–Jacobson (DJ) perovskite, $NH_3(CH_2)_4NH_3PbI_4$. Calculated formation energies indicate the improved stability observed in the DJ heterostructures as compared to the RP heterostructures. Band gaps of potential competing secondary phases can then be matched to experimental PL spectra to identify the source of the RP heterostructure degradation as a secondary phase formed by Cs-doping into the organic layer of the 2D perovskite. This work provides a basis for further computational investigations into the role of 2D perovskite capping layers which improve 3D perovskite thin film stability and device performance.

7.2 Future Work

The work detailed in this thesis opens several avenues for further investigation of perovskite optoelectronics, primarily centred around the methodology advancement of MLIPs. The field of MLIPs has developed dramatically even since the work in this thesis began. With the development of more accurate MLIP codes, more efficient training strategies, and better computational resources, a wide range of material properties can now be explored which were previously inaccessible. This thesis provides a model of ion migration

in γ-$CsPbI_3$ including dopants which was a first in the field. This model could be further improved by including features which become prominent when observing ion migration on a device level, such as grain boundaries, interfaces, and electric bias, to present a more experimentally accurate picture of macroscopic diffusion.

Another challenging application where MLIPs could be utilised is for the modelling other ligands and dopants in relation to NPL stability and, as an even further extension, for modelling NPL growth in solution. This sort of model would provide mechanistic insights into the precise role the ancillary ligands and metal additives such as ZnI_2 play during the NPL growth stages. Simulations of the perovskite synthesis would allow for the precise Zn intermediary complexes to be directly observed. This sort of understanding would pave the way for further experimental improvements to the NPL design process. In addition, the training of MLIP models would also provide insights into the degradation mechanisms that occur in 2D-3D heterostructures. These highly efficient models would allow the entire 2D-3D interface to be modelled over the long timescales necessary to observe ion migration and structural degradation.

In closing, the novel work detailed in this thesis acts as a basis for improving the efficiency and stability of perovskite optoelectronic devices by providing key insights into ion migration in γ-$CsPbI_3$ thin film solar cell devices, developing improved synthesis strategies for α-$CsPbI_3$ NPLs for polarised light emission, proposing a new low band gap Pb–Sn–S material for increasing tandem device efficiencies, and contributing new atomistic understanding towards the design of 2D-3D heterostructures for improved perovskite thin film stabilities.

Bibliography

(1) J. Gong, M. Flatken, A. Abate, J.-P. Correa-Baena, I. Mora-Seró, M. Saliba and Y. Zhou, *ACS Energy Lett.*, 2019, **4**, 861–865.

(2) A. Kojima, K. Teshima, Y. Shirai and T. Miyasaka, *J. Am. Chem. Soc.*, 2009, **131**, 6050–6051.

(3) NREL, *Best Research-Cell Efficiency Chart*, `https://www.nrel.gov/pv/cell-efficiency.html`, 2026.

(4) H. Dong, C. Ran, W. Gao, N. Sun, X. Liu, Y. Xia, Y. Chen and W. Huang, *Adv. Energy Mater.*, 2021, **12**, 2102213.

(5) G. Xing, N. Mathews, S. S. Lim, N. Yantara, X. Liu, D. Sabba, M. Grätzel, S. Mhaisalkar and T. C. Sum, *Nat. Mater.*, 2014, **13**, 476–480.

(6) Q. Zhang, S. T. Ha, X. Liu, T. C. Sum and Q. Xiong, *Nano. Lett.*, 2014, **14**, 5995–6001.

(7) Z.-K. Tan, R. S. Moghaddam, M. L. Lai, P. Docampo, R. Higler, F. Deschler, M. Price, A. Sadhanala, L. M. Pazos, D. Credgington, F. Hanusch, T. Bein, H. J. Snaith and R. H. Friend, *Nat. Nanotechnol.*, 2014, **9**, 687–692.

(8) K. Lin, J. Xing, L. N. Quan, F. P. G. De Arquer, X. Gong, J. Lu, L. Xie, W. Zhao, D. Zhang, C. Yan, W. Li, X. Liu, Y. Lu, J. Kirman, E. H. Sargent, Q. Xiong and Z. Wei, *Nature*, 2018, **562**, 245–248.

(9) T. Chiba, Y. Hayashi, H. Ebe, K. Hoshi, J. Sato, S. Sato, Y.-J. Pu, S. Ohisa and J. Kido, *Nat. Photon.*, 2018, **12**, 681–687.

(10) W. Xu, Q. Hu, S. Bai, C. Bao, Y. Miao, Z. Yuan, T. Borzda, A. J. Barker, E. Tyukalova, Z. Hu, M. Kawecki, H. Wang, Z. Yan, X. Liu, X. Shi, K. Uvdal, M. Fahlman, W. Zhang, M. Duchamp, J.-M. Liu, A. Petrozza, J. Wang, L.-M. Liu, W. Huang and F. Gao, *Nat. Photon.*, 2019, **13**, 418–424.

(11) A. Rogalski, F. Wang, J. Wang, P. Martyniuk and W. Hu, *Small Methods*, 2025, **9**, 2400709.

(12) E. K. Albrecht and A. J. Karttunen, *Dalton Trans.*, 2023, **52**, 12461–12469.

(13) D. Moia and J. Maier, *ACS Energy Lett.*, 2021, **6**, 1566–1576.

(14) D. B. Straus, S. Guo and R. J. Cava, *J. Am. Chem. Soc.*, 2019, **141**, 11435–11439.

(15) R. J. Sutton, M. R. Filip, A. A. Haghighirad, N. Sakai, B. Wenger, F. Giustino and H. J. Snaith, *ACS Energy Lett.*, 2018, **3**, 1787–1794.

(16) H. Zhu, C. Hao, X. Li, Y. Qi, X. Zhu, Y. Miao, R. Liu and J. Ding, *J. Phys. Chem. C*, 2023, **127**, 18727–18735.

(17) Q. Chen, J. Wu, X. Ou, B. Huang, J. Almutlaq, A. A. Zhumekenov, X. Guan, S. Han, L. Liang, Z. Yi, J. Li, X. Xie, Y. Wang, Y. Li, D. Fan, D. B. L. Teh, A. H. All, O. F. Mohammed, O. M. Bakr, T. Wu, M. Bettinelli, H. Yang, W. Huang and X. Liu, *Nature*, 2018, **561**, 88–93.

(18) J. Ye, A. Ren, L. Dai, T. K. Baikie, R. Guo, D. Pal, S. Gorgon, J. E. Heger, J. Huang, Y. Sun, R. Arul, G. Grimaldi, K. Zhang, J. Shamsi, Y.-T. Huang, H. Wang, J. Wu, A. F. Koenderink, L. Torrente Murciano, M. Schwartzkopf, S. V. Roth, P. Müller-Buschbaum, J. J. Baumberg, S. D. Stranks, N. C. Greenham, L. Polavarapu, W. Zhang, A. Rao and R. L. Z. Hoye, *Nat. Photon.*, 2024, **18**, 586–594.

(19) A. P. Litvin, J. Guo, J. Wang, X. Zhang, W. Zheng and A. L. Rogach, *Small*, 2025, **21**, 2408422.

(20) S. Ghimire and C. Klinke, *Nanoscale*, 2021, **13**, 12394–12422.

(21) B. Saparov and D. B. Mitzi, *Chem. Rev.*, 2016, **116**, 4558–4596.

(22) J.-C. Blancon, W. Nie, A. J. Neukirch, G. Gupta, S. Tretiak, L. Cognet, A. D. Mohite and J. J. Crochet, *Adv. Funct. Mater.*, 2016, **26**, 4283–4292.

(23) T. Ishihara, J. Takahashi and T. Goto, *Phys. Rev. B Condens. Matter*, 1990, **42**, 11099–11107.

(24) X. Gong, O. Voznyy, A. Jain, W. Liu, R. Sabatini, Z. Piontkowski, G. Walters, G. Bappi, S. Nokhrin, O. Bushuyev, M. Yuan, R. Comin, D. McCamant, S. O. Kelley and E. H. Sargent, *Nat. Mater.*, 2018, **17**, 550–556.

(25) M. D. Smith, A. Jaffe, E. R. Dohner, A. M. Lindenberg and H. I. Karunadasa, *Chem. Sci.*, 2017, **8**, 4497–4504.

(26) A. Fieramosca, L. Polimeno, V. Ardizzone, L. De Marco, M. Pugliese, V. Maiorano, M. De Giorgi, L. Dominici, G. Gigli, D. Gerace, D. Ballarini and D. Sanvitto, *Sci. Adv.*, 2019, **5**, eaav9967.

(27) Y. Zhai, S. Baniya, C. Zhang, J. Li, P. Haney, C.-X. Sheng, E. Ehrenfreund and Z. V. Vardeny, *Sci. Adv.*, 2017, **3**, e1700704.

(28) I. H. Park, Q. Zhang, K. C. Kwon, Z. Zhu, W. Yu, K. Leng, D. Giovanni, H. S. Choi, I. Abdelwahab, Q. H. Xu, T. C. Sum and K. P. Loh, *J. Am. Chem. Soc.*, 2019, **141**, 15972–15976.

(29) H. Tsai, W. Nie, J. C. Blancon, C. C. Stoumpos, R. Asadpour, B. Harutyunyan, A. J. Neukirch, R. Verduzco, J. J. Crochet, S. Tretiak, L. Pedesseau, J. Even, M. A. Alam, G. Gupta, J. Lou, P. M. Ajayan, M. J. Bedzyk and M. G. Kanatzidis, *Nature*, 2016, **536**, 312–316.

(30) M. Yuan, L. N. Quan, R. Comin, G. Walters, R. Sabatini, O. Voznyy, S. Hoogland, Y. Zhao, E. M. Beauregard, P. Kanjanaboos, Z. Lu, D. H. Kim and E. H. Sargent, *Nat. Nanotechnol.*, 2016, **11**, 872–877.

(31) L. Li, Z. Sun, P. Wang, W. Hu, S. Wang, C. Ji, M. Hong and J. Luo, *Angew. Chem. Int. Ed. Engl.*, 2017, **56**, 12150–12154.

(32) J. C. Blancon, J. Even, C. C. Stoumpos, M. G. Kanatzidis and A. D. Mohite, *Nat. Nanotechnol.*, 2020, **15**, 969–985.

(33) Z. Wang, Q. Lin, F. P. Chmiel, N. Sakai, L. M. Herz and H. J. Snaith, *Nat. Energy*, 2017, **2**, 17135.

(34) B. Zhao, S. Bai, V. Kim, R. Lamboll, R. Shivanna, F. Auras, J. M. Richter, L. Yang, L. Dai, M. Alsari, X.-J. She, L. Liang, J. Zhang, S. Lilliu, P. Gao, H. J. Snaith, J. Wang, N. C. Greenham, R. H. Friend and D. Di, *Nat. Photon.*, 2018, **12**, 783–789.

(35) H. Dong, C. Ran, W. Gao, M. Li, Y. Xia and W. Huang, *ELight*, 2023, **3**, 3.

(36) A. K. Jena, A. Kulkarni and T. Miyasaka, *Chem. Rev.*, 2019, **119**, 3036–3103.

(37) L. M. Herz, *ACS Energy Lett.*, 2017, **2**, 1539–1548.

(38) Y. Wang, Y. Zhang, P. Zhang and W. Zhang, *Phys. Chem. Chem. Phys.*, 2015, **17**, 11516–11520.

(39) Y. Huang, W.-J. Yin and Y. He, *J. Phys. Chem. C*, 2018, **122**, 1345–1350.

(40) C. C. Stoumpos and M. G. Kanatzidis, *Acc. Chem. Res.*, 2015, **48**, 2791–802.

(41) J. Song, J. Li, X. Li, L. Xu, Y. Dong and H. Zeng, *Adv. Mater.*, 2015, **27**, 7162–7167.

(42) K. Chen, S. Schünemann, S. Song and H. Tüysüz, *Chem. Soc. Rev.*, 2018, **47**, 7045–7077.

(43) T. Moot, J. Werner, G. E. Eperon, K. Zhu, J. J. Berry, M. D. McGehee and J. M. Luther, *Adv. Mater.*, 2020, **32**, 2003312.

(44) R. J. Sutton, G. E. Eperon, L. Miranda, E. S. Parrott, B. A. Kamino, J. B. Patel, M. T. Hörantner, M. B. Johnston, A. A. Haghighirad, D. T. Moore and H. J. Snaith, *Adv. Energy Mater.*, 2016, **6**, 1502458.

(45) G. Wang, S. Mei, J. Liao, W. Wang, Y. Tang, Q. Zhang, Z. Tang, B. Wu and G. Xing, *Small*, 2021, **17**, 2100809.

(46) L. N. Quan, F. P. García De Arquer, R. P. Sabatini and E. H. Sargent, *Adv. Mater.*, 2018, **30**, 1801996.

(47) Y. Fu, H. Zhu, J. Chen, M. P. Hautzinger, X. Y. Zhu and S. Jin, *Nat. Rev. Mater.*, 2019, **4**, 169–188.

(48) G. Kieslich, S. Sun and A. K. Cheetham, *Chem. Sci.*, 2014, **5**, 4712–4715.

(49) G.-W. Kim and A. Petrozza, *Adv. Energy Mater.*, 2020, **10**, 2001959.

(50) G. W. P. Adhyaksa, L. W. Veldhuizen, Y. Kuang, S. Brittman, R. E. I. Schropp and E. C. Garnett, *Chem. Mater.*, 2016, **28**, 5259–5263.

(51) L. D. Whalley, R. Crespo-Otero and A. Walsh, *ACS Energy Lett.*, 2017, **2**, 2713–2714.

(52) J.-H. Yang, W.-J. Yin, J.-S. Park and S.-H. Wei, *J. Mater. Chem. A*, 2016, **4**, 13105–13112.

(53) M. L. Agiorgousis, Y. Y. Sun, H. Zeng and S. Zhang, *J. Am. Chem. Soc.*, 2014, **136**, 14570–14575.

(54) J. S. Park, S. Kim, Z. Xie and A. Walsh, *Nat. Rev. Mater.*, 2018, **3**, 194–210.

(55) C. Eames, J. M. Frost, P. R. Barnes, B. C. O'Regan, A. Walsh and M. S. Islam, *Nat. Commun.*, 2015, **6**, 7497.

(56) A. Walsh, D. O. Scanlon, S. Chen, X. G. Gong and S.-H. Wei, *Angew. Chem. Int. Ed.*, 2015, **54**, 1791–1794.

(57) A. Senocrate, I. Moudrakovski, G. Y. Kim, T.-Y. Yang, G. Gregori, M. Grätzel and J. Maier, *Angew. Chem. Int. Ed.*, 2017, **56**, 7755–7759.

(58) S. Meloni, T. Moehl, W. Tress, M. Franckevičius, M. Saliba, Y. H. Lee, P. Gao, M. K. Nazeeruddin, S. M. Zakeeruddin, U. Rothlisberger and M. Graetzel, *Nat. Commun.*, 2016, **7**, 10334.

(59) A. Senocrate, T.-Y. Yang, G. Gregori, G. Y. Kim, M. Grätzel and J. Maier, *Solid State Ion.*, 2018, **321**, 69–74.

(60) L. Ding, *Perovskite Materials and Devices*, Wiley-VCH, Weinheim, Germany, 2022.

(61) J. Burschka, N. Pellet, S. J. Moon, R. Humphry-Baker, P. Gao, M. K. Nazeeruddin and M. Gratzel, *Nature*, 2013, **499**, 316–9.

(62) M. A. Green, A. Ho-Baillie and H. J. Snaith, *Nat. Photon.*, 2014, **8**, 506–514.

(63) M. Liu, M. B. Johnston and H. J. Snaith, *Nature*, 2013, **501**, 395–398.

(64) D. Beynon, E. Parvazian, K. Hooper, J. McGettrick, R. Patidar, T. Dunlop, Z. Wei, P. Davies, R. Garcia-Rodriguez, M. Carnie, M. Davies and T. Watson, *Adv. Mater.*, 2023, **35**, 2208561.

(65) A. Richter, M. Hermle and S. W. Glunz, *IEEE J. Photovolt.*, 2013, **3**, 1184–1191.

(66) S. Liu, J. Li, W. Xiao, R. Chen, Z. Sun, Y. Zhang, X. Lei, S. Hu, M. Kober-Czerny, J. Wang, F. Ren, Q. Zhou, H. Raza, Y. Gao, Y. Ji, S. Li, H. Li, L. Qiu, W. Huang, Y. Zhao, B. Xu, Z. Liu, H. J. Snaith, N.-G. Park and W. Chen, *Nature*, 2024, 536–542.

(67) H. Chen, C. Liu, J. Xu, A. Maxwell, W. Zhou, Y. Yang, Q. Zhou, A. S. R. Bati, H. Wan, Z. Wang, L. Zeng, J. Wang, P. Serles, Y. Liu, S. Teale, Y. Liu, M. I. Saidaminov, M. Li, N. Rolston, S. Hoogland, T. Filleter, C. C. Kanatzidis, B. Chen, Z. Ning and E. H. Sargent, *Science*, 2024, **384**, 189–193.

(68) J. Park, J. Kim, H.-S. Yun, M. J. Paik, E. Noh, H. J. Mun, M. G. Kim, T. J. Shin and S. I. Seok, *Nature*, 2023, **616**, 724–730.

(69) J. Wang, Y. Che, Y. Duan, Z. Liu, S. Yang, D. Xu, Z. Fang, X. Lei, Y. Li and S. Liu, *Adv. Mater.*, 2023, **35**, 2210223.

(70) S. S. Mali, J. V. Patil, J.-Y. Shao, Y.-W. Zhong, S. R. Rondiya, N. Y. Dzade and C. K. Hong, *Nat. Energy*, 2023, **8**, 989–1001.

(71) J. Liang, C. Wang, Y. Wang, Z. Xu, Z. Lu, Y. Ma, H. Zhu, Y. Hu, C. Xiao, X. Yi, G. Zhu, H. Lv, L. Ma, T. Chen, Z. Tie, Z. Jin and J. Liu, *J. Am. Chem. Soc.*, 2016, **138**, 15829–15832.

(72) J. Duan, H. Xu, W. E. I. Sha, Y. Zhao, Y. Wang, X. Yang and Q. Tang, *J. Mater. Chem. A*, 2019, **7**, 21036–21068.

(73) W. Zhou, Y. Zhao, X. Zhou, R. Fu, Q. Li, Y. Zhao, K. Liu, D. Yu and Q. Zhao, *J. Phys. Chem. Lett.*, 2017, **8**, 4122–4128.

(74) G. E. Eperon, G. M. Paternò, R. J. Sutton, A. Zampetti, A. A. Haghighirad, F. Cacialli and H. J. Snaith, *J. Mater. Chem. A*, 2015, **3**, 19688–19695.

(75) K. A. Bush, A. F. Palmstrom, Z. J. Yu, M. Boccard, R. Cheacharoen, J. P. Mailoa, D. P. McMeekin, R. L. Z. Hoye, C. D. Bailie, T. Leijtens, I. M. Peters, M. C. Minichetti, N. Rolston, R. Prasanna, S. Sofia, D. Harwood, W. Ma, F. Moghadam, H. J. Snaith, T. Buonassisi, Z. C. Holman, S. F. Bent and M. D. McGehee, *Nat. Energy*, 2017, **2**, 17009.

(76) G. E. Eperon, T. Leijtens, K. A. Bush, R. Prasanna, T. Green, J. T.-W. Wang, D. P. McMeekin, G. Volonakis, R. L. Milot, R. May, A. Palmstrom, D. J. Slotcavage, R. A. Belisle, J. B. Patel, E. S. Parrott, R. J. Sutton, W. Ma, F. Moghadam, B. Conings, A. Babayigit, H.-G. Boyen, S. Bent, F. Giustino, L. M. Herz, M. B. Johnston, M. D. McGehee and H. J. Snaith, *Science*, 2016, **354**, 861–865.

(77) H. Zhang and N.-G. Park, *DeCarbon*, 2024, **3**, 100025.

(78) A. Luque and S. Hegedus, in *Handbook of Photovoltaic Science and Engineering*, John Wiley & Sons, Incorporated, United Kingdom, 2011.

(79) C. C. Boyd, R. Cheacharoen, T. Leijtens and M. D. McGehee, *Chem. Rev.*, 2019, **119**, 3418–3451.

(80) A. Senocrate, E. Kotomin and J. Maier, *Helv. Chim. Acta*, 2020, **103**, e2000073.

(81) T. Niu, L. Chao, X. Dong, L. Fu and Y. Chen, *J. Phys. Chem. Lett.*, 2022, **13**, 1845–1854.

(82) A. Walsh and S. D. Stranks, *ACS Energy Lett.*, 2018, **3**, 1983–1990.

(83) M. Pols, T. Hilpert, I. A. W. Filot, A. C. T. Van Duin, S. Calero and S. Tao, *ACS Appl. Mater. Interfaces*, 2022, **14**, 40841–40850.

(84) J.-S. Park, J. Calbo, Y.-K. Jung, L. D. Whalley and A. Walsh, *ACS Energy Lett.*, 2019, **4**, 1321–1327.

(85) D. Barboni and R. A. De Souza, *Energy Environ. Sci.*, 2018, **11**, 3266–3274.

(86) S. T. Birkhold, J. T. Precht, R. Giridharagopal, G. E. Eperon, L. Schmidt-Mende and D. S. Ginger, *J. Phys. Chem. C*, 2018, **122**, 12633–12639.

(87) G. Y. Kim, A. Senocrate, T.-Y. Yang, G. Gregori, M. Grätzel and J. Maier, *Nat. Mater.*, 2018, **17**, 445–449.

(88) C. M. Guvenc, Y. Yalcinkaya, S. Ozen, H. Sahin and M. M. Demir, *J. Phys. Chem. C*, 2019, **123**, 24865–24872.

(89) J. Euvrard, Y. Yan and D. B. Mitzi, *Nat. Rev. Mater.*, 2021, **6**, 531–549.

(90) K. Dey, D. Ghosh, M. Pilot, S. R. Pering, B. Roose, P. Deswal, S. P. Senanayak, P. J. Cameron, M. S. Islam and S. D. Stranks, *Energy Environ. Sci.*, 2024, **17**, 760–769.

(91) S. Bera, D. Ghosh, A. Dutta, S. Bhattacharyya, S. Chakraborty and N. Pradhan, *ACS Energy Lett.*, 2019, **4**, 1364–1369.

(92) Q. A. Akkerman, T. P. T. Nguyen, S. C. Boehme, F. Montanarella, D. N. Dirin, P. Wechsler, F. Beiglböck, G. Rainò, R. Erni, C. Katan, J. Even and M. V. Kovalenko, *Science*, 2022, **377**, 1406–1412.

(93) M. Lu, X. Zhang, Y. Zhang, J. Guo, X. Shen, W. W. Yu and A. L. Rogach, *Adv. Mater.*, 2018, **30**, 1804691.

(94) M. Lu, X. Zhang, X. Bai, H. Wu, X. Shen, Y. Zhang, W. Zhang, W. Zheng, H. Song, W. W. Yu and A. L. Rogach, *ACS Energy Lett.*, 2018, **3**, 1571–1577.

(95) S. R. Pering, W. Deng, J. R. Troughton, P. S. Kubiak, D. Ghosh, R. G. Niemann, F. Brivio, F. E. Jeffrey, A. B. Walker, M. S. Islam, T. M. Watson, P. R. Raithby, A. L. Johnson, S. E. Lewis and P. J. Cameron, *J. Mater. Chem. A*, 2017, **5**, 20658–20665.

(96) B. Roy, S. Mahato, S. Bose, A. Ghorai, S. K. Srivastava, N. C. Das and S. K. Ray, *Chem. Mater.*, 2023, **35**, 1601–1609.

(97) R. J. Sa, B. L. Luo, Z. J. Ma, L. T. Liang and D. W. Liu, *J. Solid State Chem.*, 2022, **309**, 122956.

(98) T. Zhou, Z. Xu, R. Wang, X. Dong, Q. Fu and Y. Liu, *Adv. Mater.*, 2022, **34**, 2200705.

(99) H. J. Snaith, *Nat. Mater.*, 2018, **17**, 372–376.

(100) P. Gao, A. R. Bin Mohd Yusoff and M. K. Nazeeruddin, *Nat. Commun.*, 2018, **9**, DOI: 10.1038/s41467-018-07382-9.

(101) X. Zhang, L. Li, Z. Sun and J. Luo, *Chem. Soc. Rev.*, 2019, **48**, 517–539.

(102) J. Shamsi, A. S. Urban, M. Imran, L. De Trizio and L. Manna, *Chem. Rev.*, 2019, **119**, 3296–3348.

(103) J. Ye, M. M. Byranvand, C. O. Martínez, R. L. Z. Hoye, M. Saliba and L. Polavarapu, *Angew. Chem. Int. Ed.*, 2021, **60**, 21636–21660.

(104) R. Azmi, E. Ugur, A. Seitkhan, F. Aljamaan, A. S. Subbiah, J. Liu, G. T. Harrison, M. I. Nugraha, M. K. Eswaran, M. Babics, Y. Chen, F. Xu, T. G. Allen, A. U. Rehman, C.-L. Wang, T. D. Anthopoulos, U. Schwingenschlögl, M. De Bastiani, E. Aydin and S. De Wolf, *Science*, 2022, **376**, 73–77.

(105) S. Sidhik, Y. Wang, M. De Siena, R. Asadpour, A. J. Torma, T. Terlier, K. Ho, W. Li, A. B. Puthirath, X. Shuai, A. Agrawal, B. Traore, M. Jones, R. Giridharagopal, P. M. Ajayan, J. Strzalka, D. S. Ginger, C. Katan, M. A. Alam, J. Even, M. G. Kanatzidis and A. D. Mohite, *Science*, 2022, **377**, 1425–1430.

(106) L. C. Hirst and N. J. Ekins-Daukes, *Prog. Photovolt.*, 2011, **19**, 286–293.

(107) Y.-H. Lin, Vikram, F. Yang, X.-L. Cao, A. Dasgupta, R. D. J. Oliver, A. M. Ulatowski, M. M. McCarthy, X. Shen, Q. Yuan, M. G. Christoforo, F. S. Y. Yeung, M. B. Johnston, N. K. Noel, L. M. Herz, M. S. Islam and H. J. Snaith, *Science*, 2024, **384**, 767–775.

(108) K. Wang, L. Zheng, Y. Hou, A. Nozariasbmarz, B. Poudel, J. Yoon, T. Ye, D. Yang, A. V. Pogrebnyakov, V. Gopalan and S. Priya, *Joule*, 2022, **6**, 756–771.

(109) H. J. Yen, P. W. Liang, C. C. Chueh, Z. Yang, A. K. Jen and H. L. Wang, *ACS Appl. Mater. Interfaces*, 2016, **8**, 14513–14520.

(110) S. Hu, M. A. Truong, K. Otsuka, T. Handa, T. Yamada, R. Nishikubo, Y. Iwasaki, A. Saeki, R. Murdey, Y. Kanemitsu and A. Wakamiya, *Chem. Sci.*, 2021, **12**, 13513–13519.

(111) S. Hu, K. Otsuka, R. Murdey, T. Nakamura, M. A. Truong, T. Yamada, T. Handa, K. Matsuda, K. Nakano, A. Sato, K. Marumoto, K. Tajima, Y. Kanemitsu and A. Wakamiya, *Energy Environ. Sci.*, 2022, **15**, 2096–2107.

(112) H. Hu, S. X. An, Y. Li, S. Orooji, R. Singh, F. Schackmar, F. Laufer, Q. Jin, T. Feeney, A. Diercks, F. Gota, S. Moghadamzadeh, T. Pan, M. Rienäcker, R. Peibst, B. A. Nejand and U. W. Paetzold, *Energy Environ. Sci.*, 2024, **17**, 2800–2814.

(113) Y.-F. Li, J. Feng and H.-B. Sun, *Nanoscale*, 2019, **11**, 19119–19139.

(114) T. Chiba and J. Kido, *J. Mater. Chem. C*, 2018, **6**, 11868–11877.

(115) R. Wang, C. Shang, Q. Zhao, Q. Huang, C. Liu, W. Xu, R. Liu, W. Zhang and J. Ding, *ACS Appl. Nano Mater.*, 2024, **7**, 7632–7641.

(116) J. Guo, M. Lu, X. Zhang, S. Sun, C. Han, Y. Zhang, X. Yang, S. V. Kershaw, W. Zheng and A. L. Rogach, *ACS Nano.*, 2023, **17**, 9290–9301.

(117) Y. Miao, X. Liu, Y. Chen, T. Zhang, T. Wang and Y. Zhao, *Adv. Mater.*, 2021, **33**, 2105699.

(118) S. Lim, S. Han, D. Kim, J. Min, J. Choi and T. Park, *Adv. Mater.*, 2023, **35**, 2203430.

(119) A. L. Efros and L. E. Brus, *ACS Nano.*, 2021, **15**, 6192–6210.

(120) S. Ithurria, M. D. Tessier, B. Mahler, R. P. Lobo, B. Dubertret and A. L. Efros, *Nat. Mater.*, 2011, **10**, 936–41.

(121) L. Protesescu, S. Yakunin, M. I. Bodnarchuk, F. Krieg, R. Caputo, C. H. Hendon, R. X. Yang, A. Walsh and M. V. Kovalenko, *Nano. Lett.*, 2015, **15**, 3692–3696.

(122) Y. Hassan, J. Park, M. Crawford, A. Sadhanala, J. Lee, J. Sadighian, E. Mosconi, R. Shivanna, E. Radicchi, M. Jeong, C. Yang, H. Choi, S. Park, M. Song, F. De Angelis, C. Wong, R. Friend, B. Lee and H. Snaith, *Nature*, 2021, **591**, 72–77.

(123) X. Gu, X. Lai, Y. Zhang, T. Wang, W. L. Tan, C. R. McNeill, Q. Liu, P. Sonar, F. He, W. Li, C. Shan and A. K. K. Kyaw, *Adv. Sci.*, 2022, **9**, 2200445.

(124) A. J. Houtepen, E. H. Sargent, I. Infante, J. S. Owen, P. B. Green, R. D. Schaller, S. Bals, S. Zeiske, T. Stöferle and Z. Hens, *Nat. Rev. Methods Primers*, 2025, **5**, DOI: 10.1038/s43586-025-00413-y.

(125) M. Que, W. Chen, P. Chen, J. Liu, X. Yin, B. Gao and W. Que, *Chem. Phys.*, 2019, **517**, 80–84.

(126) Y. T. Zeng, Z. R. Li, S. P. Chang, A. Ansay, Z. H. Wang and C. Y. Huang, *Nanomater.*, 2022, **12**, 759.

(127) V. Naresh and N. Lee, *ACS Appl. Nano Mater.*, 2020, **3**, 7621–7632.

(128) W. Zheng, J. Chen, Y. Guo, X. Zhang, F. Chun, Y. Cao, X. Gao, H. Suo, X. Wei, Z. Xing, Y. Wang and F. Wang, *Nat. Commun.*, 2025, **16**, DOI: 10.1038/s41467-025-65050-1.

(129) J. Kim, W. H. Jeong, J. Ye, A. N. Arber, Vikram, D. Kim, Y.-T. Huang, Y. Wang, D. Kim, D. Lee, C.-Y. Chang, X. Shen, S. Y. Bae, A. Gaurav, Y. I. Kim, J. Yang, B. Je, C. Cho, A. Rao, H. J. Snaith, M. S. Islam, B. R. Lee, M. H. Song and R. L. Z. Hoye, *Advanced Materials*, 2026, DOI: 10.1002/adma.74023.

(130) R. Rossetti, S. Nakahara and L. E. Brus, *J. Chem. Phys.*, 1983, **79**, 1086–1088.

(131) A. I. Ekimov and A. A. Onushchenko, *JETP Lett.*, 2023, **118**, S15–S17.

(132) H. Liu, M. Worku, A. Mondal, T. B. Shonde, M. Chaaban, A. Ben-Akacha, S. Lee, F. Gonzalez, O. Olasupo, X. Lin, J. S. R. Vellore Winfred, Y. Xin, E. Lochner and B. Ma, *Adv. Energy Mater.*, 2023, **13**, 2201605.

(133) W. H. Jeong, J. Ye, J. Kim, R. Xu, X. Shen, C.-Y. Chang, E. L. Quinn, H. Ahn, M. H. Song, P. D. Nellist, H. J. Snaith, Y. Zhang, B. R. Lee and R. L. Z. Hoye, *Light Sci. Appl.*, 2026, **15**, 22.

(134) S. Sun, M. Lu, P. Lu, X. Li, F. Zhang, Z. Wu, T. Wang, F. Yan, T. Li, T. Feng, Y. Zhang and X. Bai, *Nano. Lett.*, 2024, **24**, 5631–5638.

(135) F. Giustino, *Materials Modelling Using Density Functional Theory: Properties and Predictions*, Oxford University Press, Oxford, [England] ; 1st, 2014.

(136) E. Schrödinger, *Phys. Rev.*, 1926, **28**, 1049–1070.

(137) W. Pauli, *Z. Phys.*, 1925, **31**, 765–783.

(138) J. C. Slater, *Phys. Rev.*, 1929, **34**, 1293–1322.

(139) D. R. Hartree, *Math. Proc. Camb. Philos. Soc.*, 1928, **24**, 89–110.

(140) D. R. Hartree, *Math. Proc. Camb. Philos. Soc.*, 1928, **24**, 111–132.

(141) V. Fock, *Z. Phys.*, 1930, **61**, 126–148.

(142) P. Hohenberg and W. Kohn, *Phys. Rev.*, 1964, **136**, B864–B871.

(143) W. Kohn and L. J. Sham, *Phys. Rev.*, 1965, **140**, A1133–A1138.

(144) N. Harrison, *An Introduction to Density Functional Theory*, https://www.imperial.ac.uk/media/imperial-college/research-centres-and-groups/computational-materials-science/teaching/DFT_NATO.pdf, Lecture Notes.

(145) J. Toulouse, *Review of Approximations for the Exchange-Correlation Energy in Density-Functional Theory*, 2022.

(146) D. S. Sholl and J. A. Steckel, *Density Functional Theory: A Practical Introduction*, Wiley, Hoboken, N.J, 1st, 2009.

(147) D. M. Ceperley and B. J. Alder, *Phys. Rev. Lett.*, 1980, **45**, 566–569.

(148) J. P. Perdew and A. Zunger, *Phys. Rev. B*, 1981, **23**, 5048–5079.

(149) J. P. Perdew, K. Burke and M. Ernzerhof, *Phys. Rev. Lett.*, 1996, **77**, 3865–3868.

(150) J. P. Perdew, A. Ruzsinszky, G. I. Csonka, O. A. Vydrov, G. E. Scuseria, L. A. Constantin, X. Zhou and K. Burke, *Phys. Rev. Lett.*, 2008, **100**, 136406.

(151) S. Horoz, S. Simsek, S. Palaz and A. M. Mamedov, *World J. Condens. Matter Phys.*, 2015, **05**, 78–85.

(152) G. Kresse and J. Furthmüller, *Phys. Rev. B*, 1996, **54**, 11169–11186.

(153) G. Kresse and J. Hafner, *Phys. Rev. B*, 1993, **47**, 558–561.

(154) S. Seriy, *Open J. Model. Simu.*, 2015, **03**, 96–103.

(155) P. E. Blöchl, *Phys. Rev. B*, 1994, **50**, 17953–17979.

(156) G. Kresse and D. Joubert, *Phys. Rev. B*, 1991, **59**, 1758–1775.

(157) M. Schüler, O. E. Peil, G. J. Kraberger, R. Pordzik, M. Marsman, G. Kresse, T. O. Wehling and M. Aichhorn, *J. Phys.: Condens. Matter*, 2018, **30**, 475901.

(158) K. Momma and F. Izumi, *J. Appl. Crystallogr.*, 2008, **41**, 653–658.

(159) J. Kübler, K. H. Höck, J. Sticht and A. R. Williams, *J. Appl. Phys.*, 1988, **63**, 3482–3486.

(160) W. Tang, E. Sanville and G. Henkelman, *J. Phys. Condens. Matter*, 2009, **21**, 084204.

(161) E. Sanville, S. D. Kenny, R. Smith and G. Henkelman, *J. Comput. Chem.*, 2007, **28**, 899–908.

(162) G. Henkelman, A. Arnaldsson and H. Jónsson, *Comput. Mater. Sci.*, 2006, **36**, 354–360.

(163) P. Pulay, *Chem. Phys. Lett.*, 1980, **73**, 393–398.

(164) S. R. Bahn and K. W. Jacobsen, *Comput. Sci. Eng.*, 2002, **4**, 56–66.

(165) A. H. Larsen, J. J. Mortensen, J. Blomqvist, I. E. Castelli, R. Christensen, M. Dułak, J. Friis, M. N. Groves, B. Hammer, C. Hargus, E. D. Hermes, P. C. Jennings, P. B. Jensen, J. Kermode, J. R. Kitchin, E. L. Kolsbjerg, J. Kubal, K. Kaasbjerg, S. Lysgaard, J. B. Maronsson, T. Maxson, T. Olsen, L. Pastewka, A. Peterson, C. Rostgaard, J. Schiøtz, O. Schütt, M. Strange, K. S. Thygesen, T. Vegge, L. Vilhelmsen, M. Walter, Z. Zeng and K. W. Jacobsen, *J. Phys.: Condens. Matter*, 2017, **29**, 273002.

(166) R. Fletcher, *Practical Methods of Optimization*, Wiley, Hoboken, 2nd, 2013.

(167) D. Sheppard, R. Terrell and G. Henkelman, *J. Chem. Phys.*, 2008, **128**, 134106.

(168) E. Bitzek, P. Koskinen, F. Gahler, M. Moseler and P. Gumbsch, *Phys. Rev. Lett.*, 2006, **97**, 170201.

(169) J. Nocedal, *Math. of Comput.*, 1980, **35**, 773–782.

(170) G. Henkelman, B. P. Uberuaga and H. Jónsson, *J. Chem. Phys.*, 2000, **113**, 9901–9904.

(171) G. Henkelman and H. Jónsson, *J. Chem. Phys.*, 2000, **113**, 9978–9985.

(172) M. Ångqvist, W. A. Muñoz, J. M. Rahm, E. Fransson, C. Durniak, P. Rozyczko, T. H. Rod and P. Erhart, *Adv. Theory Simul.*, 2019, **2**, 1900015.

(173) J. M. Sanchez, F. Ducastelle and D. Gratias, *Physica A*, 1984, **128**, 334–350.

(174) J. M. Sanchez, *Phys. Rev. B*, 2010, **81**, 224202.

(175) A. van de Walle, *Calphad*, 2009, **33**, 266–278.

(176) A. P. Thompson, H. M. Aktulga, R. Berger, D. S. Bolintineanu, W. M. Brown, P. S. Crozier, P. J. in 't Veld, A. Kohlmeyer, S. G. Moore, T. D. Nguyen, R. Shan, M. J. Stevens, J. Tranchida, C. Trott and S. J. Plimpton, *Comput. Phys. Commun.*, 2022, **271**, 108171.

(177) D. Frenkel and B. Smit, in *Understanding Molecular Simulation (Second Edition)*, ed. D. Frenkel and B. Smit, Academic Press, San Diego, 2002, pp. 139–163.

(178) R. Car and M. Parrinello, *Phys. Rev. Lett.*, 1985, **55**, 2471–2474.

(179) I. Batatia, D. P. Kovacs, S. N. Gregor, C. Ortner and G. Csanyi, version v2, *arXiv*, 2023, DOI: 10.48550/arXiv.2205.06643.

(180) I. Batatia, S. Batzner, D. P. Kovacs, A. Musaelian, G. N. C. Simm, R. Drautz, C. Ortner, B. Kozinsky and G. Csanyi, *Nat. Mach. Intell.*, 2025, **7**, 56–67.

(181) G. Wang, C. Wang, X. Zhang, Z. Li, J. Zhou and Z. Sun, *iScience*, 2024, **27**, 109673.

(182) A. Duval, S. V. Mathis, C. K. Joshi, V. Schmidt, S. Miret, F. D. Malliaros, T. Cohen, P. Liò, Y. Bengio and M. Bronstein, *A Hitchhiker's Guide to Geometric GNNs for 3D Atomic Systems*, 2024.

(183) R. Drautz, *Phys. Rev. B*, 2019, **99**, DOI: 10.1103/PhysRevB.99.014104.

(184) N. Leimeroth, L. Erhard, K. Albe and J. Rohrer, *Modelling Simul. Mater. Sci. Eng.*, 2025, 065012.

(185) Y. Duan, J. Wang, D. Xu, P. Ji, H. Zhou, Y. Li, S. Yang, Z. Xie, X. Hai, X. Lei, R. Sun, Z. Fan, K. Zhang, S. Liu and Z. Liu, *Adv. Funct. Mater.*, 2024, **34**, 2312638.

(186) J. Siekmann, S. Ravishankar and T. Kirchartz, *ACS Energy Lett.*, 2021, **6**, 3244–3251.

(187) Z. Ni, C. Bao, Y. Liu, Q. Jiang, W.-Q. Wu, S. Chen, X. Dai, B. Chen, B. Hartweg, Z. Yu, Z. Holman and J. Huang, *Science*, 2020, **367**, 1352–1358.

(188) P. Gratia, I. Zimmermann, P. Schouwink, J.-H. Yum, J.-N. Audinot, K. Sivula, T. Wirtz and M. K. Nazeeruddin, *ACS Energy Lett.*, 2017, **2**, 2686–2693.

(189) L. Wang, K. Wang and B. Zou, *J. Phys. Chem. Lett.*, 2016, **7**, 2556–2562.

(190) T.-Y. Yang, G. Gregori, N. Pellet, M. Grätzel and J. Maier, *Angew. Chem. Int. Ed.*, 2015, **54**, 7905–7910.

(191) D. Meggiolaro and F. De Angelis, *ACS Energy Lett.*, 2018, **3**, 2206–2222.

(192) V. Adinolfi, M. Yuan, R. Comin, E. S. Thibau, D. Shi, M. I. Saidaminov, P. Kanjanaboos, D. Kopilovic, S. Hoogland, Z.-H. Lu, O. M. Bakr and E. H. Sargent, *Adv. Mater.*, 2016, **28**, 3406–3410.

(193) Y. Chen, H. T. Yi, X. Wu, R. Haroldson, Y. N. Gartstein, Y. I. Rodionov, K. S. Tikhonov, A. Zakhidov, X. Y. Zhu and V. Podzorov, *Nat. Commun.*, 2016, **7**, 12253.

(194) D. W. De Quilettes, S. M. Vorpahl, S. D. Stranks, H. Nagaoka, G. E. Eperon, M. E. Ziffer, H. J. Snaith and D. S. Ginger, *Science*, 2015, **348**, 683–686.

(195) T. Leijtens, G. E. Eperon, A. J. Barker, G. Grancini, W. Zhang, J. M. Ball, A. R. S. Kandada, H. J. Snaith and A. Petrozza, *Energy Environ. Sci.*, 2016, **9**, 3472–3481.

(196) J. Dai, W. Tang, T. Li, C. Xu, M. Zhao, P. Ji, X. Li, F. Zhang, H. Cai and X. Wu, *Nanomater.*, 2025, **15**, 981.

(197) G. Richardson, S. E. J. O'Kane, R. G. Niemann, T. A. Peltola, J. M. Foster, P. J. Cameron and A. B. Walker, *Energy Environ. Sci.*, 2016, **9**, 1476–1485.

(198) S. Van Reenen, M. Kemerink and H. J. Snaith, *J. Phys. Chem. Lett.*, 2015, **6**, 3808–3814.

(199) Y. Zhao, W. Zhou, W. Ma, S. Meng, H. Li, J. Wei, R. Fu, K. Liu, D. Yu and Q. Zhao, *ACS Energy Lett.*, 2016, **1**, 266–272.

(200) T. Leijtens, E. T. Hoke, G. Grancini, D. J. Slotcavage, G. E. Eperon, J. M. Ball, M. De Bastiani, A. R. Bowring, N. Martino, K. Wojciechowski, M. D. McGehee, H. J. Snaith and A. Petrozza, *Adv. Energy Mater.*, 2015, **5**, 1500962.

(201) D. W. De Quilettes, W. Zhang, V. M. Burlakov, D. J. Graham, T. Leijtens, A. Osherov, V. Bulović, H. J. Snaith, D. S. Ginger and S. D. Stranks, *Nat. Commun.*, 2016, **7**, 11683.

(202) E. T. Hoke, D. J. Slotcavage, E. R. Dohner, A. R. Bowring, H. I. Karunadasa and M. D. McGehee, *Chem. Sci.*, 2015, **6**, 613–617.

(203) W. Nie, J.-C. Blancon, A. J. Neukirch, K. Appavoo, H. Tsai, M. Chhowalla, M. A. Alam, M. Y. Sfeir, C. Katan, J. Even, S. Tretiak, J. J. Crochet, G. Gupta and A. D. Mohite, *Nat. Commun.*, 2016, **7**, 11574.

(204) A. Manekkathodi, A. Marzouk, J. Ponraj, A. Belaidi and S. Ashhab, *ACS Appl. Energy Mater.*, 2020, **3**, 6302–6309.

(205) Y. Shao, Y. Fang, T. Li, Q. Wang, Q. Dong, Y. Deng, Y. Yuan, H. Wei, M. Wang, A. Gruverman, J. Shield and J. Huang, *Energy Environ. Sci.*, 2016, **9**, 1752–1759.

(206) J. Xing, Q. Wang, Q. Dong, Y. Yuan, Y. Fang and J. Huang, *Phys. Chem. Chem. Phys.*, 2016, **18**, 30484–30490.

(207) R. A. Evarestov, A. Senocrate, E. A. Kotomin and J. Maier, *Phys. Chem. Chem. Phys.*, 2019, **21**, 7841–7846.

(208) J. A. Steele, V. Prakasam, H. Huang, E. Solano, D. Chernyshov, J. Hofkens and M. B. J. Roeffaers, *J. Am. Chem. Soc.*, 2021, **143**, 10500–10508.

(209) J. E. Gonzalez, J. G. Danelon, J. L. F. Da Silva and M. P. Lima, *ACS Appl. Mater. Interfaces*, 2024, **16**, 39251–39265.

(210) M. Han, C. Peng, R. Song, F. Ke, Y. S. G. Nashed, W. L. Mao, C. Jia and Y. Lin, *J. Mater. Chem. A*, 2024, **12**, 11082–11089.

(211) K. E. Kweon, J. Varley, T. Ogitsu, L. F. Wan, M. Shelby, Z. Song, R. J. Ellingson, Y. Yan and J. R. I. Lee, *Chem. Mater.*, 2023, **35**, 2321–2329.

(212) F. Ke, C. Wang, C. Jia, N. R. Wolf, J. Yan, S. Niu, T. P. Devereaux, H. I. Karunadasa, W. L. Mao and Y. Lin, *Nat. Commun.*, 2021, **12**, 461.

(213) A. Marronnier, G. Roma, S. Boyer-Richard, L. Pedesseau, J.-M. Jancu, Y. Bonnassieux, C. Katan, C. C. Stoumpos, M. G. Kanatzidis and J. Even, *ACS Nano.*, 2018, **12**, 3477–3486.

(214) D. W. Ferdani, S. R. Pering, D. Ghosh, P. Kubiak, A. B. Walker, S. E. Lewis, A. L. Johnson, P. J. Baker, M. S. Islam and P. J. Cameron, *Energy Environ. Sci.*, 2019, **12**, 2264–2272.

(215) Y. Hu, F. Bai, X. Liu, Q. Ji, X. Miao, T. Qiu and S. Zhang, *ACS Energy Lett.*, 2017, **2**, 2219–2227.

(216) N. De Marco, H. Zhou, Q. Chen, P. Sun, Z. Liu, L. Meng, E.-P. Yao, Y. Liu, A. Schiffer and Y. Yang, *Nano Letters*, 2016, **16**, 1009–1016.

(217) J. Cao, S. X. Tao, P. A. Bobbert, C.-P. Wong and N. Zhao, *Adv. Mater.*, 2018, **30**, 1707350.

(218) M. Zhang, G. Xiang, Y. Wu, J. Liu, J. Leng, C. Cheng and H. Ma, *Opt. Express*, 2023, **31**, 28624.

(219) I. S. Torres, J. L. F. Da Silva and M. P. Lima, *J. Phys. Chem. C*, 2023, **127**, 1713–1721.

(220) Z. Fang, M. H. Shang, X. M. Hou, Y. P. Zheng, Z. T. Du, Z. B. Yang, K. C. Chou, W. Y. Yang, Z. L. Wang and Y. Yang, *Nano. Energy*, 2019, **61**, 389–396.

(221) Y. Chen, H. Jing, F. Ling, W. Kang, T. Zhou, X. Liu, W. Zeng, Y. Zhang, L. Qi, L. Fang and M. Zhou, *Chem. Phys. Lett.*, 2019, **722**, 90–95.

(222) S. Xiang, W. Li, Y. Wei, J. Liu, H. Liu, L. Zhu and H. Chen, *Nanoscale*, 2018, **10**, 9996–10004.

(223) D. H. Sidiq, S. Mahato, T. Haposan, M. Makowski, D. Kowal, M. E. Witkowski, W. Drozdowski, Arramel and M. D. Birowosuto, *J. Phys. Chem. C*, 2024, **128**, 20324–20332.

(224) C. Lee, K. Chae, Y. Ko, C. Lee, T. Kim, S. Park, M. Y. Jung, J. Kim, Y. J. Yun, M. Lee and Y. Jun, *ACS Appl. Mater. Interfaces*, 2023, **15**, 51050–51058.

(225) P. Pansa-Ngat, K. Singh, B. Patel, C. Seriwattanachai, P. Kanjanaboos and O. Voznyy, *Chem. Mater.*, 2023, **35**, 271–279.

(226) A. N. Arber, Vikram, F. C. Mocanu and M. S. Islam, *Chem. Mater.*, 2025, **37**, 4416–4424.

(227) Y. W. Woo, Y.-K. Jung, G. Y. Kim, S. Kim and A. Walsh, *Discov. Mater.*, 2022, **2**, 8.

(228) S. P. Ong, W. D. Richards, A. Jain, G. Hautier, M. Kocher, S. Cholia, D. Gunter, V. L. Chevrier, K. A. Persson and G. Ceder, *Comput. Mater. Sci.*, 2013, **68**, 314–319.

(229) V. Tyagi, M. Pols, G. Brocks and S. Tao, *J. Phys. Chem. Lett.*, 2025, **16**, 5153–5159.

(230) A. Senocrate, I. Spanopoulos, N. Zibouche, J. Maier, M. S. Islam and M. G. Kanatzidis, *Chem. Mater.*, 2021, **33**, 719–726.

(231) A. R. McCluskey, A. G. Squires, J. Dunn, S. W. Coles and B. J. Morgan, *J. Open Source Softw.*, 2024, **9**, 5984.

(232) A. R. McCluskey, S. W. Coles and B. J. Morgan, *arxiv*, 2024, DOI: `10.48550/arXiv.2305.18244`.

(233) J. Mizusaki, K. Arai and K. Fueki, *Solid State Ion.*, 1983, **11**, 203–211.

(234) R. L. Narayan, M. V. S. Sarma and S. V. Suryanarayana, *J. Mater. Sci. Lett.*, 1987, **6**, 93–94.

(235) T. A. Kuku, *Thin Solid Films*, 1998, **325**, 246–20.

(236) S. M. Islam, *J. Mater. Chem.*, 2000, **10**, 1027–1038.

(237) M. Yashima, K. Nomura, H. Kageyama, Y. Miyazaki, N. Chitose and K. Adachi, *Chem. Phys. Lett.*, 2003, **380**, 391–396.

(238) T. A. Kuku, *Solid State Ion.*, 1987, **25**, 105–108.

(239) R. L. Narayan and S. V. Suryanarayana, *Mater. Lett.*, 1991, **11**, 305–308.

(240) A. Nur'aini, S. Lee and I. Oh, *J. Electrochem. Sci. Technol.*, 2022, **13**, 71–77.

(241) S. R. G. Balestra, J. M. Vicent-Luna, S. Calero, S. Tao and J. A. Anta, *J. Mater. Chem. A*, 2020, **8**, 11824–11836.

(242) R. D. Shannon, *Acta Crystallogr. A*, 1976, **32**, 751–767.

(243) S. Hu, J. Thiesbrummel, J. Pascual, M. Stolterfoht, A. Wakamiya and H. J. Snaith, *Chem. Rev.*, 2024, **124**, 4079–4123.

(244) J. Godt, F. Scheidig, C. Grosse-Siestrup, V. Esche, P. Brandenburg, A. Reich and D. A. Groneberg, *J. Occup. Med. Toxicol.*, 2006, **1**, 22.

(245) T. Moot, J. B. Patel, G. McAndrews, E. J. Wolf, D. Morales, I. E. Gould, B. A. Rosales, C. C. Boyd, L. M. Wheeler, P. A. Parilla, S. W. Johnston, L. T. Schelhas, M. D. McGehee and J. M. Luther, *ACS Energy Lett.*, 2021, **6**, 2038–2047.

(246) R. Gehlhaar, T. Merckx, W. Qiu and T. Aernouts, *Glob. Chall.*, 2018, **2**, 1800008.

(247) S. Reichert, J. Flemming, Q. An, Y. Vaynzof, J.-F. Pietschmann and C. Deibel, *Phys. Rev. Appl.*, 2020, **13**, 034018.

(248) D. V. Talapin, J.-S. Lee, M. V. Kovalenko and E. V. Shevchenko, *Chem. Rev.*, 2010, **110**, 389–458.

(249) J. Riegler and T. Nann, *Anal. Bioanal. Chem.*, 2004, **379**, 913–919.

(250) M. A. Boles, D. Ling, T. Hyeon and D. V. Talapin, *Nat. Mater.*, 2016, **15**, 141–153.

(251) M. C. Weidman, M. Seitz, S. D. Stranks and W. A. Tisdale, *ACS Nano.*, 2016, **10**, 7830–7839.

(252) A. Dey, J. Ye, A. De, E. Debroye, S. K. Ha, E. Bladt, A. S. Kshirsagar, Z. Wang, J. Yin, Y. Wang, L. N. Quan, F. Yan, M. Gao, X. Li, J. Shamsi, T. Debnath, M. Cao, M. A. Scheel, S. Kumar, J. A. Steele, M. Gerhard, L. Chouhan, K. Xu, X. G. Wu, Y. Li, Y. Zhang, A. Dutta, C. Han, I. Vincon, A. L. Rogach, A. Nag, A. Samanta, B. A. Korgel, C. J. Shih, D. R. Gamelin, D. H. Son, H. Zeng, H. Zhong, H. Sun, H. V. Demir, I. G. Scheblykin, I. Mora-Sero, J. K. Stolarczyk, J. Z. Zhang, J. Feldmann, J. Hofkens, J. M. Luther, J. Perez-Prieto, L. Li, L. Manna, M. I. Bodnarchuk, M. V. Kovalenko, M. B. J. Roeffaers, N. Pradhan, O. F. Mohammed, O. M. Bakr, P. Yang, P. Muller-Buschbaum, P. V. Kamat, Q. Bao, Q. Zhang, R. Krahne, R. E. Galian, S. D. Stranks, S. Bals, V. Biju, W. A. Tisdale, Y. Yan, R. L. Z. Hoye and L. Polavarapu, *ACS Nano.*, 2021, **15**, 10775–10981.

(253) H. Huang, L. Polavarapu, J. A. Sichert, A. S. Susha, A. S. Urban and A. L. Rogach, *NPG Asia Mater.*, 2016, **8**, e328–e328.

(254) I. Mosquera-Lois, Y.-T. Huang, H. Lohan, J. Ye, A. Walsh and R. L. Z. Hoye, *Nat. Rev. Chem.*, 2025, **9**, 287–304.

(255) S. Han, W. H. Jeong, G. Seo, S. Choi, D. G. Lee, W. S. Chae, H. Ahn, T. K. Lee, H. Choi, J. Choi, B. R. Lee and Y. Kim, *Adv. Mater.*, 2025, **37**, e2410128.

(256) M. S. Hammer, H. Schlott, L. Lüer, C. J. Brabec, M. Sytnyk, J. Will, B. Meyer and W. Heiss, *Nat. Rev. Mater.*, 2025, **10**, 311–325.

(257) M. A. Becker, R. Vaxenburg, G. Nedelcu, P. C. Sercel, A. Shabaev, M. J. Mehl, J. G. Michopoulos, S. G. Lambrakos, N. Bernstein, J. L. Lyons, T. Stöferle, R. F. Mahrt, M. V. Kovalenko, D. J. Norris, G. Rainò and A. L. Efros, *Nature*, 2018, **553**, 189–193.

(258) D. Ghoshal, T. Wang, H.-Z. Tsai, S.-W. Chang, M. Crommie, N. Koratkar and S.-F. Shi, *Adv. Opt. Mater.*, 2019, **7**, 1900039.

(259) S. Wang, M. Dyksik, C. Lampe, M. Gramlich, D. K. Maude, M. Baranowski, A. S. Urban, P. Plochocka and A. Surrente, *Nano. Lett.*, 2022, **22**, 7011–7019.

(260) B. T. Diroll, P. Banerjee and E. V. Shevchenko, *Nano Converg.*, 2023, **10**, 18.

(261) C. Otero-Martinez, J. Ye, J. Sung, I. Pastoriza-Santos, J. Perez-Juste, Z. Xia, A. Rao, R. L. Z. Hoye and L. Polavarapu, *Adv. Mater.*, 2022, **34**, e2107105.

(262) S. Toso, D. Baranov, D. Altamura, F. Scattarella, J. Dahl, X. Wang, S. Marras, A. P. Alivisatos, A. Singer, C. Giannini and L. Manna, *ACS Nano.*, 2021, **15**, 6243–6256.

(263) H. Huang, Y. Li, Y. Tong, E.-P. Yao, M. W. Feil, A. F. Richter, M. Döblinger, A. L. Rogach, J. Feldmann and L. Polavarapu, *Angew. Chem. Int. Ed.*, 2019, **58**, 16558–16562.

(264) M. Chen, T. Zhang, A. Elsukova, Z. Hu, R. Zhang, Y. Wang, X. Liu, X. Liu and F. Gao, *Small*, 2024, **20**, 2306360.

(265) H. Song, J. Yang, W. H. Jeong, J. Lee, T. H. Lee, J. W. Yoon, H. Lee, A. J. Ramadan, R. D. J. Oliver, S. C. Cho, S. G. Lim, J. W. Jang, Z. Yu, J. T. Oh, E. D. Jung, M. H. Song, S. H. Park, J. R. Durrant, H. J. Snaith, S. U. Lee, B. R. Lee and H. Choi, *Adv. Mater.*, 2023, **35**, e2209486.

(266) L. De Trizio, I. Infante and L. Manna, *Acc. Chem. Res.*, 2023, **56**, 1815–1825.

(267) J. De Roo, M. Ibanez, P. Geiregat, G. Nedelcu, W. Walravens, J. Maes, J. C. Martins, I. Van Driessche, M. V. Kovalenko and Z. Hens, *ACS Nano.*, 2016, **10**, 2071–81.

(268) T. Kim, S. Park and S. Jeong, *Nat. Commun.*, 2021, **12**, 3013.

(269) X. Peng, J. Wickham and A. P. Alivisatos, *J. Am. Chem. Soc.*, 1998, **120**, 5343–5344.

(270) C. B. Murray, D. J. Norris and M. G. Bawendi, *J. Am. Chem. Soc.*, 1993, **115**, 8706–8715.

(271) D. Pan, Q. Wang and L. An, *J. Mater. Chem.*, 2009, **19**, 1063–1073.

(272) F. Haque, M. Wright, M. A. Mahmud, H. Yi, D. Wang, L. Duan, C. Xu, M. B. Upama and A. Uddin, *ACS Omega*, 2018, **3**, 11937–11944.

(273) J. A. S. Laranjeira, S. A. Azevedo, G. S. L. Fabris, J. R. Sambrano and M. M. Ferrer, *Comp. Mater. Sci.*, 2024, **239**, DOI: 10.1016/j.commatsci.2024.112977.

(274) S. Grimme, J. Antony, S. Ehrlich and H. Krieg, *J. Chem. Phys.*, 2010, **132**, 154104.

(275) D. M. Trots and S. V. Myagkota, *J. Phys. Chem. Solids*, 2008, **69**, 2520–2526.

(276) B. Chen, P. N. Rudd, S. Yang, Y. Yuan and J. Huang, *Chem. Soc. Rev.*, 2019, **48**, 3842–3867.

(277) X. Zhang, H. Huang, C. Zhao and J. Yuan, *Chem. Soc. Rev.*, 2025, **54**, 3017–3060.

(278) X. Shen, K. Kang, Z. Yu, W. H. Jeong, H. Choi, S. H. Park, S. D. Stranks, H. J. Snaith, R. H. Friend and B. R. Lee, *Joule*, 2023, **7**, 272–308.

(279) N. Fiuza-Maneiro, K. Sun, I. López-Fernández, P. Gómez-Graña, Sergio and Müller-Buschbaum and L. Polavarapu, *ACS Energy Lett.*, 2023, **8**, 1152–1191.

(280) M. Yu and D. R. Trinkle, *J. Chem. Phys.*, 2011, **134**, 064111.

(281) Z. Jia, R. Wang, L. Zhu, A. Altujjar, P. Jacoutot, O. M. Alkhudhari, M. Z. Mokhtar, B. F. Spencer, N. W. Hodson, X. Wang, M. Osborne-Richards, A. G. Thomas, T. Hashimoto, M. Faulkner, D. J. Lewis, S. A. Haque, M. S. Islam, J. M. Saunders and B. R. Saunders, *Energy Environ. Sci.*, 2024, **17**, 7221–7233.

(282) T. Webb, F. Vanin, D. Gao, L. Zhu, W. D. J. Tremlett, A. Azaden, A. Rodgers, P. Jacoutot, A. J. P. White, M. S. Islam, N. J. Long, Z. Zhu and S. A. Haque, *Energy Environ. Sci.*, 2026, 605–618.

(283) D. M. Powell, M. T. Winkler, H. J. Choi, C. B. Simmons, D. B. Needleman and T. Buonassisi, *Energy Environ. Sci.*, 2012, **5**, 5874.

(284) L. Duan, D. Walter, N. Chang, J. Bullock, D. Kang, S. P. Phang, K. Weber, T. White, D. Macdonald, K. Catchpole and H. Shen, *Nat. Rev. Mater.*, 2023, **8**, 261–281.

(285) H. Tong, S. Tan, Y. Zhang, Y. He, C. Ding, H. Zhang, J. He, J. Cao, H. Liu, Y. Li, J. Kang, X. Xu, C. Chen, Y. Chen, F. Sun, B. Feng, H. Sun, X. Jiang, L. Yu, J. Li, D. He, J. Li and Z. Li, *Nat. Commun.*, 2025, **16**, 5920.

(286) A. Martí and G. L. Araújo, *Sol. Energy Mater. Sol. Cells*, 1996, **43**, 203–222.

(287) D. P. McMeekin, G. Sadoughi, W. Rehman, G. E. Eperon, M. Saliba, M. T. Hörantner, A. Haghighirad, N. Sakai, L. Korte, B. Rech, M. B. Johnston, L. M. Herz and H. J. Snaith, *Science*, 2016, **351**, 151–155.

(288) M. Roß, S. Severin, M. B. Stutz, P. Wagner, H. Köbler, M. Favin-Lévêque, A. Al-Ashouri, P. Korb, P. Tockhorn, A. Abate, B. Stannowski, B. Rech and S. Albrecht, *Adv. Energy Mater.*, 2021, **11**, 2101460.

(289) *Oxford PV*, `https://www.oxfordpv.com/`, 2026.

(290) C. M. Sterling, C. Kamal, A. Garcia-Fernandez, G. J. Man, S. Svanstrom, P. K. Nayak, S. M. Butorin, H. Rensmo, U. B. Cappel and M. Odelius, *J. Phys. Chem. C Nanomater. Interfaces*, 2022, **126**, 20143–20154.

(291) Z. Zhu, K. Mao and J. Xu, *J. Energy Chem.*, 2021, **58**, 219–232.

(292) G. E. Eperon, M. T. Hörantner and H. J. Snaith, *Nat. Rev. Chem.*, 2017, **1**, 0095.

(293) F. Hao, C. C. Stoumpos, R. P. Chang and M. G. Kanatzidis, *J. Am. Chem. Soc.*, 2014, **136**, 8094–9.

(294) R. Dalven, *Infrared Phys. Technol.*, 1969, **9**, 141–184.

(295) S. Kumar, T. Sharma, M. Zulfequar and M. Husain, *Phys. B: Condens. Matter*, 2003, **325**, 8–16.

(296) J. J. H. Pijpers, R. Ulbricht, K. J. Tielrooij, A. Osherov, Y. Golan, C. Delerue, G. Allan and M. Bonn, *Nat. Phys.*, 2009, **5**, 811–814.

(297) U. Chalapathi, S.-H. Park and W. J. Choi, *Mater. Sci. Semicond. Process*, 2021, **136**, 106147.

(298) N. Koteeswara Reddy, M. Devika and E. S. R. Gopal, *Crit. Rev. Solid State Mater. Sci.*, 2015, **40**, 359–398.

(299) S. Gedi, V. R. Minnam Reddy, C. Park, J. Chan-Wook and R. R. K.T, *Opt. Mater.*, 2015, **42**, 468–475.

(300) P. Sinsermsuksakul, J. Heo, W. Noh, A. S. Hock and R. G. Gordon, *Adv. Energy Mater.*, 2011, **1**, 1116–1125.

(301) V. R. Minnam Reddy, S. Gedi, C. Park, M. R.W and R. R. K.T, *Curr. Appl. Phys.*, 2015, **15**, 588–598.

(302) W. Albers, C. Haas and F. van der Maesen, *J. Phys. Chem. Solids*, 1960, **15**, 306–310.

(303) A. Slonopas, N. Alijabbari, C. Saltonstall, T. Globus and P. Norris, *Electrochim. Acta*, 2015, **151**, 140–149.

(304) J. Kim, E. K. Ampadu, W. J. Choi and E. Oh, *Nanotechnology*, 2019, **30**, 075201.

(305) Q. Tan, L.-D. Zhao, J.-F. Li, C.-F. Wu, T.-R. Wei, Z.-B. Xing and M. G. Kanatzidis, *J. Mater. Chem. A*, 2014, **2**, 17302–17306.

(306) B. Zhou, S. Li, W. Li, J. Li, X. Zhang, S. Lin, Z. Chen and Y. Pei, *ACS Appl. Mater. Interfaces*, 2017, **9**, 34033–34041.

(307) K. J. Norton, F. Alam and D. J. Lewis, *Appl. Sci.*, 2021, **11**, DOI: 10.3390/app11052062.

(308) C. M. Zeuthen, P. S. Thorup, N. Roth and B. B. Iversen, *J. Am. Chem. Soc.*, 2019, **141**, 8146–8157.

(309) T. Chattopadhyay, J. Pannetier and H. G. Von Schnering, *J. Phys. Chem. Solids*, 1986, **47**, 879–885.

(310) A. Lebedev, I. Sluchinskaya and I. Munro, *J. Synchrotron Radiat.*, 2001, **8**, 800–802.

(311) P. Mori-Sánchez, A. J. Cohen and W. Yang, *Phys. Rev. Lett.*, 2008, **100**, 146401.

(312) T. J. Whittles, L. A. Burton, J. M. Skelton, A. Walsh, T. D. Veal and V. R. Dhanak, *Chem. Mater.*, 2016, **28**, 3718–3726.

(313) T. A. Berhe, W.-N. Su, C.-H. Chen, C.-J. Pan, J.-H. Cheng, H.-M. Chen, M.-C. Tsai, L.-Y. Chen, A. A. Dubale and B.-J. Hwang, *Energy Environ. Sci.*, 2016, **9**, 323–356.

(314) Y. Han, S. Meyer, Y. Dkhissi, K. Weber, J. M. Pringle, U. Bach, L. Spiccia and Y.-B. Cheng, *J. Mater. Chem. A*, 2015, **3**, 8139–8147.

(315) N. Aristidou, I. Sanchez-Molina, T. Chotchuangchutchaval, M. Brown, L. Martinez, T. Rath and S. A. Haque, *Angew. Chem. Int. Ed.*, 2015, **54**, 8208–8212.

(316) G. Divitini, S. Cacovich, F. Matteocci, L. Cinà, A. Di Carlo and C. Ducati, *Nat. Energy*, 2016, **1**, 15012.

(317) Z. Song, A. Abate, S. C. Watthage, G. K. Liyanage, A. B. Phillips, U. Steiner, M. Graetzel and M. J. Heben, *Adv. Energy Mater.*, 2016, **6**, 1600846.

(318) Z. Yao, W. Zhao and S. Liu, *J. Mater. Chem. A*, 2021, **9**, 11124–11144.

(319) T. L. Leung, I. Ahmad, A. A. Syed, A. M. C. Ng, J. Popović and A. B. Djurišić, *Commun. Mater.*, 2022, **3**, 63.

(320) G. Liu, H. Zheng, X. Xu, S. Xu, X. Zhang, X. Pan and S. Dai, *Adv. Funct. Mater.*, 2019, **29**, 1807565.

(321) P. Chen, D. He, X. Huang, C. Zhang and L. Wang, *ACS Nano.*, 2023, **18**, 67–88.

(322) Q. Lin, A. Armin, P. L. Burn and P. Meredith, *Acc. Chem. Res.*, 2016, **49**, 545–53.

(323) M. L. Petrus, J. Schlipf, C. Li, T. P. Gujar, N. Giesbrecht, P. Müller-Buschbaum, M. Thelakkat, T. Bein, S. Hüttner and P. Docampo, *Adv. Energy Mater.*, 2017, **7**, 1700264.

(324) B. A. Rosales, M. P. Hanrahan, B. W. Boote, A. J. Rossini, E. A. Smith and J. Vela, *ACS Energy Lett.*, 2017, **2**, 906–914.

(325) Y. An, J. Hidalgo, C. A. R. Perini, A.-F. Castro-Méndez, J. N. Vagott, K. Bairley, S. Wang, X. Li and J.-P. Correa-Baena, *ACS Energy Lett.*, 2021, **6**, 1942–1969.

(326) B. R. Wygant, A. Z. Ye, A. Dolocan, Q. Vu, D. M. Abbot and C. B. Mullins, *J. Am. Chem. Soc.*, 2019, **141**, 18170–18181.

(327) D. Thrithamarassery Gangadharan and D. Ma, *Energy Environ. Sci.*, 2019, **12**, 2860–2889.

(328) S. Ahmad, P. Fu, S. Yu, Q. Yang, X. Liu, X. Wang, X. Wang, X. Guo and C. Li, *Joule*, 2019, **3**, 794–806.

(329) C. Ma, D. Shen, T. W. Ng, M. F. Lo and C. S. Lee, *Adv. Mater.*, 2018, **30**, e1800710.

(330) Q. He, M. Worku, L. Xu, C. Zhou, H. Lin, A. J. Robb, K. Hanson, Y. Xin and B. Ma, *ACS Appl. Mater. Interfaces*, 2020, **12**, 1159–1168.

(331) Z. Peng, A. Vincze, F. Streller, V. M. Le Corre, K. Zhang, C. Li, J. Tian, C. Liu, J. Luo, Y. Zhao, A. Späth, R. Fink, T. Heumüller, A. Osvet, N. Li, M. Stolterfoht, L. Lüer and C. J. Brabec, *Energy Environ. Sci.*, 2024, **17**, 8313–8324.

(332) Akriti, Z.-Y. Lin, J. Y. Park, H. Yang, B. M. Savoie and L. Dou, *APL Mater.*, 2022, **10**, 040903.

(333) T. Niu, J. Lu, M.-C. Tang, D. Barrit, D.-M. Smilgies, Z. Yang, J. Li, Y. Fan, T. Luo, I. McCulloch, A. Amassian, S. (Liu and K. Zhao, *Energy Environ. Sci.*, 2018, **11**, 3358.

(334) L. Yan, Y. Li, S. Li, X. Sun, Y. Li, X. Han, M. Huang and X. Tao, *J. Mater. Chem. A*, 2022, **10**, 14799–14809.

(335) J. Chakkamalayath, N. Hiott and P. V. Kamat, *ACS Energy Lett.*, 2022, **8**, 169–171.

(336) F. Fiorentino, M. D. Albaqami, I. Poli and A. Petrozza, *ACS Appl. Mater. Interfaces*, 2022, **14**, 34180–34188.

(337) P. Mathew, J. Cho and P. V. Kamat, *ACS Energy Lett.*, 2024, **9**, 1103–1114.

(338) L. Luo, H. Zeng, Z. Wang, M. Li, S. You, B. Chen, A. Maxwell, Q. An, L. Cui, D. Luo, J. Hu, S. Li, X. Cai, W. Li, L. Li, R. Guo, R. Huang, W. Liang, Z.-H. Lu, L. Mai, Y. Rong, E. H. Sargent and X. Li, *Nat. Energy*, 2023, 294–303.

(339) P. Mathew, J. Cho and P. V. Kamat, *ACS Energy Lett.*, 2024, **9**, 1103–1114.

(340) G. Szabó and P. V. Kamat, *ACS Energy Lett.*, 2023, **9**, 193–200.

(341) M. Menahem, Z. Dai, S. Aharon, R. Sharma, M. Asher, Y. Diskin-Posner, R. Korobko, A. M. Rappe and O. Yaffe, *ACS Nano.*, 2021, **15**, 10153–10162.

(342) K. Xiong, W. Liu, S. J. Teat, L. An, H. Wang, T. J. Emge and J. Li, *J. Solid State Chem.*, 2015, **230**, 143–148.

(343) J. Gong, M. Hao, Y. Zhang, M. Liu and Y. Zhou, *Angew. Chem. Int. Ed. Engl.*, 2022, **61**, e202112022.

(344) A. Scardina, T. F. Loeff, Vikram, N. Mrkyvkova, R. Sala, L. Marsano, H. A. Dewi, R. Pallotta, A. Bruno, P. Siffalovic, M. S. Islam and G. Grancini, *EES Solar*, 2026, DOI: 10.1039/d6el00006a.

(345) R. E. Beal, D. J. Slotcavage, T. Leijtens, A. R. Bowring, R. A. Belisle, W. H. Nguyen, G. F. Burkhard, E. T. Hoke and M. D. McGehee, *J. Phys. Chem. Lett.*, 2016, **7**, 746–51.

(346) C. C. Stoumpos, D. H. Cao, D. J. Clark, J. Young, J. M. Rondinelli, J. I. Jang, J. T. Hupp and M. G. Kanatzidis, *Chem. Mater.*, 2016, **28**, 2852–2867.

(347) E. I. Marchenko, S. A. Fateev, A. A. Petrov, V. V. Korolev, A. Mitrofanov, A. V. Petrov, E. A. Goodilin and A. B. Tarasov, *Chem. Mater.*, 2020, **32**, 7383–7388.

(348) Z. Lin, J. Lei, P. Wang, L. Xu, X. Zhang, Y. Kang, M. Chen and G. Wei, *Phys. Status Solidi Rapid Res. Lett.*, 2021, **15**, 2100277.

Appendix A

As mentioned in the Methods section of Chapter 3, the hybrid functional HSE06 can provide a more accurate description of the perovskite lattice (Table A.1); however, the computational expense associated with using hybrid functionals in VASP is prohibitive. As a result, only GGA functionals were considered practical options for the structural relaxations due to the computational expense resulting from both the size and low-symmetry of the γ-$CsPbI_3$ cell, the number of CI-NEB calculations performed to investigate a wide range of dopants, and the thousands of structures needed to train an accurate MLIP from scratch. PBEsol was chosen, as it performs slightly better on the lattice parameter prediction.

Table A.1: Comparison of experimental and calculated unit cell parameters for PBE, PBEsol, and HSE06 on the γ-$CsPbI_3$ structure.

Parameter	**Experiment**	**PBE**	**Difference (%)**	**PBEsol**	**Difference (%)**	**HSE06**	**Difference (%)**
a (Å)	8.8561	9.0933	2.68	8.7069	-1.68	8.9105	0.61
b (Å)	8.5766	8.7354	1.85	8.6750	1.15	8.4521	-1.45
c (Å)	12.4722	12.6845	1.70	12.4439	-0.23	12.3944	-0.62
α (°)	90.0	90.0	0.00	90.0	0.00	90.0	0.00
β (°)	90.0	90.0	0.00	90.0	0.00	90.0	0.00
γ (°)	90.0	90.0	0.00	90.0	0.00	90.0	0.00
Band Gap (eV)	1.72	1.82	5.81	1.60	-6.98	2.1475	24.85

For completeness, the effects of spin-orbit coupling and the hybrid functional HSE on the band gap were also investigated (Figure A.1). The closest match to experiment is achieved by performing an electronic relaxation of HSE with a 40% Hartree–Fock component and spin-orbit coupling. However, as the focus of this work was on the perovskite lattice and the effects of ion migration, PBEsol was determined to be sufficient

for capturing both the structural and electronic effects of γ-$CsPbI_3$.

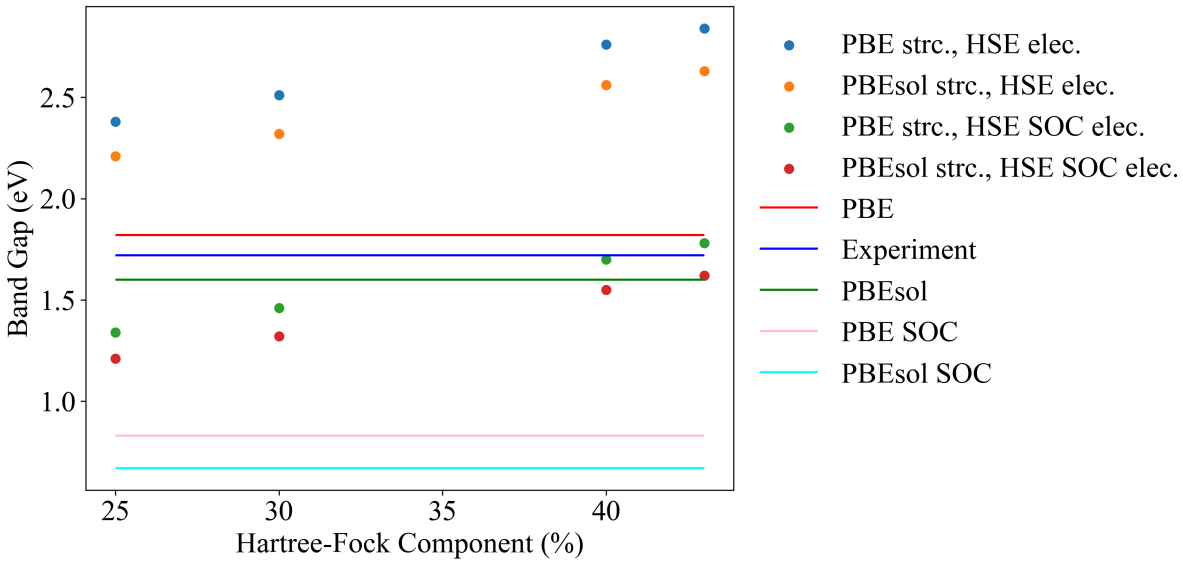


Figure A.1: Comparison of calculated band gaps on the PBE- and PBEsol-relaxed γ-$CsPbI_3$ structures. In some cases, HSE was used to perform an electronic relaxation on the already-relaxed structure. This is denoted by listing the functional used for the structural relaxation and the functional used for the electronic relaxation. A range of Hartree–Fock contributions were tested as well as the effect of spin-orbit coupling.

The electronic convergence tests for γ-$CsPbI_3$ (Figure A.2) indicate that an energy cut-off of 500 eV provides a suitable balance between computational efficiency and numerical accuracy. Increasing the cut-off beyond 500 eV results in only small changes to the total energy, with differences of less than 2 meV per cell (or 0.1 meV per atom) between 500 and 700 eV for both k-spacings. These small residual changes are characteristic of the gradual convergence of the plane-wave basis and are not expected to significantly influence the calculated structural or energetic properties. Consequently, an energy cut-off of 500 eV was selected for all subsequent calculations. A k-spacing of 0.2 was also adopted as it provides sufficiently dense Brillouin-zone sampling while maintaining a reasonable computational cost for the relatively large supercells investigated in this work.

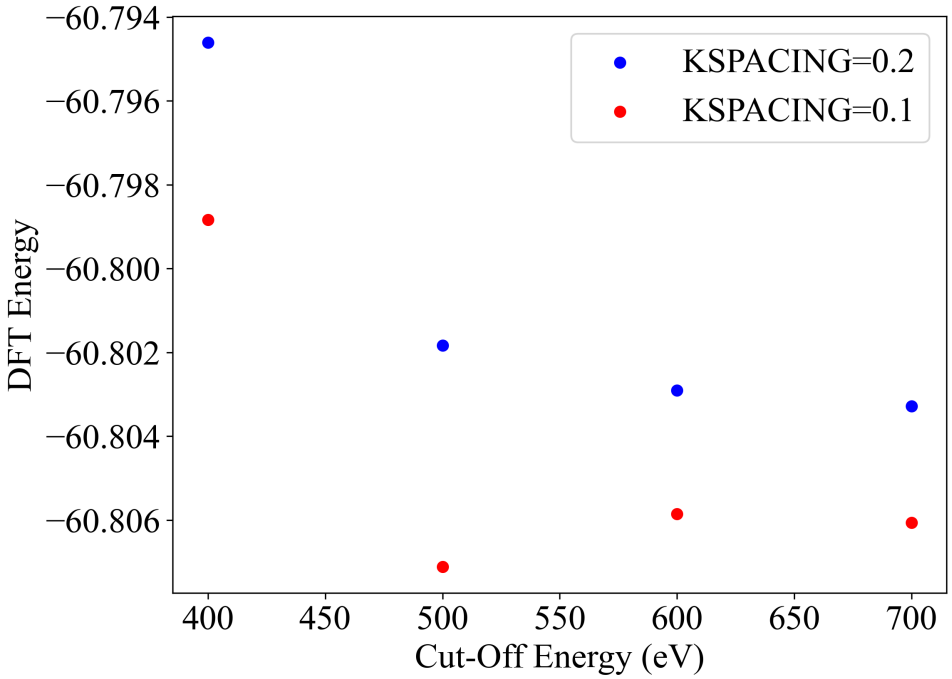


Figure A.2: DFT energies calculated for cut-off energies between 400–700 eV and k-spacings of 0.1 and 0.2 for γ-$CsPbI_3$.

Appendix B

r^{2}SCAN was initially selected as the functional for the work in Chapter 5 because it offers a balanced description of both structural and electronic properties across PbS and SnS at a moderate computational cost. While the GGA functionals PBE and PBEsol reproduce the SnS lattice parameters slightly more accurately, r^{2}SCAN provides reasonable structural agreement for both compounds without the higher computational expense of hybrid methods. More importantly, r^{2}SCAN gives the closest agreement with the experimental band gap of SnS, indicating an improved treatment of the electronic structure relative to standard GGA functionals. For PbS, where relativistic effects are significant, r^{2}SCAN also provides a suitable baseline from which spin-orbit coupling can be incorporated to improve the electronic description. For these reasons, r^{2}SCAN was adopted as the initial choice of functional, with SOC and hybrid functional calculations used selectively where needed.

Table B.1: Comparison of experimental[308] and calculated lattice parameters and lattice angles of PbS using different DFT functionals.

Functional	$a = b = c$ **(Å)**	**Difference (%)**	**Mean Angle (°)**	**Difference (%)**
Experiment	5.91	–	90.0	–
PBE	6.006	1.62	90.0	0.00
PBEsol	5.493	7.05	90.0	0.00
r^{2}SCAN	5.97	0.98	90.0	0.00
HSE06	5.965	0.94	90.0	0.00

Table B.2: Comparison of experimental[309] and calculated lattice parameters of SnS using different DFT functionals.

Functional	a (Å)	Δa (%)	b (Å)	Δb (%)	c (Å)	Δc (%)	**Angle** (°)
Experiment	4.340	–	3.970	–	11.140	–	90.0
PBE	4.368	0.63	4.040	1.77	11.283	1.29	90.0
PBEsol	4.300	0.92	3.964	0.16	11.120	0.18	90.0
r^{2}SCAN	4.423	1.92	3.991	0.53	11.308	1.51	90.0
HSE06	4.336	0.09	3.971	0.03	11.143	0.03	90.0

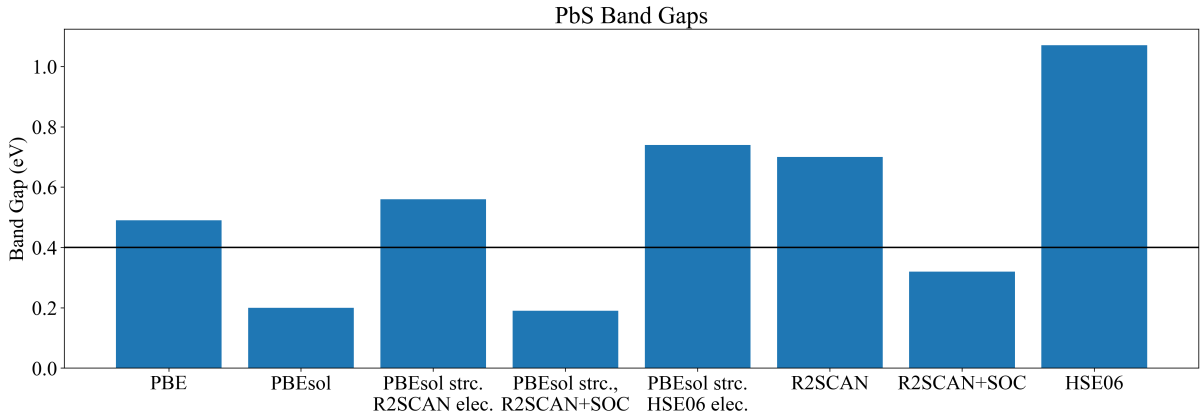


Figure B.1: Calculated band gaps for PbS obtained using the investigated functionals, compared with the experimental band gap of 0.4 eV.[308] The influence of spin-orbit coupling is also shown. In some cases, one functional was used to perform an electronic relaxation on a pre-relaxed structure of a different functional.

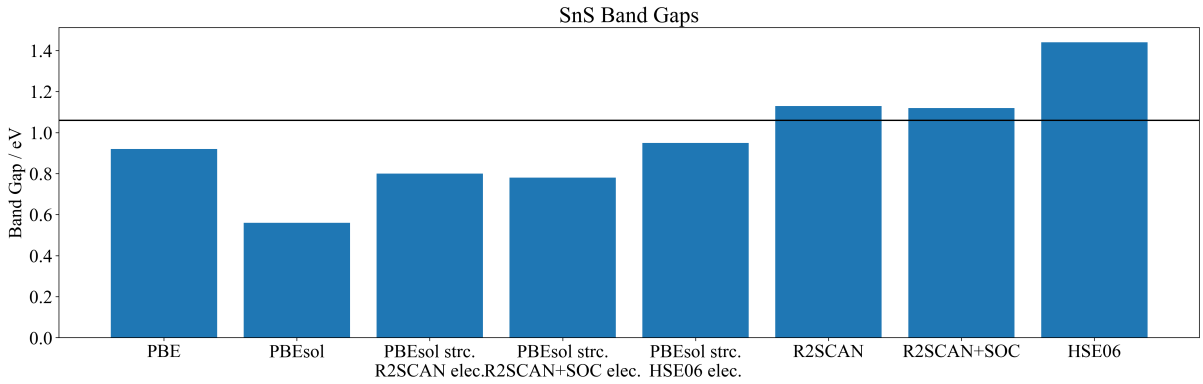


Figure B.2: Calculated band gaps for SnS obtained using the investigated functionals, compared with the experimental band gap of 1.07 eV eV.[309] The influence of spin-orbit coupling is also shown. In some cases, one functional was used to perform an electronic relaxation on a pre-relaxed structure of a different functional.

The electronic convergence behaviour of the PbS and SnS unit cells (Figures B.3 and

B.4) demonstrate that an energy cut-off of 500 eV is sufficient for reliable calculations. For both materials, increasing the cut-off from 500 to 700 eV produces only minor reductions in the total energy, corresponding to less than 1 meV per atom. Although small fluctuations are observed at higher cut-offs, these are typical of plane-wave DFT calculations and do not indicate inadequate convergence. Since the energy improvements obtained by increasing the cut-off beyond 500 eV are negligible compared with the additional computational expense, 500 eV was chosen for all subsequent simulations. A k-spacing of 0.2 was likewise employed to provide consistent and well-converged Brillouin-zone sampling across both compounds while ensuring efficient calculations.

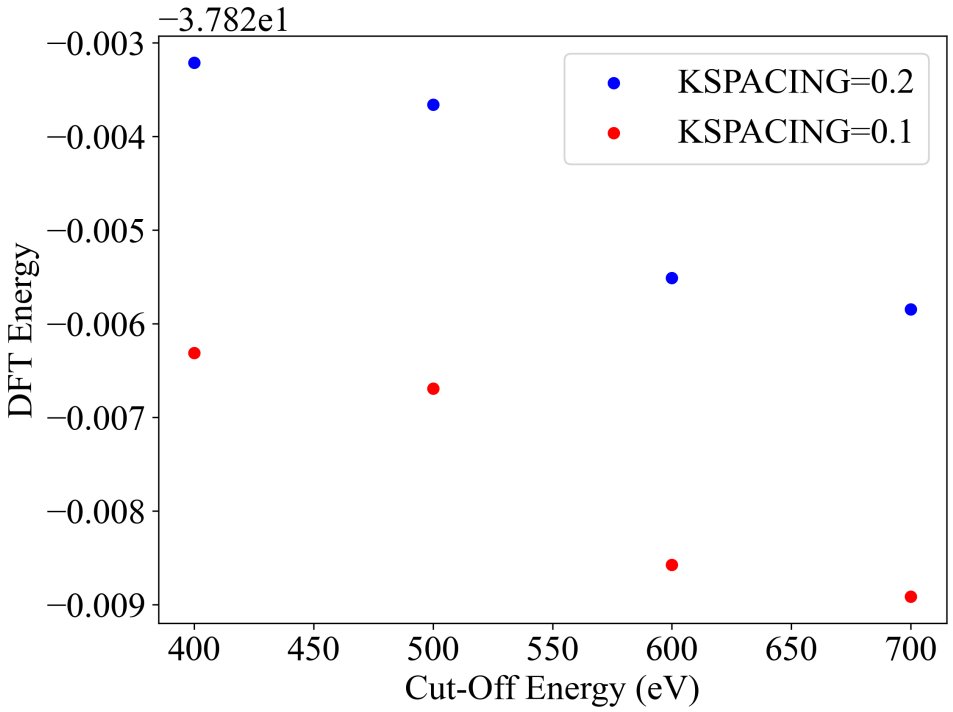


Figure B.3: DFT energies calculated for cut-off energies between 400–700 eV and k-spacings of 0.1 and 0.2 for PbS.

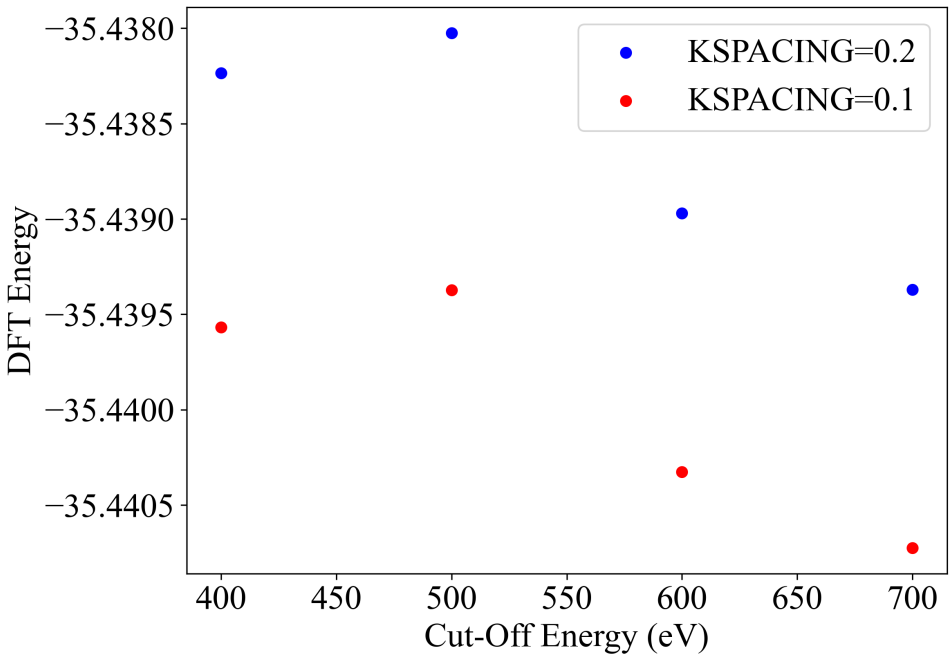


Figure B.4: DFT energies calculted for cut-off energies between 400–700 eV and k-spacings of 0.1 and 0.2 for SnS.

Appendix C

PBE with a D3 correction was selected as the methodology for for the 2D perovskite calculations described in Chapter 6 because it provides the most accurate reproduction of the experimental crystal structures. In both the Ruddlesden–Popper and Dion–Jacobson phases, the inclusion of Grimme's D3 dispersion correction reduces the lattice parameter errors relative to conventional PBE, particularly along the interlayer direction where dispersion interactions between the organic spacer cations are significant. While r^{2}SCAN produces competitive electronic properties, PBE+D3 yielded the most reliable structural description overall and is considerably less computationally demanding which is important for these large, low-symmetry structures. γ-$CsPbI_3$ was included to ensure that the methodology chosen for the 2D perovskite would also provide an accurate representation of the 3D phase for modelling heterostructures.

Table C.1: Comparison of experimental and calculated structural parameters and band gaps for the Ruddlesden–Popper structure.[341]

Functional	a (Å)	Δa (%)	b (Å)	Δb (%)	c (Å)	Δc (%)	α (°)	$\Delta\alpha$ (%)	β (°)	$\Delta\beta$ (%)	γ (°)	$\Delta\gamma$ (%)	**BG (eV)**	**ΔBG (%)**
Experiment	8.8763	–	8.6936	–	27.6162	–	90.0	–	90.0	–	90.0	–	2.30	–
PBEsol	8.7075	1.90	8.5278	1.91	28.4531	3.03	90.0	0.00	90.0	0.00	90.0	0.00	2.05	10.87
PBE	8.9398	0.72	8.7359	0.49	29.0908	5.34	90.0	0.00	90.0	0.00	90.0	0.00	2.20	4.35
PBEsol+D3	8.5475	3.70	8.3685	3.74	27.7037	0.32	90.0	0.00	90.0	0.00	90.0	0.00	1.95	15.22
PBE+D3	8.6984	2.00	8.5124	2.08	28.2328	2.23	90.0	0.00	90.0	0.00	90.0	0.00	2.13	7.39
r^{2}SCAN	8.8373	0.44	8.6647	0.33	28.4271	2.94	90.0	0.00	90.0	0.00	90.0	0.00	2.46	6.96

Although the inclusion of spin-orbit coupling within the PBE functional resulted in poorer agreement with the experimental band gaps than several of the other functionals considered (Table C.4), PBE+SOC was employed for the electronic structure mapping presented in Chapter 6 because spin-orbit coupling is essential for accurately describing

Table C.2: Comparison of experimental and calculated structural parameters and band gaps for the Dion–Jacobson structure.[342]

Functional	a (Å)	Δa (%)	b (Å)	Δb (%)	c (Å)	Δc (%)	α (°)	$\Delta\alpha$ (%)	β (°)	$\Delta\beta$ (%)	γ (°)	$\Delta\gamma$ (%)	**BG (eV)**	**ΔBG (%)**
Experiment	8.4812	–	8.7940	–	11.0562	–	76.6450	–	70.2040	–	89.2380	–	2.36	–
PBEsol	8.3999	0.96	8.7528	0.47	11.0882	0.29	77.1435	0.65	70.4732	0.38	89.3357	0.11	2.04	13.56
PBE	8.6122	1.54	8.9331	1.58	11.4384	3.46	77.1007	0.59	70.7494	0.78	89.2823	0.05	2.22	5.93
PBEsol+D3	8.2684	2.51	8.6427	1.72	10.7964	2.35	77.0661	0.55	70.3797	0.25	89.2222	0.02	1.95	17.37
PBE+D3	8.4104	0.83	8.7808	0.15	11.0630	0.06	76.8490	0.27	70.3932	0.27	89.2103	0.03	2.12	10.17
r^{2}SCAN	8.5376	0.66	8.8514	0.65	11.2237	1.51	76.7674	0.16	70.3747	0.24	89.2631	0.03	2.46	4.24

Table C.3: Comparison of experimental pseudo-cubic parameters and calculated structural parameters and band gaps for the 3D γ-$CsPbI_3$ structure.[15] The experimental lattice parameters are based on the average Pb–Pb distance.

Functional	a (Å)	Δa (%)	b (Å)	Δb (%)	c (Å)	Δc (%)	α (°)	$\Delta\alpha$ (%)	β (°)	$\Delta\beta$ (%)	γ (°)	$\Delta\gamma$ (%)	**BG (eV)**	**ΔBG (%)**
Experiment	6.0200	–	6.0200	–	12.0400	–	90.0	–	90.0	–	90.0	–	1.92	–
PBEsol	6.0500	0.50	6.0500	0.50	12.1000	0.50	90.0726	0.08	90.1609	0.18	89.9615	0.04	1.69	11.98
PBE	6.2000	2.99	6.2000	2.99	12.4000	2.99	90.0361	0.04	90.1179	0.13	90.0346	0.04	1.92	0.00
PBEsol+D3	5.9200	1.66	5.9200	1.66	11.8400	1.66	90.4679	0.52	90.1617	0.18	90.0141	0.02	1.68	12.50
PBE+D3	6.0900	1.16	6.0900	1.16	12.1800	1.16	89.9900	0.01	90.1666	0.19	90.0458	0.05	1.86	3.12
r^{2}SCAN	6.1400	1.99	6.1400	1.99	12.2800	1.99	90.0773	0.09	90.2056	0.23	90.0315	0.03	2.18	13.54

the relativistic effects associated with heavy elements such as lead. In lead halide perovskites, spin-orbit coupling has a significant influence on the conduction band, reducing the band gap and modifying the bands through the splitting of the Pb 6p states. Consequently, while the absolute values of the calculated band gaps are underestimated, the inclusion of spin-orbit coupling provides a more physically realistic representation of the electronic structure and the evolution of the band edges. As the primary objective of the electronic structure calculations was to investigate trends in the band gap as a result of structural changes, PBE+SOC represents an appropriate balance between computational efficiency and physical accuracy.

Table C.4: Comparison of the calculated band gaps of the $n = 1$ Ruddlesden–Popper (RP) and Dion–Jacobson (DJ) structures using different functional, including spin-orbit coupling.

Functional	$n = 1$ **RP**		$n = 1$ **DJ**	
	Band Gap (eV)	**Difference (%)**	**Band Gap (eV)**	**Difference (%)**
Experiment	2.30	–	2.36	–
PBEsol	2.05	10.87	2.04	13.56
PBE	2.20	4.35	2.22	5.93
PBEsol+D3	1.95	15.22	1.95	17.37
PBE+D3	2.13	7.39	2.12	10.17
r^{2}SCAN	2.46	6.96	2.46	4.24
PBE+SOC	1.40	39.13	1.47	37.71